MRI Studies of Gas Hydrodynamics in Automotive Particulate Filters

Jonathan David Cooper

Supervisor: Prof. L.F. Gladden

Department of Chemical Engineering and Biotechnology
University of Cambridge

This dissertation is submitted for the degree of
Doctor of Philosophy

St Catharine's College

October 2019

Declaration

The work presented in this thesis has been carried out at the Magnetic Resonance Research Centre and Department of Chemical Engineering and Biotechnology, University of Cambridge, United Kingdom, between October 2015 and September 2019. This thesis is the result of my own work and includes nothing which is the outcome of work done in collaboration except as declared in the Preface and specified in the text. It is not substantially the same as any that I have submitted, or, is being concurrently submitted for a degree or diploma or other qualification at the University of Cambridge or any other University or similar institution except as declared in the Preface and specified in the text. I further state that no substantial part of my thesis has already been submitted, or, is being concurrently submitted for any such degree, diploma or other qualification at the University of Cambridge or any other University or similar institution except as declared in the Preface and specified in the text. It does not exceed the prescribed word limit for the relevant Degree Committee (65,000 words and 150 figures.)

Jonathan David Cooper
October 2019

MRI Studies of Gas Hydrodynamics in Automotive Particulate Filters

Jonathan David Cooper

Particulate filters are used to remove harmful particulate matter (PM) from the exhaust gas of automobiles. They are required in most modern vehicles to achieve compliance with legal limits set on vehicle emissions and are often combined with a catalyst to increase their functionality as an emission control technology. Knowledge of the exhaust gas hydrodynamics in filter systems is crucial for the optimisation of their structure and operation. The nature of most filters, i.e. opaque and brittle, means most anemometry methods are inapplicable. In this work, magnetic resonance imaging (MRI) is applied to measure gas hydrodynamics in such filters. This methodology is used as it provides a non-invasive means of measuring gas flows in complex geometries.

The first part of this thesis focuses on the fundamental hydrodynamics of gas at the ends and in the channels of filters. The first measurements of laminar and turbulent flows at the filter entrance and exit are made. These show the features expected from literature simulations but also additional turbulent effects not previously predicted. Possible challenges facing future CFD comparisons with this work are also explored. The gas flow fields in the channels are measured, allowing calculation of the through-wall or filtration velocity. This provides data for comparison with 1D and 3D CFD models at a range of flow rates. The 3D CFD model is validated for modest Reynolds numbers and allowed parameters such as flow profile shape and wall friction to be explored. The 1D model shows agreement with the measured data when these parameters were allowed to vary with the through-wall velocity. The MRI data is also combined with an analytical filtration model to predict the filtration behaviour and total filtration efficiency of PM.

The second part of this thesis explores the preparation and operation of filters. Catalysts are applied to filters using a washcoat slurry, a process which can cause non-uniform distributions of washcoat in the filter and perturb the gas flow. Washcoat distributions are difficult to measure non-destructively due to the filter opacity. MRI allows perturbations to the gas flow fields to be measured and changes to the wall permeability estimated using the aforementioned 1D model. This is performed for three model washcoated GPF samples. The permeability estimations agree with porosimetry measurements and reveal a variety of non-uniform washcoat distributions in the filters, which is predicted to impact the pressure drop and filtration behaviour. This method is applied to commercial filters which are loaded with PM from a real-world engine to three different levels. The PM-free filters show a non-uniform washcoat distribution and the PM deposits mostly in the regions of low washcoat loading and high through-wall velocity.

Acknowledgements

I would like to start by thanking my supervisor, Professor Lynn Gladden, for all her help, support and guidance over the past four years. Her knowledge and advice has been invaluable and it has been a pleasure to be a part of her group. I would also like to thank my industrial supervisor, Dr Andrew York, for his wealth of knowledge surrounding emission control and trivia of nearly every variety. His direction has been crucial in shaping this thesis and his procurement of samples and insight has been essential for its completion.

Special thanks are due to Drs Mick Mantle and Andrew Sederman for their tuition and wealth of knowledge surrounding NMR and chemical engineering. Their support solved many problems, both major and trivial, and is greatly appreciated. This extends to other members past and present of the MRRC, including Drs Nicholas Ramskill, Adam Colbourne, Hilary Fabich and Nicholas Rice, for their training and assistance.

Thanks are due to several employees at Johnson Matthey: Dr Tim Watling for his 1D numerical model, numerous discussions regarding filter structure and operation, and literature references; Dr Li Liu for explaining and performing the 3D CFD simulations; Dr Hugh Stitt for his general and specialised advice on all things chemical engineering; Dr Iain Hitchcock and Maciah Smith for running mercury porosimetry measurements; Emily Price for preparing GPF samples.

I am grateful to both the Engineering and Physical Sciences Research Council (EPSRC) and Johnson Matthey for funding my CASE award and allowing me to study for this PhD. I would also like to thank St Catharine's College, Cambridge for financial assistance in presenting my work in Florence.

Finally, I would like to thank my friends and colleagues who shared the highs and lows of postgraduate research with me, and my family and Izzi for their unending love and support.

Exposure of work

Publications

J.D. Cooper, N.P. Ramskill, A.J. Sederman, L.F. Gladden, A. Tsolakis, E.H. Stitt, A.P.E. York. Insights into Automotive Particulate Filters using Magnetic Resonance Imaging. *Johnson Matthey Technology Review* (2020), 64, 165-179. doi:10.1595/205651320x15754757907469

J.D. Cooper, L.F. Gladden, A.J. Sederman, A.P.E. York. Magnetic Resonance Imaging of the Internal and External Hydrodynamics in Wall-flow Particulate Filters. *SAE Technical Paper Series* (2019) 2019-01-2286.

J.D. Cooper, N.P. Ramskill, A.P.E. York, T.C. Watling, L. Liu, A.J. Sederman, E.H. Stitt, L.F. Gladden. Numerical and experimental studies of gas flow in a particulate filter. *Chemical Engineering Science* (2019) 209, 115179. doi:10.1016/j.ces.2019.115179

J.D. Cooper, A.P.E. York, A.J. Sederman, L.F. Gladden. Measuring velocity and turbulent diffusivity in wall-flow filters using compressed sensing magnetic resonance. *Chemical Engineering Journal* (2019), 377, 119690. doi:10.1016/j.cej.2018.08.076.

Presentations

J.D. Cooper, A.J. Sederman, A.P.E. York, L.F. Gladden. Gas transport in particulate filters. *Johnson Matthey Academic Conference* (JMAC), University of Warwick, 9th - 10th April 2019. Oral presentaton.

J.D. Cooper, A.J. Sederman, A.P.E. York, L.F. Gladden. Measuring turbulence in wall-flow particulate filters using compressed sensing gas-phase MRI. *25th International Symposium on Chemical Reaction Engineering* (ISCRE), Florence, Italy, 20th - 24th May 2018. Oral presentation.

J.D. Cooper, A.P.E. York, L.F. Gladden. MRI studies of gas flow in particulate filters. *Department of Chemical Engineering and Biotechnology Graduate Conference*, Cambridge, 25th - 26th April 2018. Oral presentation.

J.D. Cooper, L. Liu, E.H. Stitt, A.J. Sederman, A.P.E. York, L.F. Gladden. Measuring gas flow in wall-flow filters using MRI and CFD. *Johnson Matthey Academic Conference* (JMAC), Burleigh Court, Loughborough, 10th - 11th April 2018. Poster presentaton.

J.D. Cooper, L.F. Gladden, A.J. Sederman, A.P.E. York. Gas-phase MRI Measurements of Inertial Contributions to DPF Pressure Drop. *Johnson Matthey Academic Conference* (JMAC), Burleigh Court, Loughborough, 11th - 12th April 2017. Poster and flash presentaton.

J.D. Cooper, A.P.E York, L.F. Gladden. Nuclear Magnetic Resonance Studies of Particulate Filters. *Johnson Matthey Academic Conference* (JMAC), Burleigh Court, Loughborough, 12th - 13th April 2016. Poster presentaton.

Table of contents

Chapter 1

Introduction

1.1 Automotive emissions

Fig. 1.1: Photographic comparison of pollution in Beijing taken after rain (left) and during what would be a sunny day (right) in 2005. Photgraph taken by Bobak Ha'Eri and used under the CC BY-SA 2.5 license.

It is well known that the emissions from automobiles, i.e. the combustion products of fuel, have negative impacts on the environment. Carbon dioxide (CO_2) is the most well known and an unavoidable product of combustion that contributes to the greenhouse effect [1]. However, there are many more undesirable products that have destructive effects such as acid rain and petrochemical smog (Fig. 1.1), posing both an environmental and public health risk. There are four main categories of pollutant [2]:

- **Carbon monoxide** (CO) is formed from the incomplete combustion of fuel in the engine. CO binds competitively to haemoglobin in blood to form carboxyhaemoglobin and reduces the capacity for oxygen to bind, resulting in carbon monoxide poisoning. It can also increase the concentration of ozone and methane in the troposphere, leading to an increase in the greenhouse effect, production of photochemical smog, interference with photosynthesis and oxidative damage to animal respiratory systems.

- **Hydrocarbons** (HCs) comprise a range of organic species (alkanes, olefins, aromatics etc.) formed through the incomplete or lack of combustion in the engine. This is usually due to insufficient temperature in the engine cylinders (e.g. due to a cold start), though fuel rich conditions also contribute. HCs are often toxic or carcinogenic themselves, but can also form tropospheric ozone and are a major component of petrochemical smog.

- **Oxides of nitrogen**, primarily NO and NO_2 and commonly referred to as NOx, are produced via the oxidation of nitrogen (N_2) under the high pressure and temperature conditions in engine cylinders. NOx can react with atmospheric moisture to form nitric acid (a key component of acid rain) or with volatile organic compounds (VOCs) to form ozone, petrochemical smog and toxic nitrogen-containing organic species.
- **Particulate matter** (PM), a suspension of microscopic soot particles in air, is a result of incomplete mixing and combustion in the engine cylinder. In addition to soot, it can also contain ash and condensed organic and inorganic compounds. PM deposits in the respiratory system and can cause both cardiovascular and respiratory problems, including asthma, emphysema, cancer, birth defects and premature death [3, 4]. The formation and characteristics of PM are outlined in §1.2.2.

These pollutants typically make up less than 1% of species leaving the engine, but are responsible for most of the health risks associated with automotive exhaust gas [5]. It is estimated that exposure to PM2.5 (particulates with diameters less than 2.5 µm) accounted for 4.2 million deaths in 2015 [6]. Other types of pollutants are also present, e.g. sulfur-containing compounds, however these have been significantly reduced through additional fuel processing.

The most common types of internal combustion engine used in the automotive industry are gasoline (petrol) and diesel engines. Although both are ubiquitous on the roads, there are some key differences between the two that lead to different emission profiles. First, diesel engines have a higher compression ratio[1] than petrol engines, giving a higher thermal efficiency and hence lower CO_2 emissions per distance travelled. Secondly, diesel engines are run under more lean (excess oxygen) conditions than petrol engines, resulting in well-mixed regions of fuel which undergo more complete combustion and produce fewer CO and HC emissions. Thirdly, the lean conditions and greater compression ratio of diesel engines results in a high oxygen concentration and greater temperature in the cylinder, hence more NOx is produced than in gasoline engines. Finally, gasoline is composed of lighter hydrocarbons than diesel, meaning it is less viscous, easier to atomise and ignites at a lower temperature. For gasoline direct injection (GDI) engines, fuel injection occurs during the intake stroke, meaning there is sufficient time for the fuel to uniformly disperse before ignition. Diesel engines inject fuel towards the end of the compression stroke and so there is less time for the fuel to adequately mix before ignition. This results in greater particulate matter emissions for diesel engines. Gasoline engines that use port fuel injection (PFI) have more time for mixing compared with GDI engines.

Due to the dangers of automotive pollutants to human and environmental health, legislation has been introduced to limit automotive emissions, such as the Euro directives [7]. These limits have become increasingly strict over the years in response to greater numbers

---

[1] The compression ratio is the ratio of the maximum and minimum cylinder volumes in a cycle. Typical values are between 6:1 and 12:1 for gasoline engines, and between 14:1 and 23:1 for diesel engines.

of vehicles on the roads and more awareness of the health effects of pollutants (Table 1.1). Initial attempts at reducing pollutant emissions focused on improving engine design and operation. However, it quickly became apparent that this would not be sufficient and exhaust after-treatment would be necessary for compliance. This spurred the development of emission control technologies, namely catalytic converters and particulate filters. Initially, gasoline vehicles only required catalytic converters due to their lower PM emissions, and particulate filters were exclusive to diesel (called diesel particulate filters, DPFs). As the effectiveness of DPFs increased and diesel emissions fell below those of gasoline vehicles, the legislation imposed the same limits for both and has resulted in the development of gasoline particulate filters (GPFs).

Table 1.1: European emission standards for passenger vehicles.

Engine	Stage	Year	CO	HC + NOx	HC	NOx	PM	PM number[2]
			g km^{-1}					km^{-1}
Gasoline	Euro 1	1992	3.16	-	1.13	-	-	-
	Euro 2	1996	2.2	-	0.5	-	-	-
	Euro 3	2000	2.3	0.2	-	0.15	-	-
	Euro 4	2005	1.0	0.1	-	0.08	-	-
	Euro 5	2009	1.0	0.1	-	0.06	-	-
	Euro 6	2014	1.0	0.1	-	0.06	0.005	6×10^{11}
Diesel	Euro 1	1992	3.16	-	1.13	-	-	-
	Euro 2	1996	1.0	-	0.7	-	0.08	-
	Euro 3	2000	0.64	-	0.56	0.5	0.05	-
	Euro 4	2005	0.5	-	0.3	0.25	0.025	-
	Euro 5a	2009	0.5	-	0.23	0.18	0.005	-
	Euro 5b	2011	0.5	-	0.23	0.18	0.005	6×10^{11}
	Euro 6	2014	0.5	-	0.17	0.08	0.005	6×10^{11}

1.2 Emission control technologies

1.2.1 Catalytic converters

The most common method of reducing gaseous pollutants is through chemical conversion using metal catalysts. This is usually achieved with a parallel channel, flow-through monolith coated with a catalyst and support. Due to the thermal stresses experienced from the reaction exotherm, the monolith is often made from a ceramic substrate e.g. cordierite.

The first catalytic converters widely used were two-way catalysts for gasoline engines that oxidised CO and HCs to CO_2 and H_2O. Further development saw the introduction of three-way catalysts (TWC) - the stoichiometric air-fuel ratio in gasoline engines allowed the simultaneous reduction of NOx to N_2 [8, 9]. This is not possible in diesel exhausts as

---

[2] Number limits were introduced due to the large particle size distribution of PM (§1.2.2)

the air rich conditions create a net oxidising environment. Instead, diesel after-treatment consists of a separate diesel oxidation catalyst (DOC) and NOx reducing component [10]. There are two main technologies used for this: selective catalytic reduction (SCR) and the lean NOx trap (LNT). SCR uses a reservoir of a nitrogen-based reducing agent, such as ammonia or urea, to reduce the NOx in the exhaust stream. This requires a periodic top-up of the reducing agent. LNTs function by trapping NOx on a metal oxide (e.g. barium oxide) *via* surface adsorption during normal running conditions. The trap is regenerated by creating a temporary reducing atmosphere, e.g. by introducing diesel fuel that will be oxidised by the NOx.

1.2.2 Particulate filters

In order to effectively remove PM from the exhaust stream, the origins and properties of PM must first be understood. This section focuses on diesel PM and DPFs, however the underlying principles are also applicable to gasoline vehicles. A brief overview of the differences between diesel and gasoline systems is therefore given.

Particulate matter

During the operation of a diesel engine, the diesel fuel is injected into and atomises in the engine cylinder as the compression stroke is completed. However, the fuel does not completely mix with the air before ignition occurs, resulting in incomplete combustion of the fuel and the presence of reactive intermediates. The process of PM formation is outlined below and shown in Fig. 1.2 [11].

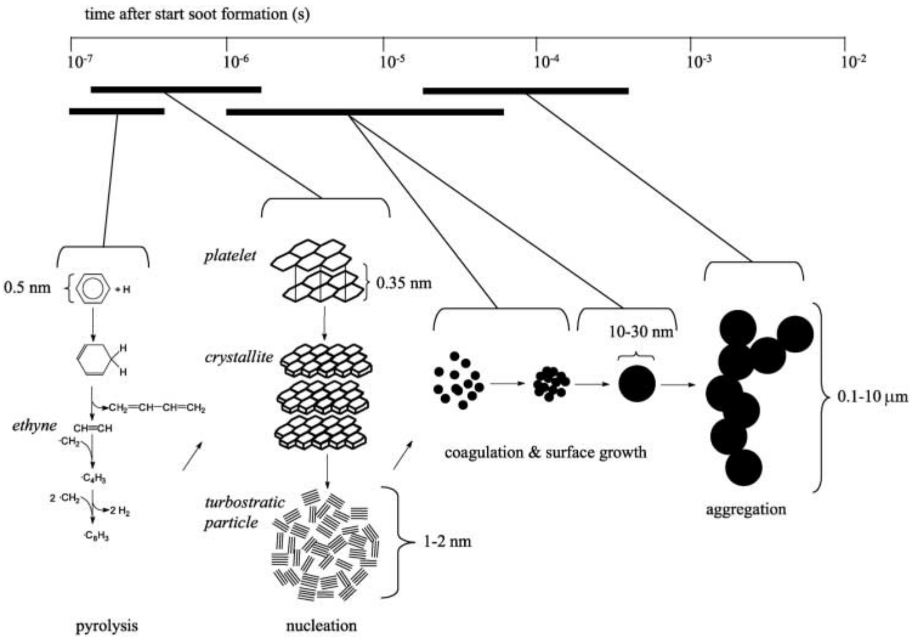

Fig. 1.2: Schematic illustration of the formation of PM. Taken from [11].

Formation of PM occurs in local fuel-rich environments, where a lack of oxygen results in pyrolysis and incomplete combustion of fuel to form small unsaturated molecules, such as acetylene. These molecules subsequently polymerise and cyclise to form polycyclic structures called *platelets*. Regular stacking of platelets, akin to graphite, results in *crystallites*, which can then stack irregularly to form *turbostratic particles*. Gas-phase species can adsorb on the surface of turbostratic particles, resulting in particle growth. Turbostratic particles also coagulate and aggregate to form *primary soot particles*. Further aggregation of primary soot particles leads to the large range of PM sizes observed (Fig. 1.3) [11].

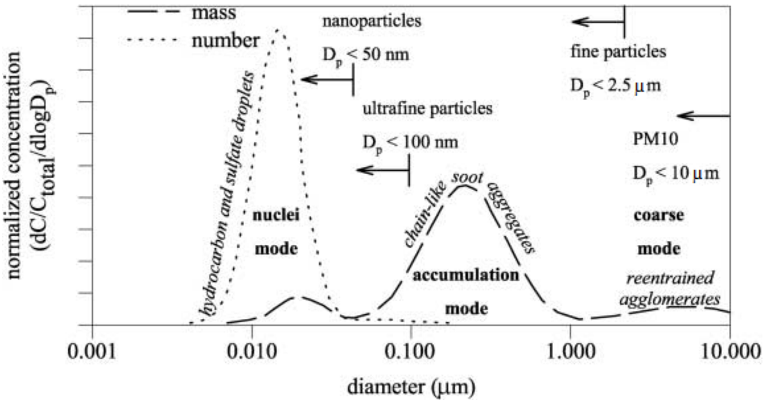

Fig. 1.3: Typical mass- and number-weighted particle size distributions of PM. Taken from [11].

Upon expulsion from the cylinder, the exhaust gas temperature lowers and species condense onto the surface of the primary soot particles. These include hydrocarbons, sulfates and other inorganic compounds. Together, these form the PM that is emitted into the atmosphere.

Filter structure and operation

The most common design for particulate filters is based on a porous, parallel channel monolith. Alternate channels are plugged at opposite ends, creating a checkerboard pattern and forcing the exhaust gas to flow through the walls of the monolith, depositing the PM in the process (Fig. 1.4). The channel geometry is most often square or octo-square (asymmetric square) (Fig. 1.5), but triangular and hexagonal filters also exist [12]. Filters are typically 100 mm to 150 mm in length and 100 mm to 200 mm in diameter. Filters typically operate under gas flows of Re = 100 - 2000 based on the mean superficial velocity in the channels.

Wall-flow filters initially filter PM through deep bed filtration. In deep-bed filtration, there are three main mechanisms of particle collection: inertial, interception and Brownian [13, 14] (Fig. 1.6). Inertial filtration occurs when soot particles with significant mass deviate from the gas stream lines and impact the collector. Interception occurs when particles follow streamlines that pass within the particle radius of the collector. Brownian filtration occurs when the random Brownian motion of small particles causes them to hit the collector. Of

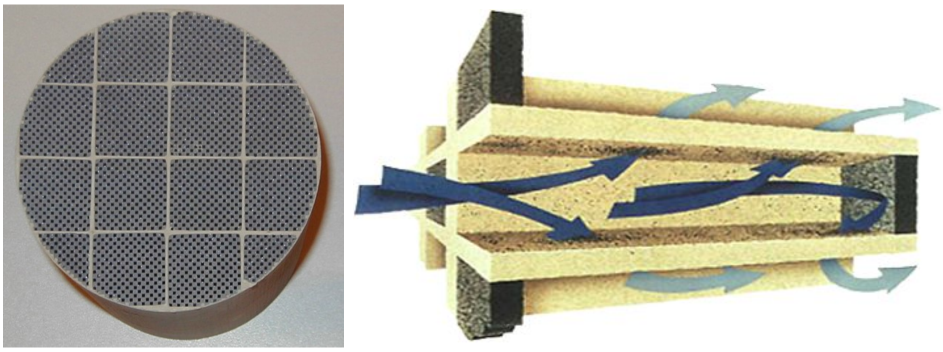

(a) (b)

Fig. 1.4: (a) Photograph of a catalysed filter illustrating the 'checkerboard' pattern (photograph by Michael Kairo in the public domain). (b) Illustration showing the operating principles of particulate filters (Corning Inc.)

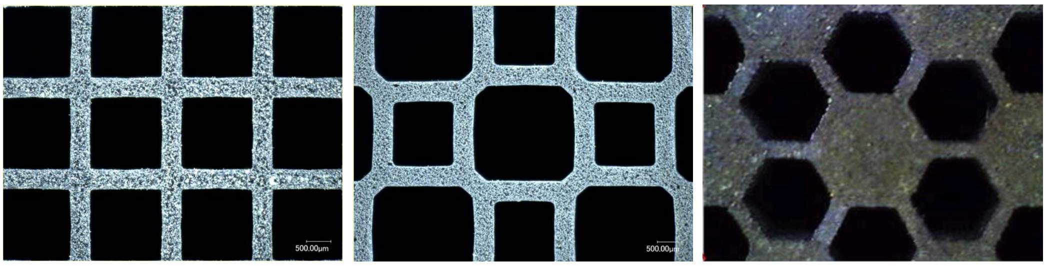

(a) (b) (c)

Fig. 1.5: Different channel geometries for DPFs. (a) Square (Sumotomi Chemical Co. Ltd.) (b) Octo-sqaure (Sumotomi Chemical Co. Ltd.) (c) Hexagonal [12]

these, only the interception and Brownian mechanisms are expected to be significant in filtration in the wall due to the size range of PM ($< 10\,\mu m$) [15], though inertial collection may be significant when considering flow down the channels. As exhaust flow continues and more PM is filtered, the filter pores become constricted and a soot cake forms on the walls of the inlet channels. This cake then filters subsequent PM.

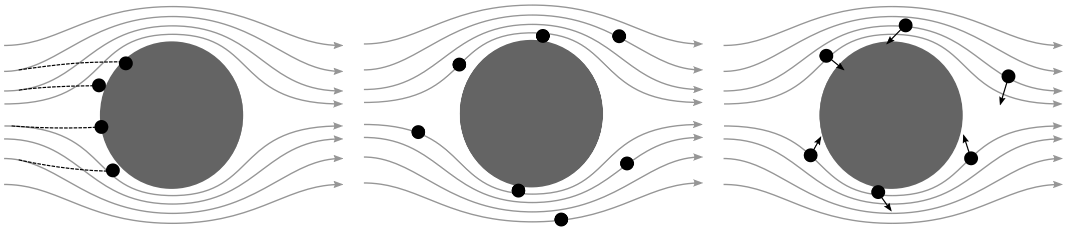

(a) (b) (c)

Fig. 1.6: Illustrations of (a) inertial, (b) interception and (c) Brownian deposition mechanisms. The grey circle represents the spherical collector and the black circles represent particles to be collected.

A small soot loading is beneficial as it increases the filtration efficiency of the filter, however as this layer grows it increases engine backpressure, reduces fuel economy and can cause irreversible damage to the filter system. In order to avoid this, the filter must be regenerated by oxidising the PM to gaseous CO_2. This can be achieved in two ways [16]. First, the PM can react with oxygen in the presence of a catalyst ($C + O_2 \longrightarrow CO_2$). This requires an exhaust temperature of 600 °C to 650 °C for light-off. As either the engine must be revved higher or fuel must be injected into the exhaust stream to achieve such temperatures, this method is called *active regeneration*. Second, the PM can be oxidised by the NO_2 present in the exhaust gas ($C + 2\,NO_2 \longrightarrow CO_2 + 2\,NO$). This occurs at 250 °C to 300 °C, is referred to as *passive regeneration* and is preferred due to the smaller exotherm generated. Other methods of regeneration, including fuel-borne catalysts, fuel burners and electric heaters, have also been used [17].

Filters are often combined with catalysts and catalytic converters in order to both improve pollutant abatement and reduce the total space under a vehicle chassis needed for engine aftertreatment [18]. For DPFs, various different combinations exist; these are illustrated in Fig. 1.7. The first to be developed was the continuously regenerating trap (CRT®), consisting of a DOC upstream of the filter. The DOC removed CO and HCs, whilst converting NO to NO_2 to facilitate passive regeneration. This was developed into the catalysed CRT® (CCRT®), which includes a DOC in the filter itself. This creates a catalytic cycle in the filter, where NO generated from passive regeneration is converted back to NO_2 to continue regeneration. The need for an additional DOC upstream was eliminated with the development of the catalysed soot filter (CSF®), in which all the DOC is located on the filter substrate. However, all diesel systems listed thus far also require a separate reduction catalyst, either SCR or LNT, downstream of the filter. Recent work has integrated SCR into the filter in the selective catalytic reducing trap (SCRT®), though this requires a separate DOC for full emission control and active regeneration of the filter. In contrast, GPFs are much simpler to combine with catalytic converters due to the stoichiometric air-fuel ratio and are usually coated with a TWC to form a three-way filter (TWF).

Due to the large thermal stresses experienced during operation, filters are typically fabricated from some ceramic material [19–21]. Cordierite ($(Mg,Fe)_2Al_3(Si_5AlO_{18})$) was initially used because of its low thermal expansion coefficient along one axis. However, its relatively low melting point of 1430 °C risks melting during the regeneration process. Silicon carbide (SiC) was later favoured as it has more mechanical, thermal and chemical resilience, as well as providing a more uniform pore structure and improving the soot load limit [22]. More recently, aluminium titanate (Al_2TiO_5) has gathered favour, showing increased filtration efficiencies and soot loading limits, and low pressure drops [23]. These materials also show chemical compatibility with both catalytic washcoats and non-carbon engine emissions.

Filters have been very successful in reducing both the mass and number of particulates emitted from vehicles. Filtration efficiencies of over 95% by mass and 99% by number are regularly reported for DPFs under a range of driving conditions [17]. This is typically

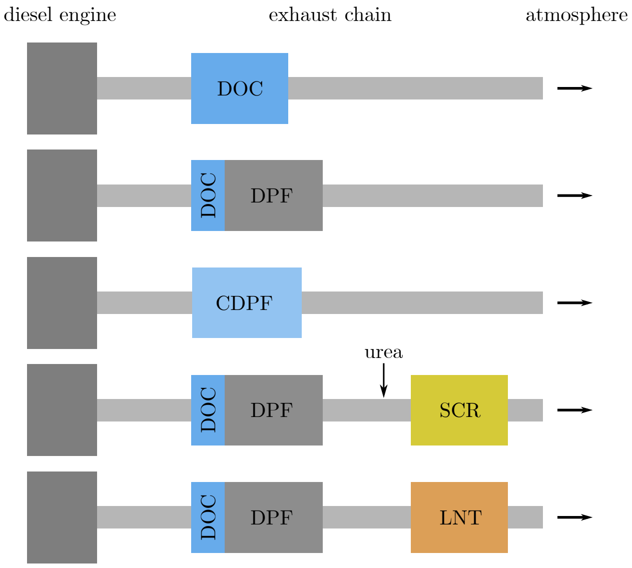

Fig. 1.7: Illustrations of typical implementations of emission control technologies in the diesel exhaust chain. Adapted from [18].

sufficient to reduce total PM emissions to within legal limits. However, this high efficiency usually occurs after some period of soot loading; the filtration efficiencies observed during initial loading of bare filters are typically >10% lower [24]. While less literature is available for gasoline systems, GPFs have seen similar success with reported filtration efficiencies of between 70 and 100% [25].

Difference between diesel and gasoline systems

Since the introduction of three-way catalysts in the 1970s and 80s, gasoline engines have generally been considered 'cleaner' vehicles than diesel ones despite their generally lower fuel economy. However, the development of emission control systems for diesel engines has resulted in comparable emissions between diesel and gasoline engines, and the focus has now returned to gasoline vehicles [17]. Between the two types of gasoline engine, PFI engines typically emit at least two orders of magnitude less PM than DI engines, but suffer from worse fuel economy and performance. As such, PFI engines are now less common and most interest in gasoline emission abatement is focused on DI engines.

The primary difference between diesel and gasoline particulate matter is the number of particles emitted. DI gasoline engines emit around 2-3 orders of magnitude fewer particles per volume than diesel engines. The particle size distribution of gasoline and diesel PM both show relatively similar log-normal distributions with modal values of about 70 nm to 110 nm [26]. However, due to the high filtration efficiency of DPFs, the particulate emissions of a diesel engine with a DPF are now less than that of a DI engine with no filter [27]. This has led to the adoption of similar PM limits for gasoline engines as discussed earlier.

Although DPFs and GPFs share the same structure and operating principles, their implementations are different due to the difference in PM number. GPFs can be manufactured shorter than DPFs, as less PM is expected to accumulate. This is due to both the lower PM numbers in gasoline exhaust and the higher exhaust temperatures in gasoline vehicles encouraging regeneration. However, the slow initial loading of soot and ash in GPFs leads to a greater filtration efficiency penalty at start-up. Initial efficiencies of ∼60% have been measured, though these increase to around 80% with 1 g to 2 g of ash [28] and potentially up to 100% with 5 g [29]. It is anticipated that continued research will improve the perfomance of GPFs as has been seen with DPFs.

1.3 Scope of thesis

In this thesis, two areas associated with the gas hydrodynamics in filters are addressed using magnetic resonance imaging (MRI) methods.

First, the fundamental hydrodynamics of gas flow in particulate filters is investigated. As the operation of filters is dependent on the gas flow through them, knowledge of the true flow behaviour is essential for optimisation. MRI, as will be outlined in Chapters 2 and 3, allows for non-invasive and spatially resolved measurement of gas velocity, which can be compared with predictions from numerical models. These comparisons can then be used to validate and inform the formulation of such models.

Second, the effect of preparation and operation of filters on the gas flow inside them is probed. As described above, catalytic washcoats are often applied to filters. This application changes the porous structure of the filter and will change the gas hydrodynamics inside the filter. Likewise, operation of particulate filters results in the deposition of soot in the filter and corresponding changes in the porous structure occur. Understanding the effects of both these processes is needed to ensure the preparation and operation of filters is optimal and reliable.

1.4 Structure of thesis

Chapter 1 provides a brief background on automotive vehicle emissions and their control, with an emphasis on diesel and gasoline particulate filters. It concludes with an outline of the thesis.

Chapter 2 describes the underlying theory behind the magnetic resonance methods used in the thesis. In particular, it covers the physical basis of the magnetic resonance phenomenon, how NMR experiments are performed and the basics of MRI and dynamic MRI. Advanced acquisition and processing methods, i.e. compressed sensing, are also covered.

Chapter 3 reviews the use of gas-phase MRI and assesses its limits for probing gas hydrodynamics. This is achieved through consideration of relaxation times and diffusion coefficients, and their impact on the achievable spatial and displacement resolutions. This information is then used to test the feasibility of experiments relating to measuring through-wall flow in filters.

Chapter 4 focuses on the hydrodynamics of gas flow entering and exiting a filter on a channel scale. Measurements of laminar and turbulent flows are made to characterise the flow fields, identify regions of pressure losses and provide comparisons to simulations in the literature.

Chapter 5 presents results from a preliminary CFD study on entrance and exit effects in filter geometries, comparing the different geometries and turbulence models, and compares predictions with the MRI results shown in Chapter 4.

Chapter 6 explores the hydrodynamics in the channels and walls of the filter. Measurements of the axial gas velocity along the length of the filter, in both the inlet and outlet channels, allow calculation of the through-wall velocity at a range of flow rates and use in an analytical filtration model. The experimental results are used to validate a 3D CFD model of filter flow, which is then used to develop and validate a simpler 1D model.

Chapter 7 extends the previous work to study the hydrodynamics in GPF substrates. The effect of applying washcoats and catalyst to filter substrates is measured through both the changes to the porous structure and the gas flow fields.

Chapter 8 investigates the effect of engine operation and soot loading on the gas transport inside a catalysed GPF.

Chapter 9 investigates the potential of NMR propagators to study gas flows in particulate filter systems. The CFD results from Chapter 6 are used to test the feasibility of using propagators to probe gas hydrodynamics in filter systems.

Chapter 10 contains a summary of results and outlines potential future work in this area.

1.5 References

[1] J. L. Sarmiento, C. L. Quere, E. Boyle, D. Kari, A. Schmittner, J. Elser, N. Gruber, K. Hibbard, P. Högberg, S. Linder, F. T. Mackenzie, B. M. III, T. Pedersen, Y. Rosenthal, S. Seitzinger, V. Smetacek, W. Steffen. Oceanic Carbon Dioxide Uptake in a Model of Century-Scale Global Warming. *Science* (1996) 274 (5291), 1346–1350. doi:10.1126/science.274.5291.1346.

[2] M. V. Twigg. Progress and future challenges in controlling automotive exhaust gas emissions. *Applied Catalysis B: Environmental* (2007) 70 (1-4), 2–15. doi:10.1016/J.APCATB.2006.02.029.

[3] C. A. Pope III, R. T. Burnett, M. J. Thun, E. E. Calle, D. Krewski, K. Ito, G. D. Thurston. Lung Cancer, Cardiopulmonary Mortality, and Long-term Exposure to Fine Particulate Air Pollution. *JAMA* (2002) 287 (9), 1132. doi:10.1001/jama.287.9.1132.

[4] D. W. Dockery, C. A. Pope, X. Xu, J. D. Spengler, J. H. Ware, M. E. Fay, B. G. Ferris, F. E. Speizer. An Association between Air Pollution and Mortality in Six U.S. Cities. *New England Journal of Medicine* (1993) 329 (24), 1753–1759. doi:10.1056/NEJM199312093292401.

[5] M. Lippmann. *Environmental Toxicants: Human Exposures and Their Health Effects: Third Edition*, volume 71. John Wiley and Sons (2008). doi:10.1002/9780470442890.

[6] A. J. Cohen, M. Brauer, R. Burnett, H. R. Anderson, J. Frostad, K. Estep, K. Balakrishnan, B. Brunekreef, L. Dandona, R. Dandona, V. Feigin, G. Freedman, B. Hubbell, A. Jobling, H. Kan, L. Knibbs, Y. Liu, R. Martin, L. Morawska, C. A. Pope, H. Shin, K. Straif, G. Shaddick, M. Thomas, R. van Dingenen, A. van Donkelaar, T. Vos, C. J. L. Murray, M. H. Forouzanfar. Estimates and 25-year trends of the global burden of disease attributable to ambient air pollution: an analysis of data from the Global Burden of Diseases Study 2015. *The Lancet* (2017) 389, 1907–1918. doi:10.1016/S0140-6736(17)30505-6.

[7] European Commission. Commission Regulation (EU) No 459/2012 of 29 May 2012 amending Regulation (EC) No 715/2007 of the European Parliament and of the Council and Commission Regulation (EC) No 692/2008 as regards emissions from light passenger and commercial vehicles (Euro 6). *Technical report* (2012).

[8] M. V. Twigg. Catalytic control of emissions from cars. *Catalysis Today* (2011) 163 (1), 33–41. doi:10.1016/J.CATTOD.2010.12.044.

[9] H. Gandhi, G. Graham, R. McCabe. Automotive exhaust catalysis. *Journal of Catalysis* (2003) 216 (1-2), 433–442. doi:10.1016/S0021-9517(02)00067-2.

[10] T. Johnson. Diesel Engine Emissions and Their Control. *Platinum Metals Review* (2008) 52 (1), 23–37. doi:10.1595/147106708X248750.

[11] B. A. A. L. van Setten, M. Makkee, J. A. Moulijn. Science and technology of catalytic diesel particulate filters. *Catalysis Reviews* (2001) 43 (4), 489–564. doi:10.1081/CR-120001810.

[12] K. Tsuneyoshi, K. Yamamoto. Experimental study of hexagonal and square diesel particulate filters under controlled and uncontrolled catalyzed regeneration. *Energy* (2013) 60, 325–332. doi:10.1016/J.ENERGY.2013.07.069.

[13] C. Gutfinger, G. I. Tardos. Theoretical and experimental investigation on granular bed dust filters. *Atmospheric Environment* (1979) 13 (6), 853–867. doi:10.1016/0004-6981(79)90276-2.

[14] K. W. Lee, J. A. Gieseke. Collection of Aerosol Particles by Packed Beds. *Environmental Science and Technology* (1979) 13 (4), 466–470. doi:10.1021/es60152a013.

[15] A. G. Konstandopoulos, J. H. Johnson. Wall-Flow Diesel Particulate Filters—Their Pressure Drop and Collection Efficiency (1989) 890405. doi:10.4271/890405.

[16] C. Goersmann. Catalytic Coatings for Active and Passive Diesel Particulate Filter Regeneration. *Monatshefte fur Chemie - Chemical Monthly* (2005) 136 (1), 91–105. doi:10.1007/s00706-004-0261-z.

[17] B. Guan, R. Zhan, H. Lin, Z. Huang. Review of the state-of-the-art of exhaust particulate filter technology in internal combustion engines. *Journal of Environmental*

Management (2015) 154, 225–258. doi:10.1016/j.jenvman.2015.02.027.

[18] M. Ahmadinejad, M. R. Desai, T. C. Watling, A. P. York. Simulation of automotive emission control systems. *Advances in Chemical Engineering* (2007) 33, 47–101. doi:10.1016/S0065-2377(07)33002-0.

[19] A. Okada. Automotive and industrial applications of structural ceramics in Japan. *Journal of the European Ceramic Society* (2008) 28 (5), 1097–1104. doi:10.1016/J.JEURCERAMSOC.2007.09.016.

[20] W. A. Cutler. Overview of Ceramic Materials for Diesel Particulate Filter Applications. pp. 421–430. John Wiley & Sons, Ltd doi:10.1002/9780470291184.ch61.

[21] J. Adler. Ceramic diesel particulate filters. *International Journal of Applied Ceramic Technology* (2005) 2 (6), 429–439. doi:10.1111/j.1744-7402.2005.02044.x.

[22] F. Millo, M. Andreata, M. Rafigh, D. Mercuri, C. Pozzi. Impact on vehicle fuel economy of the soot loading on diesel particulate filters made of different substrate materials. *Energy* (2015) 86, 19–30. doi:10.1016/J.ENERGY.2015.03.076.

[23] T. Boger, J. Jamison, J. Warkins, N. Golomb, C. Warren, A. Heibel. Next Generation Aluminum Titanate Filter for Light Duty Diesel Applications. *SAE Technical Paper Series* 2011-01-0816. doi:10.4271/2011-01-0816.

[24] M. K. Khair. A Review of Diesel Particulate Filter Technologies (2003) 2003-01-2303 (724). doi:http://dx.doi.org/10.4271/2003-01-2303.

[25] T. Johnson, A. Joshi. Review of Vehicle Engine Efficiency and Emissions. *SAE Technical Paper Series* (2018) 2018-01-0329. doi:10.4271/2018-01-0329.

[26] S. J. Harris, M. Maricq. Signature size distributions for diesel and gasoline engine exhaust particulate matter. *Journal of Aerosol Science* (2001) 32 (6), 749–764. doi:10.1016/S0021-8502(00)00111-7.

[27] P. Whitaker, P. Kapus, M. Ogris, P. Hollerer. Measures to Reduce Particulate Emissions from Gasoline DI engines. *SAE International Journal of Engines* (2011) 4 (1), 2011–01–1219. doi:10.4271/2011-01-1219.

[28] C. K. Lambert, T. Chanko, M. Jagner, J. Hangas, X. Liu, J. Pakko, C. J. Kamp. Analysis of Ash in Low Mileage, Rapid Aged, and High Mileage Gasoline Exhaust Particle Filters. *SAE International Journal of Engines* (2017) 10 (4), 2017–01–0930. doi:10.4271/2017-01-0930.

[29] T. Boger. “Global Experiences of the Adoption of Gasoline Particulate Filter (GPF) on Gasoline Direct Injection (GDI) Cars. In *13th Integer Emissions Summit Europe & AdBlueForum 2017*. Dresden (2017) .

Chapter 2

Theory of Nuclear Magnetic Resonance

2.1 Principles of Nuclear Magnetic Resonance

2.1.1 Zeeman splitting

Spin is a form of angular momentum that is an intrinsic property of subatomic particles and analogous to the dynamics of classical spinning objects. While electrons also possess spin, this chapter will exclusively focus on the spin of nuclei, without accounting for its origin from protons and neutrons. Nuclear spin is described by the quantum number, I, which is quantized and equal to zero, positive half-integers or positive integers. A nucleus with spin I has $2I + 1$ possible nuclear spin states, m_I, with values from $-I$ to I in integer steps that correspond to different orientations of the spin angular momentum. In the absence of a magnetic field, these energy levels are degenerate and the populations of all states are equal. When an external magnetic field is applied, the degeneracy is lifted and the energy of each state is given by

$$E_{m_I} = -\gamma \hbar B_0 m_I, \tag{2.1}$$

where γ is the gyromagnetic ratio of the nucleus, $\hbar$ is the reduced Planck's constant and B_0 is the magnetic field strength. This effect is called Zeeman splitting. For a nucleus with $I = 1/2$, such as ^{1}H (protons) or ^{19}F, there exists two energy levels ($m_I = \pm 1/2$, also called α and β) with an energy gap of $\Delta E = \gamma \hbar B_0$ (Fig. 2.1). It is this energy difference is responsible for the nuclear magnetic resonance (NMR) signal, meaning that only nuclei with $I \neq 0$ can be studied with NMR. The populations of each state, N_{m_I}, at thermal equilibrium is governed by the Boltzmann distribution,

$$\frac{N_{-1/2}}{N_{1/2}} = e^{-\Delta E/kT}, \tag{2.2}$$

where k is the Boltzmann constant and T is the temperature of the nuclei. The majority of experiments in this thesis are performed using a magnetic field strength of 9.4 T (corresponding to a proton resonance frequency of 400 MHz) and at 20 °C, giving a population ratio of $\sim 1 - 10^{-5}$. This is a far smaller ratio than many other spectroscopic techniques and imposes a limit on the signal-to-noise ratio (SNR) of NMR experiments. However, due to the large ensembles of nuclei used ($\sim 10^{23}$), an NMR signal is obtainable for even relatively dilute solutions.

While Zeeman splitting forms the basis for a quantum mechanical description of NMR, a superficial treatment using this method does not adequately describe the phenomenon

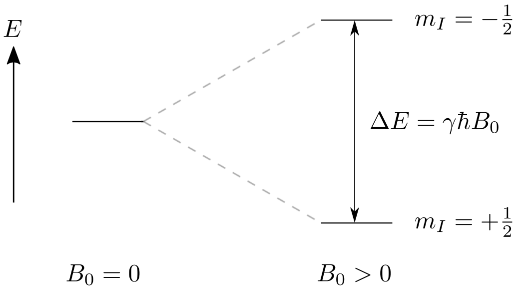

Fig. 2.1: Diagram showing the energy levels for a nucleus with $I = 1/2$ in a magnetic field of strength B_0.

without further application and understanding of quantum mechanics. However, due to the angular momentum and magnetic moment associated with nuclear spins and the large number of spins present in an NMR experiment, a vector-based model using classical mechanics exists. This model requires no quantum mechanical knowledge or treatment and satisfactorily describes the NMR and MRI experiments performed in this thesis. The textbooks by Keeler [1] and Levitt [2] offer a more complete description of NMR using quantum mechanical approach. For the rest of this chapter, a nuclear spin of $I = 1/2$ will be assumed.

2.1.2 Vector model

Atomic nuclei that posses a non-zero nuclear spin also possess a nuclear magnetic moment which can be orientated in any direction. In the absence of an applied magnetic field, there is no preference for the spins to point in any particular direction, and so the sum of all spins in an ensemble is zero. When a magnetic field $\mathbf{B}$ is applied, there is a slight energetic preference for the spins to align parallel to the magnetic field (Fig. 2.2 (a)), which gives rise to a bulk magnetisation $\mathbf{M}$ when summed over the ensemble (Fig. 2.2 (b)). Analogous to the motion of a gyroscope spinning in the presence of gravity, the angular momentum of the bulk magnetisation causes it to precess around the axis of the applied magnetic field. This motion is described by

$$\frac{\mathrm{d}\mathbf{M}}{\mathrm{d}t} = -\mathbf{M} \times \gamma\mathbf{B}. \tag{2.3}$$

If the bulk magnetisation is parallel to the applied magnetic field, as is the case at equilibrium, no motion is present. However, if the bulk magnetisation is tilted away from the applied magnetic field, the bulk magnetisation begins to precess about the magnetic field. This is known as Larmor precession. For a static magnetic field $\mathbf{B} = (0, 0, B_0)$, the precession frequency is

$$\omega_0 = -\gamma B_0, \tag{2.4}$$

where ω_0 is also known as the Larmor frequency and γ can be interpreted as the ratio of the nuclear magnetic moment to its angular momentum (Fig. 2.2 (c)). As the precession of the bulk magnetisation is what is detected in NMR experiments, Equation 2.4 is important in NMR theory.

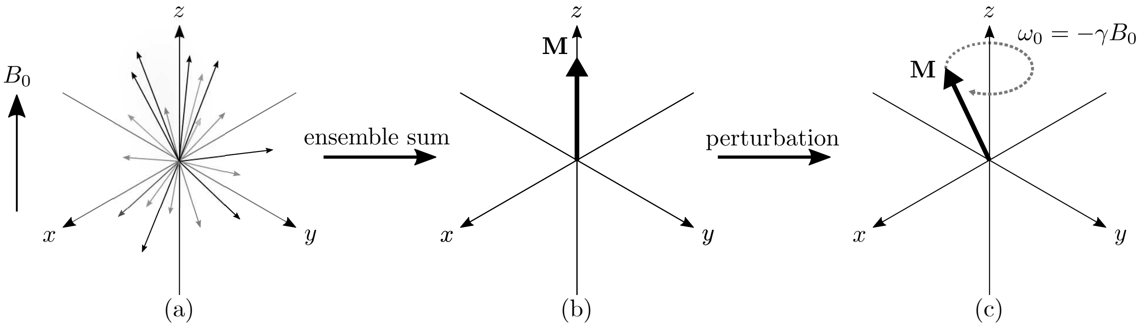

Fig. 2.2: (a) Nuclear spins have a slight preference to align with the applied magnetic field, B_0. (b) The ensemble sum of the individual spins is parallel to the applied field and called the bulk magnetisation, $\mathbf{M}$. (c) When perturbed from equilibrium, the bulk magnetisation precesses about B_0 at the Larmor frequency ω_0.

2.1.3 Signal excitation and detection

As the equilibrium state of the bulk magnetisation is parallel to the applied magnetic field, a perturbation is required to move the bulk magnetisation away from equilibrium and instigate Larmor precession. This is achieved by applying a second magnetic field, B_1, perpendicular to B_0, *via* a linearly oscillating electromagnetic field. Such a field is applied for a short period of time and is called a radiofrequency (r.f.) pulse. This oscillatory field has a frequency near that of the Larmor frequency so that it excites all frequencies of interest. Such a pulse is said to be ‘on-resonance’ and is often called a hard pulse. The oscillating field is generated by passing r.f. alternating current through a coil wound such that the generated field is perpendicular to the applied magnetic field. The linear oscillating magnetic field can be thought of as two counter-rotating magnetic fields B_1^+ and B_1^-, each rotating at the applied frequency ω_1 in opposite directions with half the strength of the net magnetic field. One of these rotating fields will be rotating in-phase with the Larmor precession and is responsible for excitation, and one will be rotating in the opposite direction which has negligible effect on the bulk magnetisation. In the rotating reference frame, this in-phase component of the applied field is not oscillating, and so will result in the rotation of the bulk magnetisation about the axis of the applied field, forgoing any complicated nutations that would result from a static applied field. This process of using an applied field to rotate the bulk magnetisation from its equilibrium orientation by up to 90° into the transverse xy plane is called excitation. The same method can also be used to rotate the bulk magnetisation by 180° for signal inversion or refocusing (Section 2.1.6). The direction of the applied pulse is called its phase (as it can be modulated by altering the phase of the applied alternating current) and is important for phase cycling (Section 2.1.7).

The signal is detected through electromagnetic induction of the rotating bulk magnetisation during Larmor precession (Fig. 2.3 (a)). The coil used for excitation of the magnetisation through r.f. pulses is also used for this detection. Through Faraday's law, the rotating bulk magnetisation induces an oscillating current in the coil, which is then recorded as a free induction decay (FID) (Fig. 2.3 (b)). In order to differentiate between positive and negative oscillations, a method known as quadrature detection is used. The key feature of quadrature detection is that the signal is split into two channels and mixed with two generated signals of identical frequency but with a phase difference of 90°. This allows the sampling of points from two orthogonal directions with only one r.f. coil. Quadrature detection encodes the signal $S(t)$ at a given time as a complex number,

$$S(t) = S_x(t) + iS_y(t), \tag{2.5}$$

by alternately sampling and digitizing the induced voltage from each channel at regular time intervals. The time difference between these samples is called the dwell time. The magnitude of the signal is proportional to the length of the bulk magnetisation vector. The signal is then Fourier transformed to give the frequency spectrum $s(\omega)$ (Fig. 2.3 (c)). As the signal is complex, the spectrum is also complex and is a superposition of absorption and dispersion lineshapes. A constant phase is often added to the signal so that the real component has a pure absorption lineshape.

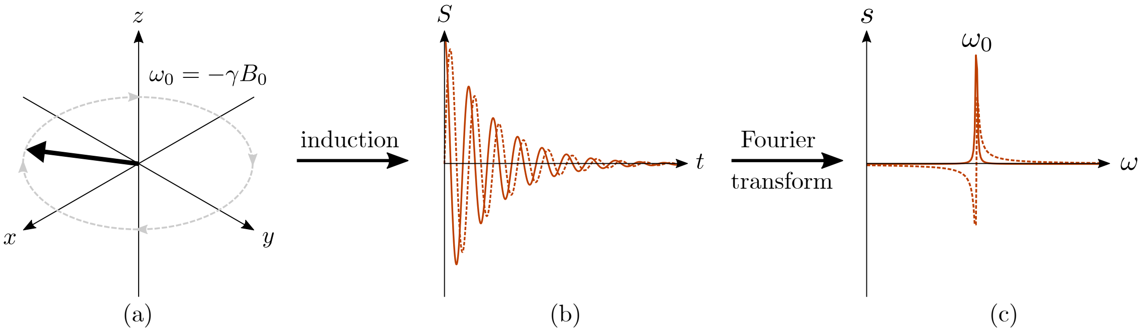

(a) (b) (c)

Fig. 2.3: (a) The precessing bulk magnetisation induces current in coils aligned with the x and y axes. (b) The induced voltage is detected as the NMR signal S. The solid and dotted lines show the induced signal, or FID, in the x and y channels respectively. The decay in signal strength is due to relaxation. (c) Fourier transformation of the NMR signal gives the frequency spectrum s. The solid and dotted lines show the absorption and dispersion lineshapes respectively.

Rotating frame

In NMR spectroscopy, the precession frequencies often occur on the order of 100-1000 MHz. However, the range of frequencies that are of interest in NMR spectroscopy and MRI typically cover less than 100 kHz, far smaller than the absolute precession frequency. If the NMR signal was detected with no intervention, the spectrometer hardware would not be able to sample all the frequencies of interest and no useful information would be obtained from the experiment. Hence, spectrometers use heterodyning to remove the higher frequency out of the induced voltage, meaning that the sampling rate only needs to cover the smaller range of frequencies. This has led to most treatments of NMR being undertaken in a rotating reference frame to reflect the heterodyne process, which has the additional benefit of simplifying the mathematical complexity of the treatment. The basis vectors of the static reference frame, (x, y, z), are transformed into the reference frame, (x', y', z') by the equation

$$\begin{pmatrix} x \\ y \\ z \end{pmatrix} = \begin{pmatrix} \cos(\omega_{\mathrm{r}}t) & \sin(\omega_{\mathrm{r}}t) & 1 \\ -\sin(\omega_{\mathrm{r}}t) & \cos(\omega_{\mathrm{r}}t) & 1 \\ 1 & 1 & 1 \end{pmatrix} \begin{pmatrix} x' \\ y' \\ z' \end{pmatrix}, \tag{2.6}$$

where ω_{r} is the receiver frequency to that is mixed out and is typically set to the Larmor frequency of the nucleus under study. For a magnetic field of strength B with Larmor frequency ω used as the receiver frequency, this transformation gives an apparent Larmor frequency of

$$\Delta\omega = -\gamma \Delta B, \tag{2.7}$$

where $\Delta\omega = \omega - \omega_0$ is called the offset and $\Delta B = B - B_0$ is the apparent or reduced magnetic field.

2.1.4 Selective excitation

During excitation in NMR, the shape of the r.f. pulse is usually described by a narrow rectangle function in the time domain. This creates a broad sinc response in the frequency domain (via the Fourier transform, $\mathcal{F}$), which provides an approximately uniform excitation profile over the frequency range of interest. These are both practical and useful for most NMR spectroscopy experiments. However, some studies warrant the selective excitation of a single frequency. This is achieved using a selective, or soft, radiofrequency pulse. The shape or envelope $E(t)$ of the pulse is chosen to give the desired shape of the frequency response $f(\omega)$ (Eq. (2.8)). This is usually a Gaussian function as the frequency response is well-behaved i.e. there are minimal artefacts due to truncation of the r.f. pulse. The frequency modulation of the pulse is used to control the central excitation frequency ω_0.

$$f(\omega - \omega_0) = \mathcal{F}\{E(t) \exp\left[-i\omega_0 t\right]\}. \tag{2.8}$$

2.1.5 Relaxation

When a sample of nuclear spins is placed in a strong magnetic field, the bulk magnetisation does not immediately exist. Instead, the bulk magnetisation develops over a period of time, typically between several milliseconds and several minutes though potentially much shorter or longer. This process of the magnetisation returning to its equilibrium state is called *relaxation* and is composed of two separate processes, *spin-lattice* and *spin-spin* relaxation.

Spin-lattice (or longitudinal) relaxation controls the return of the z-component of the bulk magnetisation to its equilibrium value M_z (here the term *lattice* refers to the surroundings). This occurs exponentially, with time constant T_1, and follows the equation

$$M_z(t) = M_{z,\mathrm{eq}} - (M_{z,\mathrm{eq}} - M_z(0))\,\mathrm{e}^{-t/T_1}, \tag{2.9}$$

where $M_{z,\mathrm{eq}}$ is the component of the equilibrium magnetisation in the z-direction and $M_z(0)$ is the magnetisation at $t = 0$. The microscopic mechanism arises from the changes in orientation and position of individual spins caused by thermal motion. As the orientation of a spin (and hence its local magnetic field) changes, it causes neighbouring spins to nutate. This results in each spin rotating in a near-random fashion; only when the ensemble of spins are considered will the Larmor precession be evident. This rotation due to local fields is the mechanism that allows the spins to return to equilibrium with their surroundings - they are now coupled with thermal motion. For this reason, spin-lattice relaxation is sometimes referred to as the enthalpic component of relaxation. Typically a recovery time of 5 × T_1 is given between r.f. excitations, allowing the magnetisation to fully recover to equilibrium. The value of T_1 is usually measured by perturbing the magnetisation from equilibrium using a 90° or 180° pulse (Fig. 2.4 (a)), waiting for some delay (Fig. 2.4 (b)), applying a 90° pulse and acquiring the FID (Fig. 2.4 (c)). By varying the delay length, the recovery of the magnetisation back to equilibrium can be measured and T_1 obtained through fitting Eq. (2.9).

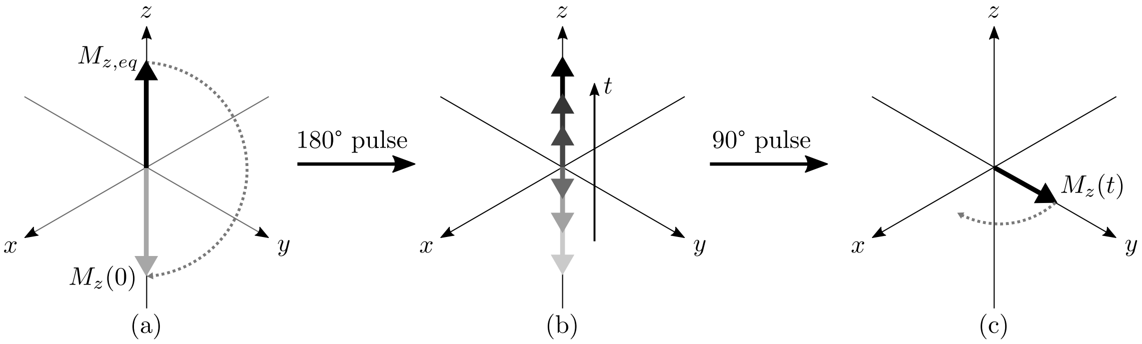

Fig. 2.4: Illustration of spin-lattice relaxation and its measurement. (a) The magnetisation is rotated away from equilibrium, either through a 90° (saturation recovery) or 180° (inversion recovery) pulse. (b) The magnetisation relaxes in the z-direction back to equilibrium as Eq. (2.9). (c) The size of the z-magnetisation can be measured at time t by applying a 90° pulse and acquiring the FID.

Spin-spin (or transverse) relaxation controls the decay of the transverse components of the magnetisation, M_{xy}, to zero. It is also an exponential process, with time constant T_2, following the equation

$$M_{xy}(t) = M_{xy}(0)\,\mathrm{e}^{-t/T_2}. \tag{2.10}$$

T_2 values can be measured by rotating the magnetisation into the transverse plane using a 90° pulse (Fig. 2.5 (a)) and acquiring the FID as the signal magnitude decays (Fig. 2.5 (b)), though for practical reasons discussed in Section 2.1.6 it is usually measured following one or more 180° pulses. A series of 180° pulses is known as a CPMG (Carr-Purcell-Meiboom-Gill) echo train and allows measurement of T_2 with minimal effects of diffusion and magnetic field inhomogeneity.

One mechanism of spin-spin relaxation is the same as spin-lattice relaxation; the local fields generated by individuals spins affect not only the z-component of the orientation of neighbouring spins, but also the transverse components, driving the transverse magnetisation to equilibrium at the same time as the longitudinal magnetisation. This is known as the non-secular component of transverse relaxation. However, there are other contributions besides this. The z-component of the local magnetic fields also affects the local Larmor frequency. The result of this is that the spins across an entire sample will be precessing at slightly different frequencies, and as such the phase of each oscillation will lose coherence, the bulk magnetisation will decrease in magnitude and the signal will appear to decay. This is called the secular component of transverse relaxation. Due to the random and irreversible nature of thermal motion, both of these components are irreversible.

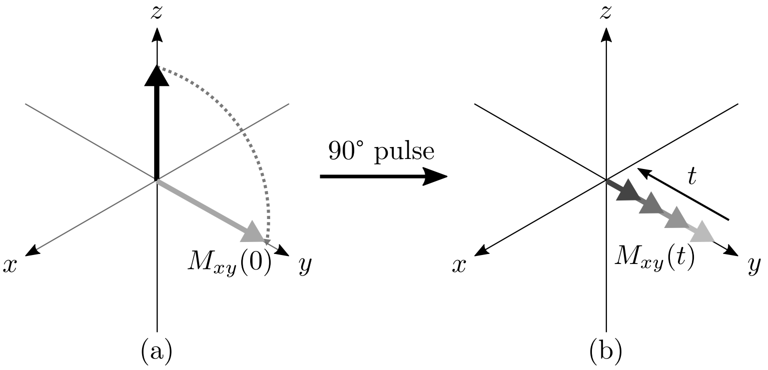

Fig. 2.5: Illustration of spin-spin relaxation and its measurement. (a) The magnetisation is rotated away from equilibrium through a 90° pulse. (b) The transverse component of the magnetisation relaxes towards the z-axis as Eq. (2.10). This can be measured by acquiring the FID of the precessing magnetisation.

The local fields responsible for relaxation can arise from many origins, but are commonly due to the magnetic fields from nearby nuclei with $I \neq 0$ and the presence of paramagnetic species (i.e. unpaired electrons.) One further component that contributes to transverse relaxation is the variation of the B_0 field across the NMR sample. As with the secular component, any inhomogeneity in the B_0 field will cause a dephasing of the precessing spins due to slightly different Larmor frequencies. However, unlike the secular component which is inherent and irreversible, the spatial distribution of the B_0 inhomogeneities stays constant, and so the effect can be reversed under certain conditions, i.e. negligible diffusion, using a spin echo (described in Section 2.1.6). This reversible contribution has a time constant T_2', which is related to the irreversible transverse relaxation time T_2 by

$$\frac{1}{T_2^*} = \frac{1}{T_2} + \frac{1}{T_2'}, \tag{2.11}$$

where T_2^* is the observed transverse relaxation time constant.

2.1.6 Spin and stimulated echoes

As described in Section 2.1.5, spins in experiencing slightly different B_0 fields due to inhomogeneity in the main field will precess at slightly different frequencies (Fig. 2.6 (a)). This results in a loss of coherence as the spins begin to dephase and is registered macroscopically as a decay in the bulk magnetisation in the transverse plane. Such dephasing can be reversed through the use of a spin echo. By applying a 180° pulse along the x- or y-axis at time τ after excitation, the phase of every spin is inverted, $\phi \rightarrow -\phi$ (Fig. 2.6 (b)). If the spins have not moved significantly within the field, their precession will begin to rephase (Fig. 2.6 (c)) until the coherence is fully restored after a second τ (Fig. 2.6 (d)). This effect is called a spin echo and is a key component of many pulse sequences (Fig. 2.7 (a)).

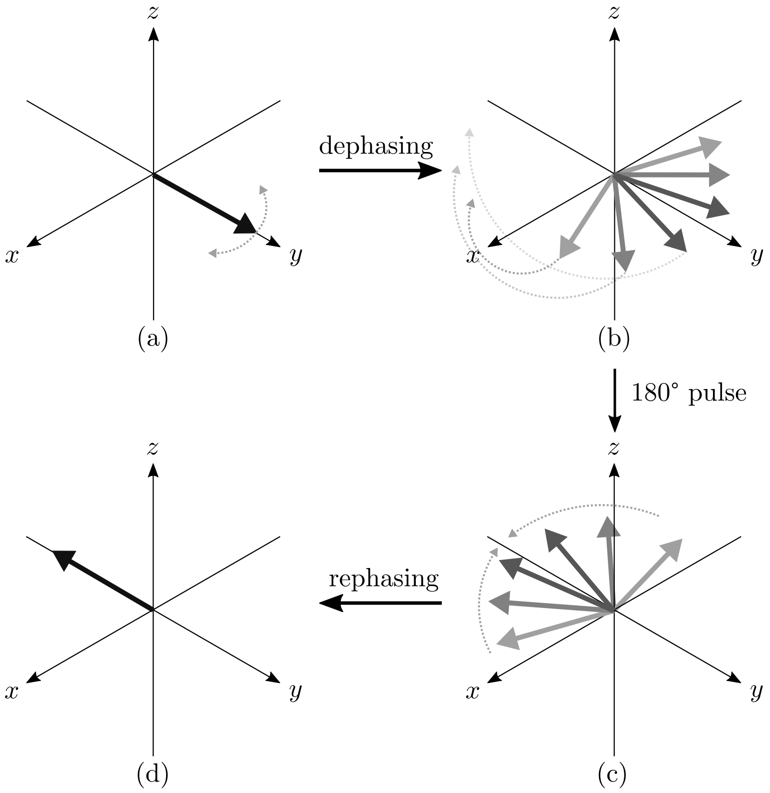

Fig. 2.6: Illustration of a spin echo formation. (a) Spins experiencing different magnetic fields precess at different frequencies, resulting in dephasing. (b) The dephased spins are rotated by 180° after time τ. (c) The dephased spins continue to precess at different frequencies, but the inverted phases mean they begin to rephase. (d) After total time 2τ, the spins have completely rephased, forming the spin echo before dephasing again.

A similar phenomena is called a stimulated echo. In a stimulated echo, a spin echo is formed through the application of two 90° pulses instead of one 180° pulse (Fig. 2.7 (b)). The first 90° pulse rotates half of the magnetisation onto the z-axis, with half still present in the xy plane. The former is said to be stored in the z-direction. The second 90° pulse recalls this stored magnetisation into the xy-plane after τ_s, where it can be detected again. For this component, the two 90° pulses act as an effective 180° pulse, refocusing the magnetisation after τ. During the storage period, half of the magnetisation continues to dephase from transverse relaxation, meaning that up to half of the signal is lost during a stimulated echo. However, as the stored magnetisation relaxes with T_1, this initial loss of magnetisation can be compensated for if

$$\frac{1}{T_1} < \frac{1}{T_2} - \frac{\ln 2}{\tau_s}. \tag{2.12}$$

Hence, for systems with relatively short T_2 values, e.g. liquids in porous media, stimulated echoes allow the magnetisation to decay with T_1 rather than T_2. This permits longer time intervals between signal excitation and detection, allowing longer observation times when displacement encoding is used (Section 2.3).

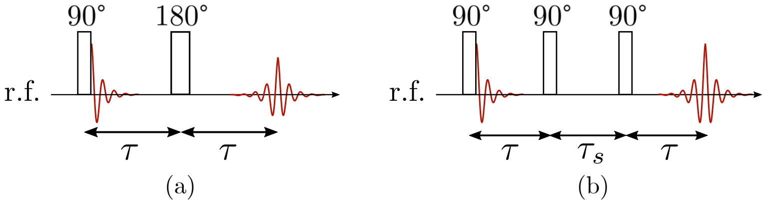

Fig. 2.7: Pulse sequences for (a) a spin echo and (b) a stimulated echo.

2.1.7 Phase cycling

Phase cycling is a method used to remove certain artefacts from NMR experiments. The principle of the technique is to change the phase (i.e. the direction of the B_1 field) of the r.f. pulses and the receiver between different scans. Through careful choice of such phases, unwanted effects and spin coherences can be removed when the acquired data is summed. Different NMR experiments require their own phase cycling scheme depending on the information desired, and most of these are beyond the range of this thesis. However, two important phase cycles will be introduced that correct for common errors in NMR and MRI sequences.

The first phase cycle, CYCLOPS, corrects for errors in the quadrature detection of the NMR signal in a 'pulse-acquire' experiment [3]. Often, the two detectors used will be non-ideal and errors in the acquisition will result in artefacts (Table 2.1). In order to correct this, CYCLOPS cycles the pulse phase by 90° increments and the receiver phase by 180° increments (Table 2.2). The effect of this is to cancel the imperfections of the detectors and return the 'true' NMR signal. This method can be extended to all other pulse sequences and phase cycles to correct the same imperfections.

The second phase cycle, EXORCYCLE, is used to cancel errors in the 180° pulse in spin-echo sequences [4]. The pulses and receiver cycle according to Table 2.3. As the number of pulses increases, the number of steps in the phase cycle also tends to increase as the number of potential coherences grows. Several novel methods, such as cogwheel phase

Table 2.1: Imperfections in quadrature detection and their resulting artefacts.

Name	Description	Artefact
DC offset	A constant voltage added to one or both channels	A peak around $\omega = 0$
Intensity mismatch	Inconsistent signal amplitudes in each channel	A ghost peak at $-\omega$, out of phase by -90°
Phase mismatch	The angle between the two channels is not 90°	A ghost peak at $-\omega$, out of phase by +90°

Table 2.2: CYCLOPS phase cycle.

Step	90° phase / °	Receiver phase / °
1	0	0
2	90	90
3	180	180
4	270	270

cycles [5] and phase incremented echo train acquisition [6] can be used to select the desired coherences.

Table 2.3: EXORCYCLE phase cycle.

Step	90° phase / °	180° phase / °	Receiver phase / °
1	0	0	0
2	0	90	180
3	0	180	0
4	0	270	180

2.2 Magnetic resonance imaging

Magnetic resonance imaging (MRI) was developed independently in the early 1970s by Peter Mansfield and Paul Lauterbur, and allowed non-invasive imaging of both clinical and non-clinical specimens without the use of ionizing radiation. In this section, the theory and implementation of MRI is briefly outlined. A more complete treatment is offered in the texts of Callaghan [7] and Haacke [8].

2.2.1 Spatial encoding and k-space

The underlying motivation of MRI is to spatially resolve NMR measurements, often with some form of relaxation or motion contrast. This is achieved using magnetic field gradients $\mathbf{G}$ that modulate the strength of the z-component of the magnetic field, B_z, in the x-, y-

and z-directions

$$\mathbf{G}(\mathbf{r}) = \left(\frac{\mathrm{d}B_z}{\mathrm{d}x}, \frac{\mathrm{d}B_z}{\mathrm{d}y}, \frac{\mathrm{d}B_z}{\mathrm{d}z}\right), \tag{2.13}$$

where $\mathbf{r} = (x, y, z)$ is the position vector. This allows the Larmor frequency to be encoded as a function of spatial position

$$\omega(\mathbf{r}) = -\gamma\left(B_0 + \mathbf{G}\cdot\mathbf{r}\right), \tag{2.14}$$

which in the rotating frame reduces to

$$\Delta\omega(\mathbf{r}) = -\gamma\mathbf{G}\cdot\mathbf{r}. \tag{2.15}$$

From this, it can be seen that a Fourier transform of the time-domain signal $S(t)$ will lead to a frequency-domain image,

$$\rho(\mathbf{r}) = \int S(t)\exp(-2\pi\gamma\mathbf{G}\cdot\mathbf{r}t)\,\mathrm{d}t. \tag{2.16}$$

In general, the image $\rho(\mathbf{r})$ will have complex elements whose phase can be exploited for more sophisticated measurements. The magnitude of the complex elements is usually taken to return the 'true' image, i.e. the spatial distribution of spins in the sample.

The principle of MRI is illustrated in Fig. 2.8 for a sample of two rectangles of different length. With no gradients applied, the expected NMR spectrum is obtained. However, with a finite gradient applied in one direction, the spectrum is the projection of the spin density onto that direction.

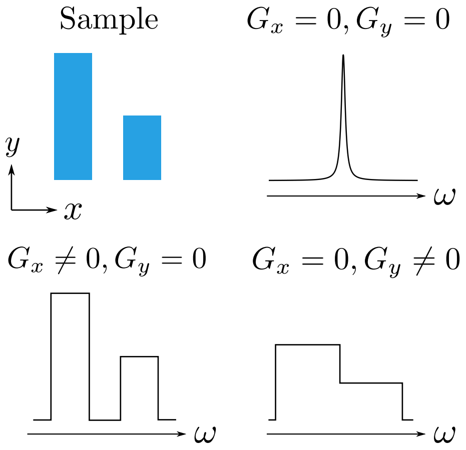

Fig. 2.8: Illustration of encoding position in frequency using magnetic field gradients G_x and G_y.

Mansfield and co-workers defined a reciprocal co-ordinate, $\mathbf{k}$, that represented the spatial frequencies of the real-space image. The $\mathbf{k}$-space coordinate is defined as

$$\mathbf{k} = \frac{\gamma\mathbf{G}t}{2\pi}. \tag{2.17}$$

Substituting this into Eq. (2.16) gives the Fourier pair

$$\rho(\mathbf{r}) = \int S(\mathbf{k}) \exp(-i\mathbf{k} \cdot \mathbf{r}) \, \mathrm{d}\mathbf{k}, \tag{2.18}$$

$$S(\mathbf{k}) = \int \rho(\mathbf{r}) \exp(i\mathbf{k} \cdot \mathbf{r}) \, \mathrm{d}\mathbf{r}. \tag{2.19}$$

Hence, to reconstruct an image mapped onto a certain real-space grid or raster, the corresponding **k**-space raster must be entirely sampled in the MRI experiment. As images are usually displayed on a Cartesian grid, the **k**-space raster is most often sampled rectilinearly. Other non-Cartesian sampling methods are sometimes used but require regridding if a Fourier transform is to be performed [9]. The dimensions of the **k**- and real-space images are related by the equations

$$FOV = \frac{1}{\Delta\mathbf{k}}, \tag{2.20}$$

$$\Delta\mathbf{r} = \frac{1}{\mathbf{k}_{\mathrm{range}}}, \tag{2.21}$$

where FOV is the field-of-view of the image (i.e. the range of sampled real space), $\Delta\mathbf{k}$ is the distance between **k**-space points, $\Delta\mathbf{r}$ is the distance between real-space points (i.e. the image resolution) and $\mathbf{k}_{\mathrm{range}}$ is the range of **k**-space sampled (Fig. 2.9).

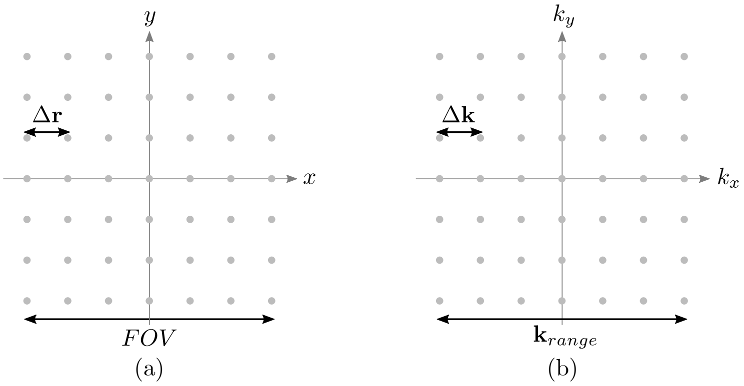

(a) (b)

Fig. 2.9: Key distances in (a) real space and (b) **k**-space.

2.2.2 Gradient echoes

When **k**-space is swept through a line from $-\mathbf{k}$ to $+\mathbf{k}$ using a dephasing and rephasing gradient, a maximum signal is observed at $\mathbf{k} = \mathbf{0}$ as most intensity is located at low spatial frequencies (Fig. 2.10 (a)). This is known as a gradient echo and will have a peak amplitude that decays as T_2^* from excitation. Gradient echoes are often formed during frequency encoded imaging sequences (covered in the following section) as they allow negative and positive **k**-space to be acquired at the same time. Gradient echoes can also be formed after spin echoes; an example of this is shown in Fig. 2.10 (b). Spin echoes also invert the position in **k**-space, $(k_x, k_y, k_z) \rightarrow (-k_x, -k_y, -k_z)$, meaning that the signs of any gradient pulses following a 180° pulse will need to be inverted relative to a sequence without a 180° pulse. By refocusing the magnetisation, the signal decays as T_2 rather than T_2^*, allowing for longer times between signal excitation and detection. This also permits more robust multi-shot sequences, as the signal can be refocused many times with less diffusion attenuation.

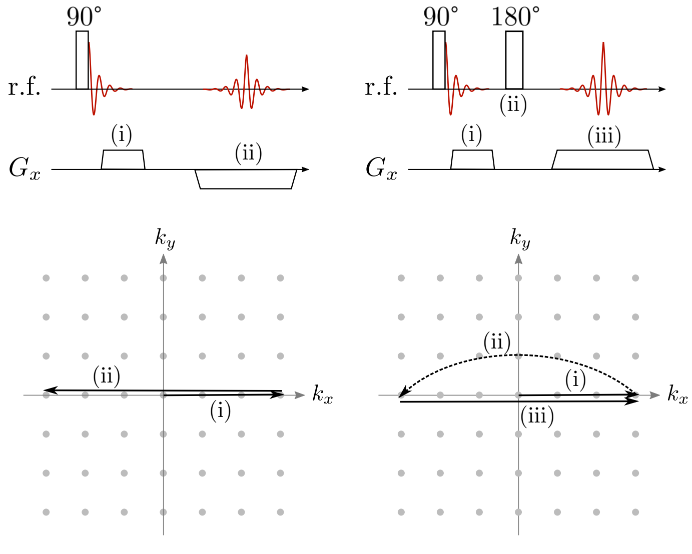

(a) (b)

Fig. 2.10: Pulse sequences and **k**-space trajectories for (a) a gradient echo with T_2^* relaxation and (b) a spin and gradient echo with T_2 relaxation.

Frequency- and phase-encoding

As a gradient echo sweeps across a single line of **k**-space, it can be combined with signal detection to acquire many data points in a single acquisition. This is called frequency encoding. Using a constant readout gradient, $\mathbf{G_r}$, during acquisition gives the **k**-space position as a function of time,

$$\mathbf{k}(t) = \frac{\gamma \mathbf{G_r} t}{2\pi}. \tag{2.22}$$

Frequency encoding is useful for fast acquisitions as it allows many **k**-space points to be sampled in a single acquisition. However, the time dependence of the acquisition means that frequency-encoding is susceptible to artefacts from in-plane motion, relaxation, chemical shift effects and magnetic susceptibility mismatches. While some of these can be abated through shimming, use of spin-echoes and tuning of parameters such as bandwidth, frequency-encoding is somewhat limited in its applicability.

As **k**-space is usually fully sampled to avoid half-sampling artefacts, the readout gradient is usually preceded by a read-dephase gradient. This dephasing moves the hypothetical experiment ‘pointer’ out to the edge of **k**-space, meaning that the readout gradient captures both sides of **k**-space in one acquisition (as illustrated in Fig. 2.10 (b)).

Phase-encoding modulates the strength of the applied gradient $\mathbf{G_{ph}}$ whilst keeping the gradient pulse length t_{ph} constant,

$$\mathbf{k}(\mathbf{G_{ph}}) = \frac{\gamma \mathbf{G}_{\mathrm{ph}} t_{\mathrm{ph}}}{2\pi}. \tag{2.23}$$

Phase encoding allows one **k**-space point to be sampled per acquisition, making it a slow sampling method. However, the advantage of phase encoding is that every point is acquired at a constant time after excitation, removing many artefacts due to motion or relaxation and making phase-encoding a more robust technique. The point-by-point nature of phase-encoding lends itself well to undersampling and compressed sensing methods, outlined in Section 2.4. Acquisition of the FID can also allow T_2^* weighted images to be acquired or the SNR improved if the FID is summed .

2.2.3 Sampling methods

There are a large number of MRI experiments commonly applied, with most using some form of both frequency and phase encoding. NMR pulse sequences are highly modular, which makes comprehensive categorisation more difficult. However, some of the most common are listed below and shown in Fig. 2.11.

- **Spin warp** - frequency and phase encoded - this is one of the simplest MRI experiments in which a single line of **k**-space is acquired per excitation. Phase-encoding is used for the second and third dimensions. A slice selective 180° pulse is used to refocus the magnetisation and the spin echo formed is coincident with the read gradient echo.

- **RARE** [10] - frequency and phase encoded - the rapid acquisition with relaxation enhancement (RARE) sequence extends the spin warp sequence by adding several 180° pulses to form an echo train. Within each spin echo, phase gradients move the **k**-space 'pointer' out in one direction, a read gradient acquires a line of **k**-space and another phase gradient returns the 'pointer' to the central line of **k**-space. This allows several lines of **k**-space to be acquired in a single excitation, reducing the total acquisition time.

- **FLASH** [11] - frequency and phase encoded - the fast low-angle shot (FLASH) sequence removes the spin echo from the spin warp sequence and relies only on a gradient echo during the frequency encoding. This allows a small excitation angle to be used, greatly reducing the recovery time required to return to equilibrium and allowing image acquisition on the order of tens of milliseconds. For this sequence, the exictation pulse must be slice selective if a 2D slice is desired.

- **EPI** [12] - frequency encoded - echo-planar imaging (EPI) was one of the first MRI sequences and allows the entire acquisition of an image in one-shot. Several gradient echoes are used to acquire lines of **k**-space, interspersed with gradient pulses to move the ‘pointer’ between different lines. This method requires excellent magnetic field inhomogeneity and is very susceptible artefacts from motion, chemical shift and magnetic susceptibility mismatches.

- **SPI** [13] - phase encoded - single point imaging (SPI) uses only phase gradients to acquire a single **k**-space point per excitation, making a slow imaging method. However, the lack of frequency encoding means it is incredibly robust and has found useful applications in imaging high Reynolds number fluids and porous materials.
- **Spiral imaging** [14] - frequency encoded - spiral imaging uses oscillating gradient pulses to acquire the entirety of **k**-space in one shot by tracing out a spiral pattern. This is one of the fastest acquisition methods along with EPI. However, it is similarly prone to artefacts. One advantage of spiral imaging is that because the spiral does not lie cleanly on a Cartesian grid, it naturally undersamples **k**-space in an incoherent manner and so can be used with compressed sensing to great effect.

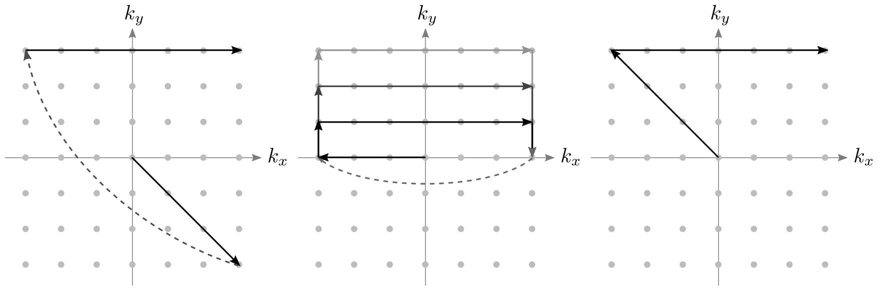

(a) Spin warp (b) RARE (c) FLASH

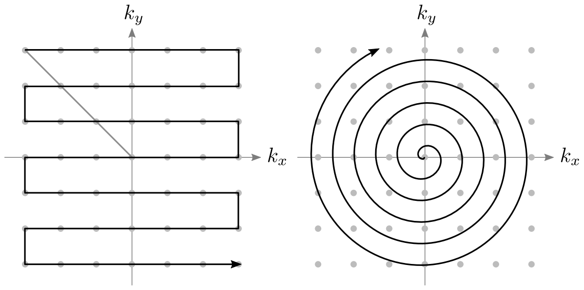

(d) EPI (e) Spiral

Fig. 2.11: Common **k**-space sampling methods. Solid lines show the trajectories through **k**-space and dotted lines show position inversions from 180° pulses.

2.2.4 Slice selection

In many MRI experiments, **k**-space is only sampled in 2 dimensions to form a 2-dimensional image. In order to avoid obtaining a projection of the entire sample, a thin slice must be selectively excited and detected. This is achieved by using the frequency-selective properties of a soft pulse with the application of a magnetic field gradient G_{slice} (Fig. 2.12). In the same way as MRI, the gradient creates a linear relation between frequency and position, allowing a slice to be excited. The vector width of this slice Δr is related to the width of the soft pulse bandwidth $\Delta\omega$ by

$$\Delta\omega = \gamma G_{\text{slice}} \Delta r. \tag{2.24}$$

To achieve a top-hat response in the frequency domain, which is desired to have a uniform averaging of spin density within the slice, a soft pulse with a sinc envelope needs to be applied. However, as the sinc function oscillates as it decays, practical implementation of such a soft pulse results in truncation artefacts in the slice profile. To circumvent this, most slice selective pulses employ a Gaussian shaped pulse, resulting in a Gaussian frequency response with no truncation artefacts but non-uniform averaging in the slice direction. The width of the slice is typically measured as the full-width half-maximum (FWHM) of the Gaussian profile.

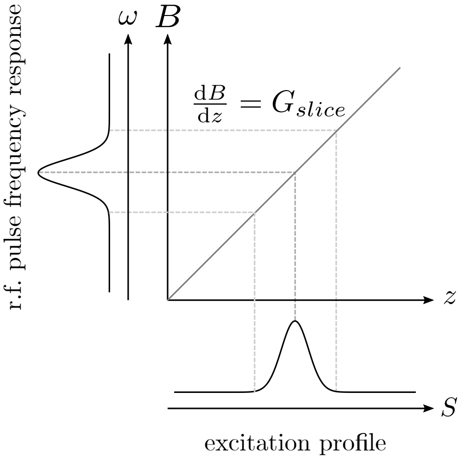

Fig. 2.12: Relationship between the r.f. pulse frequency response, the applied magnetic field gradient and the spatial excitation during slice selection.

2.3 Displacement encoding

Magnetic field gradients can also be used to encode the displacement of spins, and indeed any derivative of spin position with time. The textbook by Callaghan [15] provides an in-depth description of the subject.

Displacement encoding can be understood as an extension of the principles of MRI. In Eq. (2.15), it was implicitly assumed that the position of each spins $\mathbf{r}$ was time-independent, which is often untrue. In order to account for the displacement of spins, their time-dependent position $\mathbf{r}(t)$ can be expanded as a Taylor series,

$$\mathbf{r}(t) = \mathbf{r} + \frac{\mathrm{d}\mathbf{r}}{\mathrm{d}t}t + \frac{1}{2}\frac{\mathrm{d}^2\mathbf{r}}{\mathrm{d}t^2}t^2 + ... \tag{2.25}$$

The phase of the NMR signal is given by the integral

$$\phi = \int \omega(t)\,\mathrm{d}t = \int \gamma \mathbf{G}(t) \cdot \mathbf{r}(t)\,\mathrm{d}t. \tag{2.26}$$

Substituting Eq. (2.25) into Eq. (2.26) gives the signal phase expanded as a function of position and time,

$$\phi(\mathbf{r}) = \gamma \left[\mathbf{r} \cdot \int \mathbf{G}(t)\,\mathrm{d}t + \frac{\mathrm{d}\mathbf{r}}{\mathrm{d}t} \cdot \int t\mathbf{G}(t)\,\mathrm{d}t + + \frac{1}{2}\frac{\mathrm{d}^2\mathbf{r}}{\mathrm{d}t^2} \cdot \int t^2\mathbf{G}(t)\,\mathrm{d}t + ... \right], \tag{2.27}$$

where the derivatives of position are assumed to not change significantly across the gradient applications. The integral terms can be thought of as the moments of the magnetic field gradients, with

$$\mathbf{M}_n = \frac{1}{n!} \int t^n \mathbf{G}(t)\,\mathrm{d}t \tag{2.28}$$

defining the n-th moment. By equating the first derivative of spin position with spin velocity, it can be seen that gradients with a first moment will encode the velocity in the phase of the NMR signal, and likewise for higher derivatives and moments. This is the basis of displacement encoding in NMR and MRI.

2.3.1 Velocity encoding

Any single gradient pulse will have a first moment, and will encode the spin velocity in the signal phase. However, as it will also have a zeroth moment, the spin position will also be encoded and the phase will be a superposition of the two. In order to overcome this, velocity encoding gradients are designed such that they null the zeroth moment whilst providing a non-zero first moment. This is most simply achieved by applying a gradient pulse with strength $\mathbf{G}_v$ and duration δ, followed by another pulse with the same strength and length but in the opposite direction (Fig. 2.13 (a)). In terms of $\mathbf{k}$-space, this is the same as moving out some distance from $\mathbf{k} = \mathbf{0}$ and returning back to the centre, giving $\mathbf{M}_0 = \mathbf{0}$. Evaluating Equation 2.28 gives $\phi = \gamma \mathbf{v} \cdot \mathbf{G}_v \delta^2$. The gradient pulses are commonly separated with an evolution time Δ between the leading edge of each pulse. Often, the gradient pulses will be applied either side of a 180° pulse (Fig. 2.13 (b)) and the echo decay will be acquired. this experiment is called a pulsed gradient spin echo (PGSE). As a spin echo inverts the phase of the signal, the directions of the magnetic field gradients must be reversed when separated by an odd number of spin echoes. For this type of experiment, the phase varies as

$$\phi = \gamma \mathbf{v} \cdot \mathbf{G}_v \delta \Delta. \tag{2.29}$$

In practice, velocity data is acquired from two datasets with a different first moment, the phases of which are subtracted in order to remove other phase effects. As the phase is measured *modulo* 2π, the encoding parameters must be set such that all velocities in

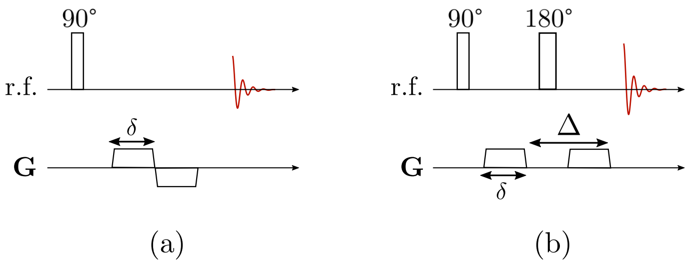

(a) (b)

Fig. 2.13: Pulse sequences for (a) a bipolar gradient pair and (b) pulsed gradient spin echo (PGSE).

the system lie in a 2π window to avoid wrapping artefacts. This window corresponds to a range of velocities called the field of flow (FOF).

2.3.2 Diffusion encoding

One of the earliest and most useful applications of displacement encoding is the measurement of diffusion using NMR. While velocity encoding imparts a finite change to the signal phase, diffusion has no net phase change as the mean displacement, $\langle\zeta\rangle$, in Brownian diffusion is zero. However, as the mean square displacement is non-zero ($\langle\zeta^2\rangle = \sqrt{2Dt}$, where D is the diffusion coefficient and t is the observation time) there will be a dispersion of phase changes centred about zero. This results in a net attenuation of the NMR signal. For a PGSE pulse sequence, this is described by the Stejskal-Tanner equation [16],

$$S(\mathbf{G}, \delta, \Delta) = S_0 \exp\left[-\gamma^2 \mathbf{G}^2 \delta^2 \left(\Delta - \delta/3\right) D\right]. \tag{2.30}$$

By increasing the gradient strength, the attenuation also increases and allows the extraction of the diffusion coefficient through fitting of the equation. It is also possible to increase the observation time Δ to achieve this, though different diffusion behaviour may be observed over different timescales. Stimulated echoes are often useful in achieving this.

2.3.3 q-space and NMR propagators

In addition to quantifying the mean displacement, $\langle\zeta\rangle = \mathbf{v}\Delta$, and diffusion coefficient, D, via the phase and attenuation of the NMR signal respectively, it is possible to extract the entire distribution of spin displacements in a system. This distribution is often referred to as the NMR propagator and provides more information about the dynamics of a system than individual velocity of diffusion measurements. As the evolution time Δ is known, this can be transformed into the velocity distribution of the spins. For a PGSE pulse sequence, the NMR signal S is described by

$$S(\mathbf{G}) = S_0 \exp\left[-i\gamma\delta\mathbf{G}\cdot\zeta\right] \exp\left[-\gamma^2\delta^2\mathbf{G}^2 \left(\Delta - \delta/3\right) D\right], \tag{2.31}$$

where the exponential terms describe the phase accrual and signal attenuation due to advection and diffusion respectively. Analogous to **k**-space encoding for spin position, a reciprocal space called $\mathbf{q}$-space can be defined that encodes for spin displacement,

$$\mathbf{q} = \frac{\gamma \mathbf{G} \delta}{2\pi}. \tag{2.32}$$

By substituting Eq. (2.32) into Equation 2.31, a Fourier relationship is generated between the NMR signal $S(\mathbf{q})$ and the NMR propagator $P(\zeta)$,

$$P(\zeta) = \int S(\mathbf{q}) \exp\left[-4\pi^2 \mathbf{q}^2 \left(\Delta - \delta/3\right) D\right] \exp\left[-2\pi i \mathbf{q} \cdot \zeta\right] \mathrm{d}\mathbf{q}. \tag{2.33}$$

When the integral in Eq. (2.33) is evaluated, the form of the propagator is a convolution of the normalised pure advection displacement distribution, $P_{\mathrm{adv}}(\zeta)$, and the symmetric displacement due to diffusion,

$$P(\zeta) = P_{\mathrm{adv}}(\zeta) * \left\{ \sqrt{\frac{4D(\Delta - \delta/3)}{\pi}} \exp\left[\frac{-\zeta^2}{8D(\Delta - \delta/3)}\right] \right\}. \tag{2.34}$$

The propagator can be transformed from displacement to velocity coordinates through division by the evolution time Δ.

2.4 Compressed sensing

Compressed sensing is a signal acquisition and processing method that uses the principles of image compression to reduce the number of sampled points, and therefore the time required, to reconstruct a signal. This is particularly useful in the study of highly transient effects [17, 18] or when many signal averages are required to improve SNR [19]. Compressed sensing MRI was first developed by Lustig *et al.* [20] and has been shown to furnish quantitative images of both spin density [21] and phase [22, 23]. Image compression exploits the underlying *sparsity* of images; sparsity is the property that an image can be expressed as a small number of high intensity coefficients. Some images are inherently sparse, whereas some require a transformation into a different domain to become sparse. As the majority of coefficients are zero or nearly zero, they can be disregarded and the image can be stored as a small subset of coefficients, in essence compressing the image with minimal loss of fidelity. Compressed sensing takes this concept and applies it to the acquisition of data rather than the storage. The critera for successful implementation of compressed sensing methods are the following:

1. the artefacts in the reconstruction must be incoherent and resemble noise,
2. the desired image must have a sparse representation in some domain,
3. the image is reconstructed using a non-linear algorithm that enforces sparsity in the appropriate domain while retaining consistency with the acquired data.

These criteria can be met relatively easily as follows.

MRI is acquired in the reciprocal **k**-space, and must be Fourier transformed in order to reconstruct the actual image (Fig. 2.14 (i)). It is well known that sampling beneath the Nyquist-Shannon rate results in artefacts in the reconstructed image [24]. For regular under-sampling, such as acquiring every other line or truncating the **k**-space signal, the artefacts are coherent and cannot be removed (such as the aliasing in Fig. 2.14 (ii)). However, random under-sampling creates incoherent artefacts that resemble noise (Fig. 2.14 (iii)). Hence, sampling **k**-space in a stochastic manner will satisfy criterion 1. As the spectral density is highest near the centre of **k**-space, it is common to bias the random sampling towards this area. Lustig *et al.* [20] achieved this using a polynomial probability density function, P, of the form,

$$P(r) \propto (1-r)^p, \tag{2.35}$$

where r is the normalised distance from the centre of **k**-space and p is a constant. For a raster of the same size as the desired image, a sampling pattern can be produced by randomly selecting **k**-space points according to this distribution until the level of under-sampling is achieved. All under-sampling patterns used in this thesis were obtained using this method, with values of p between 2 and 2.5. A representative distribution and 2D sampling patterns are shown in Fig. 2.15.

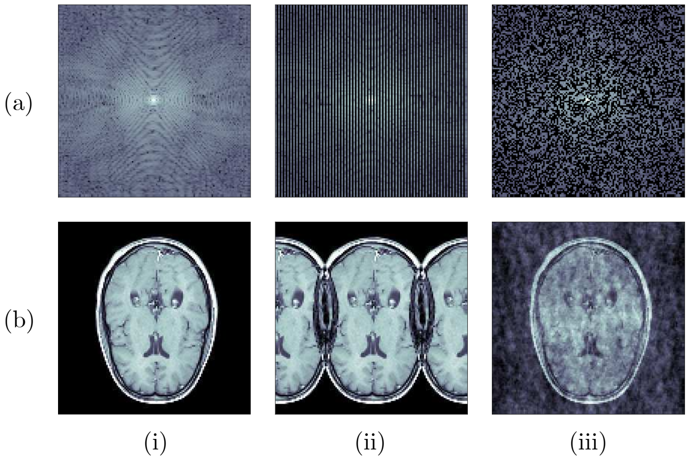

Fig. 2.14: Images of (a) k-space and (b) real-space reconstructions for (i) full sampling, (ii) regular 50% undersampling and (iii) irregular 50% undersampling.

Most MR images are not inherently sparse and require transformation into an alternative domain to achieve a sparse representation. Many systems have hard phase interfaces which manifest as sharp edges in the MRI data. These can be made sparse by finding the finite differences and producing a gradient image. This is the basis of Total Variation (TV) regularisation, which is described shortly. Other transforms can be used for more complex images, such as the Wavelet transform. This allows criterion 2 to be satisfied.

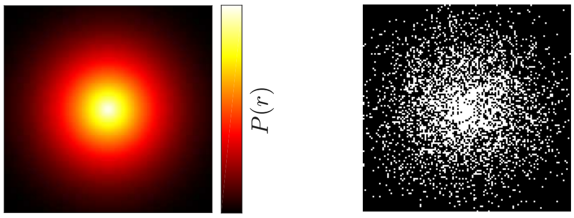

(a) (b)

Fig. 2.15: (a) Probability density function for under-sampling patterns with $p = 2.5$ (Eq. (2.35)). (b) Example 3D sampling pattern for 20% sampling of a 128×128 array.

The relation of a MR image, contained in the vector $\mathbf{x}$, to acquired data $\mathbf{y}$ can be expressed as

$$S\mathcal{F}\mathbf{x} + \nu = \mathbf{y}, \tag{2.36}$$

where S is the sampling pattern, $\mathcal{F}$ is the Fourier transform operator and ν is Gaussian noise. Direct inversion is sufficient to recover the true image for fully-sampled MRI data (i.e. S is the identity matrix), but the problem is ill-posed for under-sampled data as the Nyquist criterion is violated and will result in artefacts. To overcome this, a variational method can be applied, balancing consistency and sparsity, to generate an approximate solution i.e. the reconstructed image. This is commonly formulated as the minimisation

$$\mathbf{x}_\alpha \in \text{argmin}_{\mathbf{x}} \left\{ \frac{1}{2} ||\mathbf{y} - S\mathcal{F}\mathbf{x}||_2^2 + \alpha J(\mathbf{x}) \right\}, \tag{2.37}$$

where J is the regularisation function, α is the regularisation parameter and $||\mathbf{x}||_n$ is the Euclidean n-norm given by

$$||\mathbf{x}||_n = \sqrt[n]{\sum \mathbf{x}^n}.$$

The two terms in the objective function represent the data consistency and prior information (sparsity). In all cases in this thesis, the regularisation function J was chosen to be the total variation (TV) function,

$$\text{TV}(\mathbf{x}) = ||\nabla \mathbf{x}||_2 = \sqrt{\sum_{i \in N} \nabla \mathbf{x}(i)^2}, \tag{2.38}$$

where N is the number of data in the image $\mathbf{x}$. TV regularisation is useful in reconstructing data with hard edges [25]. An illustration of the method is given in Fig. 2.16. To reconstruct the incoherent image (b) produced from the undersampled **k**-space data (a), the sparse representation of the image (c) is minimised with respect to its arguments (i.e. pixels). This is done subject to maintaining consistency between the reconstructed **k**-space data (d) and the original acquired data (a).

Compressed sensing reconstruction was achieved in all cases using the in-house Object Orientated Methods For Inverse Problems (OOMFIP) [23], developed by Dr Martin Benning, and satisfies criterion 3.

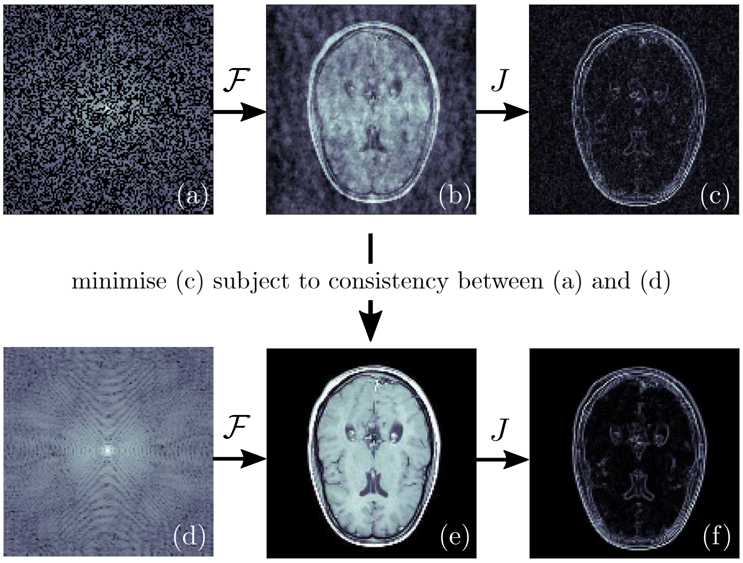

Fig. 2.16: Compressed sensing reconstruction method. (a) Undersampled **k**-space data. (b) Undersampled MR image with incoherent artefacts. (c) TV image of (b). (d) Reconstructed **k**-space data. (e) Reconstructed MR image. (f) TV image of (e).

2.5 References

[1] J. H. Keeler. *Understanding NMR Spectroscopy.* John Wiley and Sons (2002).

[2] M. H. Levitt. *Spin Dynamics: Basics of Nuclear Magnetic Resonance.* John Wiley & Sons (2013).

[3] D. Reichert, G. Hempel. Receiver imperfections and CYCLOPS: An alternative description. *Concepts in Magnetic Resonance Part B: Magnetic Resonance Engineering* (2002) 14 (2), 130–139. doi:10.1002/cmr.10004.

[4] G. Bodenhausen, R. Freeman, D. L. Turner. Suppression of artifacts in two-dimensional J spectroscopy. *Journal of Magnetic Resonance* (1977) 27 (3), 511–514. doi:10.1016/0022-2364(77)90016-6.

[5] M. H. Levitt, P. Madhu, C. E. Hughes. Cogwheel Phase Cycling. *Journal of Magnetic Resonance* (2002) 155 (2), 300–306. doi:10.1006/JMRE.2002.2520.

[6] J. H. Baltisberger, B. J. Walder, E. G. Keeler, D. C. Kaseman, K. J. Sanders, P. J. Grandinetti. Communication: Phase incremented echo train acquisition in NMR spectroscopy. *The Journal of Chemical Physics* (2012) 136 (21), 211104. doi:10.1063/1.4728105.

[7] P. T. Callaghan. *Principles of Nuclear Magnetic Resonance Microscopy.* Oxford University Press (1991).

[8] E. M. Haacke. *Magnetic resonance imaging: physical principles and sequence design.* Wiley, New York (1999).

[9] H. T. Fabich, M. Benning, A. J. Sederman, D. J. Holland. Ultrashort echo time (UTE) imaging using gradient pre-equalization and compressed sensing. *Journal of Magnetic Resonance* (2014) 245, 116–124. doi:10.1016/j.jmr.2014.06.015.

[10] J. Hennig, A. Nauerth, H. Friedburg. RARE imaging: a fast imaging method for clinical MR. *Magnetic resonance in medicine* (1986) 3 (6), 823–33.

[11] A. Haase, J. Frahm, D. Matthaei, W. Hanicke, K.-D. Merboldt. FLASH imaging. Rapid NMR imaging using low flip-angle pulses. *Journal of Magnetic Resonance* (1986) 67 (2), 258–266. doi:10.1016/0022-2364(86)90433-6.

[12] P. Mansfield, A. A. Maudsley. Planar spin imaging by NMR. *Journal of Magnetic Resonance (1969)* (1977) 27 (1), 101–119. doi:10.1016/0022-2364(77)90197-4.

[13] S. D. Beyea, B. J. Balcom, P. J. Prado, A. R. Cross, C. B. Kennedy, R. L. Armstrong, T. W. Bremner. Relaxation Time Mapping of ShortT*2Nuclei with Single-Point Imaging (SPI) Methods. *Journal of Magnetic Resonance* (1998) 135 (1), 156–164. doi:10.1006/JMRE.1998.1537.

[14] C. B. Ahn, J. H. Kim, Z. H. Cho. High-speed spiral-scan echo planar NMR imaging-I. *IEEE transactions on medical imaging* (1986) 5 (1), 2–7. doi:10.1109/TMI.1986.4307732.

[15] P. T. Callaghan. *Translational Dynamics & Magnetic Resonance: Principles of Pulsed Gradient Spin Echo NMR*. 2nd edition. Oxford University Press (2011).

[16] E. O. Stejskal, J. E. Tanner. Spin diffusion measurements: Spin echoes in the presence of a time-dependent field gradient. *The Journal of Chemical Physics* (1965) 42 (1), 288–292. doi:10.1063/1.1695690.

[17] A. B. Tayler, D. J. Holland, A. J. Sederman, L. F. Gladden. Time resolved velocity measurements of unsteady systems using spiral imaging. *Journal of Magnetic Resonance* (2011) 211 (1), 1–10. doi:10.1016/j.jmr.2011.03.017.

[18] A. B. Tayler, D. J. Holland, A. J. Sederman, L. F. Gladden. Applications of ultrafast MRI to high voidage bubbly flow: Measurement of bubble size distributions, interfacial area and hydrodynamics. *Chemical Engineering Science* (2012) 71, 468–483. doi:10.1016/j.ces.2011.11.014.

[19] N. P. Ramskill, A. P. York, A. J. Sederman, L. F. Gladden. Magnetic resonance velocity imaging of gas flow in a diesel particulate filter. *Chemical Engineering Science* (2017) 158, 490–499. doi:10.1016/j.ces.2016.10.017.

[20] M. Lustig, D. Donoho, J. M. Pauly. Sparse MRI: The application of compressed sensing for rapid MR imaging. *Magnetic Resonance in Medicine* (2007) 58 (6), 1182–1195. doi:10.1002/mrm.21391.

[21] P. Parasoglou, D. Malioutov, A. J. Sederman, J. Rasburn, H. Powell, L. F. Gladden, A. Blake, M. L. Johns. Quantitative single point imaging with compressed sensing. *Journal of Magnetic Resonance* (2009) 201 (1), 72–80. doi:10.1016/j.jmr.2009.08.003.

[22] D. Holland, D. Malioutov, A. Blake, A. Sederman, L. Gladden. Reducing data acquisition times in phase-encoded velocity imaging using compressed sensing. *Journal of Magnetic Resonance* (2010) 203 (2), 236–46. doi:10.1016/j.jmr.2010.01.001.

[23] M. Benning, L. Gladden, D. Holland, C. B. Schönlieb, T. Valkonen. Phase reconstruction from velocity-encoded MRI measurements - A survey of sparsity-promoting variational approaches. *Journal of Magnetic Resonance* (2014) 238, 26–43. doi:10.1016/j.jmr.2013.10.003.

[24] L. Erasmus, D. Hurter, M. Naude, H. Kritzinger, S. Acho. A short overview of MRI artefacts. *South African Journal of Radiology* (2004) 8 (2), 13. doi:10.4102/sajr.v8i2.127.

[25] D. Strong, T. Chan. Edge-preserving and scale-dependent properties of total variation regularization. *Inverse Problems* (2003) 19 (6), S165–S187. doi:10.1088/0266-5611/19/6/059.

Chapter 3

Applications and measurement limits of gas-phase MRI

3.1 Introduction

Magnetic resonance has primarily been used to study systems in the solid and liquid phases, with comparatively few studies of gases. The main reason for this is the significantly lower spin density in the gas-phase, which further reduces the sensitivity of already insensitive NMR experiments. Additionally, the small number of species that are gaseous at near-ambient conditions and the smaller number of these that possess high abundance NMR-active nuclei with large gyromagnetic ratios heavily restricts the scope of gas-phase NMR. However, the insight gained from gas-phase NMR studies has spurred the field in spite of the fundamental challenges [1].

Gas-phase NMR and MRI can be separated into two main categories: those that use thermally polarised gases (i.e. the magnetisation is at thermal equilibrium prior to excitation), and that use hyperpolarised gases (i.e. the magnetisation is perturbed from thermal equilibrium before the experiment to increase the available signal). This chapter will focus on the former, but a short review of hyperpolarised gas studies is also presented for context.

Due to the difficulties and limitations associated with gas-phase NMR and MRI, the choice of gas species and pulse sequence is of high importance in achieving useful measurements. The experimental parameters that are desired to be optimised, such as SNR, spatial resolution and temporal resolution, are functions of the gas and experiment properties, such as density, relaxation times, diffusion coefficients and observation times. An understanding of these relationships are key in designing and optimising gas-phase NMR experiments.

This chapter has two principle aims: to review the previous applications of thermally polarised gas-phase MRI and to assess the suitability of different candidate gases for use in gas-phase MRI based on their potential image and velocity resolutions.

3.2 Scope of study

This chapter has three major sections. First, the literature surrounding gas-phase MRI is reviewed in regard to its application, measurement achievements and methods that may improve its utility. Secondly, the properties of three candidate gases are measured in order to predict their relative sensitivity and measurement resolutions. Finally, these predictions are used to choose the most suitable gas for subsequent experiments and determine the limits of the measurements that can be made.

3.3 Literature review

3.3.1 Hyperpolarised gases

Hyperpolarisation is an important and widespread technique for clinical and *in vivo* gas-phase MRI [2]. The principle of the technique is that the bulk magnetisation of a sample can be increased well beyond its thermal equilibrium value through angular momentum transfer. Such increases overcome the inherent sensitivity problem associated with NMR and exacerbated by the low density of gases, and permit previously infeasible studies such as single-acquisition lung imaging.

The most commonly used hyperpolarisable gases are ^{3}He and ^{129}Xe, though ^{53}Ke is also hyperpolarisable. These are usually polarised using spin-exchange optical pumping, whereby the angular momentum of circularly polarised laser light is transferred to the gas via an alkali metal intermediate e.g. caesium or rubidium. This occurs before the gas is introduced to the system of interest. The resultant increase in magnetisation can be as great as 5 orders of magnitude, more than overcoming the density difference between liquids and gases. However, the use of hyperpolarised gases also presents some issues. The noble gases used are often much more expensive than thermally polarised gases. Further, the hardware required for hyperpolarisation is also expensive, and together introduce a large economic barrier to hyperpolarisation studies. As such, it is mostly applications that require the benefits of this technique, i.e. medical, that can justify the investment. One possible alternative is to use dynamic nuclear polarisation (DNP) to facilitate hyperpolarisation. *para*-H_2 can be used to hydrogenate unsaturated hydrocarbons, e.g. propylene, and hyperpolarise neighbouring spins [3]. However, this requires the production and reaction of *para*-H_2, which has its own associated cost and safety concerns.

From a research perspective, while hyperpolarised gases offer increased sensitivity and contrast, they present difficulties in accurately quantifying measurements due to the difficulty in supplying the gas at a constant polarisation. This is most prevalent in the study of porous materials and catalysts, where the pore structure or catalyst often affects the relaxation behaviour of the NMR species. As particulate filters rely on gas passing through a porous wall and washcoats containing paramagnetic metals, hyperpolarised gases are inherently unsuitable for their study.

With regard to chemical engineering applications, hyperpolarised gases have seen use in the study of pipe flow [4], flow through [5] and around [6] obstructions, diffusion-diffraction pore imaging [7] and packed beds [8].

3.3.2 Thermally polarised gases

The low density of gases, some 3-4 orders of magnitude lower than liquids, causes a great reduction in the NMR signal available for gas-phase NMR studies. Hence, thermally polarised gas has been limited to species and systems that offer the greatest sensitivity. This has excluded most nuclei apart from ^{1}H and ^{19}F ($\gamma_{^{19}\mathrm{F}} = 0.94\gamma_{^{1}\mathrm{H}}$). Despite these difficulties, the increased practicality and affordability of such gases has encouraged their use. The review by Beyea *et al.* covers the early development of such techniques for the study of porous media [9], but the field to-date is summarised now.

Gases containing ^{1}H nuclei, most notably hydrocarbons, are an obvious candidate for gas-phase MRI as the hardware for ^{1}H NMR is ubiquitous. Smaller species, such as hydrogen and methane, have short relaxation times dominated by the spin-rotation relaxation mechanism and large diffusion coefficients that limit their use in high resolution MRI and advective transport studies. However, this property has been exploited to study restricted diffusion in larger geometries. Larger species, e.g. propane and butane, have longer relaxation times and smaller diffusion coefficients, but relatively low vapour pressures, meaning that any pressurisation strategy to increase the spin density and hence the sensitivity is limited in its effectiveness. Other hydrocarbon moieties, such as light alkenes or alkynes, can also be used but suffer from similar issues as their alkane counterparts. However, the unsaturated nature of such molecules allows hyperpolarisation through the use of *para*-H_2 hydrogenation. An extra consideration for hydrocarbon gases is their high flammability, necessitating extra care from a safety perspective.

Despite these challenges, such gases have found use in several studies. Prado *et al.* imaged methane inside a phantom, demonstrating the potential to image gases with short T_2 times [10]. However, this was limited to a 1D profile at a resolution of $700\,\mu\mathrm{m\,px}^{-1}$. Koptyug *et al.* showed the feasibility of imaging flowing hydrocarbon gases by acquiring 2D velocity images of propane, butane and acetylene flowing through a monolith at an in-plane resolution of $760\,\mu\mathrm{m\,px}^{-1}$ [11]; hydrogen gas was attempted but imaging was precluded by the short relaxation times. Szomolanyi *et al.* later succeeded in imaging H_2 gas using their rapid SPIRAL-SPRITE method, albeit at a relatively low resolution of $2\,\mathrm{mm\,px}^{-1}$ due to diffusion blurring [12]. Koptyug and co-workers later used MRI and NMR propagator measurements to study gas flow in pipes, showing agreement between the two methods and predicting a limiting channel diameter of 0.5 mm to 1 mm that can be studied using velocity encoded MRI [13]. These methods were later applied to flow through bead packs [14]. Codd and Altobelli similarly used NMR propagators to measure the flow of propane through a porous bead pack; the propane was pressurised to 170 kPa to increase the available signal [15]. Zhang *et al.* used a 1D phase-encoded sequence to measure the transport of hydrogen gas across a polymeric membrane [16]. Stevenson *et al.* measured the restricted diffusion of propane inside a gas-liquid foam to extract a bubble size distribution, exploiting the high diffusivity exhibited by gases [17]. Honari *et al.* used

1D MRI of methane to observe the displacement of carbon dioxide inside a rock, acquiring profiles at a resolution of 0.8 mm px^{-1} [18]. Recently, Mirdrikvand *et al.* used methane as the probe gas for NMR propagator measurements inside monolithic structured catalysts [19].

Fluorinated gases, notably perfluorinated gases (i.e. no C-H bonds) offer several advantages over proton-containing gases despite the lower gyromagnetic ratio of the ^{19}F nucleus. As a heavier nucleus, fluorinated gases typically have a smaller self-diffusion coefficent than their hydrocarbon analogues and therefore suffer from less diffusion blurring. The high electronegativity of fluorine also acts to reduce intermolecular bond strengths and increase the vapour pressure, allowing the gases to be compressed to a higher pressure and hence offer a greater increase in sensitivity. Finally, perfluorinated molecules are very chemically inert so the risk of combustion or material incompatibility is lower. However, fluorine-containing species typically have much shorter relaxation times than protonated species and offer less flexibility in experiment choice. Fluorinated compounds are also extremely potent greenhouse gases (SF_6 has a global warming potential over 10,000 times that of CO_2) and so their use and release must be carefully controlled.

The first use of fluorinated gases in MRI was by Rinck *et al.* to image rat lungs [20], and such gases continued to find some use in the study of pulmonary structure and function [21–28] but have largely been superseded by hyperpolarised noble gases. Lizak *et al.* was the first to use fluorinated gas in a non-medical application, using C_2F_6 at 5 bar(g) to probe the structure of porous ceramics at an in-plane resolution of 100 µm px^{-1} [29]. Several studies have since followed suit in using fluorinated gases to study porous media [30–33]. Sulfur hexafluoride has been the most popular gas for most studies, and has allowed highly dynamic flowing systems to be explored. Newling *et al.* used SF_6 to study gas flows over different geometries at high Reynolds numbers, measuring velocities as high as 48 m s^{-1} [34]. Sankey *et al.* measured the flow fields of both gas and liquid phases in a packed bed, using SF_6 at 3.7 bar(g) as the active gas and achieving an in-plane resolution of 708 µm px^{-1} in a 4 cm diameter column [35]. Several studies by Boyce and co-workers have made use of SF_6 as the gaseous phase in model fluidised beds [36–38]. Ramskill *et al.* incorporated compressed sensing with SF_6 velocity imaging to obtain gas velocity measurements inside an opaque DPF sample [39], reaching a resolution of 140 µm px^{-1} (or $\sim$9 pixels per channel diameter) in under 14 min. Most recently, Gauthier and Newling used SF_6 to measure gas flow in a recorder whistle for comparison with CFD predictions [40].

3.3.3 Advanced methods

As low sensitivity is one of the main limiting factors to gas-phase MRI, methods that allow reduced sampling may increase the accuracy and resolution of the measurements. Two such methods that have found utility in magnetic resonance are Bayesian analysis and compressed sensing [41].

Bayesian analysis uses Bayes' theorem to extract probability distributions for fitted parameters and so is most useful for systems whose behaviour is expected to follow one or more specific models. The use of Bayesian methods in magnetic resonance was popularised by Bretthorst, who used it to extract relaxation times and pick appropriate multi-component models in NMR relaxation experiments [42, 43]. Since then, it has found useful application where SNR is limited, transience is high, or experimental times need to be short. Quantification in low-sensitivity NMR spectroscopy (e.g. ^{13}C NMR) can be increased using Bayesian methods [44]. Holland *et al.* used Bayesian analysis to rapidly obtain size distributions for bubbles rising in a column of water [45], a feat that is near-impossible using conventional 2D imaging, through optimal sampling of **k**-space. Ross *et al.* used a similar approach to measure sphere sizes using an Earth's field NMR instrument [46], achieving a resolution an order of magnitude greater than with conventional imaging. Bayesian methods were similarly applied to the measurement of **q**-space by Blythe *et al.*, who obtained accurate rheological parameters of fluid in pipe flow with less than 12% of the points required for a complete propagator sampled [47]. As Bayesian analysis can allow significant subsampling of data, it may facilitate greater SNR in a given time by allowing more signal averages in gas-phase systems.

Compressed sensing (CS) has similarly allowed the reduction of acquisition time in NMR experiments. It was first demonstrated by Lustig *et al.* [48] for clinical MRI but has found great use outside of medical imaging. Wu *et al.* used CS to reduce the acquisition time of COSY experiments from >5 to <1.5 h, allowing the study of reaction kinetics with greater spectroscopic resolution [49]. Parasoglou *et al.* used CS with optimised sampling patterns to qualitatively recover the moisture conent inside wafers during hydration [50]. Holland *et al.* applied CS to MRI velocimetry, allowing accurate recovery of velocity data from >30% of the fully sampled data [51]. Benning *et al.* also demonstrated qualitative CS velocimetry with a range of sparsifying transforms [52]. CS has been used to improve the quality and decrease the acquisition times of ultra-fast imaging sequences, such as spiral [53] and radial ultrashort echo time (UTE) imaging [54]. Ramskill *et al.* applied CS to gas-phase velocimetry [39] and it has now become a practical and routine methodology for such measurements.

3.4 Theoretical

In this section, theoretical treatments of magnetic resonance imaging and displacement measurements are used to derive estimated best-case limits for both.

3.4.1 Sensitivity

The sensitivity of NMR experiments is of much interest given the relative insensitivity of the technique compared to most other analytical methods. The SNR of an NMR experiment depends on many parameters of both the sample and the equipment, and is difficult to calculate. Hence, the focus will be on the relative sensitivities of different species. From Callaghan [55], the SNR varies as

$$\mathrm{SNR} \propto \gamma^{11/4} B_0^{7/4} \rho_\mathrm{S}, \tag{3.1}$$

where γ is the gyromagnetic ratio of the nucleus, B_0 is the applied magnetic field strength and ρ_S is the spin density.

3.4.2 Measurement limits

Image resolution

The theoretical resolution limit of MRI is determined by a number of factors, including various properties of the spectrometer, the experiment and the sample. Callaghan [55] derived an analytical expression for the MRI resolution limit in the T_2-broadened case (Eq. (3.2)). This expression was then modified to include broadening from diffusion. The contributions of the relaxation and diffusion components are expected to vary depending on the system under study. More immobile samples, such as solids or viscous liquids, will tend to have smaller diffusion coefficients and smaller T_2 constants due to restricted molecular motions and so relaxation will likely be the limiting factor. Conversely, gases will have a much higher diffusion coefficient and so diffusion will likely be the limiting factor. The other major factor in limiting any measurement is the SNR. While this can be increased through the averaging of multiple scans, the relationship between it and the number of scans, $\mathrm{SNR} \propto N_\mathrm{s}^{1/2}$, means that the experiment time grows quadratically with SNR and improvements diminish quickly. This can place a practical limit on resolution if dynamic systems are under study.

The expected T_2-broadened in-plane resolution Δx for an acquired image is

$$\Delta x_{T_2} = 16 a^{1/2} F_\mathrm{s}^{1/4} \sigma_\mathrm{s}^{1/4} \left(\mathrm{SNR}\right)^{1/4} \Delta z^{-1/4} f^{-7/8} N_\mathrm{s}^{-1/4} N_\mathrm{px}^{-1/4} T_2^{-1/4}, \tag{3.2}$$

with the symbol definitions given in Table 3.1 [55]. This equation assumes that the bandwidth of the acquisition has been optimised for the T_2 value of the system, i.e. that $1/T = N_\mathrm{px}/\pi T_2$. While the equation is superficially complex, most terms are related to the sensitivity and are not necessarily fluid dependent.

In many studies, the sample size can be optimised to fill the coil (or vice versa) so $a = N\Delta x/2$. The spectrometer noise figure F_s is equal to unity in an ideal case but greater than unity in any real spectrometer. As the noise figure is non-trivial to measure, the ideal case has been assumed for the theoretical treatment. The skin depth reduction factor σ is used to correct the current resistance of the r.f. coil for proximity effects. For a simple single-layer solenoid, $\sigma \approx 5$.

In a system where spins undergo Brownian diffusion, the expected displacement during acquisition time period T in one direction is $\Delta x_\mathrm{dif} = \sqrt{2DT}$, where D is the self-diffusion

Table 3.1: Symbol definitions for Eq. (3.2)

Symbol	Definition
a	r.f. coil radius
F_{s}	spectrometer noise figure
σ_{s}	skin depth reduction factor
SNR	desired signal to noise ratio
Δz	slice thickness
f	spectrometer frequency
N_{s}	number of accumulated scans
N_{px}	number of pixels

coefficient. Diffusion of spins during the application of a magnetic field gradient results in dephasing of the magnetisation, akin to T_2 relaxation, causing broadening and attenuation in the acquired image. Such dephasing is proportional to G^2t^3, while frequency encoding is proportional to Gt, meaning that this dephasing can be made arbitrarily small by using short but intense gradient pulses. This works well for phase encoding methods (e.g. SPI, SPRITE) and so minimising the self-diffusion coefficient is the only concern, but the acquisition time for frequency encoding is limited by the dwell time and desired image raster size. By considering the diffusive attenuation as an additional broadening, an extension to the T_2-limit can be written as

$$\Delta x = 1.34 \left(\Delta x_{\mathrm{dif}} \Delta x_{T_2}^2\right)^{\frac{1}{3}}, \tag{3.3}$$

for an optimum bandwidth dependent on the gradient strength.

Velocity resolution

Propagators are often interpreted as probability distributions for the motion of spins during an experiment. They take the form of a convolution between a Dirac delta function and a Gaussian in the simplest instance. The position of the delta function on the x-axis informs the average velocity of the spins, while the width of the Gaussian encodes the incoherent motion due to diffusion or diffusion-like processes.

From Callaghan [56], the resolution of a velocity measurement, Δv, made from a propagator is

$$\Delta v = \sqrt{\frac{2D}{\Delta}\frac{1}{\mathrm{SNR}_P}}, \tag{3.4}$$

where Δ is the observation time and SNR_P is the signal-to-noise ratio of the propagator. However, this only describes the uncertainty in measuring the *mean* velocity of single peak given the noise level and diffusion broadening. In some cases, including measuring the through-wall velocity of a wall-flow filter, it is the existence of two separate velocities that needs to be determined and so the resolution calculated using Eq. (3.4) will be for a 'best-case' scenario. Conceptually, the successful discrimination between two peaks relies on the difference in their means being sufficiently larger than the widths of the peaks. In this situation, this relies on the displacement due to advection being sufficiently greater than the displacement due to diffusion. Hence the ratio of advective to diffusive displacement in one dimension,

$$\frac{\langle\zeta\rangle_{adv}}{\langle\zeta\rangle_{dif}} = \frac{vt}{\sqrt{2Dt}} = \sqrt{\frac{v^2 t}{2D}}, \tag{3.5}$$

is a useful metric in predicting whether a particular gas velocity will be measurable over a given timescale. A reasonable criterion for this, given a sufficiently high SNR, is a ratio of unity or greater.

3.5 Experimental

3.5.1 Materials

The three gases used in this study were propane (Calor, UK), butane (Calor, UK) and sulfur hexafluoride (BOC, UK). The propane and butane supplied by Calor did not have a specified purity but some minor unidentified impurities were seen in the NMR spectrum. The sulfur hexafluoride was stated to be 99.9% pure and only one signal was observed in the NMR spectrum.

All gases were contained inside an 18 mm internal diameter PEEK flow cell, pressure rated to 9 bar(g), which was held inside the NMR spectrometer during experiments and taken to be representative of the sample sizes expected in this thesis. The propane and butane were supplied directly from the cylinders into the flow cell following a nitrogen flush, and vented to atmosphere at concentrations below the lower explosion limit after use. The sulfur hexafluoride was supplied using the recirculating rig described in Appendix A.

3.5.2 Magnetic resonance

All magnetic resonance experiments were performed using a 9.4 T superconducting magnet controlled by a Bruker AV400 spectrometer, tuned to either 400 MHz or 376 MHz (for ^{1}H and ^{19}F experiments respectively). Displacement encoding was afforded by three orthogonal magnetic field gradient coils, each with a maximum strength of 146.15 $\mathrm{G\,cm^{-1}}$. To minimise the effect of convection, only gradient pulses in the horizontal plane were used. Signal excitation and detection was provided with a 25 mm diameter birdcage r.f. coil.

Relaxation measurements

For T_1 measurements, an inversion recovery sequence was used (Fig. 3.1 (a)). The delay time τ was varied to sample between 0.5 ms and $\sim 5T_1$ ms for each species. The data was integrated over all spectral peaks and fitted to Eq. (2.9) with $\left(M_{z,\mathrm{eq}} - M_z(0)\right)/M_z(0) = 2$.

T_2 measurements were made using the CPMG pulse sequence (Fig. 3.1 (b)). The echo time T_E was 5 ms, corresponding to the highest possible r.f. duty cycle, in order to reduce diffusion attenuation of the signal that would overestimate T_2. The T_2 weighting was controlled by varying the number of echoes, n. The value of n was chosen to allow complete decay of the signal. For propane and butane, a PROJECT sequence comprising alternating spin and perfect echoes was used to mitigate the effects of J-coupling (Fig. 3.1 (c)) [57, 58]. The signal attenuation was fitted to Eq. (2.10) with $t = n\tau$.

Diffusion measurements

Due to the fast diffusion of gases and short effective relaxation times, a PGSE sequence was employed with a short echo time (Fig. 3.1 (d)). Gradient pulses of length 1 ms, evolution time 2 ms and maximum strength 29.2 G cm^{-1} were used. The echo time was 5 ms. The data was fitted to the Stejskal-Tanner equation (Eq. (2.30)).

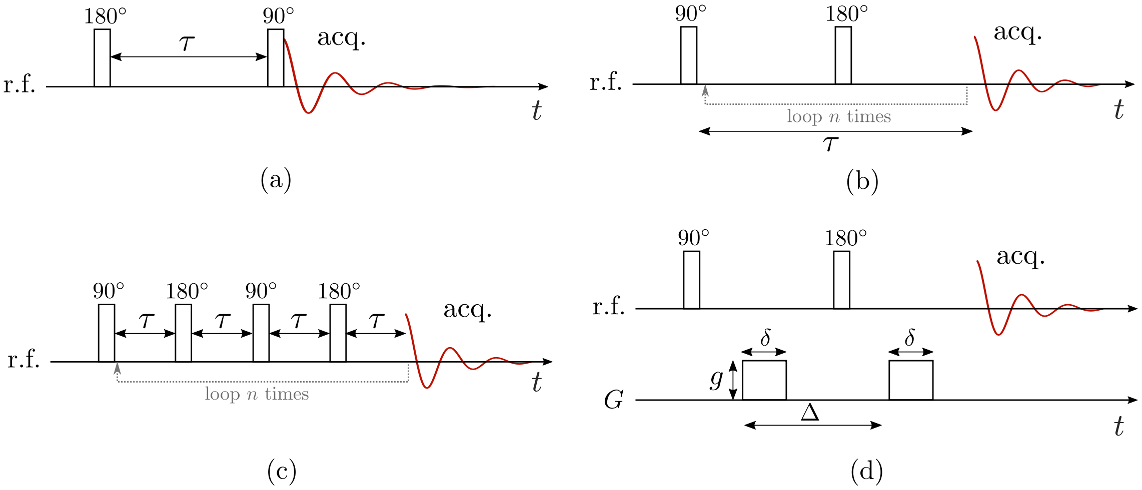

(a) (b) (c) (d)

Fig. 3.1: Pulse sequences used to measure properties of the candidate gases. (a) Inversion recovery for T_1. (b) CPMG for T_2. (c) CPMG-PROJECT for T_2. (d) PGSE for D_0.

3.6 Results

The main properties that affect the performance of fluids in NMR experiments are the sensitivity, relaxation times and self-diffusion coefficient. Increasing the pressure of the gas increases the density of the gas and hence the sensitivity. It also increases the relaxation times and decreases the diffusion coefficient. These all improve the theoretical resolution limit achievable by the gas, but the increased relaxation times require a longer recycle time per experiment. As such, a maximum safe operating pressure is required for each gas.

In this study, propane, butane and sulfur hexafluoride were used as practical examples of the two proton- and fluorine-containing gases. For each gas, the relaxation times and diffusion coefficients are used to calculate the relative sensitivities at elevated operating pressures. The equations given in Section 3.4 are then used to explore the theoretical limits of measurements using these gases.

3.6.1 Properties of candidate gases

The values of T_1, T_2 and D_0 for all three gases at both atmospheric and running pressures are shown in Table 3.2. The values at atmospheric pressure, p_{atm}, were taken from the literature [14, 34], while those at the operating pressures were measured using the techniques in Section 3.5.2; these values are used for all subsequent calculations. The operating pressures were limited by the vapour pressure for butane, the regulator outlet pressure for propane and the safe operating pressure of the recirculating rig for SF_6. All subsequent analysis is performed assuming the gases are at the stated operating pressures unless otherwise stated.

Table 3.2: Measured parameters for candidate gases.

Gas	p_{op} / bar(a)	$p = p_{\mathrm{atm}}$			$p = p_{op}$		
		T_1 / s	T_2 / s	D_0 / $\mathrm{m^2\,s^{-1}}$	T_1 / s	T_2 / s	D_0 / $\mathrm{m^2\,s^{-1}}$
Propane	4.9	1.0	0.59	1.2×10^{-5}	4.2	0.98	1.1×10^{-6}
Butane	2.5	1.3	0.75	8.9×10^{-6}	2.7	0.77	1.6×10^{-6}
SF_6	6	2×10^{-3}	2×10^{-3}	3.5×10^{-6}	14×10^{-3}	11×10^{-3}	3×10^{-7}

The values of T_1 for each fluid allows the relative available signal from excitation, $S_{\mathrm{rel}}(t)$, to be calculated,

$$S_{\mathrm{rel}}(t) = 1 - \frac{M_z(t)}{M_z(0)} = \exp\left[-\frac{t}{T_1}\right]. \tag{3.6}$$

The decay of available signal with time is important as sets an upper limit on the feasible observation times in a velocity or propagator measurement. Figure 3.2 shows the available signal calculated for the candidate gases using the measured T_1 and liquid water for comparison. Propane, butane and water all have T_1 values of the order of a few seconds, meaning usable signal is potentially available up to around 10 s after excitation. For SF_6, the much shorter value of T_1 means that the usable signal has effectively disappeared 100 ms after excitation. As such, much shorter observation times are feasible for SF_6 than the other species.

The ratio of advective to diffusive displacement (Eq. (3.5)) was calculated for the candidate gases and water as a function of T_1 for velocities of (a) $10\,\mathrm{mm\,s^{-1}}$, (b) $1\,\mathrm{mm\,s^{-1}}$ and (c) $0.1\,\mathrm{mm\,s^{-1}}$. For $1\,\mathrm{mm\,s^{-1}}$, the ratio for SF_6 achieves unity at about $0.5 \times T_1$ which is not shown on the plot. It can be seen that all gases achieve the criterion of a unity ratio within T_1 for $10\,\mathrm{mm\,s^{-1}}$ but none achieve it for $0.1\,\mathrm{mm\,s^{-1}}$. For $1\,\mathrm{mm\,s^{-1}}$, propane and butane achieve the criterion but SF_6 does not. Water is heavily dominated by advective motion at all velocities.

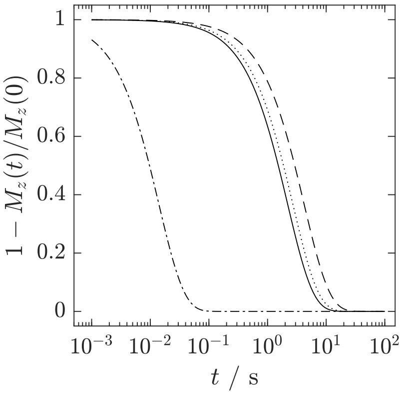

Fig. 3.2: The relative available signal for the propane (- - -), butane (·····), SF_6 (-·-·) and water (——) as a function of time.

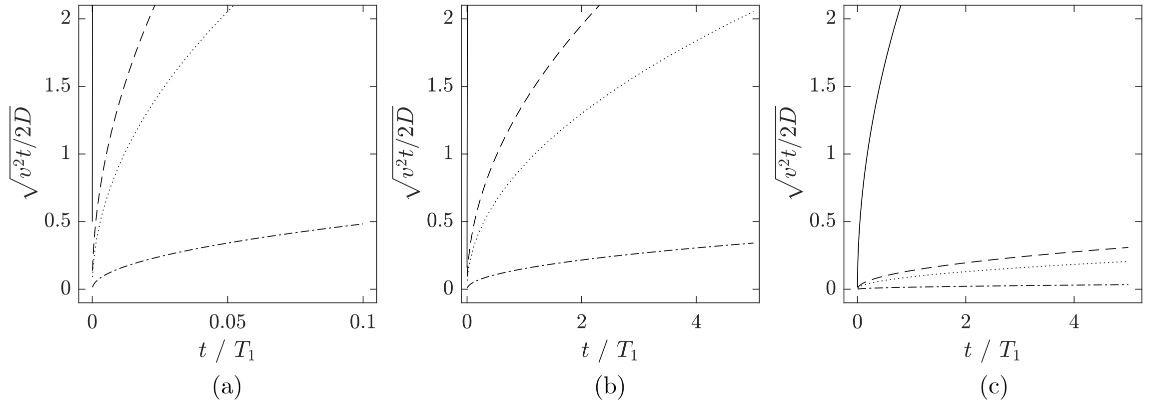

(a)

(b)

(c)

Fig. 3.3: The ratio of advective to diffusive displacement calculated for propane (- - -), butane (·····), SF_6 (-·-·) and water (——) for velocities of (a) $10\,\mathrm{mm\,s^{-1}}$, (b) $1\,\mathrm{mm\,s^{-1}}$ and (c) $0.1\,\mathrm{mm\,s^{-1}}$. N.B. the different timescale shown in (a).

3.6.2 Sensitivity

While it is difficult to calculate the absolute sensitivity of a NMR experiment with a given nucleus and species, it is possible to calculate the relative sensitivity between different ones. From Eq. (3.1), it is clear that the gyromagnetic ratio, gas pressure and number of nuclei per molecule all influence the relative sensitivity, which is calculated relative to propane in Table 3.3. Additionally, the relative sensitivity per time is calculated by dividing the relative sensitivity by the T_1 value of the species. As many more signal averages can be made with SF_6 in the same experimental time, it has a greater relative SNR than propane and butane per unit time. Sensitivity can be maximised by using the highest field strength available, which was 9.4 T in this study.

3.6.3 Measurement limits

In this section, the resolution limits are calculated from the equations in Section 3.4. One important concept to note is that resolution here is expressed as the smallest difference

Table 3.3: Relative sensitivity of gases at p_{op}.

Species	γ / $\gamma_{^1\text{H}}$	p_{op} / bar(a)	Nuclei per molecule	Rel. SNR per acquisition	Rel. SNR per unit time
Propane	1	4.9	8	1	1
Butane	1	2.5	10	0.64	1
SF_6	0.94	6	6	0.77	15.8

in position (Δx) or velocity (Δv) that can be resolved, such that smaller Δx and Δv are considered better resolutions and vice versa. As MRI and NMR propagator acquisitions have many parameters that need to be optimised for a given experiment, the limits described here are to give a relative comparison between the candidate gases and may not represent the ‘hard’ limit achievable.

Equations 3.2 and 3.3 show that the resolution limit is highly dependent both upon the system under study and the desired properties of the final image. As such, it is helpful to observe how the resolution limit varies as a function of one or two variables. Fig. 3.4 shows how the image resolution achievable varies with T_2 and D_0, with the candidate gases and liquid water ($T_1 \approx T_2 = 2.2\,\text{s}$, $D_0 = 2.0 \times 10^{-9}\,\text{m}^2\,\text{s}^{-1}$) labelled. The desired SNR was 20, with 128 pixels in the read direction, a slice thickness of 1 cm and 4 signal averages. This allows the image resolutions of the gases to be compared like-for-like, although the calculated values will not reflect the best resolutions achievable and the image acquisition times will vary.

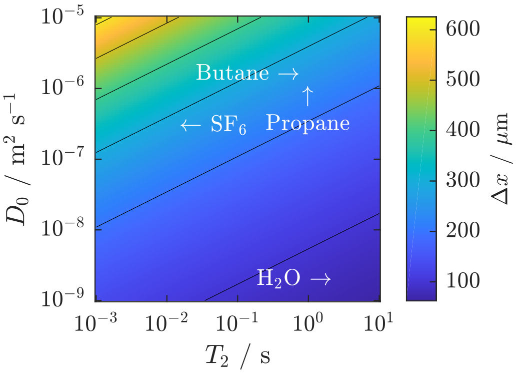

Fig. 3.4: 2D plot showing the MRI image resolution limit as a function of T_2 and D_0. Contours show lines of equal resolution corresponding to the colour bar labels. The value for each species is indicated at the end of the arrow.

As with the MRI resolution limit, the velocity resolution of propagators depends on both the gas and experimental parameters, and the desired properties of the propagator. Again, it is useful to observe how the resolution varies as a function of multiple variables. Fig. 3.5 shows the NMR propagator resolution limit as a function of T_2 and Δ for a desired SNR_P of 20. The candidate species are indicated, with $\Delta = T_1$ so that all gases are considered with an equal amount of relaxation weighting during a hypothetical stimulated echo sequence.

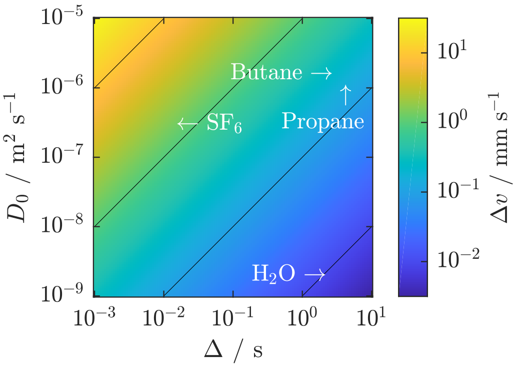

Fig. 3.5: 2D plot showing the NMR propagator resolution limit as a function of T_2 and Δ. Contours show lines of equal resolution corresponding to the colour bar labels. The value for each species is indicated at the end of the arrow.

Table 3.4: Calculated measurement limits of the candidate gases and liquid water.

Species	Δx / µm	Δv / mm s^{-1}
Propane	245	0.18
Butane	260	0.22
SF_6	280	1.56
H_2O	78	0.01

3.7 Discussion

Several objectives need to be considered when selecting the NMR active gas for experiments. The sensitivity must be high enough such that the desired SNR and measurement resolutions can be achieved in a reasonable experimental time. The image resolution must be sufficient that the spatial features can be accurately resolved. The velocity resolution must be sufficient that different velocities can be distinguished and that advective motion can be distinguished from random diffusive motion. These three objectives depend on the physical and magnetic properties of the candidate gases, and the nature of the magnetic resonance experiments performed.

From Eq. (3.1), it is obvious that the NMR signal can be maximised by maximising the magnetic field strength and spin density, and by choosing nuclei with large gyromagnetic ratios. The highest field magnet available was 9.4 T and so was used for this reason. The only nucleus with a gyromagnetic ratio comparable to ^1H is ^{19}F; all other nuclei either have less than 10% the relative signal per nucleus than ^1H or have low natural abundance. Hence, only protonated or fluorinated gases are feasible for thermally-polarised gas-phase MRI. The spin density can be increased in two ways - using gases with more NMR-active nuclei attached to each molecule, and increasing the pressure of the gas under study. However, the pressure can only be increased to the vapour pressure of the gas, at which point it will liquefy. The vapour pressure of a gas is usually inversely proportional to its size (due to increased intermolecular bonding for large molecules,) meaning that any increase in sensitivity due to having more NMR active nuclei in a molecule will reduce the increase in sensitivity obtainable from pressurising the gas. This can be observed for propane and butane - butane has two more protons than propane but its vapour pressure is about 2.5 bar(a) compared to 8.5 bar(a) for propane. So while butane has a higher sensitivity than propane at atmospheric pressure, propane has a higher sensitivity when pressurised. Due to the high electron density present around fluorine atoms, fluorinated gases have weaker van de Waal forces between molecules and can be pressurised to higher pressures than hydrocarbon gases. From Table 3.3, propane has the highest relative sensitivity of the three candidate gases, followed by SF_6 and butane. However, this is only the innate sensitivity of the nuclei and does not factor in other physical and experimental considerations. Reconstruction methods such as compressed sensing can improve the sensitivity by allowing undersampling and hence more signal averaging, which is most effectively done using pure phase-encoding methods.

The experimental or acquisition time of a MRI experiment is important for both the temporal resolution but also for the steadiness and stability of the physical system, e.g. whether the system is in steady state or if parameters are changing during the experiment. For a flowing gas system, it is important that the imaging sequence is fast enough that the gas velocity and pressure can be held steady and that any source of gas does not deplete. The propane and butane cylinders have a finite supply of gas and so it is imperative that these not run out in the event of a longer imaging sequence. Likewise, the compressor used for the recirculating SF_6 rig increases the gas temperature and hence changes the pressure and volume flow rate of the gas. The experimental time is determined fundamentally by the value of T_1 but also by the experimental parameters e.g. the image raster size. From Table 3.2, SF_6 has the shortest T_1 by over two orders of magnitude, meaning many more acquisitions can be made per unit time compared with propane and butane. This is important for the sensitivity as SF_6 can achieve ~ 16 times the SNR of propane and butane in the same time due to rapid signal averaging (Table 3.3). One drawback of short T_1 values is the limit on imaging sequences. Experiments such as RARE utilise many spin echoes to acquire a larger number of **k**-space points in one acquisition and so require long T_1 values to facilitate this. SF_6 is precluded from such sequences as the signal is virtually zero in under 100 ms after acquisition (Fig. 3.2). In principle, propane and butane could be used with extended echo trains due to their longer T_1 and T_2 values (Table 3.2), however their large self-diffusion coefficients cause additional signal attenuation that precludes such experiments.

The spatial resolution of a MR image varies with many parameters, including the desired SNR, the sample size and the image size. However, in terms of the NMR active species used, it is only the values of D and T_2 that are expected to influence the resolution (Eqs. (3.2) and (3.3).) Figure 3.4 illustrates the greater dependence on D than T_2, hence the resolution achievable for SF_6 is similar to that of propane and butane (Table 3.4) despite the orders of magnitude difference in T_2. However, due to the rapid signal averaging possible with SF_6, 250 times more signal averages can be acquired in the same experimental time. This manifests as a $15.8^{1/4} \approx 2$ times improvement in the spatial resolution ($\Delta x = 140\,\mu\text{m}$) and suggests that SF_6 is the best choice for maximising image resolution for frequency encoding. This appears to agree with the literature review presented in Section 3.3 where studies using fluorinated gases achieved better resolutions than those using hydrocarbons. For phase encoding, only the diffusion coefficient is important and so SF_6 is also the best choice for purely phase-encoded imaging.

The resolution of a velocity image or propagator measurement depends on the observation time (Δ), the self-diffusion coefficient of the gas and the SNR of the measurement. The equation of Callaghan (Eq. (3.4)) gives a useful illustration of how the resolution will change with these parameters (Fig. 3.5). For longer observation times and smaller self-diffusion coefficients, the relative displacement due to Brownian motion is lower and so slower velocities can be probed (Fig. 3.3), albeit at the cost of signal availability (Fig. 3.2). Likewise, the resolution is improved with greater SNR. For the same SNR, SF_6 can only resolve velocities an order of magnitude faster than propane or butane. This is due to the short T_1 of SF_6 only permitting short observation times. However, as with the spatial resolution, the rapid signal averaging allows an improvement in SNR of $15.8^{1/2} \approx 4$ times in the same timescale for SF_6. This gives a resolution of $\Delta v = 0.18\,\text{mm}\,\text{s}^{-1}$, the same order of magnitude as for propane and butane. However, this value is only useful relative to the values for propane and butane (Table 3.4) - the ratio of advective to diffusive motion at this velocity and observation time is much lower than one for all three gases (Fig. 3.3). It is expected that the velocity resolution of all three gases will be on the order of $1\,\text{cm}\,\text{s}^{-1}$. It is not known how this limit compares to the findings of other workers - only studies that exploited the large diffusion coefficients of gases for restricted diffusion [7, 17] or worked to measure high gas velocities [34, 40] were found in the literature.

3.8 Conclusions

In this chapter, the challenges surrounding gas-phase MRI measurements and the methods used to overcome these are outlined. The applications of such measurements have been briefly reviewed to show the utility of the methods. Theoretical treatments of NMR sensitivity, image resolution and propagator resolution are given from the literature and used to critically assess the measurement limits of three candidate gases: propane, butane and SF_6.

For both image and propagator measurements, better resolution has been predicted for hydrocarbon gases than SF_6 at operating pressures, though these are still a least one order of magnitude worse than is predicted for liquid water. However, this does not consider the time required to acquire said measurements. Due to the much shorter relaxation times, SF_6 is 250 times more sensitive than propane and butane per unit time. When considering the achievable image resolution in a given time, SF_6 is superior to both propane and butane. Short relaxation times also favour phase encoded imaging sequences which are more robust (i.e. insensitive to motion and magnetic susceptibility artefacts) and readily combined with compressed sensing. Phase encoding will be particularly important for particulate filter samples with catalyst content as the catalyst metal will likely distort the magnetic field. For propagators, a similar velocity resolution is expected for all three gases. This is more than sufficient to measure the gas flow along channels in a particulate filter system. Hence, SF_6 was chosen as the probe gas for studies in this thesis.

3.9 References

[1] B. Newling. Gas flow measurements by NMR. *Progress in Nuclear Magnetic Resonance Spectroscopy* (2008) 52 (1), 31–48. doi:10.1016/j.pnmrs.2007.08.002.

[2] D. A. Barskiy, A. M. Coffey, P. Nikolaou, D. M. Mikhaylov, B. M. Goodson, R. T. Branca, G. J. Lu, M. G. Shapiro, V.-V. Telkki, V. V. Zhivonitko, I. V. Koptyug, O. G. Salnikov, K. V. Kovtunov, V. I. Bukhtiyarov, M. S. Rosen, M. J. Barlow, S. Safavi, I. P. Hall, L. Schröder, E. Y. Chekmenev. NMR Hyperpolarization Techniques of Gases. *Chemistry - A European Journal* (2017) 23 (4), 725–751. doi:10.1002/chem.201603884.

[3] L.-S. Bouchard, K. Kovtunov, S. Burt, M. Anwar, I. Koptyug, R. Sagdeev, A. Pines. Para-Hydrogen-Enhanced Hyperpolarized Gas-Phase Magnetic Resonance Imaging. *Angewandte Chemie International Edition* (2007) 46 (22), 4064–4068. doi:10.1002/anie.200700830.

[4] L. G. Kaiser, J. W. Logan, T. Meersmann, A. Pines. Dynamic NMR microscopy of gas phase Poiseuille flow. *Journal of Magnetic Resonance* (2001) 149 (1), 144–148. doi:10.1006/jmre.2000.2283.

[5] E. Brunner, M. Haake, L. Kaiser, A. Pines, J. Reimer. Gas Flow MRI Using Circulating Laser-Polarized ^{129}Xe. *Journal of Magnetic Resonance* (1999) 138 (1), 155–159. doi:10.1006/jmre.1998.1675.

[6] S. I. Han, K. L. Pierce, A. Pines. NMR velocity mapping of gas flow around solid objects. *Physical Review E - Statistical, Nonlinear, and Soft Matter Physics* (2006) 74 (1), 016302. doi:10.1103/PhysRevE.74.016302.

[7] T. A. Kuder, P. Bachert, J. Windschuh, F. B. Laun. Diffusion Pore Imaging by Hyperpolarized Xenon-129 Nuclear Magnetic Resonance. *Physical Review Letters* (2013) 111 (2), 028101. doi:10.1103/PhysRevLett.111.028101.

[8] G. Pavlovskaya, J. Six, T. Meersman, N. Gopinathan, S. P. Rigby. NMR imaging of low pressure, gas-phase transport in packed beds using hyperpolarized xenon-129.

AIChE Journal (2015) 61 (11), 4013–4019. doi:10.1002/aic.14929.

[9] S. D. Beyea, S. L. Codd, D. O. Kuethe, E. Fukushima. Studies of porous media by thermally polarized gas NMR: Current status. *Magnetic Resonance Imaging* (2003) 21 (3-4), 201–205. doi:10.1016/S0730-725X(03)00125-5.

[10] P. Prado, B. Balcom, I. Mastikhin, A. Cross, R. Armstrong, A. Logan. Magnetic Resonance Imaging of Gases: A Single-Point Ramped Imaging with T1 Enhancement (SPRITE) Study. *Journal of Magnetic Resonance* (1999) 137 (2), 324–332. doi: 10.1006/jmre.1998.1674.

[11] I. Koptyug, S. Altobelli, E. Fukushima, A. Matveev, R. Sagdeev. Thermally polarized 1H NMR microimaging studies of liquid and gas flow in monolithic catalysts. *Journal of Magnetic Resonance* (2000) 147 (1), 36–42. doi:10.1006/jmre.2000.2186.

[12] P. Szomolanyi, D. Goodyear, B. Balcom, D. Matheson. SPIRAL-SPRITE: a rapid single point MRI technique for application to porous media. *Magnetic Resonance Imaging* (2001) 19 (3-4), 423–428. doi:10.1016/S0730-725X(01)00260-0.

[13] I. V. Koptyug, L. Y. Ilyina, A. V. Matveev, R. Z. Sagdeev, V. N. Parmon, S. A. Altobelli. Liquid and gas flow and related phenomena in monolithic catalysts studied by1H NMR microimaging. *Catalysis Today* (2001) 69 (1-4), 385–392. doi:10.1016/S0920-5861(01)00396-0.

[14] I. V. Koptyug, A. V. Matveev, S. A. Altobelli. NMR studies of hydrocarbon gas flow and dispersion. *Applied Magnetic Resonance* (2002) 22 (2), 187–200. doi:10.1007/BF03166102.

[15] S. L. Codd, S. A. Altobelli. A PGSE study of propane gas flow through model porous bead packs. *Journal of Magnetic Resonance* (2003) 163 (1), 16–22. doi: 10.1016/S1090-7807(03)00111-3.

[16] Z. Zhang, A. V. Ouriadov, C. Willson, B. J. Balcom. Membrane gas diffusion measurements with MRI. *Journal of Magnetic Resonance* (2005) 176 (2), 215–222. doi:10.1016/J.JMR.2005.06.009.

[17] P. Stevenson, A. J. Sederman, M. D. Mantle, X. Li, L. F. Gladden. Measurement of bubble size distribution in a gas-liquid foam using pulsed-field gradient nuclear magnetic resonance. *Journal of Colloid and Interface Science* (2010) 352 (1), 114–20. doi:10.1016/j.jcis.2010.08.018.

[18] A. Honari, S. J. Vogt, E. F. May, M. L. Johns. Gas–Gas Dispersion Coefficient Measurements Using Low-Field MRI. *Transport in Porous Media* (2015) 106 (1), 21–32. doi:10.1007/s11242-014-0388-2.

[19] M. Mirdrikvand, J. Ilsemann, J. Thöming, W. Dreher. Spatially Resolved Characterization of Gas Propagator in Monolithic Structured Catalysts Using NMR Diffusiometry. *Chemical Engineering & Technology* (2018) 41 (9), 1871–1880. doi: 10.1002/ceat.201800201.

[20] P. A. Rinck, S. B. Petersen, P. C. Lauterbur. NMR-Imaging von fluorhaltigen Substanzen. 19Fluor-Ventilations- und -Perfusionsdarstellungen. *Fortschr Röntgenstr* (1984) 140 (3), 239–243. doi:10.1055/s-2008-1052964.

[21] D. O. Kuethe, A. Caprihan, E. Fukushima, R. A. Waggoner. Imaging lungs using inert fluorinated gases. *Magnetic Resonance in Medicine* (1998) 39 (1), 85–88. doi:10.1002/mrm.1910390114.

[22] D. O. Kuethe, A. Caprihan, H. M. Gach, I. J. Lowe, E. Fukushima. Imaging obstructed ventilation with NMR using inert fluorinated gases. *Journal of Applied Physiology* (2000) 88 (6), 2279–86. doi:10.1152/jappl.2000.88.6.2279.

[23] R. E. Jacob, Y. V. Chang, C. K. Choong, A. Bierhals, D. Zheng Hu, J. Zheng, D. A. Yablonskiy, J. C. Woods, D. S. Gierada, M. S. Conradi. ^{19}F MR imaging of ventilation and diffusion in excised lungs. *Magnetic Resonance in Medicine* (2005) 54 (3), 577–585. doi:10.1002/mrm.20632.

[24] J. Ruiz-Cabello, J. M. Pérez-Sánchez, R. Pérez de Alejo, I. Rodríguez, N. González-Mangado, G. Peces-Barba, M. Cortijo. Diffusion-weighted ^{19}F-MRI of lung periphery: Influence of pressure and air–SF_6 composition on apparent diffusion coefficients. *Respiratory Physiology & Neurobiology* (2005) 148 (1-2), 43–56. doi:10.1016/J.RESP.2005.04.007.

[25] U. Wolf, A. Scholz, C. P. Heussel, K. Markstaller, W. G. Schreiber. Subsecond fluorine-19 MRI of the lung. *Magnetic Resonance in Medicine* (2006) 55 (4), 948–951. doi:10.1002/mrm.20859.

[26] N. L. Adolphi, D. O. Kuethe. Quantitative mapping of ventilation-perfusion ratios in lungs by ^{19}F MR imaging of T1 of inert fluorinated gases. *Magnetic Resonance in Medicine* (2008) 59 (4), 739–746. doi:10.1002/mrm.21579.

[27] A.-W. Scholz, U. Wolf, M. Fabel, N. Weiler, C. P. Heussel, B. Eberle, M. David, W. G. Schreiber. Comparison of magnetic resonance imaging of inhaled SF_6 with respiratory gas analysis. *Magnetic Resonance Imaging* (2009) 27 (4), 549 – 556. doi:https://doi.org/10.1016/j.mri.2008.08.010.

[28] M. Couch, A. Ouriadov, M. Albert. Pulmonary Imaging Using ^{19}F MRI of Inert Fluorinated Gases. In *Hyperpolarized and Inert Gas MRI*, pp. 279–292. Elsevier (2017) doi:10.1016/B978-0-12-803675-4.00018-X.

[29] M. J. Lizak, M. S. Conradi, C. G. Fry. NMR imaging of gas imbibed into porous ceramic. *Journal of Magnetic Resonance* (1991) 95 (3), 548–557. doi:10.1016/0022-2364(91)90168-S.

[30] A. Caprihan, C. Clewett, D. Kuethe, E. Fukushima, S. Glass. Characterization of partially sintered ceramic powder compacts using fluorinated gas NMR imaging. *Magnetic Resonance Imaging* (2001) 19 (3-4), 311–317. doi:10.1016/S0730-725X(01)00242-9.

[31] S. D. Beyea, A. Caprihan, S. J. Glass, A. DiGiovanni. Nondestructive characterization of nanopore microstructure: Spatially resolved Brunauer–Emmett–Teller isotherms using nuclear magnetic resonance imaging. *Journal of Applied Physics* (2003) 94 (2), 935–941. doi:10.1063/1.1581348.

[32] D. O. Kuethe, M. D. Scholz. Imaging cracks in marble with magnetic resonance imaging of inert fluorinated gases. *Applied Magnetic Resonance* (2007) 32 (1-2), 3–12. doi:10.1007/s00723-007-0004-5.

[33] T. R. Brosten, S. L. Codd, K. V. Romanenko, S. W. Sofie, J. D. Seymour. Magnetic resonance microscopy analysis of transport in a novel Tape-Cast porous ceramic. *AIChE Journal* (2009) 55 (10), 2506–2514. doi:10.1002/aic.11872.

[34] B. Newling, C. C. Poirier, Y. Zhi, J. A. Rioux, A. J. Coristine, D. Roach, B. J. Balcom. Velocity imaging of highly turbulent gas flow. *Physical Review Letters* (2004) 93 (15), 154503. doi:10.1103/PhysRevLett.93.154503.

[35] M. H. Sankey, D. J. Holland, A. J. Sederman, L. F. Gladden. Magnetic resonance velocity imaging of liquid and gas two-phase flow in packed beds. *Journal of Magnetic Resonance* (2009) 196 (2), 142–8. doi:10.1016/j.jmr.2008.10.021.

[36] C. Boyce, N. Rice, A. Sederman, J. Dennis, D. Holland. 11-interval PFG pulse sequence for improved measurement of fast velocities of fluids with high diffusivity in systems with short T_2*. *Journal of Magnetic Resonance* (2016) 265, 67–76. doi: 10.1016/j.jmr.2016.01.023.

[37] C. Boyce, N. Rice, J. Davidson, A. Sederman, J. Dennis, D. Holland. Magnetic resonance imaging of gas dynamics in the freeboard of fixed beds and bubbling fluidized beds. *Chemical Engineering Science* (2016) 147, 13–20. doi:10.1016/j.ces.2016.03.005.

[38] C. M. Boyce, N. P. Rice, A. Ozel, J. F. Davidson, A. J. Sederman, L. F. Gladden, S. Sundaresan, J. S. Dennis, D. J. Holland. Magnetic resonance characterization of coupled gas and particle dynamics in a bubbling fluidized bed. *Physical Review Fluids* (2016) 1 (7), 074201. doi:10.1103/PhysRevFluids.1.074201.

[39] N. P. Ramskill, A. P. York, A. J. Sederman, L. F. Gladden. Magnetic resonance velocity imaging of gas flow in a diesel particulate filter. *Chemical Engineering Science* (2017) 158, 490–499. doi:10.1016/j.ces.2016.10.017.

[40] A.-R. P. Gauthier, B. Newling. Gas Flow Mapping in a Recorder: An Application of SPRITE MRI. *Applied Magnetic Resonance* (2018) 49 (10), 1151–1162. doi: 10.1007/s00723-018-1034-x.

[41] D. J. Holland, L. F. Gladden. Less is more: how compressed sensing is transforming metrology in chemistry. *Angewandte Chemie (International Edition)* (2014) 53 (49), 13330–40. doi:10.1002/anie.201400535.

[42] G. L. Bretthorst, W. C. Hutton, J. R. Garbow, J. J. Ackerman. Exponential parameter estimation (in NMR) using Bayesian probability theory. *Concepts in Magnetic*

Resonance Part A (2005) 27A (2), 55–63. doi:10.1002/cmr.a.20043.

[43] G. L. Bretthorst, W. C. Hutton, J. R. Garbow, J. J. Ackerman. Exponential model selection (in NMR) using Bayesian probability theory. *Concepts in Magnetic Resonance Part A* (2005) 27A (2), 64–72. doi:10.1002/cmr.a.20042.

[44] Y. Matviychuk, E. von Harbou, D. J. Holland. An experimental validation of a Bayesian model for quantification in NMR spectroscopy. *Journal of Magnetic Resonance* (2017) 285, 86–100. doi:10.1016/J.JMR.2017.10.009.

[45] D. Holland, A. Blake, A. Tayler, A. Sederman, L. Gladden. Bubble size measurement using Bayesian magnetic resonance. *Chemical Engineering Science* (2012) 84, 735–745. doi:10.1016/j.ces.2012.08.024.

[46] J. Ross, D. Holland, A. Blake, A. Sederman, L. Gladden. Extending the use of Earth's Field NMR using Bayesian methodology: Application to particle sizing. *Journal of Magnetic Resonance* (2012) 222, 44–52. doi:10.1016/j.jmr.2012.05.023.

[47] T. W. Blythe, A. J. Sederman, E. H. Stitt, A. P. York, L. F. Gladden. PFG NMR and Bayesian analysis to characterise non-Newtonian fluids. *Journal of Magnetic Resonance* (2017) 274, 103–114. doi:10.1016/j.jmr.2016.11.003.

[48] M. Lustig, D. Donoho, J. M. Pauly. Sparse MRI: The application of compressed sensing for rapid MR imaging. *Magnetic Resonance in Medicine* (2007) 58 (6), 1182–1195. doi:10.1002/mrm.21391.

[49] Y. Wu, C. D'Agostino, D. J. Holland, L. F. Gladden. *In situ* study of reaction kinetics using compressed sensing NMR. *Chem. Commun.* (2014) 50 (91), 14137–14140. doi:10.1039/C4CC06051B.

[50] P. Parasoglou, D. Malioutov, A. J. Sederman, J. Rasburn, H. Powell, L. F. Gladden, A. Blake, M. L. Johns. Quantitative single point imaging with compressed sensing. *Journal of Magnetic Resonance* (2009) 201 (1), 72–80. doi:10.1016/j.jmr.2009.08.003.

[51] D. Holland, D. Malioutov, A. Blake, A. Sederman, L. Gladden. Reducing data acquisition times in phase-encoded velocity imaging using compressed sensing. *Journal of Magnetic Resonance* (2010) 203 (2), 236–46. doi:10.1016/j.jmr.2010.01.001.

[52] M. Benning, L. Gladden, D. Holland, C. B. Schönlieb, T. Valkonen. Phase reconstruction from velocity-encoded MRI measurements - A survey of sparsity-promoting variational approaches. *Journal of Magnetic Resonance* (2014) 238, 26–43. doi:10.1016/j.jmr.2013.10.003.

[53] A. B. Tayler, D. J. Holland, A. J. Sederman, L. F. Gladden. Exploring the Origins of Turbulence in Multiphase Flow Using Compressed Sensing MRI. *Physical Review Letters* (2012) 108 (26), 264505. doi:10.1103/PhysRevLett.108.264505.

[54] H. T. Fabich, M. Benning, A. J. Sederman, D. J. Holland. Ultrashort echo time (UTE) imaging using gradient pre-equalization and compressed sensing. *Journal of Magnetic Resonance* (2014) 245, 116–124. doi:10.1016/j.jmr.2014.06.015.

[55] P. T. Callaghan. *Principles of Nuclear Magnetic Resonance Microscopy* (1991). doi: 10.1118/1.596918.

[56] P. T. Callaghan. *Translational Dynamics & Magnetic Resonance: Principles of Pulsed Gradient Spin Echo NMR*. 2nd edition. Oxford University Press (2011).

[57] J. A. Aguilar, M. Nilsson, G. Bodenhausen, G. A. Morris. Spin echo NMR spectra without J modulation. *Chemical Communications* (2012) 48 (6), 811–813. doi: 10.1039/C1CC16699A.

[58] K. Takegoshi, K. Ogura, K. Hikichi. A perfect spin echo in a weakly homonuclear J-coupled two spin-12 system. *Journal of Magnetic Resonance* (1989) 84 (3), 611–615. doi:10.1016/0022-2364(89)90127-3.

Chapter 4

Laminar and turbulent flow at the filter entrance and exit

Work presented in this chapter has been published in the Chemical Engineering Journal: J.D. Cooper, A.P.E. York, A.J. Sederman, L.F. Gladden. Measuring velocity and turbulent diffusivity in wall-flow filters using compressed sensing magnetic resonance. *Chemical Engineering Journal* (2018), Article in press. doi:10.1016/j.cej.2018.08.076.

4.1 Introduction

While most work surrounding gas flow in particulate filters has focused on the internal hydrodynamics [1, 2], the behaviour of real-world filter systems is coupled to their installation in the exhaust stream. Due to spatial restrictions, filters are often much wider than the exhaust pipes than connect to them. This creates two problems. First, the difference in pipe diameters necessitates expansion and contraction geometries either side of the filter. The exact shape of these geometries can vary and have been found to create both flow and temperature inhomogeneities at the filter inlet [3]. Second, the large difference in diameter between the exhaust stream and individual filter channels creates large differences in the Reynolds numbers of the exhaust flow. Even under modest flow rates, the gas flow changes from Reynolds numbers of $\mathcal{O}(10^4)$ upstream, to $\mathcal{O}(10^2)$ inside the monolith, to $\mathcal{O}(10^4)$ again downstream [4]. The implication of this is that even for fully laminar flow inside the monolith channels, there will be transitional regimes at both the entrance and exit, and the development of laminar flow at the entrance. Such effects are predicted to increase the pressure drop across the filter and perturb filtration behaviour inside the filter.

Most work exploring entrance and exit effects has focused on flow-through monoliths with applications as two- and three-way catalysts. It is unclear as to how relevant these effects are in filter geometries. Most of the studies performed for filter geometries are concerned with the uniformity of flow entering the filter on the scale of the entire filter [3, 5, 6]. Few studies look at the behaviour of these flows at the channel scale, yet this may have important impacts on the pressure drop and filtration behaviour of filters. Such effects are expected to be less significant for flow-through monoliths as the small cross-section of the walls results in a very minor flow contraction and expansion. However, the plugs present in wall-flow filters cause a severe reduction in flow cross-sectional area of 60 % to

70 %, meaning contraction and expansion effects are significant. Masoudi [7] reported that for moderately soot-loaded filters, the entrance and exit regions contributed up to 10% of the total pressure drop; for lightly soot-loaded filters, this contribution increases to 25%. As such, it is necessary to consider such effects when modelling filter operation.

Measurements of gas flows at the entrance and exit regions of filters are desired to observe the flow phenomena and understand their impact on filter performance. However, most work in this area has focused on numerical simulations and few experimental measurements exist. As established in Chapter 3, MRI methods are well suited to measure gas flow fields in difficult geometries and provide data for comparison with simulations. Additionally, such methods can be extended to quantify the level of turbulence and hence provide a more complete understanding of the hydrodynamics; this is reviewed in Section 4.3. Together, these measurements can provide data for comparison with previous modelling studies and inform future work in this area.

This chapter is structured as follows. First, the prior work exploring entrance and exit effects in both FTMs and filters is reviewed, along with the use of NMR to study turbulence. Second, the theory behind the turbulence measurements used herein is derived and the experimental methods are stated. Third, the results of the studies are presented, discussed in the context of the current literature and conclusions are drawn.

4.2 Scope of study

The aim of this chapter is to characterise the hydrodynamics of gas entering and exiting a wall-flow filter, in particular to identify regions of turbulent flow that contribute to an additional pressure drop across the system and to compare experimental measurements with simulations from the literature. This is achieved in three sections of work. First, MRI measurements of magnetic field strength were used to characterise the magnetic susceptibility match of different filter substrates with sulfur hexafluoride. A good susceptibility match is necessary to ensure a homogeneous magnetic field across the sample and minimise this as a source of measurement artefacts. The timescale of the velocity fluctuations was also verified using a PGSE method to allow quantification of the turbulent diffusivity measurements. Second, two-dimensional MRI velocimetry is used to measure the axial flow fields at the entrance and exit of a wall-flow filter, followed by the use of three-dimensional MRI to measure the axial velocity field and the turbulent diffusivity distribution at the exit of the filter. This allows co-registration of the data to study the structural relationship between the gas velocity and the turbulence. Finally, the MRI results are compared with previous predictions in the literature in order to validate and provide future suggestions for simulation work.

4.3 Literature review

4.3.1 Turbulence in square channels and FTMs

Studies of hydrodynamics in square channels have focused on the mass and heat transfer from the axial flow to the catalyst located on the channel walls in flow-through monoliths. Inside the channels, laminar, developing laminar, transitional and turbulent regimes have all been studied [8–10], with both developing flow and turbulent flow found to increase mass and heat transfer to the walls. Mixing due to turbulent eddies increases the effective diffusion above that of Brownian and viscous mechanisms. The additional mass transfer is more important for gaseous species; the increase in mass transfer of particulates is less due to their higher inertia. In addition to the expected flow development following sudden pipe entry, turbulent effects upstream of the monolith are predicted to enter the channels before decaying over some characteristic length scale [11]. Two mechanisms have been predicted for this. The first is that upstream turbulent eddies much larger than the channel diameter cause flow in the first section of the channel to be perturbed. The second is that eddies of similar or smaller size to the channel diameters can enter the channels completely. These effects could also occur in filter geometries and influence flow behaviour in the inlet channels, however no literature has been found that focuses on mass and heat transport in this context. However, the flow of gas through the porous wall (and washcoat, if present) in filter geometries can increase mass and heat transfer, there may be no benefit from having high turbulent diffusivity in the filter channels.

CFD simulation work has been performed by Cornejo and co-workers [4, 12, 13] that focuses on entrance and exit effects in FTMs. While such work is not directly applicable to filters due to the differences in substrate geometry, they both experience similar changes in gas Reynolds numbers and so may provide qualitative insight. Cornejo *et al.* found that even at low Reynolds numbers ($\mathrm{Re_c} \sim 100$), significant velocity fluctuations were predicted at the beginning of the monolith channels due to upstream turbulence [12]; such effects could persist for up to 8 channel diameters into the filter depending on the location of the channel within the whole filter [13]. At the monolith exit, flow instability was observed that led to turbulence generation if the Reynolds number based on the channel corner width exceeded 160 [4]. These fluctuations and turbulent effects were predicted to continue for tens of channel widths downstream of the filter exit.

4.3.2 Entrance and exit effects in filters

Due to the opaque and brittle nature of filter substrates and the complexity of their geometry, most conventional anemometry methods (e.g. LDA, HWA, PIV) are inapplicable; the only reported measurement is by Oxarango *et al.* using HWA to demonstrate spatial heterogeneity in jets formed at the filter exit [14]. Hence, studies of gas flow in filters, especially at the ends, have been performed using numerical simulations. The most notable of these are by Konstandopoulos *et al.* [15] and Liu and Miller [16]. Konstandopoulos studied a square channel geometry for $\mathrm{Re_c}$ of 530 - 2120, whereas Liu and Miller studied a triangular channel geometry for $\mathrm{Re_c}$ of 186 - 1859. Both studies predicted broadly similar flow patterns: relatively clean contraction at the filter entrance, and jet formation at the exit with recirculating flows developing between the jets. However, there are some differences between the two. Konstandopoulos predicted completely smooth contraction of gas into the inlet channels, whereas Liu and Miller found recirculating flow developing in front of the outlet channel plugs. Similarly, at the exit Liu and Miller found recirculating flows develop at the end of the inlet channels, whereas Konstandopoulos did not. The combined predictions of these two studies are illustrated in Fig. 4.1. Both studies predicted their respective flow phenomena at all flow rates considered. Konstandopoulos also reported that the exit jets induced strong mixing and pressure fluctuations that continued for several plug lengths downstream of the filter. Liu and Miller predicted that the observed flow behaviours could affect the filtration behaviour of particulate matter. Both studies used the k-ϵ turbulence model, however neither study commented on the turbulent kinetic energy.

Other CFD studies, while not focussing on the entrance and exit effects, have included the entrance and exit geometry in the model mesh. Liu *et al.* [17] used a 2D Eulerian-Lagrangian model to track particle trajectories in a square-channel filter and showed recirculating flow between exit jets. Sbrizzai *et al.* [18] used 3D CFD and Lagrangian particle tracking to study particle deposition in a square channel filter; it was reported that a *vena contracta* formed by the entrance condition caused the particle steamlines to bend away from the channel walls, resulting in little to no filtration occurring in the first fifth of the filter length. A *vena contracta* was also predicted by both Bensaid *et al.* [19] and Liu *et al.* [20], though the impact on filtration was less severe. Sbrizzai also noted that despite earlier literature predictions of vortex development in the corners of square ducts [21], no such vortices were predicted in the corners of the filter channels. This was attributed to the presence of porous walls in the filter geometry.

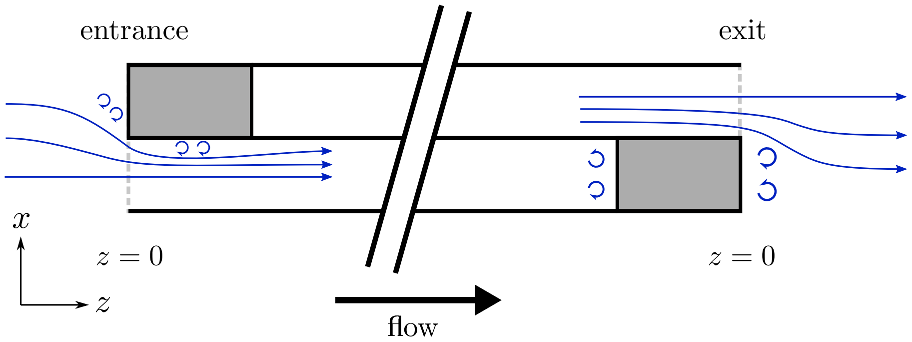

Fig. 4.1: Schematic showing all flow phenomena predicted to occur at the filter entrance and exit [15, 16]. The direction of flow is parallel to the z axis and the front and rear faces are defined at position $z = 0$ for their respective images.

Low-dimensionality models often use correlations and results from simple geometries, such as the Borda-Carnot equation (Eq. (4.1), where Δp is the pressure loss across the expansion/contraction, ξ is an empirical loss coefficient, ρ is the fluid density and Δv is the change in velocity across the expansion/contraction) for sudden expansion/contractions in tubes [22, 23] or perforated plates [24, 25], in order to simulate the pressure losses incurred at the entrance and exit. However, these fail to capture the exact geometry of the wall-flow filter entrance and exit, and the interaction with flow inside the channels and walls. As a result, both the absolute and relative contributions of the entrance and exit effects to the overall pressure drop varies between studies. Watling *et al.* [26] compared the relative contributions of entrance and exit effects as modelled in the literature; the findings are summarised in Table 4.1.

$$\Delta p = \frac{1}{2}\xi\rho(\Delta v)^2. \tag{4.1}$$

Table 4.1: Relative contributions of entrance and exit effects in different studies

Study	Entrance / %	Exit / %
Konstandopoulos *et al.* [15]	50	50
Masoudi [7]	25	75
Haralampous *et al.* [27]	67	33
Bouteiller *et al.* [28]	94	6
Torregrosa *et al.* [29]	33	67
Watling *et al.* [26]	76	24

4.3.3 NMR studies of turbulent flow

Interest in the effect of turbulent flow on the NMR signal has been present since the first studies of flow using NMR and MRI. The study of turbulence using MRI has largely followed two routes: ‘snap-shot’ methods that capture an instantaneous picture of the flow field and resolve transient features, and time-averaged methods that look at the system over an extended period of time to identify regions with higher or lower amounts of turbulence.

Snap-shot MRI velocimetry began as an extension of the original EPI sequence developed by Mansfield and Maudsley [30]. The addition of velocity encoding gradients allowed the phase encoding of velocity in one or more directions. Kose [31] used spin-echo EPI to acquire both transverse velocity components in a single excitation to observe turbulent pipe flow. Sederman *et al.* [32] expanded on this work with GERVAIS (Gradient Echo Rapid Velocity and Acceleration Imaging Sequence), permitting all three components of the fluid velocity vector to be measured in a single acquisition, allowing not only a comprehensive instantaneous study of turbulent pipe flow but also measurement of the velocity autocorrelation function of the system and subsequent validation of the ‘snap-shot’ claim. Tayler *et al.* [33, 34] incorporated compressed sensing to spiral imaging, allowing images with full velocity vectors to be acquired in under 16 ms. This permitted the study of fluid motion in rising bubbles. While these methods are incredibly powerful, their use is limited to a small number of systems. High sensitivity is required to achieve a satisfactory SNR in a single scan, precluding most gas-phase and non-proton based studies. The relaxation times must also exist in a narrow optimal range - they need to be long enough to allow full image acquisition without significant relaxation weighting of the signal but short enough to allow quick repetitions for temporal resolution. The fastest image acquisition sequences typically use frequency-encoding, necessitating excellent magnetic field homogeneity and magnetic susceptibility matches between phases. Most 'snap-shot' studies use Gd^{3+} or Dy^{3+} doped water to achieve these criteria [33].

Time-averaged studies of turbulence generally have fewer requirements and so are more widely applicable. However, good magnetic field homogeneity is still required in order to not overestimate the degree of turbulence. In a pseudo-steady system, the velocity distribution $v(t)$ can be decomposed into the steady, mean velocity, $\bar{v}$, and time-dependent velocity fluctuations, $v'(t)$:

$$v(t) = \bar{v} + v'(t). \tag{4.2}$$

Over a time interval, the velocity fluctuations v' associated with turbulence, create a velocity dispersion or distribution (Fig. 4.2 (a)). When motion encoding gradients are applied, this causes a corresponding phase dispersion. For a volume element, the net magnetisation is the sum of all spins and so the degree of phase dispersion will result in an attenuation of the signal magnitude which can then be related to the degree of turbulence present (Fig. 4.2 (b-c)). The phase of the net magnetisation is related to the mean velocity, $\bar{v}$, by Eq. (2.29). Several models have been developed that relate the turbulent fluctuations to the phase dispersion [35–39]. This has allowed insight through imaging studies such as those by Evans *et al.* [40], Gao *et al.* [41] and Kose [42], which use the image signal attenuation to map regions of higher turbulence and shear in pipe flows of water. Kuethe and Gao [39] demonstrated the validity of different models at different measurement timescales and showed that for observation times much longer than the correlation time of the velocity fluctuations, the turbulence resembles Brownian diffusion and can be characterised using turbulent diffusivity, D_{turb}. Measurements of turbulent diffusivity have been made for jets of water exiting a nozzle [43], water flowing through a stenosis [36], SF_6 gas flow over a bluff obstruction and a wing section [44] and water flowing through a dysfunctional mechanical heart valve [45].

There has been some concern over the validity of time-averaged MR studies of turbulence and their agreement with other methods, though any discrepancy is minimal under appropriate experimental conditions. Elkins *et al.* [46] found good agreement between MRI turbulent velocity measurements and particle imaging velocimetry (PIV), while Kadbi *et al.* [47] showed that short echo times minimise flow artefacts and increase agreement with Doppler methods. The effects of intravoxel velocity and SNR on MRI turbulence were

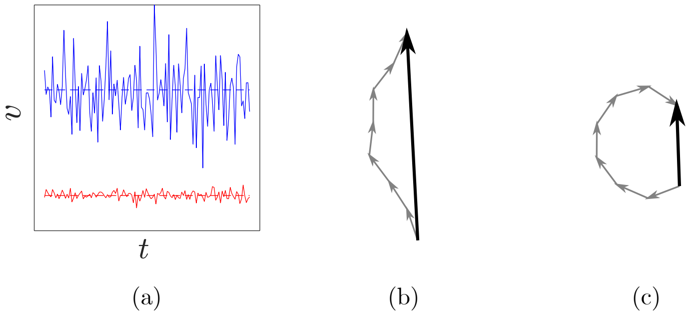

Fig. 4.2: (a) Plot illustrating the velocity fluctuations about a constant mean value expected during measurements of a system with high (blue) and low (red) turbulence. (b) The net magnetisation for a system with small velocity fluctuations, resulting in a low phase dispersion and a high overall magnitude. (c) The net magnetisation for a system with large velocity fluctuations and high phase dispersion, resulting in a lower magnitude.

studied by Dyverfeldt *et al.* [48], showing that while the former has no significant impact, the strength of the motion encoding gradients need to be optimised relative to the noise level in the image to minimise uncertainty and under-measurement. Newling *et al.* also found good qualitative agreement between the measured turbulent diffusivity and the mean square fluctuations predicted using CFD methods [44].

4.4 Theory

4.4.1 NMR measurements of turbulence

The principle behind the turbulent diffusivity measurements used in the research reported here is based on the method of Gao and Gore [35], Gatenby and Gore [36] and Kuethe and Gao [39]. For a pair of bipolar gradients of strength G, duration δ and separation Δ, the phase of the NMR signal from a spin j is described by

$$\phi_j = \int \gamma G(t) x(t)\,\mathrm{d}t = -\gamma G \int_0^{\delta} \left[x(t+\Delta) - x(t)\right]\,\mathrm{d}t. \tag{4.3}$$

This gives an ensemble mean square phase of

$$\left\langle \phi_j^2 \right\rangle = \gamma^2 G^2 \int_0^{\delta}\int_0^{\delta} \left\langle \left[x(t_1+\Delta) - x(t_1)\right] \times \left[x(t_2+\Delta) - x(t_2)\right] \right\rangle \mathrm{d}t_1 \mathrm{d}t_2. \tag{4.4}$$

This expression can be evaluated by using Taylor's expression [49] for the normalised Lagrangian autocorrelation function,

$$R_T = \frac{\left\langle v'_t v'_{t+T} \right\rangle}{\left\langle v'^2 \right\rangle} \approx \exp\left[-|T|/\tau_C\right], \tag{4.5}$$

where v' is the time-dependent component in the Reynolds decomposed velocity, $v(t) = \bar{v} + v'(t)$, and τ_C is the Lagrangian correlation time. By expanding the integrand product and substituting the autocorrelation function, the integrand is evaluated as

$$\left\langle \phi_j^2 \right\rangle = 2\gamma^2 G^2 \left\langle v'^2 \right\rangle \tau_C \big[\delta^2 \left(\Delta - \delta/3\right) - 2\tau_C^2 \delta + \tau_C^3 (2 - 2\mathrm{e}^{-\Delta/\tau_C} + \mathrm{e}^{-(\Delta-\delta)/\tau_C} + \mathrm{e}^{-(\Delta+\delta)/\tau_C} - 2\mathrm{e}^{-\delta/\tau_C})\big]. \tag{4.6}$$

This result simplifies greatly in the limits $\tau_C << \Delta$ and $\tau_C << \delta$, reducing to

$$\left\langle \phi_j^2 \right\rangle = 2\gamma^2 G^2 \delta^2 (\Delta - \delta/3) D_{turb}, \tag{4.7}$$

where $D_{turb} = \tau_C \left\langle v'^2 \right\rangle$. This gives a net signal attenuation of

$$S/S_0 = \exp\left[-\gamma^2 G^2 \delta^2 (\Delta - \delta/3) D_{\mathrm{turb}}\right], \tag{4.8}$$

which is readily identified as the Stejskal-Tanner equation [50]. The motion of the spins decorrelates during the experiment and the turbulence appears to behave like diffusion, hence the use of turbulent diffusivity[1]. In the opposite limit, the equation reduces to that of Fukuda *et al.* [38]. As the turbulent diffusivity coefficient is typically two orders of magnitude greater than the self-diffusion coefficient, $D \approx D_{turb}$ for the current treatment.

Any imaging gradients will also contribute to the signal attenuation from diffusive processes. For a purely phase-encoded sequence, the calculation is simplified. For a single gradient pulse of length δ and strength $G_{im,i}$ (for $i = x, y, z$), the signal attenuation is given by

$$S/S_0 = \exp\left[-\frac{1}{12}\gamma^2 D_{\mathrm{turb}} \delta^3 \sum_i \left\langle G_{\mathrm{im},i}^2 \right\rangle\right], \tag{4.9}$$

in the same limit as Equation 4.8. The total signal attenuation is the product of Equations 4.8 and 4.9. In practice, maps of turbulent diffusivity were obtained using the relationship

$$D_{\mathrm{turb}}(\mathbf{r}) = \frac{\log[|\rho_{\mathrm{static}}(\mathbf{r})|] - \log[|\rho_{\mathrm{flow}}(\mathbf{r})|]}{\gamma^2 M_1}, \tag{4.10}$$

where ρ_{static} and ρ_{flow} are spin density images acquired with flowing and static fluid respectively, and M_1 is the total first gradient moment at the time of acquisition, given by

$$M_1 = G^2 \delta^2 (\Delta - \delta/3) + \frac{1}{12}\delta^3 \sum_i \left\langle G_{\mathrm{im},i}^2 \right\rangle. \tag{4.11}$$

Table 4.2: Relevant properties of the DPF sample used

material	aluminium titanate
filter length / mm	153
sample diameter / mm	15
channel width / mm	1
wall thickness / mm	0.33
plug length / mm	5
no. inlet channels	30
no. outlet channels	31
porosity / %	52

4.5 Experimental

4.5.1 Materials and equipment

In this study, a cylindrical sample of an aluminium titanate DPF was used, the details of which are given in Table 4.2. The long axis of the filter sample was parallel to the B_0 field (z axis) of the spectrometer. In all experiments, only the channels with 8 neighbouring channels are used for analysis in order that all channels are subject to the same boundary conditions (i.e. any wall-effects are minimised). The flow configuration is illustrated in Fig. 4.3. The sample (A) was wrapped in PTFE tape to minimise flow bypass and held in a cylindrical polyetheretherketone (PEEK) cell (B), of internal diameter 18 mm, that operates at pressures up to 10 bar(g) inside the magnet (C). Gas was delivered into the PEEK cell 5 cm upstream of the filter entrance through a perforated plate gas distributor (D), resulting in an approximately uniform entrance condition to the filter. A 2 cm long conical geometry with a tapering diameter was placed 10 cm downstream from the filter exit at the end of the flow cell (E). Gas was supplied using the recycling SF_6 rig described in Appendix A through 1/8 in Swagelok tubing. The SF_6 was pressurised to 5.25±0.25 bar(g) and mass flow rates of $25\,\mathrm{g\,min^{-1}}$, $50\,\mathrm{g\,min^{-1}}$, $100\,\mathrm{g\,min^{-1}}$ and $150\,\mathrm{g\,min^{-1}}$ were used, corresponding to channel Reynolds numbers, $\mathrm{Re_c}$, of 210, 360, 720 and 1140 respectively, where $\mathrm{Re_c}$ is defined as

$$\mathrm{Re_c} = \frac{\rho v_{\mathrm{sf}} d_c}{\mu}, \tag{4.12}$$

where ρ is the gas density (taken to be $40.1\,\mathrm{kg\,m^{-3}}$), v_{sf} is the superficial axial velocity in the channel, d_c is the channel side length and μ is the gas dynamic viscosity (taken to be $15.1 \times 10^{-6}\,\mathrm{Pa\,s}$). The experiments were performed at 21±1 °C.

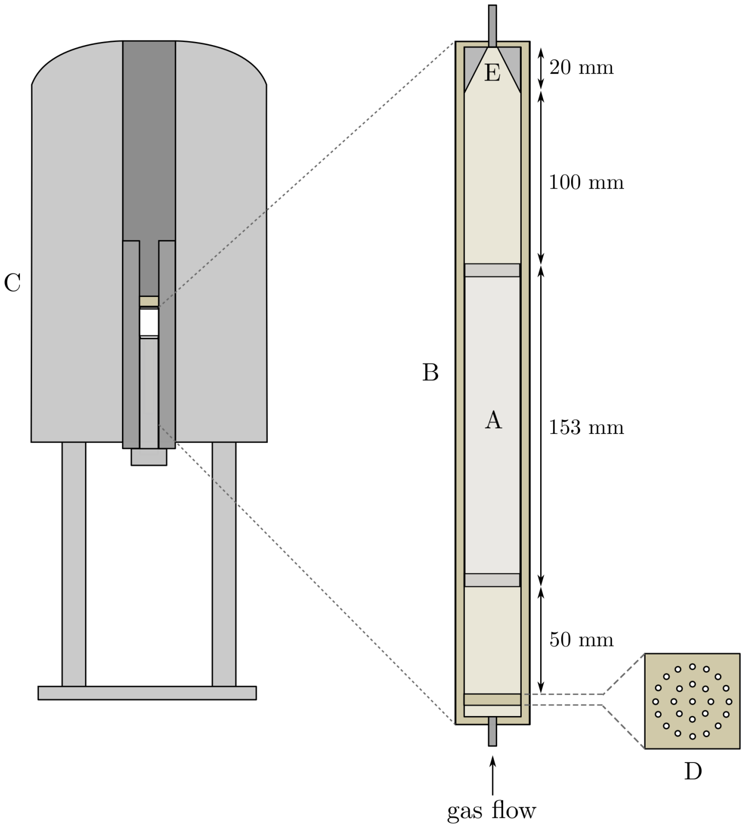

Fig. 4.3: Schematic showing the DPF sample inside the PEEK flow cell and magnet.

4.5.2 Magnetic resonance

All MRI experiments were performed using a 9.4 T superconducting magnet controlled by a Bruker AV 400 spectrometer tuned to the ^{19}F resonant frequency, 376.19 MHz. Spatial resolution and displacement encoding was provided by three orthogonal micro-imaging gradient coils, each with a maximum strength of 146 G cm^{-1}. A matrix rotation was applied to align the gradient axes with the natural axes of the filter sample. A recycle time of 32 ms was used. Table 4.3 shows the relevant parameters for the technique described in this section.

The imaging method used was based on spin-echo single point imaging (SESPI) [51, 52] shown in Fig. 4.4. For each **k**-space point sampled, a FID of 128 complex points was acquired at a sweep width of 200 kHz and summed to increase the SNR. Compressed sensing was used for all imaging experiments; data was under-sampled in all imaging directions according to the polynomial probability density function of Lustig *et al.* [53] shown in §2.4. A single gradient pulse, of duration 0.74 ms, in each direction was used for phase-encoding (G_{phase}). In the 2D imaging sequence, a 256 µs Gaussian-shaped 180° soft pulse, with a FWHM of 8000 Hz, was applied with a gradient (G_{slice}) for slice selection in

---

[1] As this process is driven by non-ideal flow and not random motion, it is actually a dispersion. However, diffusivity is used for consistency with the literature.

Table 4.3: MRI parameters for SESPI experiments

Parameter	2D imaging	3D imaging
full image size	128×128	$64 \times 64 \times 32$
field of view / mm	$18 \times 18\,(xy), 18 \times 50\,(xz)$	$18 \times 18 \times 40$
resolution / µm	$140 \times 140\,(xy), 140 \times 390\,(xz)$	$280 \times 280 \times 1300$
soft 180° pulse duration / µs	256	512
soft pulse shape	Gaussian	Hermite
slice thickness / mm	25	300
under-sampling rate / %	20	25
gradient pulse duration δ / ms	0.74	0.74
observation time Δ / ms	1.48	1.74
echo time T_E / ms	2.65	2.80
acquisition time per image / min	7	58

the third dimension. A PGSE-like pair of gradient pulses were used for motion encoding (G_{vel}), with the second pulse coincident with the imaging phase gradients. A four-step EXORCYCLE phase cycle was used for all experiments.

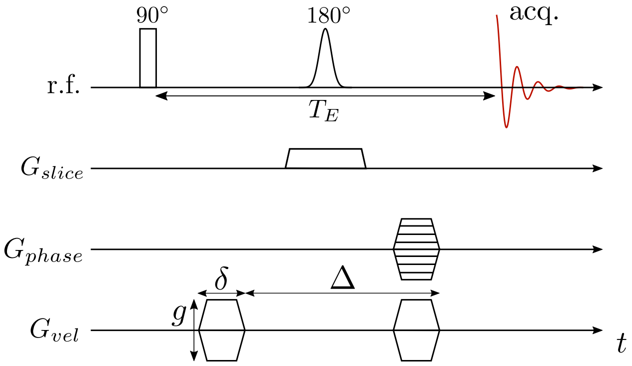

Fig. 4.4: Pulse sequence for the spin echo single point imaging (SESPI) method used. The phase gradients, G_{phase}, were applied in two and three separate directions for the 2D and 3D imaging respectively.

Extension to three-dimensional MRI

The imaging method was extended to sample all three dimensions for the turbulent diffusivity and corresponding velocity map measurements. This was to eliminate the need for a non-uniform slice selection and better resolve both the channels and the filter ends. A slice selective 180° pulse was used to reduce the FOV and increase the resolution along the z-axis. The envelope of the soft pulse was the Bruker *Hermite* function, which gives a more top-hat shaped response in the frequency domain. The hard edges of this pulse allow for more effective reduction in the FOV as well as aiding CS reconstruction using the TV regularisation. The under-sampling pattern used for the three-dimensional imaging was based on the same used for the two-dimensional imaging, with the polynomial p.d.f. extended to all three **k**-space dimensions. An additional term was added to the CS reconstructions that penalises pixels known to lack signal due to the smaller raster size of the 3D imaging method [54]. This was achieved by acquiring a fully-sampled static image to generate a binary mask $\mathbf{M_b}$ prior to the experiments. The full CS reconstruction problem can be formulated as

$$\mathbf{x}_{\alpha,\beta} \in \operatorname{argmin}_{\mathbf{x}} \left\{ \frac{1}{2} || \mathbf{y} - S\mathcal{F}\mathbf{x} ||_2^2 + \alpha \mathrm{TV}\left(\mathbf{x}\right) + \beta || \left(1 - \mathbf{M_b}\right) \circ \mathbf{x} ||_2 \right\}, \tag{4.13}$$

where α and β are heuristically determined coefficients and $\circ$ is the element-wise Hadamard product.

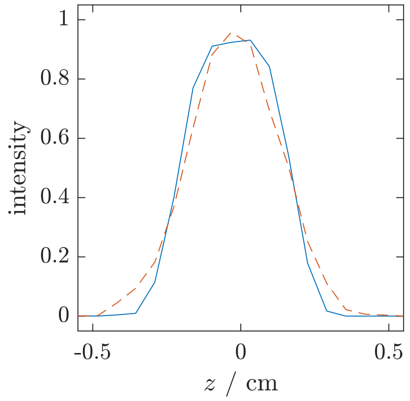

Fig. 4.5: Image intensity responses using (—) Gaussian and (- - -) Hermite soft pulse shapes.

Measurements of magnetic field strength

Measurements of the local variation in the B_0 field strength, ΔB_0, are possible using an asymmetric spin echo pulse sequence [55]. By adding an extra delay $\Delta\tau$ on one side of the 180° pulse, an extra phase of $-\gamma\Delta B_0\Delta\tau$ is accrued in the signal. When combined with an imaging sequence, this allows a map of the magnetic field homogeneity to be recovered from the phase,

$$\Delta B(\mathbf{r}) = -\frac{\Delta\phi(\mathbf{r})}{\gamma\Delta\tau}. \tag{4.14}$$

A delay of 5 ms was used for all data acquisitions in this study. An example of such a measurement combined with MRI is shown in Fig. 4.6 for two 10 mm diameter glass spheres in a 14 mm diameter tube of water. The deviation of the magnetic field strength is due to the difference in magnetic susceptibility between the water and the glass spheres.

Velocity and turbulent diffusivity measurements

Displacement encoding was afforded by a PGSE-like pair of gradient pulses, G_{vel}, applied in the z-direction, with one lobe either side of the 180° pulse. The gradient pulse duration, δ, was 0.74 ms and the observation time, Δ, was 1.48 ms and 1.74 ms respectively for the

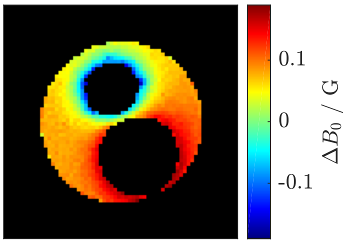

Fig. 4.6: Spatially resolved measurement of ΔB_0 for glass spheres in a tube of water.

2D and 3D imaging. Two sets of velocity encoded images were acquired. The first set were acquired under flowing conditions with two increments of the velocity encoding gradients (of strength $\pm g$ such that two $\mathbf{q}$-space points, symmetric about $\mathbf{q} = 0$, are acquired.) The second set were acquired similarly but under static fluid conditions. The final velocity image was obtained through finding the phase difference of the two $\mathbf{q}$-space increments according to Eq. (2.29) for the flowing and static images, and then subtracting the latter from the former to compensate for any eddy currents induced by the gradients. The velocity encoding gradient strength, g, was chosen such that the FOF contained the full range of velocities present in each image. In practice, these gradient strengths, g, were in the range $0.73\,\mathrm{G\,cm^{-1}}$ to $2.92\,\mathrm{G\,cm^{-1}}$. Similarly, two sets of images were acquired for the turbulent diffusivity images (flowing and static.) However, only one $\mathbf{q}$-space point was sampled with gradient strength $0.73\,\mathrm{G\,cm^{-1}}$. The magnitude of these images were then processed according to Eq. (4.10).

The MR signal is acquired as separate real and imaginary data, each with normally-distributed noise. This results in a Rician distribution of noise in the magnitude data and a non-trivial, non-linear distribution in the phase data. It has been shown that for SNR > 3, both distributions are well approximated as normal distributions [56]. As the lowest SNR in this study was 6, this approximation is valid. The errors quoted are calculated from the standard deviation of noise in the FID using standard error propagation methods. The error in the 2D velocity measurements is calculated to be less than $\pm 1.4\,\mathrm{cm\,s^{-1}}$, while the error in the 3D velocity map is less than $\pm 0.1\,\mathrm{cm\,s^{-1}}$. The error in the measurement of D_{turb} is less than $\pm 0.03\,\mathrm{cm^2\,s^{-1}}$.

4.6 Results

This section is presented in four parts. First, the susceptibility match of different filter substrates is tested in order to find the most appropriate sample. Second, the assumption that the velocity fluctuations occur on a much shorter timescale than the observation time is validated for all flow rates used. Third, two-dimensional velocity imaging is used to characterise the general flow patterns at the entrance and exit of the filter sample at $\mathrm{Re_c} = 360$. Finally, three-dimensional turbulent diffusivity is used to probe regions of high velocity fluctuation associated with eddies and pressure losses, and the relationship to the flow fields measured prior.

4.6.1 Choice of substrate

In order to obtain artefact-free images and accurate, quantitative transport measurements, excellent magnetic field homogeneity is required across the sample. However, most materials have different magnetic susceptibilities and so magnetic field gradients exists at material interfaces inside the spectrometer, resulting in image artefacts. This can be somewhat corrected using the shim gradients in the spectrometer. However, the best method is to prevent such artefacts by choosing the sample materials such that the magnetic susceptibilities are the same or closely matched.

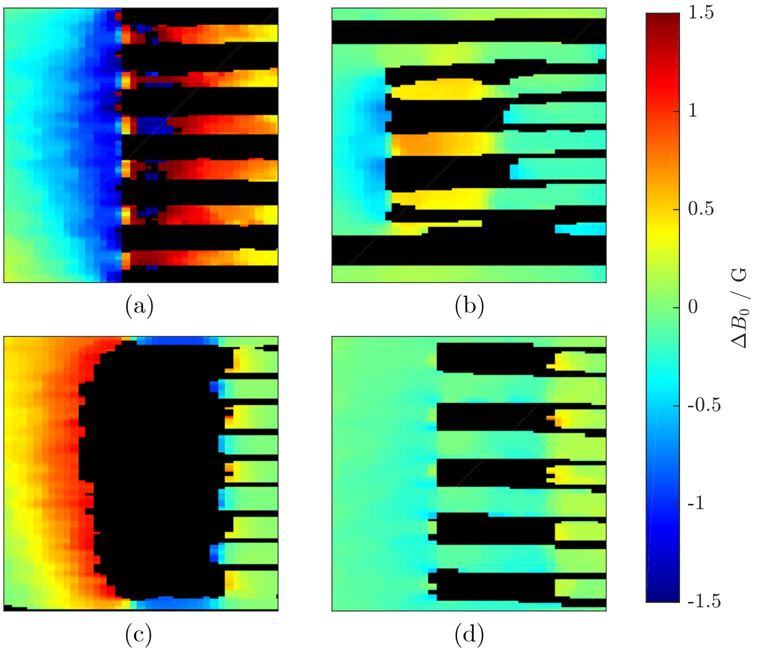

Fig. 4.7: Magnetic field inhomogeneity maps for the end regions of (a) the 3D printed geometry, (b) a silicon carbide filter, (c) a cordierite filter and (d) an aluminium titanate filter. The isotropic FOV shown for all images is 15 mm. The black colour shows areas with no NMR signal.

The magnetic susceptibility match between sulfur hexafluoride and four different candidate substrates was tested by measuring the local deviation in B_0 strength using the asymmetric spin echo pulse sequence described in §4.5.2. The candidate substrates were three common filter materials (cordierite, silicon carbide and aluminium titanate) and a 3D printed polymer geometry designed to mimic the entrance and exit geometry of filters. The latter was included to assess the feasibility of using bespoke 3D printed geometries to mimic the expansion and contraction experienced in filters. All samples had a channel diameter of 1 mm. The ΔB_0 maps were measured in the xz plane and are shown in Fig. 4.7. It is readily observed that (d) aluminium titanate provides the best magnetic susceptibility match and thus was chosen as the substrate. This is consistent with the observed behaviour of alumina and titania in NMR studies of porous media. Of the others, (b) silicon carbide has a reasonable match, (a) the 3D printed geometry has a poor match and (c) cordierite has such a large difference in susceptibilities that most signal is lost in the plugged region. This is attributed to the material used to plug the cordierite filters, fire cement, which contains many paramagnetic species and greatly enhances the local T_2 relaxation.

4.6.2 Validation of Lagrangian timescale regime

In order to validate the assumption that the Lagrangian timescale of the fluid is much shorter than the timescales of the gradient pulses, the signal attenuation with increasing evolution time Δ was measured. The echo time T_E was kept constant to remove any relaxation weighting and outflow effects from the signal attenuation. The attenuation of the signal was approximately linear for all flow rates used (Fig. 4.8). This validates the 'long observation time' assumption ($\tau_C << \Delta, \delta$) discussed in Section 4.4 and allows the subsequent theoretical treatment to be used. The upper bound of the Lagrangian correlation time is consistent with the range of correlation times found by Newling *et al.* [44] for SF_6 at 1 atm.

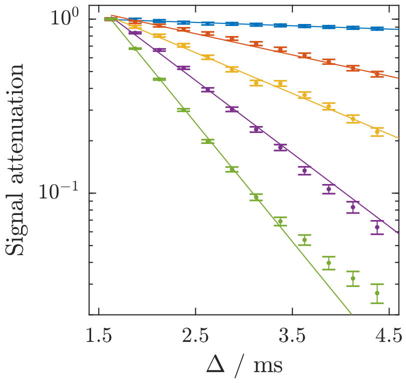

Fig. 4.8: Attenuation of the NMR signal with observation time, Δ, measured at flow rates of 0 (blue), 25 (red), 50 (yellow), 100 (purple) and 150 (green) g min^{-1}. Markers show measured values and solid lines show monoexponential fits. Error bars show the standard deviation of noise in the NMR signal. For the 150 g min^{-1} dataset, the final points deviate as the primary diffusivity component has completely decayed and the self-diffusion coefficient is observable.

4.6.3 Two-dimensional velocimetry

In this section, velocity maps acquired at the entrance and exit region are used to characterise the gas flow fields in those areas. The pixel colour indicates the local axial gas velocity at that location, with the black regions indicating areas lacking NMR signal (i.e. the filter substrate.)

Figure 4.9 shows the images acquired of the z-component of the flow velocity, v_z, at the entrance and exit of the filter, allowing the general form of the flow patterns to be observed.

(a) shows that the contraction of flow into the filter channels is smooth and well-behaved with no visible eddies present. Flow upstream of the filter is approximately uniform at ∼6 cm $\mathrm{s^{-1}}$. Upon entering the channels, the gas velocity increases to around ∼20 cm $\mathrm{s^{-1}}$, with some variation between channels, consistent with the reduction in cross-sectional area. A plug flow profile is seen as expected from the flow contraction. The channel flow profile becomes more curved further into the plugged region as laminar flow develops, but the parabolic profile expected from fully-developed flow is not reached until beyond the plugged region (z = 5 mm); the results in Chapter 6 suggest that this can require up to one-fifth of the filter length. There appear to be no regions of flow contraction or recirculation at the entrance. (b) shows the gas expansion at the exit of the filter. Jets are clearly visible as the high velocity gas exits the channels, with regions of low, zero and negative velocities between them. This indicates the formation of eddies which extend around 4 mm from the filter exit. The jets appear to coalesce within 20 mm of exiting the filter. While these velocity images are highly informative, they suffer from averaging in the y-direction over more than a single channel which may obscure additional details.

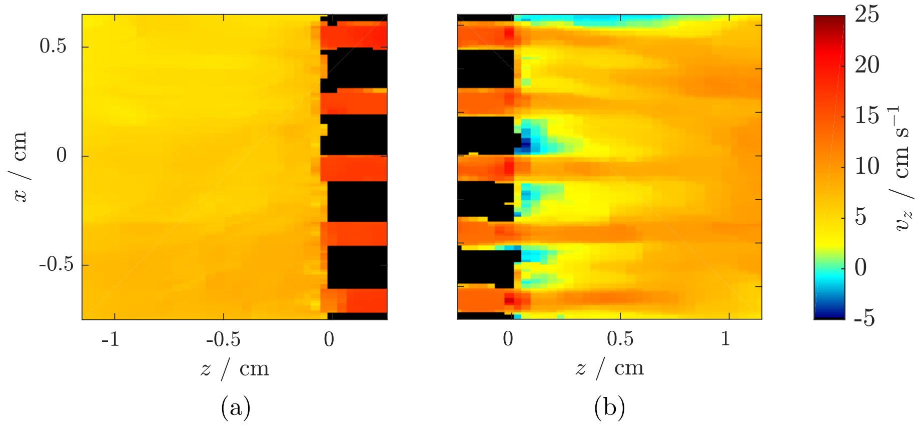

(a)

(b)

Fig. 4.9: Axial velocity images at the filter (a) entrance and (b) exit in the xz plane for $\mathrm{Re_c} = 360$. The isotropic FOV shown is 14 mm and the slice thickness is 2.5 mm. Gas flow is from left to right.

To better understand the flow fields seen in Fig. 4.9, similar images of v_z were acquired in the xy plane, perpendicular to the previous images. Figure 4.10 shows velocity images of gas flow entering the filter at different z positions and is consistent with the xz image. Upstream flow is again approximately uniform (a) and can be seen to increase velocity as it begins to enter the filter (b). Once in the filter, the flow again looks flat (c) and slowly begins to develop (d). Again, no recirculations are observed. Figure 4.11 shows similar velocity images of gas flow exiting the filter and reveals flow heterogeneity not seen in the xz image. Flow inside the channels is parabolic (a) but some variation between channels is observed, consistent with the variation seen in channel velocities at the entrance. At 2.5 mm from the filter exit, the high velocity jets and recirculating gas flows can clearly be seen. However, the recirculations are not present between every jet. The jets have largely begun to coalesce by 5 mm downstream (c), though a single jet persists for around 20 mm from the exit. In (c-f), a larger region of negative velocity is observed in the bottom right of the images, indicating a larger recirculating flow phenomenon.

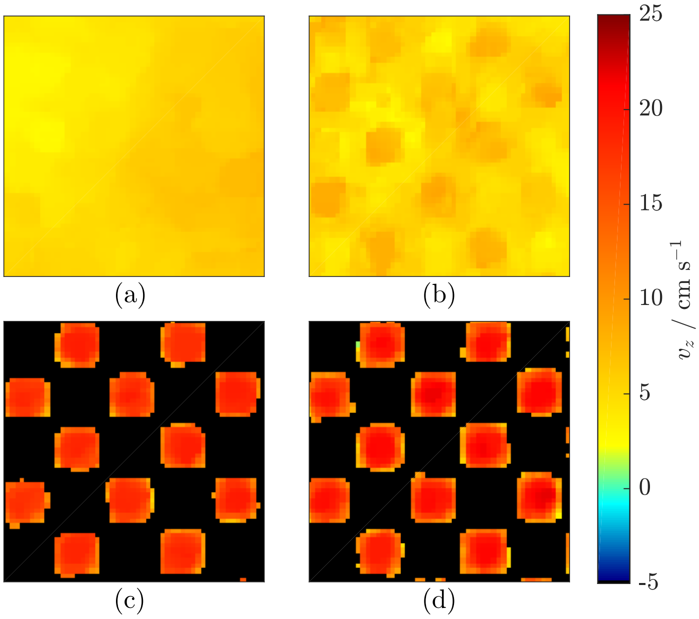

Fig. 4.10: Axial velocity images at the filter entrance in the xy plane, centred at z = (a) -3.8 mm, (b) -1.3 mm, (c) 1.3 mm and (d) 3.8 mm relative to the front face of the filter (z = 0 mm.). The isotropic FOV shown is 7 mm and the slice thickness is 2.5 mm.

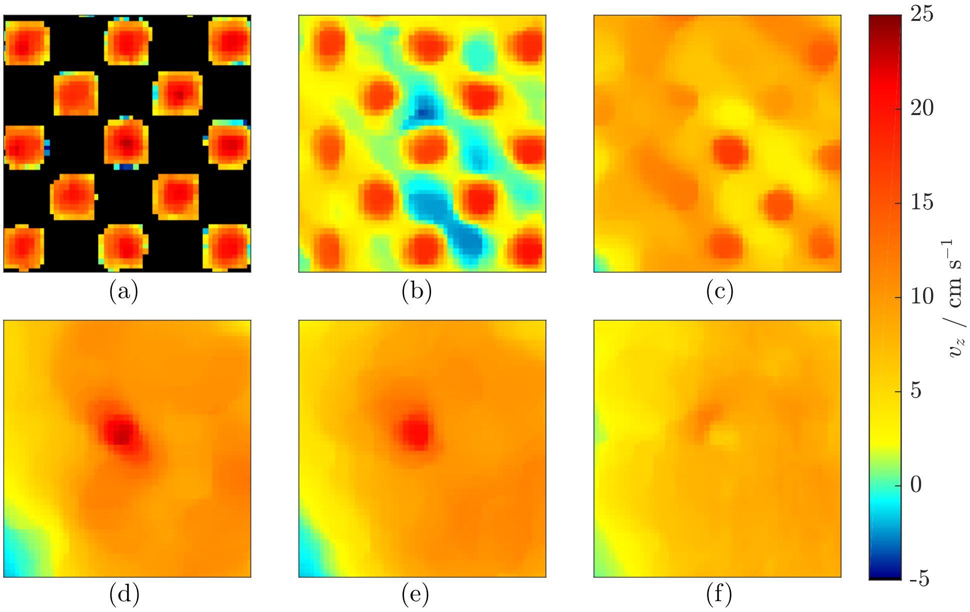

Fig. 4.11: Axial velocity images at the filter exit in the xy plane, centred at z = (a) -2.5 mm, (b) 2.5 mm, (c) 7.5 mm, (d) 12.5 mm, (e) 17.5 mm and (f) 22.5 mm relative to the rear face of the filter (z = 0 mm.) The isotropic FOV shown is 7 mm and the slice thickness is 2.5 mm.

4.6.4 Three-dimensional velocimetry and diffusometry

3D images of the turbulent diffusivity were acquired at the entrance and exit regions of the filter sample for each of $\mathrm{Re_c} = 210$, 360, 720 and 1140. These measurements characterise the range of velocities existing within each voxel over the data acquisition time; laminar flow is expected to have a low range of velocities in a volume element and hence a small turbulent diffusivity, and a high range for turbulent flow. Whilst the magnitude and spatial extent of the turbulent diffusivity increased with increase in $\mathrm{Re_c}$, the general behaviour for all $\mathrm{Re_c}$ was very similar. The measurements shown correspond to $\mathrm{Re_c} = 1140$. A 3D image of the axial gas velocity at the same flow rate was also acquired at the filter exit. This 3D data was rendered in Avizo Fire (Fisher Thermo Scientific, USA).

Figure 4.12 shows the turbulent diffusivity distribution at the filter entrance, which is located in three main regions: upstream of the filter in front of the plugs, just inside the inlet channels in the plugged region, and in the inlet channels just downstream of the plugs. The first two regions are shown in Fig. 4.13 through 2D *xy* slices of the 3D dataset. (a) shows the turbulent diffusivity ahead of the plugged regions, between the open inlet channels. (b) and (c) show development of turbulent diffusivity at the walls and corners of the inlet channels inside the plugged region. These regions of turbulent flow are not readily identified from the 2D flow velocity maps, such as those shown in Figs. 4.9 and 4.10. The third region also occurred at the corners of the inlet channels.

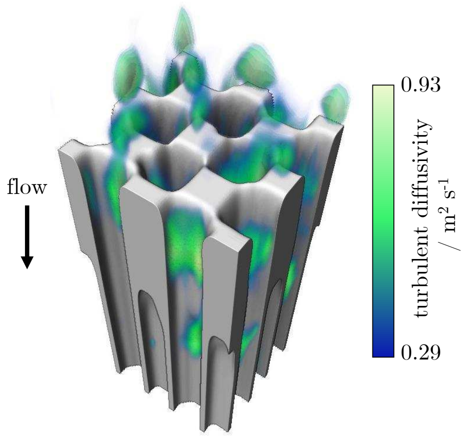

Fig. 4.12: 3D image showing the turbulent diffusivity distribution of gas entering the filter with $\mathrm{Re_c} = 1140$. The filter substrate is shown in grey.

Figure 4.14 shows the 3D measurements at the filter exit, specifically (a) the high positive velocities, (b) negative velocities and (c) turbulent diffusivity. From (a), the high positive velocities clearly show the jet structures observed from the 2D velocity images (Fig. 4.11). The recirculating flow between these jets is identified through the presence of negative velocities (b) which are located between the jets and also at the end of the inlet channels. The MRI and 3D CFD results in Chapter 6 also revealed reverse flows at the end of the inlet channels at similar Reynolds numbers. (c) shows three regions of turbulent

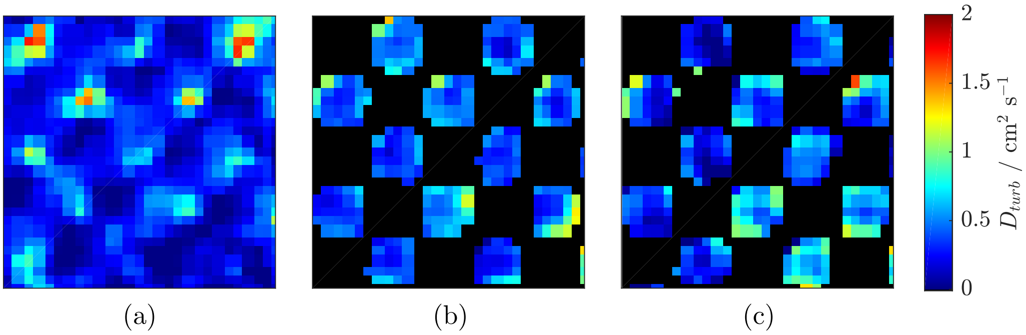

Fig. 4.13: Turbulent diffusivity images at the filter entrance in the xy plane, taken from the 3D dataset and centred at $z =$ (a) -0.4 mm, (b) 0.7 mm and (c) 1.4 mm relative to the front face of the filter ($z = 0$ mm.) The isotropic FOV shown is 7 mm and the voxel thickness is 1.3 mm.

diffusivity: at the end of the inlet channels, in the plugged region of the outlet channels, and at the interface of the high velocity jets and the recirculating flows downstream of the filter exit. Figure 4.15 shows 2D slices of the region inside the outlet channels, where the turbulent diffusivity is observed near the walls and corners of the channels. These features persist for approximately half the plug length. Figure 4.16 shows similar slices at axial positions 0.7 mm, 2.0 mm and 3.3 mm from the filter exit. Turbulent diffusivity is observed as annuli around the high velocity jets, with peak values around half those as seen in Fig. 4.15. These annuli exist to about 0.4 cm downstream from the filter exit, over a shorter range than the jets in the velocity field. Figure 4.17 shows co-registered images of the velocity and turbulent diffusivity. The jets shown in the velocity map again extend much further than the turbulent diffusivity.

The turbulent diffusivity distributions at both ends of the filter show some variation between individual channels, as is expected from the non-uniform gas flow shown in Figs. 4.9 to 4.11. In order to better understand the development of the turbulent diffusivity along the filter axis, the 3D datasets were projected onto the z axis through averaging along the x and y axes. The projections at the entrance and exit are shown in Fig. 4.18 for $\mathrm{Re_c} = 210$, 360, 720 and 1140. At the entrance (a), two peaks (A and B) in the turbulent diffusivity are clearly seen at $\mathrm{Re_c} = 720$ and 1140. Some evidence of these two features is also seen at $\mathrm{Re_c} = 360$. From Fig. 4.12, peak B can be identified as the turbulent phenomena in the inlet channels. (b) shows the data obtained for the exit region. Again, 2 peaks in the turbulent diffusivity are observed. The larger peak (Peak C) exists in the outlet channels over the length-scale of the plugged region of the inlet channel. The 3D dataset shows that this region is located at the edges of the outlet channel (Fig. 4.15), starting just ahead of the plugged region. The smaller peak (Peak D) occurring at $z = 13$ mm beyond the filter exit corresponds to the turbulent structure seen in Figs. 4.16 and 4.17.

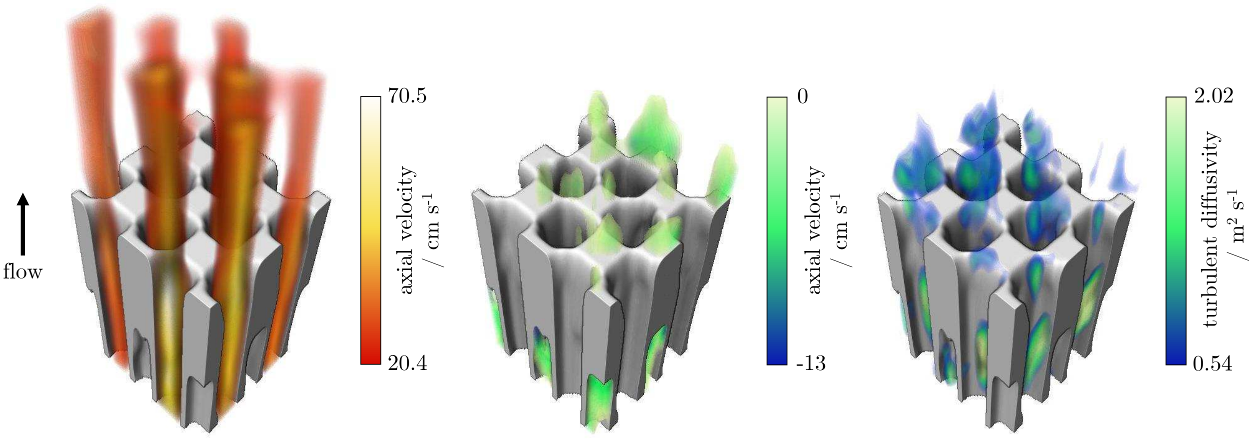

(a) (b) (c)

Fig. 4.14: 3D images showing (a) high velocity jets, (b) negative velocities and (c) turbulent diffusivity distribution of gas exiting the filter with $\mathrm{Re_c} = 1140$. The filter substrate is shown in grey. Flow is from bottom-top-top.

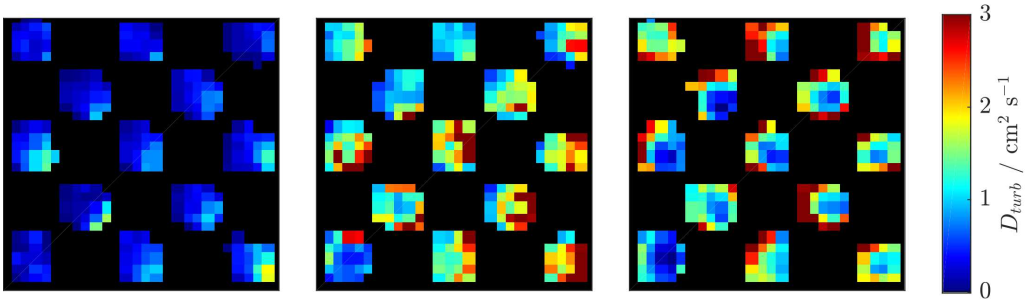

(a) (b) (c)

Fig. 4.15: Turbulent diffusivity images at the filter exit in the xy plane, taken from the 3D dataset and centred at z = (a) −1.9 mm, (b) −3.2 mm and (c) −4.5 mm relative to the rear face of the filter (z = 0 mm.) The isotropic FOV shown is 7.8 mm and the voxel thickness is 1.3 mm.

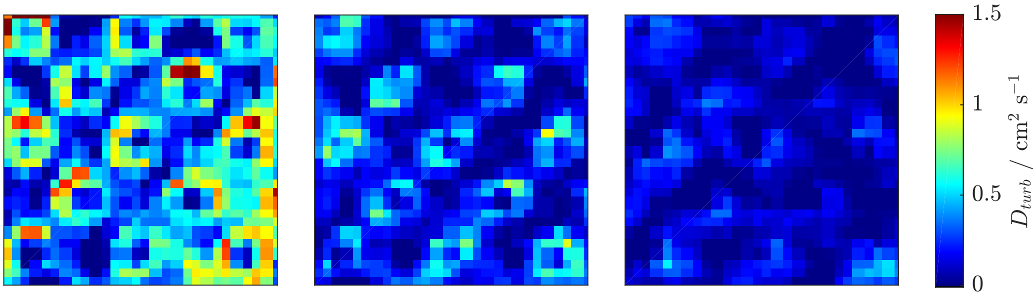

(a) (b) (c)

Fig. 4.16: Turbulent diffusivity images at the filter exit in the xy plane, taken from the 3D dataset and centred at z = (a) 0.7 mm, (b) 2.0 mm and (c) 3.3 mm relative to the rear face of the filter (z = 0 mm.) The isotropic FOV shown is 7.8 mm and the voxel thickness is 1.3 mm.

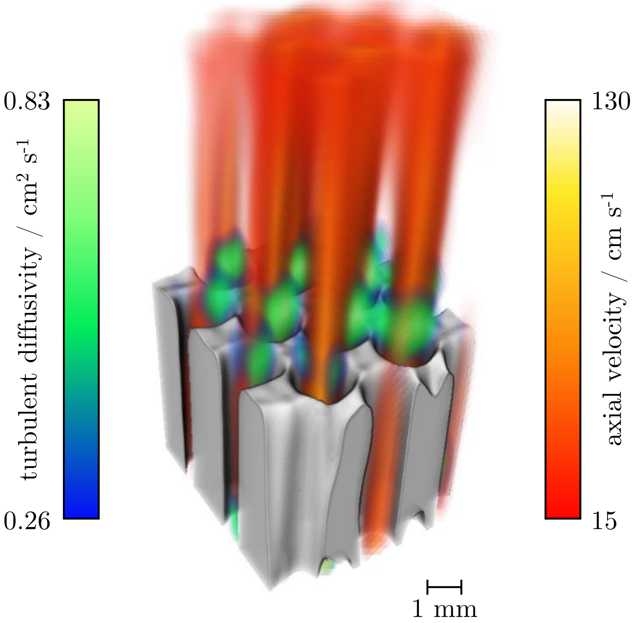

Fig. 4.17: 3D images of axial velocity, v_z, and turbulent diffusivity, D_{turb}, distributions of gas exiting the filter (i.e. flow from bottom-to-top) with $\mathrm{Re_c} = 1140$. The filter substrate is shown in grey. The apparently flat profile at the limit of the jets arises from that z-position being the limit of the FOV in the imaging experiment.

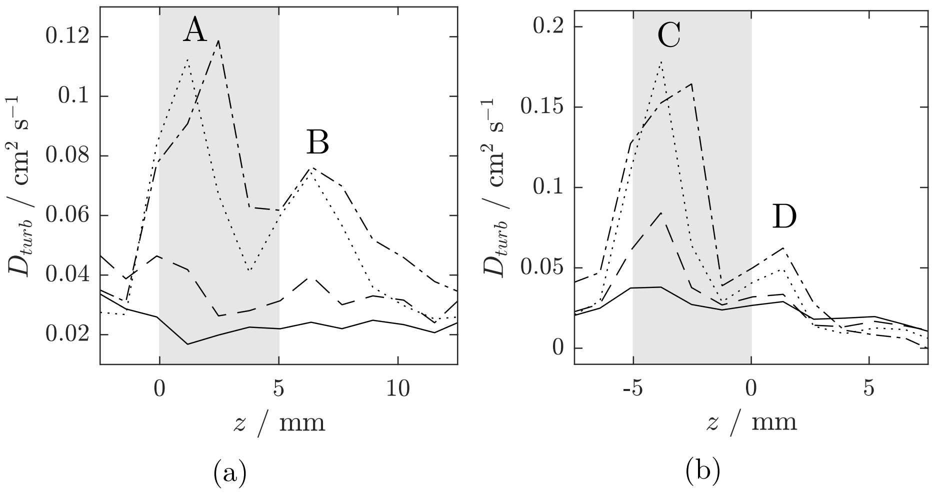

(a) (b)

Fig. 4.18: Turbulent diffusivity averaged onto the z-axis from the 3D dataset at (a) the entrance and (b) the exit region for $\mathrm{Re_c} = 210$ (——), 360 (- - -), 720 (·····) and 1140 (-·-·). The grey boxes show the plugged regions.

4.7 Discussion

Due to the very limited number of experimental studies of entrance and exit flows in filter systems, most comparisons are made with simulation results. The only reported measurement is by Oxarango *et al.* whose HWA data showed clear jet formation at least 2.2 mm from the filter exit [14], in agreement with Figs. 4.9 and 4.10 at the lower $\mathrm{Re_c}$ of 360. The flow between jets is flat, and while the velocity direction is not ascertained, it suggests that any eddies must be present within 2.2 mm of the filter exit. This is consistent with the smaller eddies seen in Figs. 4.9 and 4.11.

As noted in §4.3, CFD studies of entrance and exit effects in wall-flow filters are also limited in number. Here, the MR results are primarily compared with the predictions reported by Konstandopoulos *et al.* [15] and Liu and Miller [16]; these simulations represent work in which the channel geometry and Re are closest to those studied in the present work and their general predictions are illustrated in Fig. 4.1. These studies also provide the most detailed descriptions of the flow features seen in the CFD predictions. The MRI data are in good agreement with the main predictions of both studies. While the velocity maps (Figs. 4.9 to 4.11) showed no recirculating flow at the entrance, the turbulent diffusivity maps (Fig. 4.13) do indicate turbulent flow occurring ahead of the inlet plugs as predicted by Liu and Miller. Negative axial velocities were observed at the end of the inlet channel (Fig. 4.14 (b)), indicating recirculating flow, again confirming the predictions of Liu and Miller. Fig. 4.9 shows the formation of jets at the exit as predicted in both studies. From Fig. 4.11, most exit jets coalesce within 1.5 cm of leaving the filter, but the flow field has not redeveloped fully by 25 mm downstream and appears to be influenced by a larger recirculating feature. This may result in local pressure fluctuations for at least 5 plug lengths downstream, consistent with the predictions of Konstandopoulos *et al.* [15] and Cornejo *et al.* [4]. Neither CFD study predicted any unsteady flow that accounts for the additional turbulent diffusivity peaks (Peaks B and C) observed in Fig. 4.18 despite their significant contribution to the overall turbulent diffusivity. It is thought that these flow features may be caused by the high transverse velocity through the filter walls; the through-wall velocity is typically parabola-shaped at low $\mathrm{Re_c}$ [52] and increases rapidly at the rear with increasing $\mathrm{Re_c}$ (Section 6.6.1). There may also be some contribution from the plugs, which create a sudden decrease in the through-wall velocity at the entrance and exit.

From Fig. 4.13, the turbulent diffusivity develops around the edge of the channels. A similar effect has been seen in the study of transitional and turbulent flows in pipes - Gatenby and Gore [57] found that turbulent fluctuations develop at the edge of the pipe first before growing towards the centre. However, the turbulent diffusivity seen in the filter inlet decays quickly despite the Reynolds number not expected to change significantly in the plugged reason. Hence, this appears to be consistent with the *vena contracta* effect predicted in other studies and not due to turbulence development inside the channels at higher $\mathrm{Re_c}$. As no *vena contracta* effects can be seen in the velocity images, it is expected that the scale of the *vena contracta* is smaller than the image resolution (~140 µm).

The only studies that have focused on turbulent entrance and exit effects from square channel monoliths are simulations by Cornejo *et al.* [4]. At the entrance, Cornejo predicted that turbulent effects could extend far along the channels. From Fig. 4.12 and Fig. 4.18 (a), turbulent diffusivity is localised within around 10 mm of the entrance face even at $\mathrm{Re_c}=1140$. This could be due to influence of the through-wall flow, which may also act to damp eddies inside the channels. At the exit, Cornejo defined the wall Reynolds number, $\mathrm{Re_w}$, based on the monolith wall thickness, and showed that turbulent effects are significant above a threshold of $\mathrm{Re_w} \sim 125$; the shape of the axial projections in Cornejo's work are somewhat similar to that seen in peak D in Fig. 4.18 (b), though are predicted to persist for a much greater distance downstream than is observed experimentally. However, this could be due to the low SNR inherent to the MRI method only revealing the regions of highest turbulence. The filter geometry in this study presents an extra complication due to the different distances between adjacent outlet channels: the nearest neighbour distance is $\sqrt{2}$ times the wall thickness, similar to the distance in Cornejo's work, while the distance across the plugs is around ten times this. When correcting Cornejo's threshold $\mathrm{Re_w}$ ($\sim 100-160$) for the larger distance experienced in the filter geometry, a threshold $\mathrm{Re_c}$ of about 800 is obtained. This is larger than the threshold expected from Fig. 4.18 (between $\mathrm{Re_c} = 360$ and 720), though not by a large amount. It could be possible that two 'transitions' occur, one for each nearest-neighbour distance, although this would require additional MRI measurements at lower $\mathrm{Re_c}$ to probe such behaviour.

The measurements of turbulent diffusivity permit the relative contributions of the entrance and exit to be found. While numerical models often consider the combined contribution of entrance and exit effects to the pressure drop in a single term, the turbulent contributions measured are still useful in understanding the relative important of each end. First, considering only the turbulent features predicted by simulations (peaks A and D in Fig. 4.18), it appears that the entrance effects contribute more at a ratio of around 2:1. This is in agreement with the work of Haralampous *et al.* [27] and Watling *et al.* [26]. However, when the unpredicted turbulent features (peaks B and C) and included, the exit effects are dominant and more consistent with the work of Masoudi [7] and Torregrosa *et al.* [29]. Spatially unresolved measurements of turbulent diffusivity at the entrance and exit of a silicon carbide filter (with the same channel geometry) corroborate this, as shown in Fig. 4.19. The turbulent diffusivity increases with the square of $\mathrm{Re_c}$, as is commonly modelled for inertial effects [26], and the ratio of the entrance and exit coefficients is 23:77.

The strict periodic boundary conditions used in CFD simulations of Konstandopoulos and Liu and Miller enforces uniform flow in all channels which is not observed experimentally nor anticipated in practice. Exhaust gas entering wall-flow filters is usually supplied from a much smaller exhaust tube that increases in diameter through a linear cone. CFD simulations of gas flow through the inlet cone [3, 5, 6] have predicted a large degree of

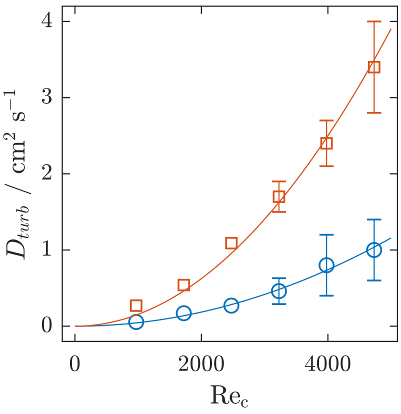

Fig. 4.19: Turbulent diffusivity measurements at the entrance (○) and exit (□) of a silicon carbide DPF sample. Lines show the fit to the curve $D_{turb} = a\mathrm{Re_c}^2$ and error bars show the uncertainty in the fit to the Stejskal-Tanner equation for each flow rate. The increasing uncertainty with $\mathrm{Re_c}$ is attributed to the greater signal attenuation and hence greater relative uncertainty in points in the Stejskal-Tanner fits.

inhomogeneity in the velocity distribution of gas as it enters the filter and large recirculating flow fields between the face of the filter and the cone, which has been observed using PIV by Turner *et al.* [6]. Through simulations, Mu *et al.* [3] calculated 88% of the exhaust gas enters the central 53% of the filter, causing an inherent non-uniformity in the flow across the filter and impacting the filtration efficiency. This non-uniformity will also be present in the gas exiting the filter, as the velocity of gas in the filter is highly anisotropic [52, 58], and will cause a non-uniform velocity distribution at the filter exit face, consistent with the flow seen in Figs. 4.9 to 4.16.

4.8 Conclusions

In this chapter, compressed sensing MRI measurements of gas velocity and turbulent diffusivity have been applied to study gas flow behaviour at the entrance and exit regions of a wall-flow filter. 2D velocity-encoded images of the flow velocity in the direction of the superficial flow were obtained in the xz and xy planes, with $\mathrm{Re_c} = 360$. This allowed measurement of the entrance and exit flow fields both inside and outside the filter for the first time. The evolution of flow velocity at the filter entrance is seen to be smooth, and the evolution of the flow in the inlet channels from plug to laminar flow is observed along the length of the channel. Some evidence of back flow at the end of the inlet channel in front of the plugged region was observed. At the filter exit, jets leaving the outlet channel are observed, as are regions of stagnant and recirculating gas at the face of the filter associated with the plugged inlet channels.

3D images of the local turbulent diffusivity distributions at the filter entrance and exit were acquired, allowing areas of turbulent flow to be identified at length scales below the image pixel resolution. At the entrance, two distinct regions of turbulent diffusivity are identified inside the filter. The first exists predominantly along the walls of the filter immediately after entry, whilst the second region is downstream of the plugged channels. Both regions of turbulence exist within the inlet channels. At the exit, significant turbulent diffusivity was observed before the filter exit (in the outlet channels) with a second region just beyond the filter exit where the high velocity exit jets interact with stagnant and recirculating flows present between the jets. Co-registration of 3D images of gas velocity and turbulent diffusivity at the filter exit enables the spatial location and range of the flow velocity and turbulent diffusivity to be visualised at the filter exit.

The MRI velocity and turbulent diffusivity data has allowed qualitative comparison with the limited number of numerical simulations available, allowing validation of the predicted entrance and exit flow fields for the first time. Most predictions were confirmed, and some discrepancies between different simulations were resolved. However, there were some effects not predicted by the simulations that were observed in the MRI data. Significant regions of turbulent diffusivity were observed inside the filter, where the plugged region meets the bulk of the channels. This is thought to be due to the through-wall flows unique to the wall-flow filter geometry.

The MRI data has also allowed the relative contributions of the entrance and exit to turbulent diffusivity, which itself causes inertial pressure losses. It was found that of the predicted regions of turbulence, the entrance is the main contributor. However, when considering all measured turbulence, the exit is dominant. This information may be useful for describing the contributions of entrance and exit effects in low-dimensional models; such models do not resolve the entire flow field and often rely on correlations to model the entrance and exit effects.

4.9 References

[1] G. Koltsakis, O. Haralampous, C. Depcik, J. C. Ragone. Catalyzed diesel particulate filter modeling. *Reviews in Chemical Engineering* (2013) 29 (1), 1–61. doi:10.1515/revce-2012-0008.

[2] S. Yang, C. Deng, Y. Gao, Y. He. Diesel particulate filter design simulation: A review. *Advances in Mechanical Engineering* (2016) 8 (3), 1–14. doi:10.1177/1687814016637328.

[3] M. Mu, X. Li, J. Aslam, Y. Qiu, H. Yang, G. Kou, Y. Wang. A Study of Shape Optimization Method on Connection Cones for Diesel Particulate Filter (DPF). In *International Mechanical Engineering Congress and Exposition*, volume 12. American Society of Mechanical Engineers (2016) doi:10.1115/IMECE2016-66080.

[4] I. Cornejo, P. Nikrityuk, R. E. Hayes. Turbulence generation after a monolith in automotive catalytic converters. *Chemical Engineering Science* (2018) 187, 107–116. doi:10.1016/j.ces.2018.04.041.

[5] L. Ma, M. Paraschivoiu, J. Yao, L. Blackman. Improving flow uniformity in a diesel particulate filter system. In *International Spring Fuels & Lubricants Meeting.* SAE International (2001) doi:10.4271/2001-01-1944.

[6] C. Turner, D. Thornhill, G. McCullough, S. Patel. Comparison of Experimental PIV Data and CFD Simulations for Flow in a Diesel Particulate Filter Inlet Diffuser. *SAE International Journal of Engines* (2011) 4, 1556–1570. doi:10.4271/2011-01-1241.

[7] M. Masoudi. Hydrodynamics of Diesel Particulate Filters. *SAE Technical Paper Series* (2002) 2002-01-1016. doi:10.4271/2002-01-1016.

[8] I. Calmet, J. Magnaudet. Large-eddy simulation of high-Schmidt number mass transfer in a turbulent channel flow. *Physics of Fluids* (1997) 9 (2), 438–455. doi:10.1063/1.869138.

[9] S. Garimella, W. J. Dowling, M. Van Der Veen, J. D. Killion. The effect of simultaneously developing flow on heat transfer in rectangular tubes. *Heat Transfer Engineering* (2001) 22 (6), 12–25. doi:10.1080/014576301317048406.

[10] D. H. West, V. Balakotaiah, Z. Jovanovic. Experimental and theoretical investigation of the mass transfer controlled regime in catalytic monoliths. *Catalysis Today* (2003) 88 (1-2), 3–16. doi:10.1016/j.cattod.2003.08.002.

[11] H. Ström, S. Sasic, B. Andersson. Effects of the turbulent-to-laminar transition in monolithic reactors for automotive pollution control. *Industrial and Engineering Chemistry Research* (2011) 50 (6), 3194–3205. doi:10.1021/ie102291t.

[12] I. Cornejo, P. Nikrityuk, R. E. Hayes. Turbulence Decay Inside the Channels of an Automotive Catalytic Converter Monolith. *Emission Control Science and Technology* (2017) 3 (4), 302–309. doi:10.1007/s40825-017-0070-6.

[13] I. Cornejo, P. Nikrityuk, R. E. Hayes. Multiscale RANS-based modeling of the turbulence decay inside of an automotive catalytic converter. *Chemical Engineering Science* (2018) 175, 377–386. doi:10.1016/j.ces.2017.10.004.

[14] L. Oxarango, P. Schmitz, M. Quintard, S. Bardon. 3D macroscopic model for fluid flow and soot deposit in wall flow honeycomb DPF. *SAE Transactions* (2003) 2003-01-0834. doi:papers://B3F20CA2-9ACD-4BA1-A510-19A2EC38FE78/Paper/p399.

[15] A. G. Konstandopoulos, E. Skaperdas, M. Masoudi. Inertial Contributions to the Pressure Drop of Diesel Particulate Filters. *SAE Technical Paper Series* (2001) 2001-01-09. doi:10.4271/2001-01-0909.

[16] Z. G. Liu, R. K. Miller. Flow Distributions and Pressure Drops of Wall-Flow Diesel Particulate Filters. *SAE Technical Paper Series* (2002) 2002-01-1311. doi:10.4271/2002-01-1311.

[17] Y. Liu, J. Gong, L. Cai, E. Jiaqiang, Y. Deng, L. Tan. Numerical simulation of gas-particle two-phase flow characteristic during deep bed filtration process. In *SAE World Congress & Exhibition.* SAE International (2007) doi:https://doi.org/10.4271/

2007-01-1135.

[18] F. Sbrizzai, P. Faraldi, A. Soldati. Appraisal of three-dimensional numerical simulation for sub-micron particle deposition in a micro-porous ceramic filter. *Chemical Engineering Science* (2005) 60 (23), 6551–6563. doi:10.1016/j.ces.2005.05.038.

[19] S. Bensaid, D. Marchisio, D. Fino, G. Saracco, V. Specchia. Modelling of diesel particulate filtration in wall-flow traps. *Chemical Engineering Journal* (2009) 154 (1-3), 211–218.

[20] Y. Liu, J. Gong, J. Fu, H. Cai, G. Long. Nanoparticle motion trajectories and deposition in an inlet channel of wall-flow diesel particulate filter. *Journal of Aerosol Science* (2009) 40 (4), 307–323. doi:10.1016/J.JAEROSCI.2008.12.001.

[21] S. Gavrilakis. Numerical simulation of low-reynolds-number turbulent flow through a straight square duct. *Journal of Fluid Mechanics* (1992) 244 (1), 101–129. doi:10.1017/S0022112092002982.

[22] F. F. Abdelall, G. Hahn, S. M. Ghiaasiaan, S. I. Abdel-Khalik, S. S. Jeter, M. Yoda, D. L. Sadowski. Pressure drop caused by abrupt flow area changes in small channels. *Experimental Thermal and Fluid Science* (2005) 29 (4), 425–434. doi:10.1016/j.expthermflusci.2004.05.001.

[23] R. P. Benedict, J. S. Wyler, J. A. Dudek, A. R. Gleed. Generalized Flow Across an Abrupt Enlargement. *Journal of Engineering for Power* (1976) 98 (3), 327. doi:10.1115/1.3446171.

[24] P. A. Kolodzie, M. Van Winkle. Discharge coefficients through perforated plates. *AIChE Journal* (1957) 3 (3), 305–312. doi:10.1002/aic.690030304.

[25] P. L. Smith, M. Van Winkle. Discharge coefficients through perforated plates at reynolds numbers of 400 to 3,000. *AIChE Journal* (1958) 4 (3), 266–268. doi:10.1002/aic.690040306.

[26] T. Watling, M. Ravenscroft, J. Cleeton, I. Rees, D. Wilkins. Development of a Particulate Filter Model for the Prediction of Backpressure: Improved Momentum Balance and Entrance and Exit Effect Equations. *SAE International Journal of Engines* (2017) 10 (4), 1765–1794. doi:10.4271/2017-01-0974.

[27] O. A. Haralampous, I. P. Kandylas, G. C. Koltsakis, Z. C. Samaras. Diesel particulate filter pressure drop Part 1: Modelling and experimental validation. *International Journal of Engine Research* (2004) 5 (2), 149–162. doi:10.1243/146808704773564550.

[28] B. Bouteiller, S. Bardon, A. Briot, P. Girot, V. Gleize, P. Higelin. One dimensional backpressure model for asymmetrical cells dpf. *SAE Technical Paper Series* (2007) 2007-01-0045. doi:10.4271/2007-01-0045.

[29] A. J. Torregrosa, J. R. Serrano, F. J. Arnau, P. Piqueras. A fluid dynamic model for unsteady compressible flow in wall-flow diesel particulate filters. *Energy* (2011) 36 (1), 671–684. doi:10.1016/j.energy.2010.09.047.

[30] P. Mansfield, A. A. Maudsley. Planar spin imaging by NMR. *Journal of Magnetic Resonance* (1977) 27 (1), 101–119. doi:10.1016/0022-2364(77)90197-4.

[31] K. Kose. Instantaneous flow-distribution measurements of the equilibrium turbulent region in a circular pipe using ultrafast NMR imaging. *Physical Review A* (1991) 44 (4), 2495–2504. doi:10.1103/PhysRevA.44.2495.

[32] A. J. Sederman, M. D. Mantle, C. Buckley, L. F. Gladden. MRI technique for measurement of velocity vectors, acceleration, and autocorrelation functions in turbulent flow. *Journal of Magnetic Resonance* (2004) 166 (2), 182–189. doi:10.1016/j.jmr.2003.10.016.

[33] A. B. Tayler, D. J. Holland, A. J. Sederman, L. F. Gladden. Time resolved velocity measurements of unsteady systems using spiral imaging. *Journal of Magnetic Resonance* (2011) 211 (1), 1–10. doi:10.1016/j.jmr.2011.03.017.

[34] A. B. Tayler, D. J. Holland, A. J. Sederman, L. F. Gladden. Applications of ultrafast MRI to high voidage bubbly flow: Measurement of bubble size distributions, interfacial area and hydrodynamics. *Chemical Engineering Science* (2012) 71, 468–483. doi:10.1016/j.ces.2011.11.014.

[35] J.-H. Gao, J. C. Gore. Turbulent flow effects on NMR imaging: Measurement of turbulent intensity. *Medical Physics* (1991) 18 (5), 1045–1051. doi:10.1118/1.596645.

[36] J. C. Gatenby, J. C. Gore. Characterization of Turbulent Flows by NMR Measurements with Pulsed Gradients. *Journal of Magnetic Resonance* (1994) 110 (1), 26–32. doi:10.1006/jmra.1994.1176.

[37] P. G. de Gennes. Theory of Spin Echoes in a Turbulent Fluid. *Physics Letters* (1969) 29A (1), 20–21.

[38] K. Fukuda, A. Hirai. A pulsed NMR study on the flow of fluid. *Journal of the Physical Society of Japan* (1979) 47 (6), 1999–2006. doi:10.1143/JPSJ.47.1999.

[39] D. O. Kuethe, J. H. Gao. NMR signal loss from turbulence: Models of time dependence compared with data. *Physical Review E* (1995) 51 (4), 3252–3262. doi:10.1103/PhysRevE.51.3252.

[40] A. J. Evans, R. A. Blinder, R. J. Herfkens, C. E. Spritzer, D. O. Kuethe, E. K. Fram, L. W. Hedlund. Effects of turbulence on signal intensity in gradient echo images. *Investigative Radiology* (1988) 23 (7), 512–518. doi:10.1097/00004424-198807000-00006.

[41] J. H. Gao, S. K. Holland, J. C. Gore. Nuclear magnetic resonance signal from flowing nuclei in rapid imaging using gradient echoes. *Medical Physics* (1988) 15 (6), 809–814. doi:10.1118/1.596197.

[42] K. Kose. Visualization of local shearing motion in turbulent fluids using echo-planar imaging. *Journal of Magnetic Resonance* (1992) 96 (3), 596–603. doi:10.1016/0022-2364(92)90345-8.

[43] D. O. Kuethe. Measuring distributions of diffusivity in turbulent fluids with magnetic-resonance imaging. *Physical Review A* (1989) 40 (8), 4542–4551. doi:10.1103/PhysRevA.

40.4542.

[44] B. Newling, C. C. Poirier, Y. Zhi, J. A. Rioux, A. J. Coristine, D. Roach, B. J. Balcom. Velocity imaging of highly turbulent gas flow. *Physical Review Letters* (2004) 93 (15), 154503. doi:10.1103/PhysRevLett.93.154503.

[45] O. Adegbite, L. Kadem, B. Newling. Purely phase-encoded MRI of turbulent flow through a dysfunctional bileaflet mechanical heart valve. *Magnetic Resonance Materials in Physics, Biology and Medicine* (2014) 27 (3), 227–235. doi: 10.1007/s10334-013-0408-1.

[46] C. J. Elkins, M. T. Alley, L. Saetran, J. K. Eaton. Three-dimensional magnetic resonance velocimetry measurements of turbulence quantities in complex flow. *Experiments in Fluids* (2009) 46 (2), 285–296. doi:10.1007/s00348-008-0559-4.

[47] M. Kadbi, M. Negahdar, J. W. Cha, M. Traughber, P. Martin, A. A. Amini. Validation of 3D ultra-short TE (UTE) Phase-Contrast MRI for imaging of steady flow: Initial phantom experiments. In *Proceedings of the Annual International Conference of the IEEE Engineering in Medicine and Biology Society, EMBS.* IEEE (2012) pp. 372–376. doi:10.1109/EMBC.2012.6345946.

[48] P. Dyverfeldt, R. Gårdhagen, A. Sigfridsson, M. Karlsson, T. Ebbers. On MRI turbulence quantification. *Magnetic Resonance Imaging* (2009) 27 (7), 913–922. doi: 10.1016/j.mri.2009.05.004.

[49] G. I. Taylor. Diffusion by continuous movements. *Proc. Lond. Math. Soc. A* (1921) 20 (1), 196–211. doi:10.1112/plms/s2-20.1.196.

[50] E. O. Stejskal, J. E. Tanner. Spin diffusion measurements: Spin echoes in the presence of a time-dependent field gradient. *Journal of Chemical Physics* (1965) 42 (1), 288–292. doi:10.1063/1.1695690.

[51] D. Xiao, B. J. Balcom. Restricted k-space sampling in pure phase encode MRI of rock core plugs. *Journal of Magnetic Resonance* (2013) 231, 126–132. doi:10.1016/j.jmr.2013.04.001.

[52] N. P. Ramskill, A. P. York, A. J. Sederman, L. F. Gladden. Magnetic resonance velocity imaging of gas flow in a diesel particulate filter. *Chemical Engineering Science* (2017) 158, 490–499. doi:10.1016/j.ces.2016.10.017.

[53] M. Lustig, D. Donoho, J. M. Pauly. Sparse MRI: The application of compressed sensing for rapid MR imaging. *Magnetic Resonance in Medicine* (2007) 58 (6), 1182–1195. doi:10.1002/mrm.21391.

[54] D. Holland, D. Malioutov, A. Blake, A. Sederman, L. Gladden. Reducing data acquisition times in phase-encoded velocity imaging using compressed sensing. *Journal of Magnetic Resonance* (2010) 203 (2), 236–46. doi:10.1016/j.jmr.2010.01.001.

[55] K. Bartusek, Z. Dokoupil, E. Gescheidtova. Magnetic field mapping around metal implants using an asymmetric spin-echo MRI sequence. *Measurement Science and*

Technology (2006) 17 (12), 3293–3300. doi:10.1088/0957-0233/17/12/015.

[56] H. Gudbjartsson, S. Patz. The Rician distribution of noisy MRI data. *Magnetic Resonance in Medicine* (1995) 34 (6), 910–914. doi:10.1002/mrm.1910340618.

[57] J. C. Gatenby, J. C. Gore. Echo-planar-imaging studies of turbulent flow. *Journal of Magnetic Resonance - Series A* (1996) 121 (2), 193–200. doi:10.1006/jmra.1996.0160.

[58] C. Hinterberger, M. Olesen, R. Kaiser. 3d simulation of soot loading and regeneration of diesel particulate filter systems. *SAE Technical Paper Series* (2007) 2007-01-1143. doi:10.4271/2007-01-1143.

Chapter 5

Preliminary CFD studies of entrance and exit effects

5.1 Introduction

As outlined in Chapter 4, the behaviour of gas entering and exiting the filter can have important effects for the pressure drop and filtration behaviour of particulate filters. MRI has proven to be a useful methodology in measuring the gas behaviour in these areas. However, the technique is limited in its applicability; from Section 4.6.1, common filter substrates such as cordierite are not suitable for the measurements. As such, it is desirable to use numerical models to study the gas behaviour in these regions. In Section 4.3, the previous applications of CFD in simulating gas flow at the filter entrance and exit were outlined. However, this work is relatively old, the simulations were performed for different fluids and the data is not available, making them unsuitable for direct comparison with the MRI results. As such, it is desirable to perform new CFD work for validation against the results presented in Chapter 4.

One major difficulty in comparing experimental and simulated data is ensuring that the data describe exactly the same system. This not only includes the geometry, boundary conditions and physical parameters of the system but any spatial or temporal averaging that occurs when acquiring the experimental data. This chapter aims to explore some of these areas with regard to the entrance and exit regions of particulate filters in order to inform any future CFD work and comparisons with MRI data.

5.2 Scope of study

In this chapter, preliminary CFD simulations are performed to predict the gas flow fields in geometries representing the entrance and exit of a filter. Two meshes were tested, one representing the entire filter with the porous wall, one only reflecting the contraction and expansion expected at the entrance and exit. The effects of applying a turbulence model and averaging due to a finite-width slice were explored. Finally, the preliminary CFD results are compared with the MRI results at the filter exit obtained in Chapter 4.

5.3 Numerical methods

The three-dimensional CFD method used to simulate gas flow is described here. All simulations were performed by Dr Li Liu at Johnson Matthey Technology Centre, Billingham, UK in January 2018.

As incompressible flow was assumed, the continuity equation was expressed as

$$\nabla \cdot \mathbf{v} = 0, \tag{5.1}$$

where $\mathbf{v}$ is the gas velocity field. The momentum equations solved were

$$\rho \left(\mathbf{v} \cdot \nabla \right) \mathbf{v} = -\nabla P + \nabla \boldsymbol{\tau} + \mathbf{S}, \tag{5.2}$$

where ρ is the gas density, P is the gas pressure and $\boldsymbol{\tau}$ is the viscous stress tensor. The gas was assumed to be Newtonian and hence the term $\nabla \boldsymbol{\tau}$ was equal to $\mu \nabla^2 \mathbf{v}$, where μ is the gas dynamic viscosity. $\mathbf{S}$ was the momentum source term; Darcy's law was used to represent porous media where appropriate,

$$\mathbf{S} = -\frac{\mu}{k} \mathbf{v}, \tag{5.3}$$

where k is the wall permeability. The flow was taken to be non-reactive and no energy equations were solved. Two turbulence models were considered. The first was a laminar model in which no additional equations were solved. The second was the k-ϵ model, which solves the equations,

$$\frac{\partial \rho k_e}{\partial t} + \nabla \cdot (\rho k_e \mathbf{v}) = \nabla \cdot \left[\frac{\mu_t}{\sigma_{k_e}} \nabla k_e \right] + 2\mu_t \mathbf{E}\mathbf{E}^T - \rho \epsilon, \tag{5.4}$$

$$\frac{\partial \rho \epsilon}{\partial t} + \nabla \cdot (\rho \epsilon \mathbf{v}) = \nabla \cdot \left[\frac{\mu_t}{\sigma_\epsilon} \nabla \epsilon \right] + C_{1\epsilon} \frac{\epsilon}{k_e} 2\mu_t \mathbf{E}\mathbf{E}^T - C_{2\epsilon} \rho \frac{\epsilon^2}{k_e}, \tag{5.5}$$

where k_e is the turbulent kinetic energy, ϵ is the rate of turbulent energy dissipation, $\mathbf{E}$ is the strain rate, $\mu_t = \rho C_\mu k_e^2 / \epsilon$ is the eddy viscosity and $C_\mu = 0.09$, $C_{1\epsilon} = 1.44$, $C_{2\epsilon} = 1.92$, $\sigma_{k_e} = 1$ and $\sigma_\epsilon = 1.3$ are adjustable constants.

Two geometries were used in the simulations. Geometry A was based on the full filter geometry with the porous walls represented by Darcy's law (Fig. 5.1 (a)); a permeability of $6 \times 10^{-13}\,\mathrm{m}^2$ was used. Geometry B used a shortened geometry with no porous walls and only flow-through channels to simulate only the contraction and expansion of flow expected at the filter entrance and exit (Fig. 5.1 (b)). Alternating channels were completely blocked to ensure the reduction in cross sectional area was the same as in geometry A. The wall thickness for both geometries was 0.33 mm. The meshes were created using snappyHexMesh (OpenFOAM Ltd) and was made of hexahedral cells. Due to the large aspect ratio of the filter channels ($L/d_c \approx 1500$), ~2.6 million cells were used for geometry A. Approximately

500,000 cells were used for geometry B. No surface enhancements applied during the meshing process. The dimensions of each cell were of the order 40 µm×40 µm×300 µm. The solutions were regridded in MATLAB®.

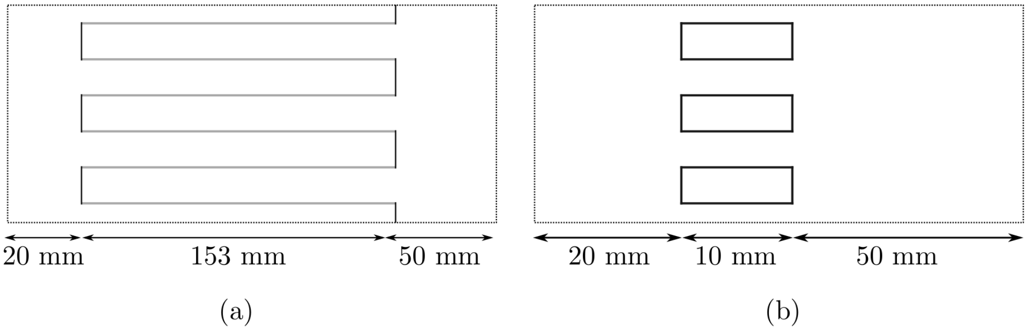

Fig. 5.1: Illustrations showing cross-sections of (a) geometry A and (b) geometry B.

5.4 Results

5.4.1 CFD simulations

Slices in the *xz* plane from the axial velocity results of both geometries are shown in Fig. 5.2. Both datasets were simulated using the laminar model. Due to an early error, the superficial velocities of the gas are not matched in the simulations; geometry A has a channel Reynolds number of ~240 whereas geometry B is ~600. However, the colour bar has been scaled to allow qualitative comparison.

The entrance regions of the results presented in Fig. 5.2 were expanded and are shown in Fig. 5.3. Similar behaviour is observed in both geometries. The contraction of flow is clean with no reverse or recirculating flows present. The axial velocity decreases to zero upstream of the plugged regions of each geometry. Geometry A (a) appears to show a *vena contracta* in the first 0.1 mm of the channel, with non-zero axial flow present in the porous walls further into the filter. Geometry B shows unusual periodic behaviour inside the channels; it is thought that this is an artefact of the regridding process or a difficulty in solution convergence using the laminar model.

Similarly, the exit regions of the CFD results shown in Fig. 5.2 were expanded and are shown in Fig. 5.4. Both geometries again show similar behaviour; a jet of gas is present as gas exits the filter geometry with reverse flows either side. The jet and reverse flow length is longer in geometry B due to the higher gas flow rate. These features appear more spatially 'unsteady' in geometry B, which is again attributed to the higher flow rate but also from difficulty in solution convergence using the laminar model. The periodic feature observed in Fig. 5.3 (b) is also observed in Fig. 5.4 (b).

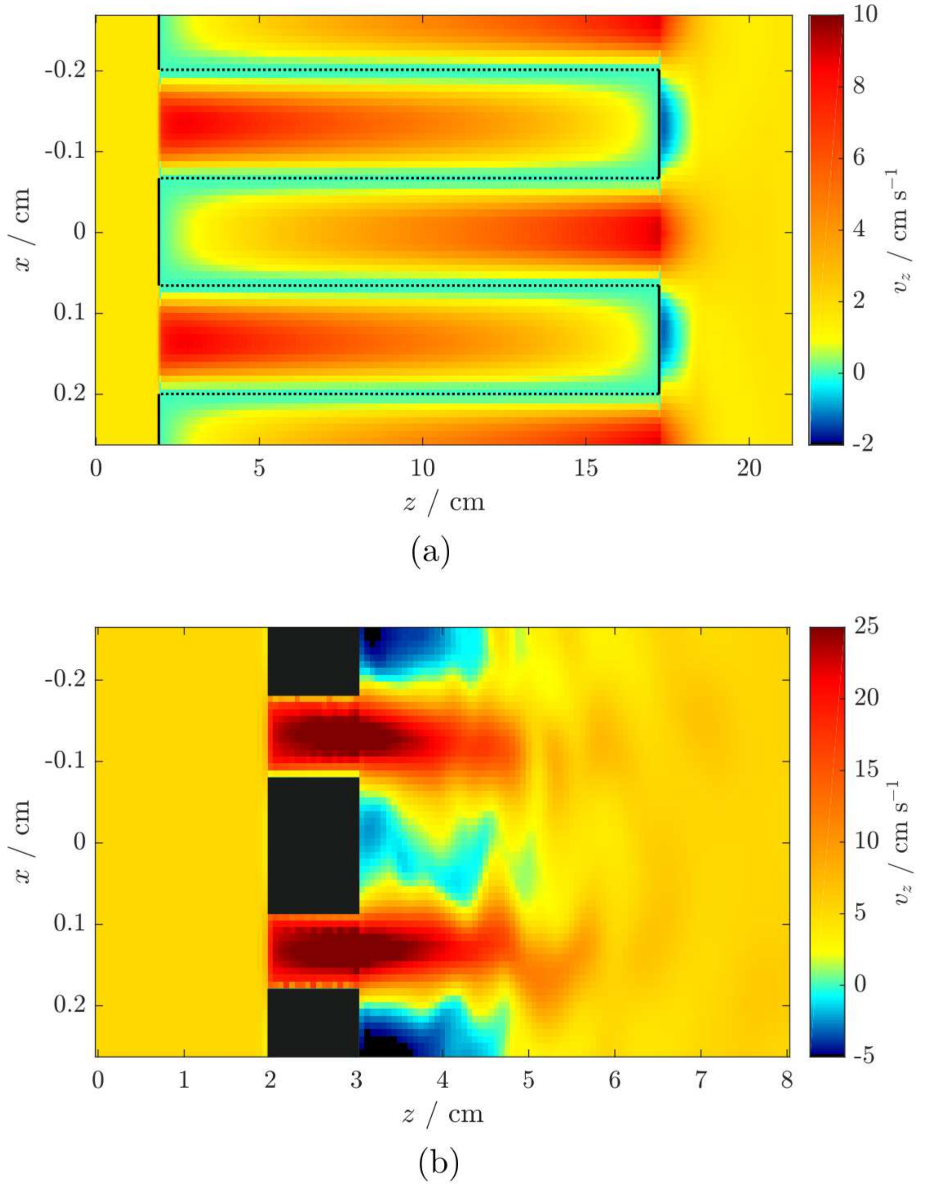

Fig. 5.2: xz slices of v_z from the CFD results, regridded onto a 128 × 128 × 256 raster, for (a) geometry A and (b) geometry B. The laminar model was used. The porous walls are indicated by dotted lines, zero flow boundary conditions are indicated by black lines and regions with no gas are represented by black boxes. The slice is at the midpoint of the channel.

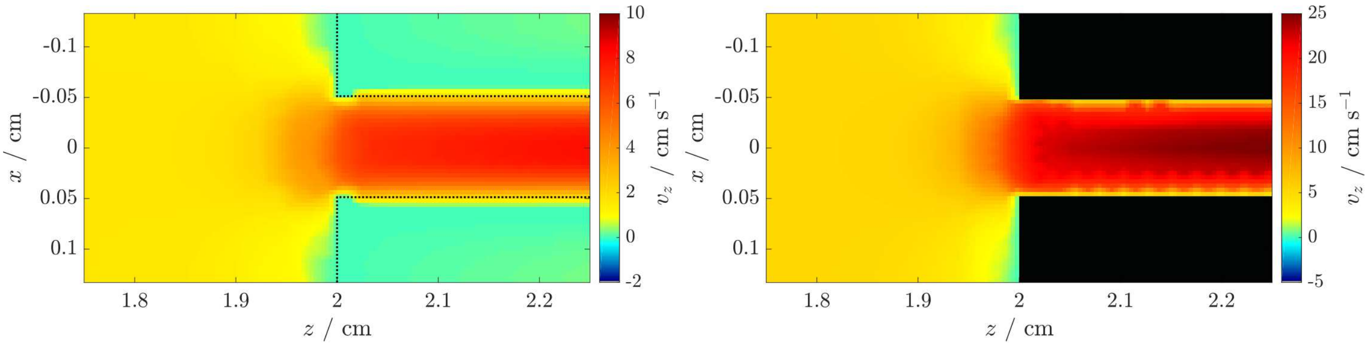

(a) (b)

Fig. 5.3: xz slices of v_z at the entrance region of (a) geometry A and (b) geometry B. The laminar model was used. The porous walls are indicated by dotted lines, zero flow boundary conditions are indicated by black lines and regions with no gas are represented by black boxes. The slice is at the midpoint of the channel.

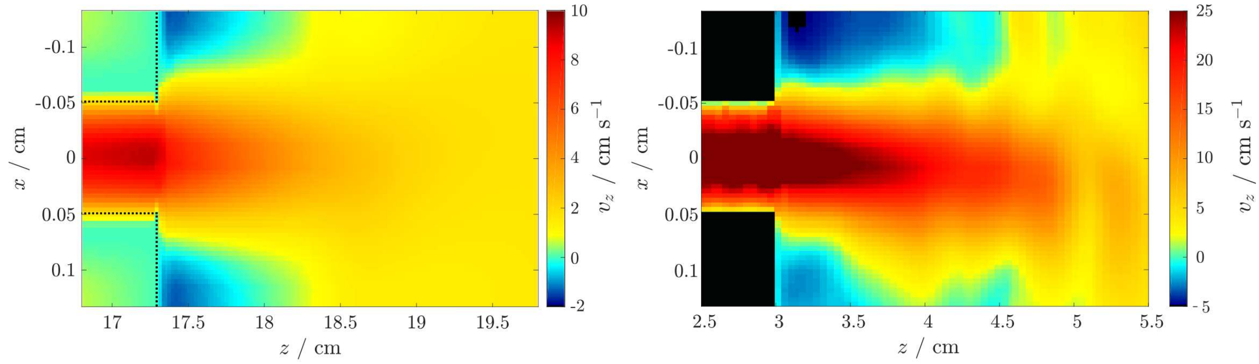

(a) (b)

Fig. 5.4: xz slices of v_z at the entrance region of (a) geometry A and (b) geometry B. The laminar model was used. The porous walls are indicated by dotted lines, zero flow boundary conditions are indicated by black lines and regions with no gas are represented by black boxes. The slice is at the midpoint of the channel.

Simulations were performed using geometry B with both a laminar and k-ϵ turbulence model (Fig. 5.5). While the laminar model (a) shows the jet and recirculating flow structure described previously, the k-ϵ shows no similar features at the present spatial resolution.

5.4.2 Comparisons with MRI

In order to observe the effects of slice averaging on the observed flow fields, the axial velocity data at the exit was averaged across two different widths in the y-direction: 0.8 mm and 1 mm. This was done at a reduced resolution to better reflect the resolution of the MRI data and is shown in Fig. 5.6. For a thinner slice (a), the velocity distribution resembles the distribution at the original resolution (Fig. 5.4 (b)). When averaged over 1 mm (b), the extreme velocities, both positive and negative, are reduced in magnitude.

The CFD results at the exit of geometry B were compared with the MRI velocity data acquired at the filter exit in Chapter 4 (Fig. 4.11). The CFD data are shown in Fig. 5.7

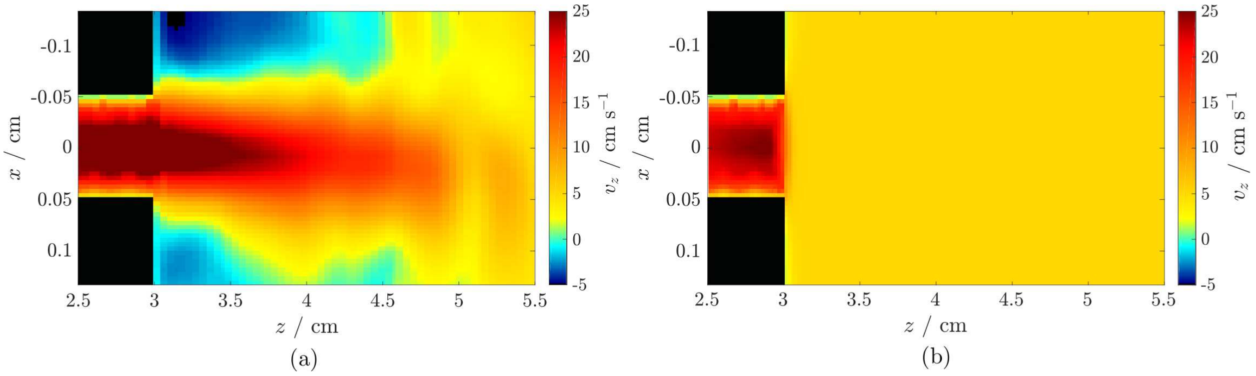

(a)

(b)

Fig. 5.5: xz slices of v_z at the exit of geometry B using (a) the laminar model and (b) the k-ϵ turbulence model. The slice is at the midpoint of the channel.

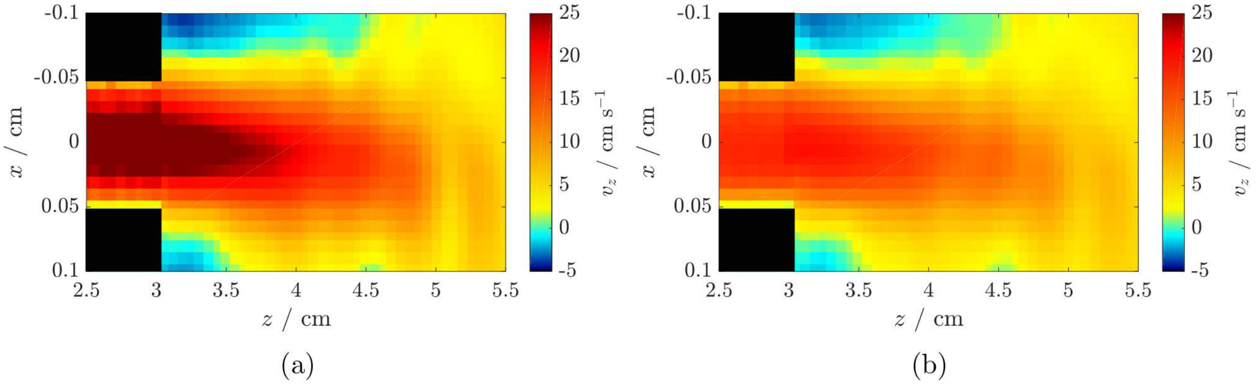

(a)

(b)

Fig. 5.6: xz slices of v_z at the exit region of geometry B at a reduced resolution (∼10 px per channel) with (a) uniform slice averaging over 0.8 mm and (b) uniform slice averaging over 1 mm. The laminar model was used. The regions with no gas are represented by black boxes. The slice is at the midpoint of the channel.

and the MRI data in Fig. 5.8. The average channel velocity was not fully matched (a) but comparisons can be made qualitatively. The CFD results show the same high velocity jets and interspersed reverse flows seen in the MRI data (b). However, the CFD data show reverse flows between every jet whereas the MRI data only show reverse flows between some jets. The jets persist for a longer axial distance downstream of the filter than in the MRI data. In the MRI data, the jet structures have largely coalesced by 12.5 mm downstream whereas the CFD data predicts them to persist for over 22.5 mm. The CFD results shows some asymmetry in the jet shape in agreement with the MRI data.

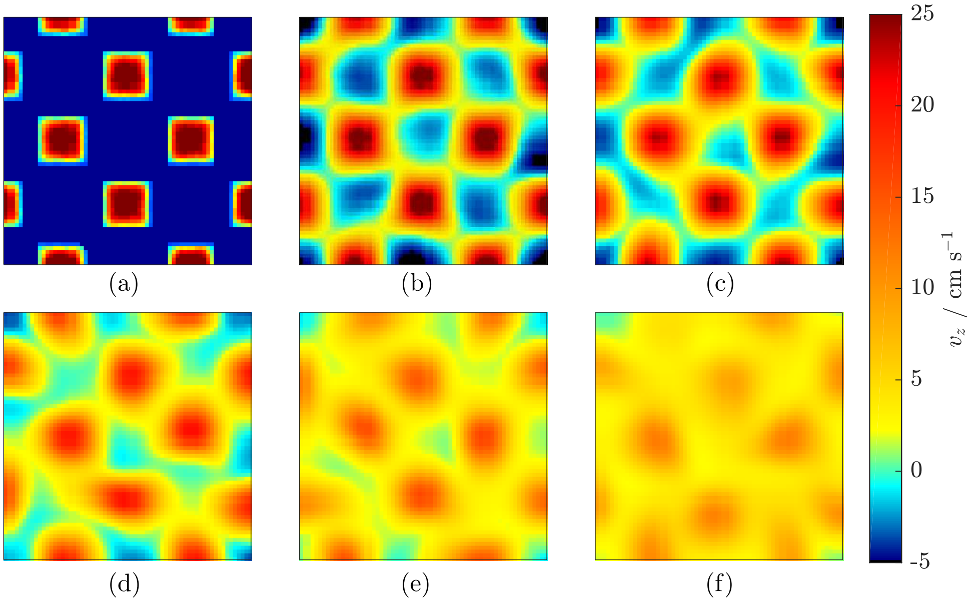

Fig. 5.7: Axial velocity images predicted using CFD at the exit of geometry B in the *xy* plane. The laminar model was used. The images are centred at z = (a) -2.5 mm, (b) 2.5 mm, (c) 7.5 mm, (d) 12.5 mm, (e) 17.5 mm and (f) 22.5 mm relative to the rear face of the geometry ($z = 0$ mm.) The isotropic FOV shown is 5.1 mm and the slice thickness is 1 mm across a square profile.

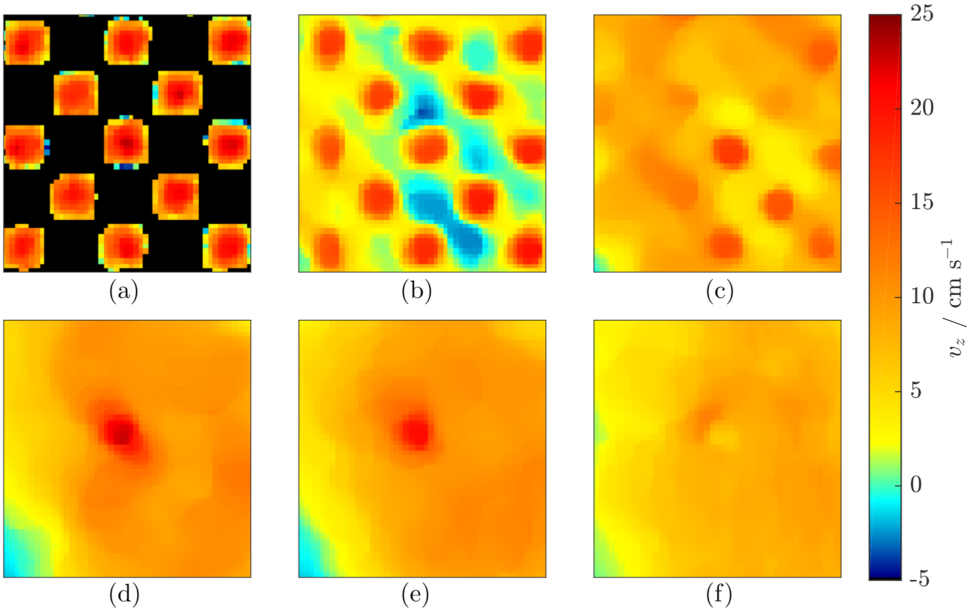

Fig. 5.8: Axial velocity images measured using MRI at the filter exit in the *xy* plane. Images are centred at z = (a) -2.5 mm, (b) 2.5 mm, (c) 7.5 mm, (d) 12.5 mm, (e) 17.5 mm and (f) 22.5 mm relative to the rear face of the filter ($z = 0$ mm.) The isotropic FOV shown is 7.28 mm and the slice thickness is 2.5 mm across a Gaussian profile.

5.5 Discussion

One problem of interest for CFD simulations of filter geometries is the interaction of the entrance and exit regions with the internal hydrodynamics. Due to the high aspect ratio of filters, simulating the entire filter length is computationally demanding and so any reduction in complexity would improve simulation times and the utility of CFD as an optimisation tool. One possible simplification would be to reduce the length of the filter and remove the porous wall, leaving just the contraction and expansion of the cross-sectional area i.e. geometry B. Figures 5.3 and 5.4 suggest that this reduced geometry still predicts the major flow phenomena at the entrance and exit. However, it is not clear whether the turbulent features observed in Fig. 4.18 are predicted in either geometry. This is possibly due to the low gas flow rates or the lack of a turbulence model used in these simulations.

Turbulence presents a major challenge in performing CFD work and has been the subject of an enormous amount of work over the past century. Many turbulence models have been developed to allow solutions to converge, with different models performing better under various different circumstances [1–3]. The k-ϵ model is one of the most popular and is frequently used in more ‘routine’ simulations. In the present study, the model appears to cause a large amount of turbulent mixing, resulting in a loss of many flow features in the CFD predictions (Fig. 5.5). While the laminar model is appropriate at low flow rates within the channels, the transition to high Reynolds number flows at the entrance and exit will require some turbulence modelling; the longer persistence of the high velocity jets at the exit region (Fig. 5.7) is attributed to a lack of turbulent mixing due to the laminar model. Hence, future CFD simulations will need to pick a more appropriate turbulence model or tune the parameters of the k-ϵ model to produce more congruent results.

Partial volume effects and slice averaging are often observed in MR images and create some obstacles in directly comparing other data, whether experimental or simulated, with MRI measurements. Hence, it is important to know what the effects of these are and to account for them in any simulations. Figure 5.6 shows the effect of finite resolution and slice averaging on the velocity distribution at the filter exit. The averaging reduces the extreme values of the velocity in the data and may cause an underestimation in the average velocity. This occurred in the present study. As such, it may be important to estimate the gas velocity using independent methods to validate the average velocity extracted from MRI data.

5.6 Conclusions

In this chapter, preliminary CFD simulations were performed to test different geometries and turbulence models, observe the effects of slice averaging and compare the flow features predicted with those observed with MRI. Both a full filter geometry and a reduced non-porous geometry predicted the major flow phenomena expected at the filter entrance and exit, suggesting that the latter may be useful in studying entrance and exit effects in isolation of the internal filter hydrodynamics. The turbulence model used in future work will need to be selected carefully. A laminar model predicted the correct flow features but these were exaggerated in scale, whereas the k-ϵ model overpredicted the level of turbulent mixing. Slice averaging effects were found to be significant and need to be considered when matching the gas velocity for comparison between MRI and CFD data.

5.7 References

[1] V. C. Patel, W. Rodi, G. Scheuerer. Turbulence models for near-wall and low reynolds number flows — a review. *AIAA Journal* (1985) 23 (9), 1308–1319. doi:10.2514/3.9086.

[2] M. Nallasamy. Turbulence models and their applications to the prediction of internal flows: A review. *Computers & Fluids* (1987) 15 (2), 151–194. doi:10.1016/S0045-7930(87)80003-8.

[3] W. Rodi. *Turbulence models and their application in hydraulics: A state-of-the-art review.* 3rd edition. CRC Press (2017). doi:10.1201/9780203734896.

Chapter 6

Numerical filter models: validation and development

The work presented in this chapter has been included in the following manuscript:
J.D. Cooper, L. Liu, N.P. Ramskill, T.C. Watling, A.P.E. York, E.H. Stitt, A.J. Sederman, L.F. Gladden. Numerical and experimental studies of gas flow in a particulate filter. *Chemical Engineering Science* (2019) 209, 115179. doi:10.1016/j.ces.2019.115179

6.1 Introduction

Optimum operation of a particulate filter relies heavily on the behaviour of the gas phase in the system. The filtration of particulate matter is a complex process involving the behaviour of the exhaust gas, the suspended PM and the filter substrate [1–3]. The pressure drop across the system is caused by the interaction of the gas and the solid filter substrate, soot cake and any washcoat [4]. For catalysed filters, the transport of chemical species and thermal energy is also mediated by the gas hydrodynamics [5]. As such, an accurate and comprehensive understanding of the gas hydrodynamics is essential in predicting filter behaviour and optimising both the structure and operating conditions.

Despite its importance, there is a severe lack of experimental work measuring the internal gas hydrodynamics in filter systems. This is largely due to the difficulty in applying standard anemometry methods to such systems, as discussed in Chapter 4. As a result, the study of such behaviour has been largely performed via numerical simulations which are outlined in Section 6.3. While such models are invaluable for understanding and predicting filter behaviour, they rely on validation against global measurements and so there is little confidence in their predictions of microscopic gas behaviour. This chapter aims to validate two models representative of those in the literature, provide confidence in their predictions and provide feedback for their development.

Magnetic resonance velocity imaging has found great utility in probing hydrodynamics in difficult systems, including one- and two-phase flow in flow through monoliths [6–8], and is appropriate for studying particulate filters as discussed in Section 4.6.1. In particular, MR velocimetry has allowed direct comparison between experimental velocity measurements and predictions from numerical models. These have included full CFD simulations, such as for gas flow over obstructions and foils [9], liquid flow in a packed bed [10, 11] and rising plugs in fluidised beds [12], and simpler models, such as for the drying of liquids in porous pellets [13]. Recent work by Ramskill *et al.* [14] used MRI to measure the axial gas velocity inside a filter for the first time. The present study builds on this work to both empirically study the behaviour of the gas inside a real filter and to validate and develop numerical models commonly used to predict filter behaviour.

6.1.1 Fluid dynamics in wall-flow filters

Despite having a relatively simple geometry, the fluid behaviour associated with wall-flow filters is surprisingly complex. As discussed in Chapter 4, significant flow contraction and expansion occurs at the entrance and exit of the filter and creates non-ideal flow behaviour. However, this section will only describe the gas behaviour internal to the filter.

As gas flows into the inlet channels it is subject to two pressure gradients. The first is across the porous wall, which drives gas through the wall and is associated with filtration. The second is down the channel, and is mediated by the momentum convection of the gas and the viscous losses associated with shear stress near the wall. At the end of the inlet channel, the plugged region creates a zero-flow boundary condition and hence the axial velocity of the gas decreases along the length of the inlet channel. The plugs used are often porous in nature and so it is feasible that gas will flow through these. However, as the path through the plugs is ∼10-20 times longer than through the filter wall, such flows will likely be insignificant.

In the outlet channel, similar behaviour is observed. Gas is injected into the outlet channel via the wall from the higher pressure inlet channel, and the axial velocity of the gas increases along the length of the channel in order to conserve mass flux. Like the inlet channel, the gas in the outlet channel is subject to viscous losses from shear stress and so a pressure gradient along the channel is formed. The gas momentum will have fully transferred into the outlet channel at the end of the filter length and the pressure will have decreased to its minimum inside the filter.

The through-wall velocity depends on the local pressure difference between the inlet and outlet channels, and is typically paraboloid in shape with a minimum in the centre of the filter. At the front of the filter, where the inlet channel velocity is high and the outlet channel low, more viscous losses will occur in the inlet channel and hence the inlet channel pressure will decrease more quickly along the filter length. This results in a reduction of the through-wall velocity. However, after the centre of the filter, the outlet channel velocity is greater than the inlet channel and so the reverse occurs, with the outlet channel pressure decreasing more quickly; hence the pressure gradient increases and the through-wall velocity increases. The exact form of the through-wall velocity will depend on the flow rate under study and the properties of the porous substrate.

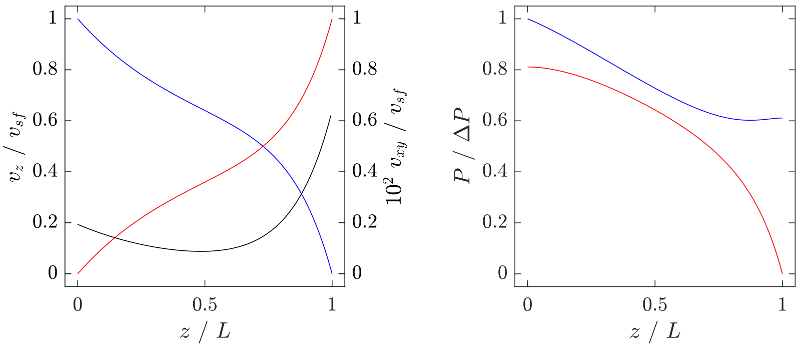

(a) (b)

Fig. 6.1: Illustrative (a) inlet (——) and outlet (——) channel axial velocities v_z, through wall velocity v_{xy} (——) relative to the superficial velocity v_{sf}, and (b) inlet (——) and outlet (——) channel pressure profiles for gas flow in a DPF.

6.2 Scope of study

In this chapter, MRI velocimetry is used to measure the axial channel velocities of gas flow in a DPF sample at a range of gas flow rates. These measurements are then used to calculate the through-wall gas velocities. These measurements are compared with numerical predictions from both 1D and 3D CFD simulations to assess the validity of such models, including the effects of recent developments in the 1D modelling literature. The spatial resolution of the MRI and CFD data is then used to assess the validity of these developments. Finally, the through-wall velocity is used to predict the filtration behaviour of the filter at the flow rates measured.

6.3 Literature review

6.3.1 Impact of gas hydrodynamics

As described in Section 6.1.1, the interaction of the gas flow and the porous filter walls creates pressure losses, which cause backpressure in the engine. This reduces the fuel economy of the vehicle and can potentially damage the engine in extreme cases. Frictional losses are unavoidable and can only be minimised by shortening the filter, which then reduces the surface area available for filtration and increases the through-wall velocities. The origin of frictional loss is the viscous forces at the gas-solid interface. As the Reynolds numbers expected in filter channels are typically below 2000, the roughness of the wall is not expected to influence the frictional losses [15]. In practice, the frictional losses are typically modelled using correlations for the asymptotic losses experienced in a smooth square duct.

Pressure losses from through-wall flow are typically modelled using Darcy's law [4], as is common for porous materials. The quadratic Forchheimer extension is often included, though it is typically only important for systems with high through-wall velocities and low frictional losses. As Darcy's law scales with the permeability of the porous medium, accurate estimations of the permeability are needed to correctly predict the pressure drop contributions. However, the permeability is difficult to measure directly. Experimental methods rely on carefully cutting a wafer of the filter material and measuring the pressure losses across it [16]. While this method provides the best results, it is not feasible for many filter samples due to the fragility and brittleness of the substrates. Most estimations are made by fitting the pressure drop predictions of numerical models to measurements, using the permeability as the fitting coefficient [5]. However, this method assumes that all contributions to the pressure drop have been accurately modelled, which has not yet been established. Recently, numerical simulations using X-ray μ-CT images of the substrate porous structure have been able to estimate the permeability [17], although many images and simulations are required to provide a macroscopic value of the permeability.

The gas hydrodynamics are also predicted to impact the behaviour of the suspended solid phase and hence the filtration behaviour of the filter. Konstandopoulos and Johnson developed an analytical model of filtration that predicted higher through-wall velocities to reduce the filtration efficiency of particles with sizes $\sim$1 µm [1]. Sbrizzai *et al.* used a Lagrangian CFD approach to model the deposition of 0.2 µm and 2 µm particles in a filter [18]. While the deposition probability profile largely mirrored the behaviour of the through-wall velocity, it was predicted that the first fifth of the filter had nearly zero probability of particles depositing. This is attributed to the *vena contracta* that develops at the filter entrance and a corresponding higher deposition probability is seen at the filter rear. Bensaid *et al.* used an Eulerian-Eulerian CFD method and found similar results [2, 3]. However, the effect of the *vena contracta* was much less pronounced and only affected the largest particle size considered (2 µm).

6.3.2 Numerical models of filters

Numerical models used to simulate behaviour in particulate filters span a wide range of dimensionalities and complexities, most of which are beyond the scope of this chapter. Comprehensive reviews of the modelling literature are given by Koltsakis and Yang [19, 20]. In this section, 1D and 3D single channel models are briefly outlined as they are the most relevant to the modelling utilised in this chapter.

One-dimensional modelling of DPFs began with the work of Bissett [21], which modelled the thermal regeneration of an inlet-outlet channel pair by considering only the axial component of flow. Most 1D models since have been derived in some part from this work. Several studies have focussed on improved modelling of filtration and regeneration. Konstandopoulos and Johnson included an analytical filtration model, based on deep bed filtration, allowing the collection efficiency of PM to be simulated [1]. Konstandopoulos subsequently developed a model allowing transient simulation of PM filtration and regeneration [22]. Peters *et al.* later allowed variation of the channel diameter in response to soot loading [23]. Other workers have focused on the modelling of catalytic reactions, including a separate catalytic layer for oxidation of soot [24], NO_2 assisted regeneration [22] and the catalytic removal of other pollutants [25, 26]. However, little work has been done to validate or improve the descriptions of the underlying gas hydrodynamics. Konstandopoulos and Johnson noted that the wall friction factor F will vary with the local through-wall velocity, though they used a constant value across the filter length [1]. Oxarango *et al.* suggested including the effects of gas suction and injection at the wall in one-dimensional models, and that it may be significant for the spatial distribution of captured PM [27]. It was not until the work of Bissett *et al.* and Kostoglou *et al.* that this development was fully explored [28, 29]. The two studies used numerical methods to solve the velocity and pressure fields for flow in a square pipe with a non-zero transverse velocity at the wall. Using this method, they developed correlations to relate the changes in the flow profile shape (characterised by $\alpha = \langle v_z^2 \rangle / \langle v_z \rangle^2$ across the cross-sectional area of the channel) and wall friction factor. It was predicted that both these factors depend strongly and non-linearly on the local through-wall velocity. However, Watling *et al.* found that inclusion of these correlations in a 1D model had no observable effect on the pressure drop predictions. Bissett *et al.* later extended this method to channels with triangular cross-sections [30]. Watling *et al.* posited that the magnitude of the axial momentum convection term was overstated in the original model of Bissett and proposed an alternate derviation; the new term was one-half the magnitude of the original [5] and resulted in lower backpressure predictions at higher flow rates. However, the effect of these developments on the gas flow field predictions has not been tested.

Three-dimensional simulations of DPF systems typically utilise commercial computational fluid dynamics (CFD) packages, though some studies have avoided this by coupling various low-dimension models [31, 32]. Early studies using CFD focused on resolving the gas hydrodynamics in the filter. Konstandopoulos *et al.* [33] simulated an inlet-outlet channel pair, including regions upstream and downstream of the filter, observing entrance and exit effects not possible with 1D models. Liu and Miller [34] performed 3D CFD simulations for triangular channels and observed similar effects. Since these early studies, CFD simulations have primarily been used to study processes that are difficult to model otherwise, e.g. soot deposition and regeneration [2, 18, 35–37]. While such studies offer greater accuracy in their representation of the physical system, they typically require expensive hardware and software, user experience and long times to achieve solutions. As such, application of 3D simulations has been limited in comparison to lower dimensionality and multi-scale models.

Most models, regardless of their complexity, are validated against one or more macroscopic measurements. These have previously included pressure drop [1, 5, 18, 22, 34, 38], filtration behaviour [22], chemical species concentration [25, 26, 38] and temperature [3, 24, 38]. The predicted flow fields from 1D and 3D models have also shown reasonable agreement [34, 39]. However, direct validation of the gas flow fields is rare. To the best of the author's knowledge, there have only been two comparisons of numerical model predictions and measured values of the gas velocity inside a DPF. The first is Dr Nicholas

Ramskill's thesis [40], where the axial channel and through-wall velocity measurements are compared to a 1D model prediction at low Reynolds numbers. The second is the work of Lao *et al.* [41], which used through-wall velocity measurements of Ramskill *et al.* [14] at a single flow rate to validate a model of secondary particulate emissions.

6.4 Experimental

6.4.1 Materials and equipment

A 5 × 5 sample of a bare silicon carbide DPF, with properties listed in Table 6.1, was used for all experiments. As reported in Section 4.6.1, silicon carbide has a good susceptibility match with SF_6 away from the plugged region. The DPF sample (A) was secured with PTFE tape in a square Perspex sample holder (B) and held inside a custom-built polyetheretherketone (PEEK) flow cell (internal diameter 18 mm) (C) designed to operate at pressures of up to 9 bar(a) (Fig. 6.2). The flow cell was held inside the NMR spectrometer (D) and supplied using a recirculating SF_6 rig as described in Appendix A. The position of the flow cell within the magnet and r.f. coil (E) was controlled using several plastic spacers (F), allowing the axial position z to be varied. A perforated plate distributor (G) was used to provide uniform flow upstream of the sample. The SF_6 gas was supplied at 5.0±0.1 bar(g) and 22±2 °C. Five gas flow rates were used; the superficial velocities are listed in Table 6.2 and correspond to channel Reynolds numbers, $\mathrm{Re_c} = \rho v_{\mathrm{sf}} d_c / \mu$, in the range 751 – 2972, representative of flow expected in operating filters and higher. Additionally, three datasets at lower flow rates ($\mathrm{Re_c}$ = 102 - 450), acquired by Dr Nicholas Ramskill [14], were included to extend the range of Reynolds numbers compared with numerical predictions. The gas density and dynamic viscosity were taken to be $38.5\,\mathrm{kg\,m^{-3}}$ and $15.1 \times 10^{-6}\,\mathrm{Pa\,s}$ respectively.

6.4.2 Magnetic resonance imaging

All MRI experiments were performed using a 9.4 T superconducting magnet controlled by a Bruker AV 400 spectrometer tuned to the ^{19}F resonant frequency, 376.19 MHz. Spatial resolution and displacement encoding was provided by three orthogonal micro-imaging gradient coils, each with a maximum strength of $146\,\mathrm{G\,cm^{-1}}$. A maximum imaging gradient strength of $11.7\,\mathrm{G\,cm^{-1}}$ was used to achieve the spatial resolution quoted and velocity gradient strengths between $0.73\,\mathrm{G\,cm^{-1}}$ and $5.84\,\mathrm{G\,cm^{-1}}$ were used to provide adequate fields of flow. A matrix rotation was applied to align the gradient axes with the natural axes of the filter sample. A recycle time of 32 ms was used. The SESPI imaging method used was the same as used for the 2D images in Chapter 4 and derived from the work of Ramskill *et al.* [14], with the relevant parameters shown in 6.3.

Axial velocity images were acquired along the length of the filter sample, each with a slice thickness of 12 mm. Only the central 9 channels, i.e. those with 8 neighbouring

Table 6.1: Relevant properties of the DPF sample used

material	silicon carbide
filter length / mm	155
plug length / mm	0.5
permeable channel length, L / mm	145
sample diameter / mm	6.2
channel width, d_{c} / mm	1
wall thickness, w_{w} / mm	0.2
cell density / cpsi	300
no. inlet channels	13
no. outlet channels	12
porosity / %	52±4
mean pore diameter / µm	23±5

Table 6.2: Gas mass flow rates, superficial velocities and channel Reynolds numbers used. Velocities marked with an asterisk indicate acquisition by Dr Nicholas Ramskill [14].

mass flow rate, $\dot{m}$ / $\mathrm{g\,min^{-1}}$	superficial velocity, v_{sf} / $\mathrm{cm\,s^{-1}}$	channel Reynolds number, $\mathrm{Re_c}$
-	4.4±0.2*	102±5
-	10.8±0.6*	257±14
-	18.9±0.6*	450±14
12	31.5±0.5	751±12
16	42.6±1.2	1016±29
20	52.5±1.6	1251±29
25	63.7±1.4	1518±34
50	124.8±4.1	2972±98

Table 6.3: MRI parameters for SESPI experiments

Parameter	Value
image size	128 × 128
field of view / mm	18 × 18
resolution / µm	140 × 140
soft 180° pulse duration / µs	256
soft pulse shape	Gaussian
slice thickness / mm	12
under-sampling rate / %	20
gradient pulse duration δ / ms	0.74
observation time Δ / ms	1.48
echo time T_E / ms	2.65
acquisition time / min	14

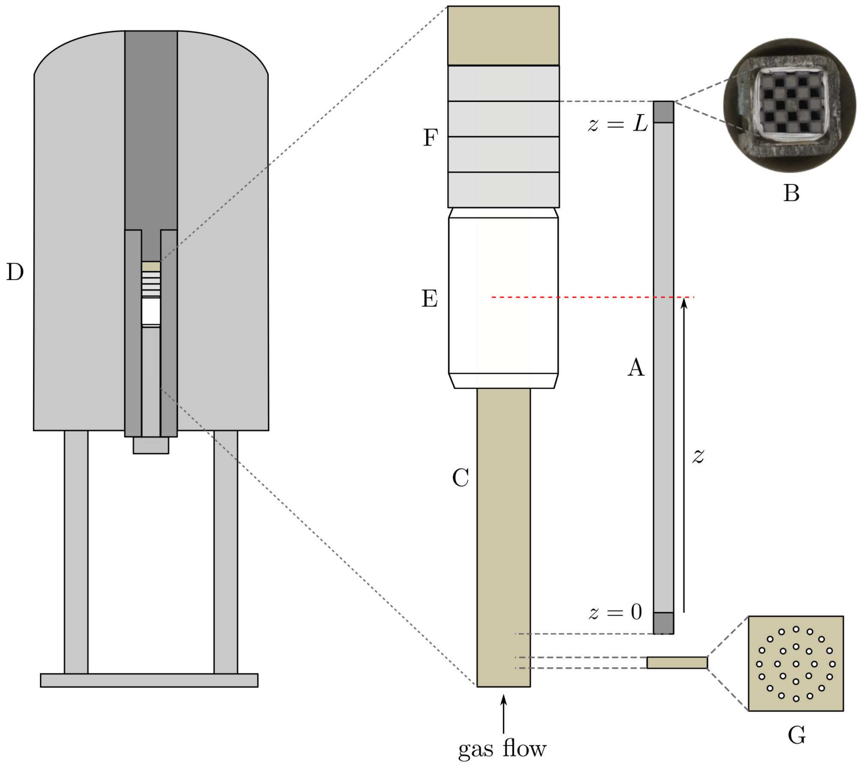

Fig. 6.2: Schematic showing the DPF sample inside the PEEK flow cell and magnet.

channels, were analysed to avoid any unrepresentative boundary effects. Representative velocity images are given in Fig. 6.3. The mean inlet and outlet channel velocities, $v_{z,i}$ and $v_{z,o}$, were calculated from the MR images. For the lowest three flow rates, ten images were acquired. An eleventh image was acquired for the higher flow rates in order to better resolve the flow profile at the rear of the filter. The superficial velocities were calculated from the sum of the mean inlet and outlet channel velocities. In order to assess if flow through the porous plugs was significant, two velocity images were acquired in the plugged regions at the front and rear of the filter for $\mathrm{Re_c}= 1251$. There was no difference in the mean axial velocity within error between the front and rear of the filter. As such, the mean superficial velocity for each flow rate was used as an additional velocity measurement for the inlet and outlet channels at $z = 0$ and $z = L$ respectively; zero velocities were also included at the plugs. This allowed completion of the mass balance. The through-wall velocity, v_{xy}, was calculated from the mass balance of axial velocities at each data axial point j for both inlet and outlet channels using the equations,

$$v_{xy,i} = \frac{\left[v_{z,i}(j) - v_{z,i}(j+1)\right] d_\mathrm{c}^2}{4 d_\mathrm{c} \Delta z}, \tag{6.1}$$

$$v_{xy,o} = \frac{\left[v_{z,o}(j+1) - v_{z,o}(j)\right] d_\mathrm{c}^2}{4 d_\mathrm{c} \Delta z}, \tag{6.2}$$

where Δz is the axial distance between data points (usually 14 mm apart from the distances between the first two and last two data points) and d_c is the channel side length. The quoted through-wall velocity was taken as the mean of the velocities calculated from the inlet and outlet channels. The momentum convection correction factor, α, was calculated using the equation,

$$\alpha = \frac{\langle v_z^2 \rangle}{\langle v_z \rangle^2}, \tag{6.3}$$

where $\langle ... \rangle$ denotes the mean calculated over the cross-sectional area of each channel. Due to the relatively low resolution of the MRI data in the present study, the values of α calculated will be underestimated. To account for this, a correction factor was calculated by simulating a laminar flow profile on a fine and coarse mesh to reflect the resolution of the MRI data [42]. This factor was then used to correct the values of α calculated from the MRI data.

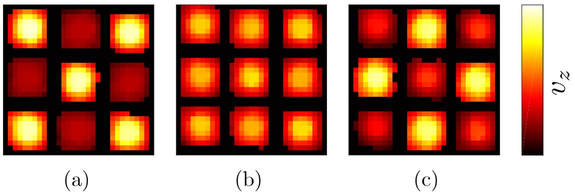

(a) (b) (c)

Fig. 6.3: Representative MRI velocity images of the axial gas velocity v_z at the (a) front, (b) centre and (c) rear of the DPF sample.

6.5 Numerical Methods

This section outlines the models used to simulate gas flow in wall-flow filters and filtration efficiency for the present study. Both the 3D CFD and 1D models used are ‘single channel pair’ models, i.e. they simulate pairs of inlet and outlet channels and do not consider radial variation in the filter. The simulations are limited to the simplest case of isothermal, non-reactive gas flow in a bare (i.e. soot- and washcoat-free) filter with no suspended PM.

6.5.1 Three-dimensional model

The method used to perform the three-dimensional CFD simulations is described here. All 3D CFD simulations were performed by Dr Li Liu at Johnson Matthey Technology Centre, Billingham, UK.

Due to the small pressure drops expected in a DPF geometry ([2, 18, 33]) and the low Mach numbers in the system (Ma < 0.02), incompressible flow was assumed and the continuity equation was expressed as

$$\nabla \cdot \mathbf{v} = 0, \tag{6.4}$$

where **v** is the gas velocity field. The momentum equations solved were

$$\rho\,(\mathbf{v}\cdot\nabla)\,\mathbf{v} = -\nabla P + \nabla\boldsymbol{\tau} + \mathbf{S}, \tag{6.5}$$

where ρ is the gas density, P is the gas pressure, $\boldsymbol{\tau}$ is the viscous stress tensor and $\mathbf{S}$ is the momentum source term. The gas was assumed to be Newtonian and hence the term $\nabla\boldsymbol{\tau}$ was equal to $\mu\nabla^2\mathbf{v}$, where μ is the gas dynamic viscosity. The source term $\mathbf{S}$ was set to zero everywhere except inside the porous wall. Inside the wall, Darcy's law was used as a momentum sink,

$$\mathbf{S} = -\frac{\mu}{k}\mathbf{v}, \tag{6.6}$$

where k is the permeability of the porous wall. The flow was taken to be non-reactive and no energy equations were solved. Given the low Reynolds numbers under study, a laminar model was used.

The geometry used described four filter channels, two inlet and two outlet, with dimensions matching those of the DPF sample described in Section 6.4. Only the length of the filter with a permeable wall was simulated. It is expected that the effects of the plugged regions on the flow fields are not significant as the plug length is less than 4% of the total filter length. The entire geometry had dimensions 2.4 mm×2.4 mm×145 mm, with a channel width of 1 mm and wall thickness of 0.2 mm, as illustrated in Fig. 6.4. The permeability of the porous wall was taken to be $6 \times 10^{-13}\,\mathrm{m}^2$. The mesh was created using snappyHexMesh (OpenFOAM Ltd) and was made of hexahedral cells. Due to the large aspect ratio of the filter channels ($L/d_\mathrm{c} \approx 1500$), ~2.1 million cells were used in the mesh. As laminar flow was expected, no surface enhancements applied during the meshing process. The dimensions of each cell were of the order 40 µm×40 µm×300 µm. Solutions were found to be mesh independent.

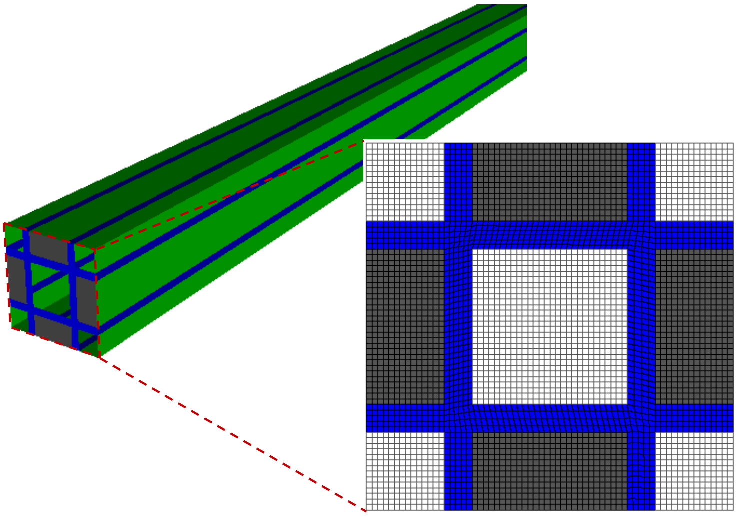

Fig. 6.4: Mesh used for the 3D CFD simulations.

The boundary conditions imposed reflected those used for the 1D model. The lateral faces of the geometry were set as symmetric boundary conditions. The effects of the plugs were simulated by setting the front face of the outlet channel and the rear face of the inlet channel to zero velocity. The front face of the inlet channel was set uniformly as the superficial gas velocity, v_{sf}. The rear face of the outlet channel was allowed free flow at pressure P_{sys}. No velocity boundary conditions were set in the porous walls or the channel-wall interface. The fluid was set to have the properties of SF_6 at 5 bar(g) and 295 K as described in Section 6.5.2.

The simulations were run using the open-source CFD software OpenFOAM® on an in-house computer cluster at JMTC Billingham. Solutions were considered to have converged when all residuals were less than 10^{-4} and typically required ~8 h to compute. The solutions were re-gridded in MATLAB® R2018a for post-processing. The velocity and pressure data were discretised into 32 axial points. Mean axial velocities, v_z, and pressures, P were calculated for the inlet and outlet channels across the cross-sections of each channel. The through-wall velocity was calculated using Eqs. (6.1) and (6.2). The values of α were calculated at each axial location using Eq. (6.3). The wall friction factor, F, was calculated using the equation of Bissett *et al.* [28],

$$F = -\frac{d_{\mathrm{c}}^2}{\mu v_z}\left(\frac{\mathrm{d}P}{\mathrm{d}z} + \rho\alpha\frac{\mathrm{d}v_z^2}{\mathrm{d}z}\right). \tag{6.7}$$

6.5.2 One-dimensional model

The one-dimensional model used was that of Watling *et al.* [5], developed by Dr Timothy Watling (Johnson Matthey Technology Centre, Sonning Common, UK) and derived originally from the work of Bissett [21]. The model simulates steady-state gas flow in an soot-free inlet-outlet channel pair with the same dimensions as given in Table 6.1, shown schematically with nomenclature in Fig. 6.5.

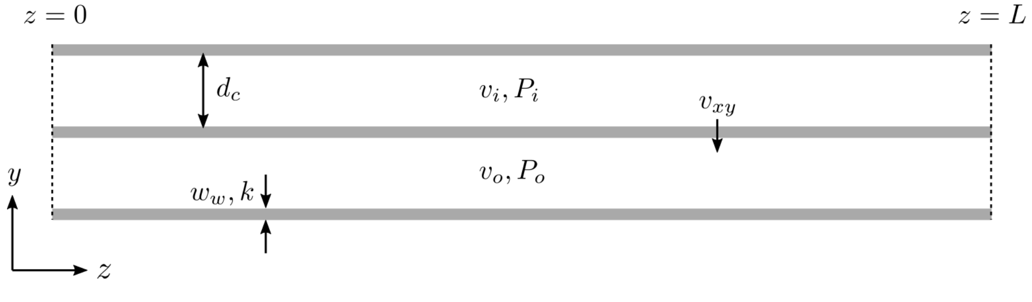

Fig. 6.5: Schematic showing the geometry and nomenclature of the 1D DPF model.

The continuity equations solved were

$$\frac{\partial \rho_i v_i}{\partial z} = -\frac{4}{d_{\mathrm{c}}}\rho_w v_{xy}, \tag{6.8}$$

$$\frac{\partial \rho_o v_o}{\partial z} = \frac{4}{d_\mathrm{c}} \rho_w v_{xy}, \tag{6.9}$$

where ρ is the gas density and v is the mean gas velocity in the inlet (i) and outlet (o) channels. The equations describe the conservation of mass as gas flows along the channels and through the porous walls. The momentum equations solved are

$$\frac{\partial P_i}{\partial z} + n\alpha_i \rho_i v_i \frac{\partial v_i}{\partial z} = -\frac{F_i \mu v_i}{d_\mathrm{c}^2}, \tag{6.10}$$

$$\frac{\partial P_o}{\partial z} + n\alpha_o \rho_o v_o \frac{\partial v_o}{\partial z} = -\frac{F_o \mu v_o}{d_\mathrm{c}^2}, \tag{6.11}$$

where P is the local gas pressure, μ is the gas dynamic viscosity, n is the momentum convection correction scalar, α is the momentum convection correction factor and F is the wall friction factor. The terms in each equation, from left to right, describe the change in pressure, the force required to accelerate/decelerate the gas (often called the momentum convection) and the loss of momentum due to shear stress (friction) at the channel wall. n was allowed to take values of 1 or 2, describing the momentum convection terms of Watling *et al.* [5] and Bissett *et al.* [21] respectively. The values of α and F were either set to uniform values in both channels of 1.377 [42] and 28.48 [43] respectively, reflecting the analytical results for laminar flow in a square duct with non-porous walls (referred to as model A), or allowed to vary with the local wall Reynolds number ($\mathrm{Re_w}$) according to the correlations of Bissett *et al.* [28] (referred to as model B),

$$\alpha_i = 1.377 + 0.0389\mathrm{Re_w} - 0.0182{\mathrm{Re_w}}^2 + 0.0106{\mathrm{Re_w}}^3, \tag{6.12}$$

$$\alpha_o = 1.377 - 0.031\mathrm{Re_w} + 0.0052{\mathrm{Re_w}}^2. \tag{6.13}$$

Similarly for the wall friction factor, F,

$$F_i = 28.48 - 2.92\mathrm{Re_w} + 1.12{\mathrm{Re_w}}^2 - 0.54{\mathrm{Re_w}}^3, \tag{6.14}$$

$$F_o = 28.48 + 1.66\mathrm{Re_w} - 0.14{\mathrm{Re_w}}^2, \tag{6.15}$$

where all are defined for $\mathrm{Re_w} < 3.5$, where $\mathrm{Re_w} = \rho v_{xy} d_c/\mu$. Pressure losses due to flow through the porous wall were calculated using Darcy's law,

$$-\frac{\partial P}{\partial y} = \frac{\mu v_{xy}}{k}, \tag{6.16}$$

where k is the wall permeability. The flow was assumed to be non-reactive and so no energy equations were considered. While incompressibility was not explicitly assumed, the variation in pressure across the filter was negligible ($\Delta P/P_\mathrm{sys} < 0.01\%$ for all flow rates) and the gas density could be considered as a constant.

The geometry used was based on the dimensions of the DPF sample described in Section 6.4. The wall permeability was set to $6 \times 10^{-13}\,\mathrm{m}^2$, consistent with the 3D CFD simulations. The channels were assumed to be free of soot and so a constant channel diameter was used. The geometry was discretised into 30 axial elements; increasing the number of elements was found to have no effect on the model predictions.

Equations (6.8) to (6.16) were solved to give the inlet channel, outlet channel and through-wall velocity profiles (v_i, v_o and v_{xy}) subject to the boundary conditions in Equations (6.17) to (6.20)

$$P_o\left(z = L\right) = P_{sys}, \tag{6.17}$$

$$v_i\left(z = 0\right) = v_{sf}, \tag{6.18}$$

$$v_i\left(z = L\right) = 0, \tag{6.19}$$

$$v_o\left(z = 0\right) = 0, \tag{6.20}$$

where P_{sys} is the pressure of the system. Equation (6.17) sets the downstream pressure of the gas. Equation (6.18) sets the gas velocity at the filter inlet to the superficial gas velocity as measured with MRI. Equations (6.19) and (6.20) simulate the effects of the plugs. The fluid properties were set to match those of SF_6 under the conditions described in Section 6.4. A density of $38.5\,\mathrm{kg\,m^{-3}}$ and a dynamic viscosity of $1.51 \times 10^{-6}\,\mathrm{Pa\,s}$ were used, consistent with SF_6 at 5 bar(g) and 295 K.

The governing equations were solved using the ‘bvp4c’ boundary problem solver in MATLAB® (Mathworks, USA). Convergent solutions took under 0.5 s to compute using an Intel i5-7200U CPU running at 2.71 GHz. The simulation returned the pressure and axial velocity fields for both channels. The through-wall velocity was calculated from the axial velocities using Eqs. (6.1) and (6.2).

6.5.3 Analytical filtration model

The analytical filtration model developed by Konstandopoulos and Johnson [1] allows the filtration efficiency to be calculated for particulates of a given diameter transported through a porous medium at a given superficial velocity. Due to the size of the particulates expected in vehicle exhausts, only the Brownian and interception deposition mechanisms are considered. The full model is described in Appendix B and is used here to predict the filtration efficiency across the porous wall of a particulate filter. The model was run using the parameters listed in Table 6.4. The porosity and mean pore size were taken from the porosimetry data described in Section 6.4. The variation of the predicted filtration efficiency with through-wall velocity and particle diameter is shown in Fig. 6.6. The model was combined with the 3D CFD model predictions to simulate the filtration efficiency along the length of a DPF at multiple gas flow rates. The CFD predicted through-wall velocity at each axial point was used as the superficial velocity input for the filtration model. A representative PM number distribution,

$$N_\mathrm{p}(d_\mathrm{p}) = 10^{14} \exp\left[\frac{-(\log_{10}(d_\mathrm{p}) + 7.15)^2}{2(0.25)^2}\right], \qquad d_\mathrm{p} \in [10^{-8}, 10^{-6}] \tag{6.21}$$

was used to simulate the expected PM filtration profile along the filter length. The distribution is representative of diesel and GDI engine emissions under steady-state driving conditions [44, 45] and corresponds to a log-normal distribution with a modal particulate diameter of 70 nm (Fig. 6.7). The PM was assumed to follow the gas streamlines and so the number flux at each spatial point was proportional to the local gas through-wall velocity. The number flux was multiplied with the filtration efficiency to give the number of filtered particles for a given axial position and particle diameter. The total filtration efficiency across the whole filter was simulated by calculating the ratio of the number of filtered particles, found by integrating the PM deposition profiles for all sizes along the filter length, and the total number of particles.

Table 6.4: Parameters used in the filtration efficiency analysis

porosity, ϵ / %	52
mean pore size, d_pore / µm	23.4
single sphere collector diameter, D_p / µm	32
mean free path, λ / nm	68
particle diameter, d_p / µm	0.01 - 10

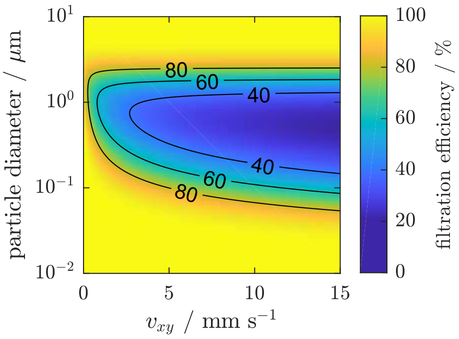

Fig. 6.6: Variation of the total filtration efficiency across the porous wall as a function of through-wall velocity v_{xy} and particle diameter.

6.6 Results

This section is presented in five parts. First, the MRI velocimetry method used is shown to be quantitative through agreement with independent mass flow measurements. Second, the gas velocities measurements made using the MRI method in the DPF sample are presented and the change in the cross-sectional flow profile is calculated for three flow rates. Third, the 3D CFD predictions of gas velocities are compared with the MRI measurements and

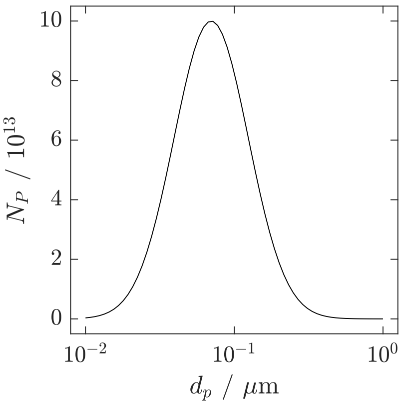

Fig. 6.7: Particle number distribution, N_{P}, used for simulating filtration behaviour.

1D model predictions. The values of α and F are calculated and compared with the MRI measurement values and correlations from literature. Fourth, the 1D model predictions of the gas velocities are compared with the MRI measurements. The sensitivity of the model predictions to three model parameters, α, F and k, are observed. The effects of recent literature developments, i.e. the developments of Watling *et al.*[5], Bissett *et al.*[28] and Kostoglou *et al.*[29], are also tested. Finally, a 1D analytical model is used with the MRI measurements to predict the filtration efficiency of the DPF sample at a range of flow rates.

6.6.1 Magnetic resonance imaging

Quantification of velocity measurements

Magnetic resonance velocity images were acquired along the length of the DPF sample at the range of flow rates listed in Table 6.2. In order to verify that MRI velocimetry accurately quantifies the gas velocity, volumetric flow rates calculated using the MRI data were compared with those measured using a mass flow controller. Temperature and pressure measurements were used to convert the mass flow rate, $\dot{m}$ to the volumetric flow rate, $\dot{V}$ using the relationship

$$\dot{V} = \frac{\dot{m}}{\rho}, \tag{6.22}$$

where ρ is the density of SF_6, taken to be $38.5\,\mathrm{kg\,m^{-3}}$ at 5 bar(g) and 22 °C [46].

Fig. 6.8 shows the mean volumetric flow rate across all axial positions calculated from the MRI measurements plotted against the expected volumetric flow rate from the mass flow controller. The error in the expected volumetric flow rate was calculated from the variation of gas pressure during the experiment (±0.1 bar(g)) and the error in the MRI volumetric flow rate is the standard deviation of the volumetric flow rate calculated at all axial positions. A strong agreement between the two is observed and the maximum deviation between individual flow rates was 3.1%. The data acquired by Dr Nicholas Ramskill agreed with gas rotameter measurements to within 17%.

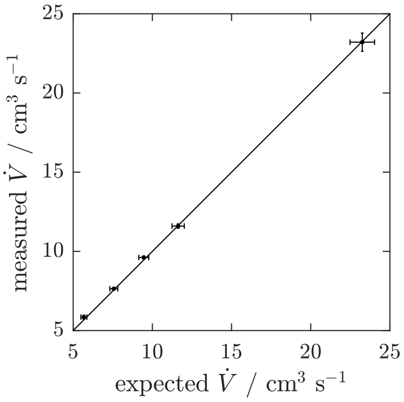

Fig. 6.8: Agreement between the expected (mass flow controller) and measured MRI volumetric flow rates. The solid line indicates perfect agreement.

Velocity profile measurements

The MRI measurements of the axial gas velocity in the inlet and outlet channels are presented in Fig. 6.9. Inlet velocities are shown by the blue circles and outlet velocities by the red squares; this colour scheme is maintained for the rest of this thesis. The vertical error bars show the standard deviation in the mean axial velocity between different channels; this variation is greater than the experimental error in the individual channel velocity measurements (i.e. from the SNR of the images) and hence reflects the heterogeneity in flow across the channels. The horizontal error bars reflect the slice thickness of the MR images. At all flow rates, the respective velocity decrease and increase in the inlet and outlet channels is seen to be non-linear. At low $\mathrm{Re_c}$, the inlet and outlet channel velocities are largely symmetrical, with the 'cross-over' point of the inlet and outlet channel velocities moving towards the rear of the filter as $\mathrm{Re_c}$ increases.

The through-wall velocity profiles calculated from the axial velocity data are shown in Fig. 6.10. The vertical error quoted was calculated using standard error propagation methods from the uncertainties in the axial velocity measurements. The horizontal error bars show the distance between the axial velocity measurements used. All flow rates demonstrate non-uniform through-wall velocity profiles as a result of the non-linear changes in axial velocity. At low $\mathrm{Re_c}$, the through-wall velocity is largely symmetric about $z/L = 0.5$. As $\mathrm{Re_c}$ increases, the gas flow through the rear of the filter increases rapidly and the through-wall velocity profiles become less uniform and symmetric.

Variation in α

The shape of the flow profile is characterised in the momentum flux factor α, which can be calculated using the MR velocity images. The values of α calculated for the MRI data in the range $\mathrm{Re_c}$ = 751 - 1251 are shown by the markers in Fig. 6.11. The horizontal error bars show the image slice width for each axial point and the vertical error bars show the variation between individual channels. The dotted line shows the value of α for laminar

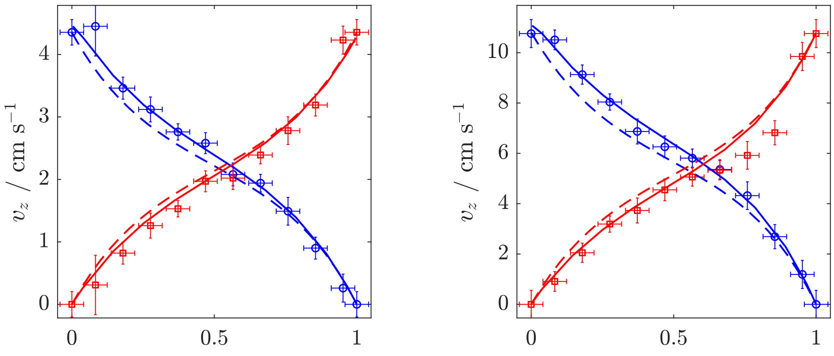

(a) $\mathrm{Re_c} = 102$ (b) $\mathrm{Re_c} = 257$

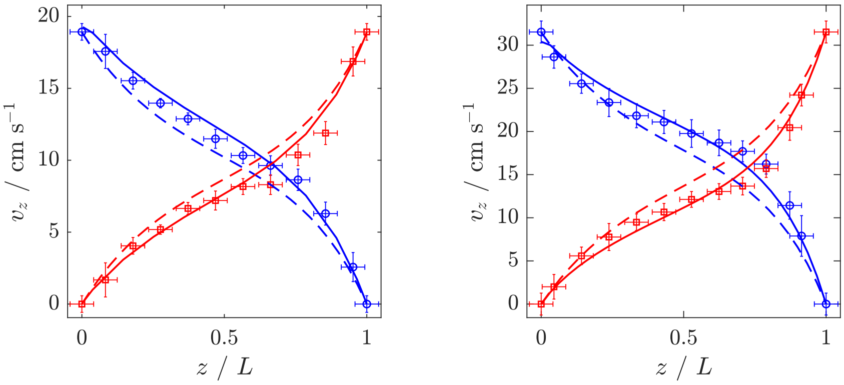

(c) $\mathrm{Re_c} = 450$ (d) $\mathrm{Re_c} = 751$

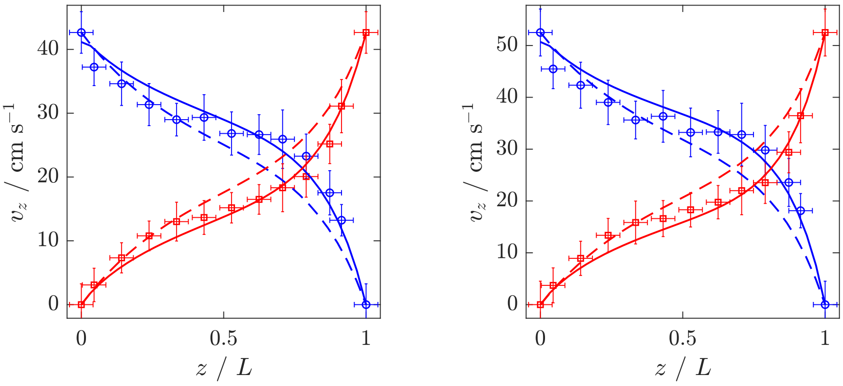

(e) $\mathrm{Re_c} = 1016$ (f) $\mathrm{Re_c} = 1251$

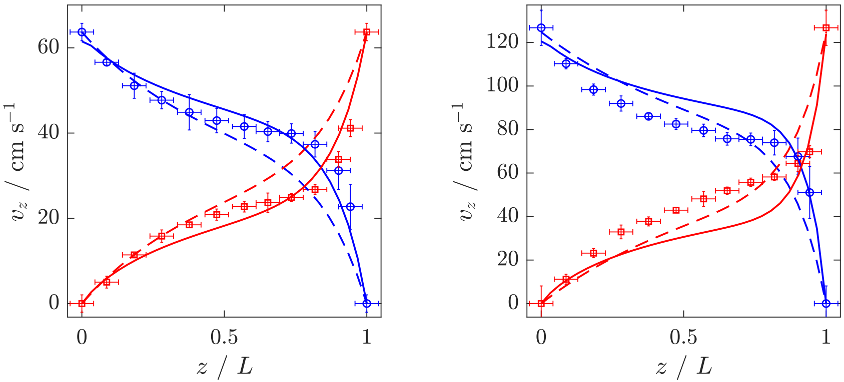

(g) $\mathrm{Re_c} = 1518$ (g) $\mathrm{Re_c} = 2972$

Fig. 6.9: Comparison of MRI measurements (markers), 1D model predictions (dotted lines, $n = 1$, model A) and 3D CFD predictions (solid lines) of inlet (—) and outlet (—) channel axial velocities.

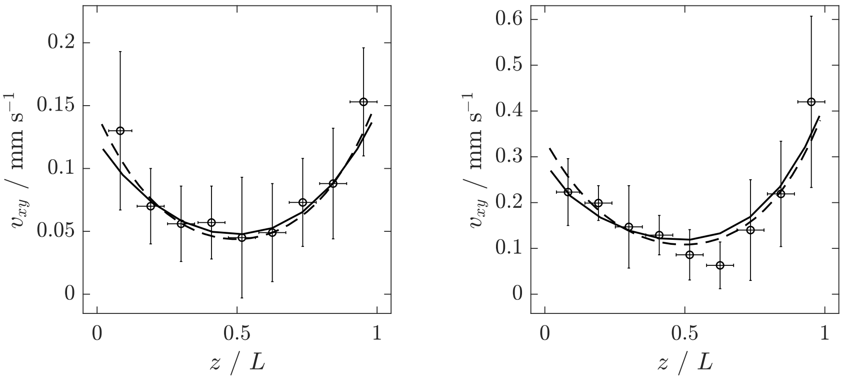

(a) $\mathrm{Re_c} = 102$ (b) $\mathrm{Re_c} = 257$

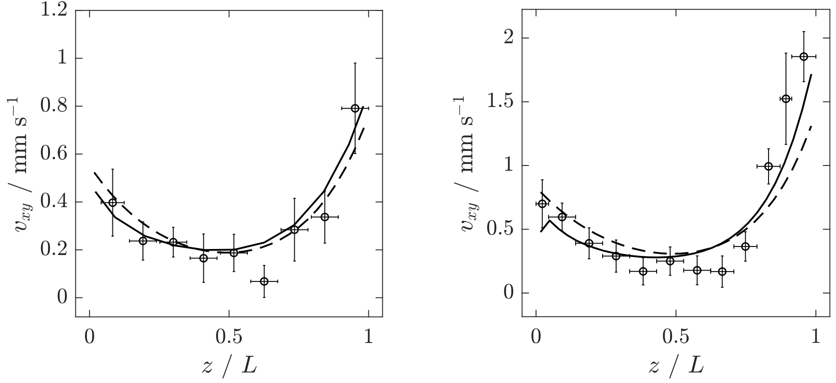

(c) $\mathrm{Re_c} = 450$ (d) $\mathrm{Re_c} = 751$

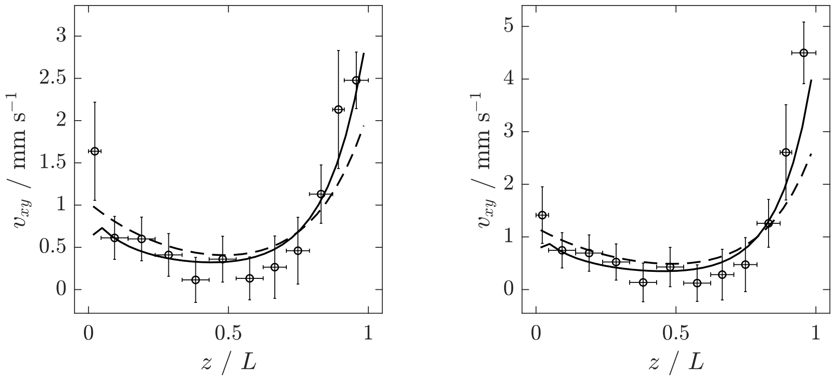

(e) $\mathrm{Re_c} = 1016$ (f) $\mathrm{Re_c} = 1251$

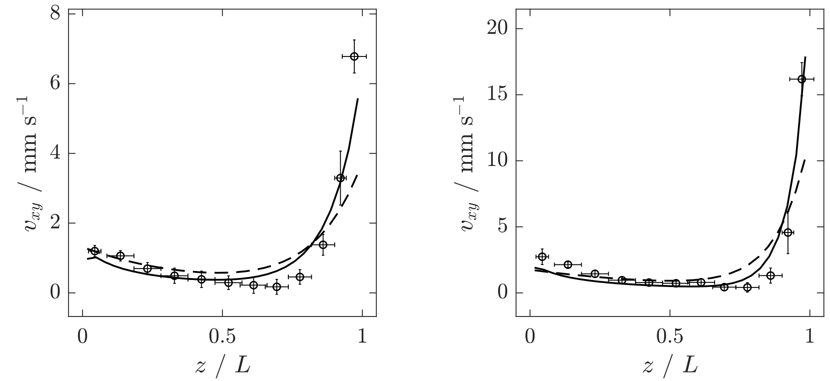

(g) $\mathrm{Re_c} = 1518$ (g) $\mathrm{Re_c} = 2972$

Fig. 6.10: Comparison of MRI measurements (markers), 1D model predictions (dotted lines, $n = 1$, model A) and 3D CFD predictions (solid lines) of through-wall velocities.

flow in a square duct, 1.377. The inlet channels show an increase in α from the front to the middle of the filter, with a largely uniform value in the centre, followed by a larger increase at the rear of the filter. As $\mathrm{Re_c}$ increases, the increase at the filter front occurs over a longer length and the increase at the filter rear is more pronounced. The outlet channels show a generally uniform profile across the filter length. The errors for the inlet and outlet channels are larger at the rear and front respectively due to the low absolute velocities in these regions.

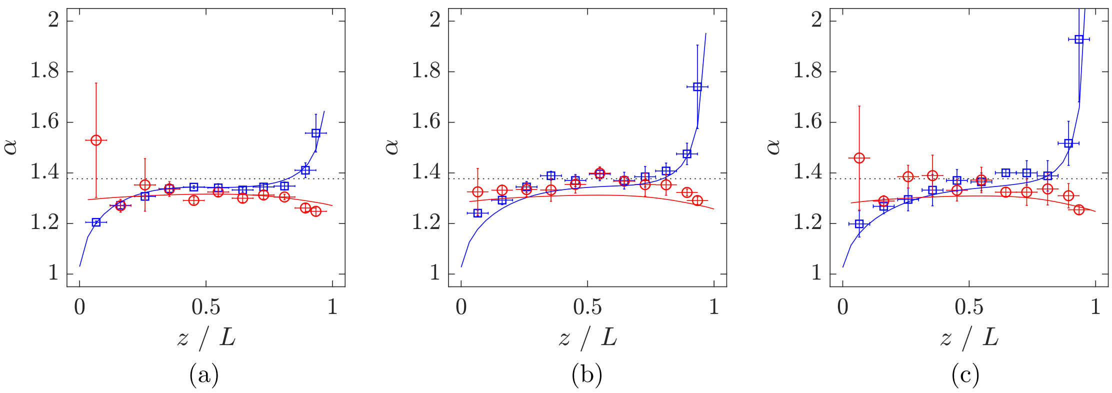

(a) (b) (c)

Fig. 6.11: Comparison of the momentum flux factor α calculated from MRI measurements (markers) and 3D CFD predictions (solid lines), resolved between the inlet (blue) and outlet (red) channels. Results are shown for $\mathrm{Re_c}$ = (a) 751, (b) 1016 and (c) 1251. The dotted horizontal line denotes $\alpha = 1.377$.

6.6.2 Three-dimensional model

Velocity profile predictions

The predictions of the three-dimensional CFD method described in Section 6.5.1 are shown by the solid lines in Fig. 6.9. The predictions agree well for $\mathrm{Re_c} = 102 - 1251$. The CFD predictions begin to deviate from the MRI measurements at $\mathrm{Re_c} = 1518$ and show little agreement at $\mathrm{Re_c} = 2972$. Similar behaviour is observed for the calculated through-wall velocities, shown in Fig. 6.10. As agreement was only seen in the range $\mathrm{Re_c} = 102 - 1251$, the data at higher Reynolds numbers was excluded from further analysis.

Variation of α and F

As with the MRI measurements, the spatial resolution of the 3D CFD predictions allows measurement of the cross-sectional flow profile and hence calculation of α. This was performed for $\mathrm{Re_c}$ = 751 - 1251 and the data are shown by the solid lines in Fig. 6.11. Good agreement is seen between the MRI and CFD values of α. The value of α in the centre region is slightly below the model value of 1.377.

As the 3D CFD prediction include both velocity and pressure fields, the wall friction factor F can also be estimated. This was performed for $\mathrm{Re_c}$ = 751 - 1251, which are shown in Fig. 6.12. All three flow rates show similar behaviour. In the inlet channels, the friction factor is initially very large and decreases to slightly under the model value of 28.48 around the middle of the filter before decreasing rapidly at the filter rear. The outlet channels show a smaller effect in the opposite direction. Both channels are approximately uniform in the centre of the filter, with the value of F lower than the model value.

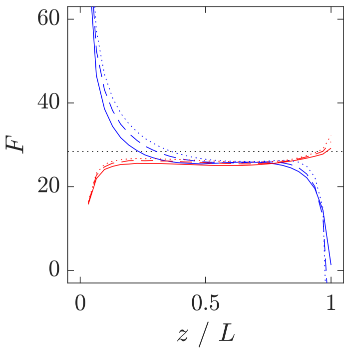

Fig. 6.12: Variation of F along the filter length for $\mathrm{Re_c} = 751$ (solid), 1016 (dashed) and 1251 (dotted), resolved between inlet (blue) and outlet (red) channels. The dotted horizontal line denotes $F = 28.48$.

Comparison with literature correlations

Figure 6.13 shows the calculated values of (a) α and (b) F plotted as a function of the local wall Reynolds number, $\mathrm{Re_w}$, resolved between the inlet and outlet channels. These are plotted with the correlations of Bissett *et al.* (Eqs. (6.12) to (6.15)) for comparison. For α (Fig. 6.13 (a)), the outlet channel correlation agrees with the CFD results within the valid region ($\mathrm{Re_w} < 3$) for all $\mathrm{Re_c}$. The inlet channel correlation agrees moderately well for data points corresponding to the rear half of the filter length, though there is a consistent overprediction. However, the data for the front half of the filter deviates strongly, showing the opposite trend to that expected from the correlation. For F (Fig. 6.13 (b)), similar effects are seen. The data from the second half of the filter show the same trends as the correlations for both inlet and outlet channels but are similarly overpredicted. The overprediction appears to increase at larger $\mathrm{Re_c}$. The data from the front half of the filter again deviate strongly and show the opposite trend to the correlations, though do not vary much with $\mathrm{Re_c}$.

6.6.3 One-dimensional model

Velocity profile predictions

The axial velocity predictions from the 1D model ($n = 1$, model A) are shown in Fig. 6.9 by the dashed lines. At low $\mathrm{Re_c}$, good agreement is observed with both the MRI data and the 3D CFD predictions. However, as $\mathrm{Re_c}$ increases, the agreement of the 1D model decreases and the the 'cross-over' point is predicted too far towards the filter front. The through-wall

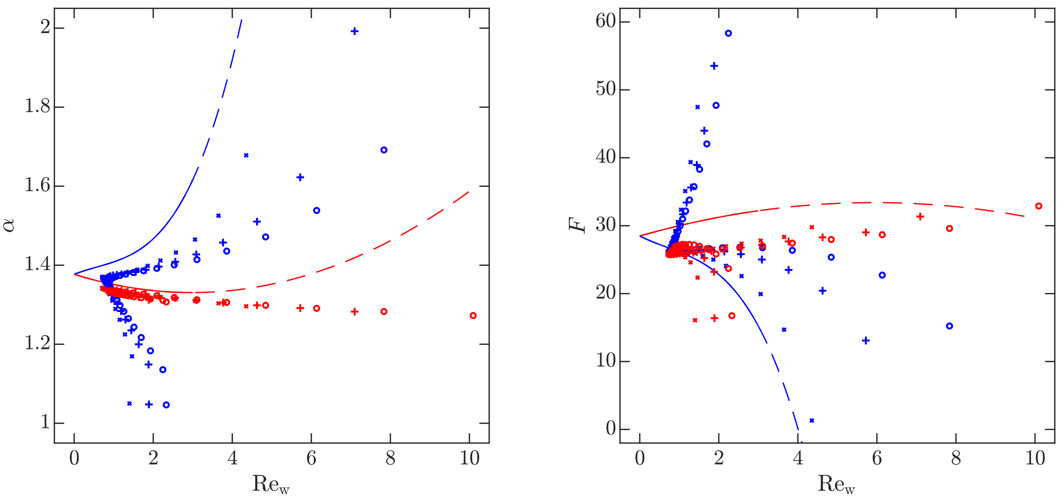

(a) (b)

Fig. 6.13: Comparison of (a) α and (b) F in the inlet (blue) and outlet (red) channels from the correlations of Bissett *et al.* (solid lines) and calculated from the 3D CFD data at $\mathrm{Re_c} = 751$ ($\times$), 1016 ($+$) and 1251 ($\circ$). The dashed lines indicate the correlation predictions outside the valid regime ($\mathrm{Re_w} > 3$).

velocity was also calculated and in similarly shown in Fig. 6.10. As with the axial velocities, agreement with the MRI data and 3D CFD predictions is good at lower $\mathrm{Re_c}$. At higher $\mathrm{Re_c}$, the agreement decreases as the 1D model overpredicts the through-wall velocity at the front of the filter and underpredicts it at the rear. To ensure that any differences between the 1D model and the MRI data were due to the formulation of the model and not inaccurate measurement of the gas velocity, the model predictions were fitted to the MRI data allowing variation of the superficial velocity. This was performed using non-linear least squares regression between the measured and predicted velocity profiles. The fitted superficial velocities agreed with the measured MRI values within error.

Sensitivity to parameters

To understand the effect of different model parameters on the predicted gas velocity, a sensitivity study was performed. In Fig. 6.14, the effects of (a) α, (b) F and (c) k on the (i) axial and (ii) through-wall velocity profile predictions are shown for $\mathrm{Re_c} = 751$. Each parameter was varied independently from the ‘default’ values given in Section 6.5.2 i.e. $\alpha = 1.377$, $F = 28.48$ and $k = 6 \times 10^{-13}\,\mathrm{m}^2$, shown by the solid lines. Model A was used with $n = 1$. Inspection of Fig. 6.14 (a) reveals that α controls the position of the ‘cross-over’ of the inlet and outlet channel velocities. A value of $\alpha = 0$ corresponds to symmetric profiles about $z/L = 0.5$, and increasing α moves the ‘cross-over’ towards the rear of the filter. This results in a skewness towards the rear of the filter in the through-wall velocity. In Fig. 6.14 (b), the effect of wall friction can better be seen. Under zero-friction conditions, the axial profile shape changes substantially and the through-wall velocity profile has no minimum as the only mechanism for pressure loss down the the channels is from momentum convection. Under higher friction conditions, there are more pressure losses at the front of the inlet and the rear of the outlet channels, causing more curvature in the axial velocity profiles and higher through-wall velocities at the front and rear of the filter. In Fig. 6.14 (c), the effect of different wall permeabilities can be seen. For low permeabilities, e.g. due to low porosity or high soot/washcoat loading, the axial profiles are linear and the through-wall velocity is near uniform across the filter length. For high permeabilities, the axial profiles are very non-linear and near-constant in the centre of the filter. The corresponding through-wall velocity profile is high at the front and rear and near-zero in the centre. These are exaggerated examples of the behaviour described in the chapter introduction.

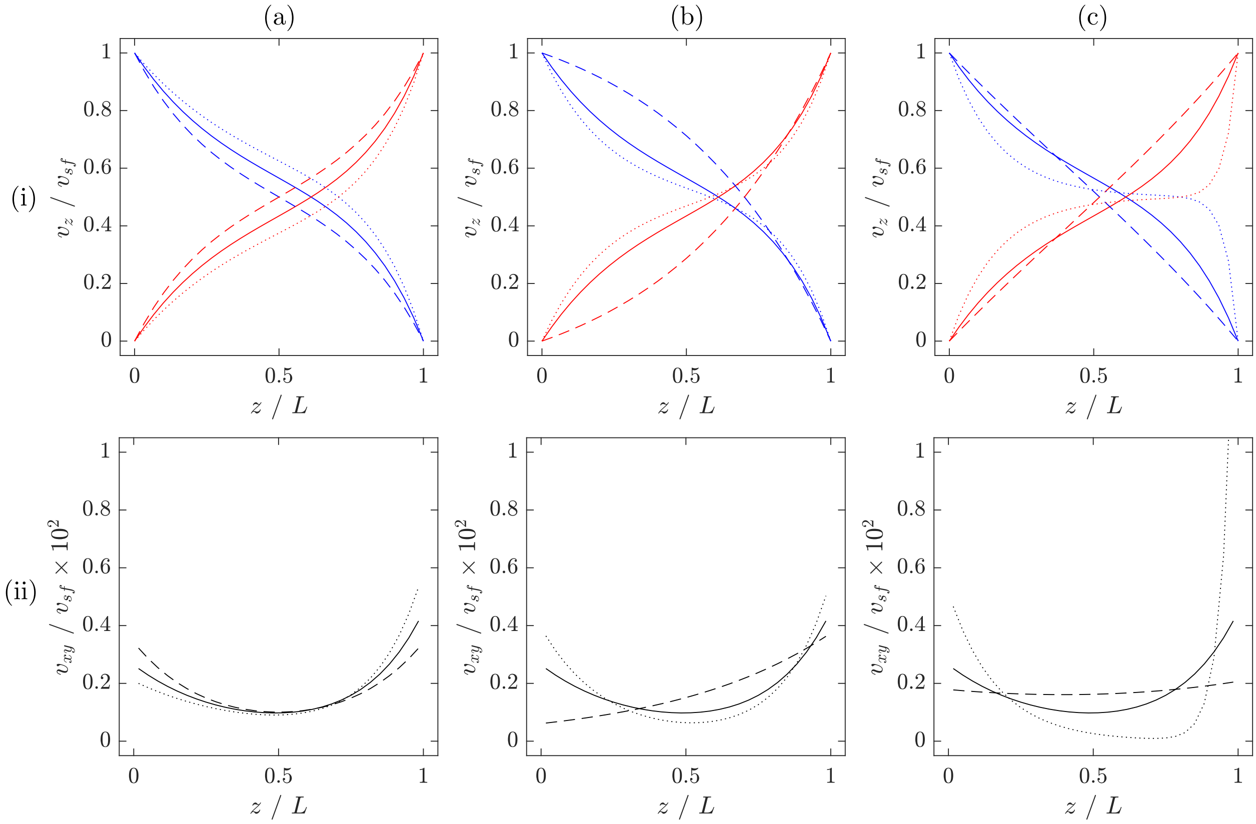

Fig. 6.14: Plots showing the sensitivity of the (i) axial and (ii) through-wall velocity profiles to the value of (a) α, (b) F and (c) k using model A and $n = 1$. The solid lines correspond to the 'default' values given in Section 6.5.2. In (a), α values of 0 (dashed lines) and 2.754 (dotted lines) were used. In (b), F values of 0 (dashed lines) and 56.96 (dotted lines) were used. In (c), k values of $6 \times 10^{-14}\,\mathrm{m}^2$ (dashed lines) and $6 \times 10^{-12}\,\mathrm{m}^2$ (dotted lines) were used.

Effects of literature developments

The effects of recent model developments, i.e. model B (correlation values of α and F) and $n = 1$ as described in Section 6.5.2, on the axial gas velocity predictions are shown in Fig. 6.15. The new model formulations were run for the superficial velocities corresponding to $\mathrm{Re_c} = 102$ - 1251 and the axial velocity prediction were compared to the MRI measurements. The effects of the different model developments on the velocity predictions for $\mathrm{Re_c} = 751$ are shown in Fig. 6.15. Both setting $n = 2$ (c,d) and using model B (b,d) move the 'cross-over' point toward the rear of the filter and improve agreement with the MRI data. When both are used (d), the predictions are almost coincident with the 3D CFD results.

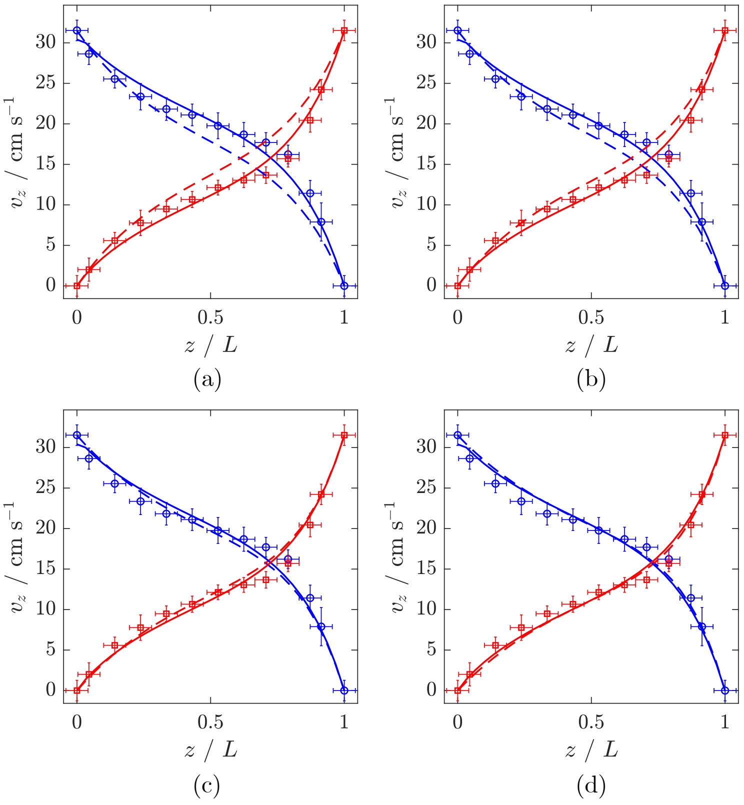

Fig. 6.15: Comparison of the inlet (blue) and outlet (red) channel axial velocity predictions for the different 1D model implementations (dashed lines) with the MRI (markers) and 3D CFD (solid lines) results for $\mathrm{Re_c} = 751$. (a) $n = 1$, model A. (b) $n = 1$, model B. (c) $n = 2$, model A. (d) $n = 2$, model B.

The weighted root mean squared error (RMSE) between the 1D model predictions and the MRI data was calculated for each model formulation using the formula,

$$\mathrm{RMSE} = \frac{1}{2}\left\|\frac{\mathbf{v}_{\mathrm{MRI}} - \mathbf{v}_{\mathrm{1D}}}{\sigma_{\mathrm{MRI}}}\right\|_2, \tag{6.23}$$

where $\mathbf{v}_{\mathrm{1D}}$ are the 1D model predicted velocity data, $\mathbf{v}_{\mathrm{MRI}}$ are the MRI measured velocity data and σ_{MRI} is the error in the velocity measurement. These data are shown in Fig. 6.16. For $\mathrm{Re_c} = 102$ - 751, the same trend is observed between the different models. The RMSE calculated for $n = 2$ are lower than for $n = 1$, and the RMSE calculated for model B are lower than for model A. Hence it appears that $n = 2$ and model B give improved predictions of the 1D model for these flow rates. However, for $\mathrm{Re_c} = 1016$ and 1251, the RMSE for model B is larger when $n = 2$ is used. For $\mathrm{Re_c} = 1251$, when using $n = 2$, also using model B increasse the RMSE compared with using model A, contrary to the trends seen at lower $\mathrm{Re_c}$. These anomalous behaviours are believed to be a result of the peak $\mathrm{Re_w}$ exceeding 3.5, hence the correlations are not valid across the whole filter length.

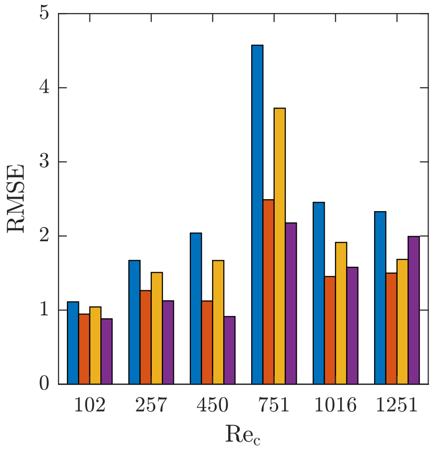

Fig. 6.16: Comparison of the root mean squared errors of the axial velocity predictions for different 1D model implementations. (🟦) $n = 1$, model A. (🟧) $n = 1$, model B. (🟨) $n = 2$, model A. (🟪) $n = 2$, model B.

6.6.4 Impact on filtration efficiency

The filtration efficiency for filters with $\mathrm{Re_c} = 102$ - 1251 are shown in Fig. 6.17. As the gas flow rate increases, the through-wall velocity increases predominately at the rear of the filter and so the filtration efficiency of particles with diameters 0.1 µm to 1 µm decreases quickest in this region.

The number deposition profiles are shown in Fig. 6.18. At low flow rates (a), most particles are deposited at the front and rear of the filter due to their higher number flux, with relatively few filtered in the centre. As the flow rate increases, fewer particles are filtered at the front and most particles are filtered in the final fifth of the filter.

The total filtration efficiency was calculated as the ratio of filtered particles, found by integrating over the profiles in Fig. 6.18, and the total number of particles for all flow rates; this is shown in Fig. 6.19. The filtration efficiency is predicted to decrease with increasing $\mathrm{Re_c}$ and hence gas flow rate.

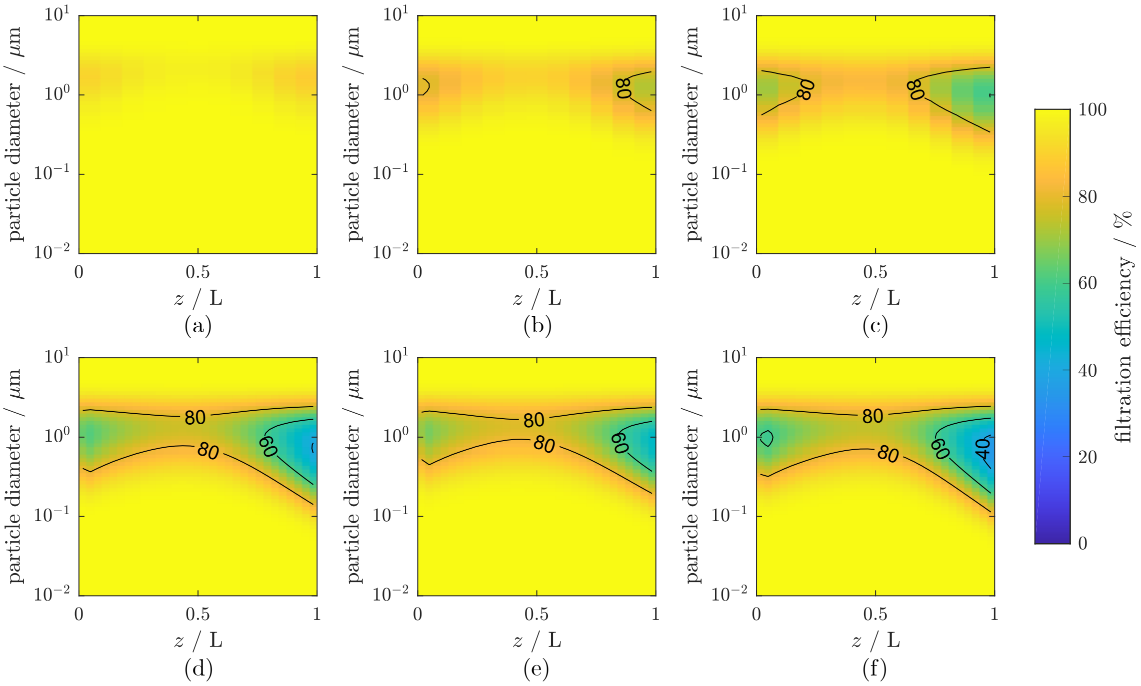

Fig. 6.17: Filtration efficiency as a function of PM diameter and axial position for $\mathrm{Re_c}$ = (a) 102, (b) 257, (c) 450, (d) 751, (e) 1016 and (f) 1251.

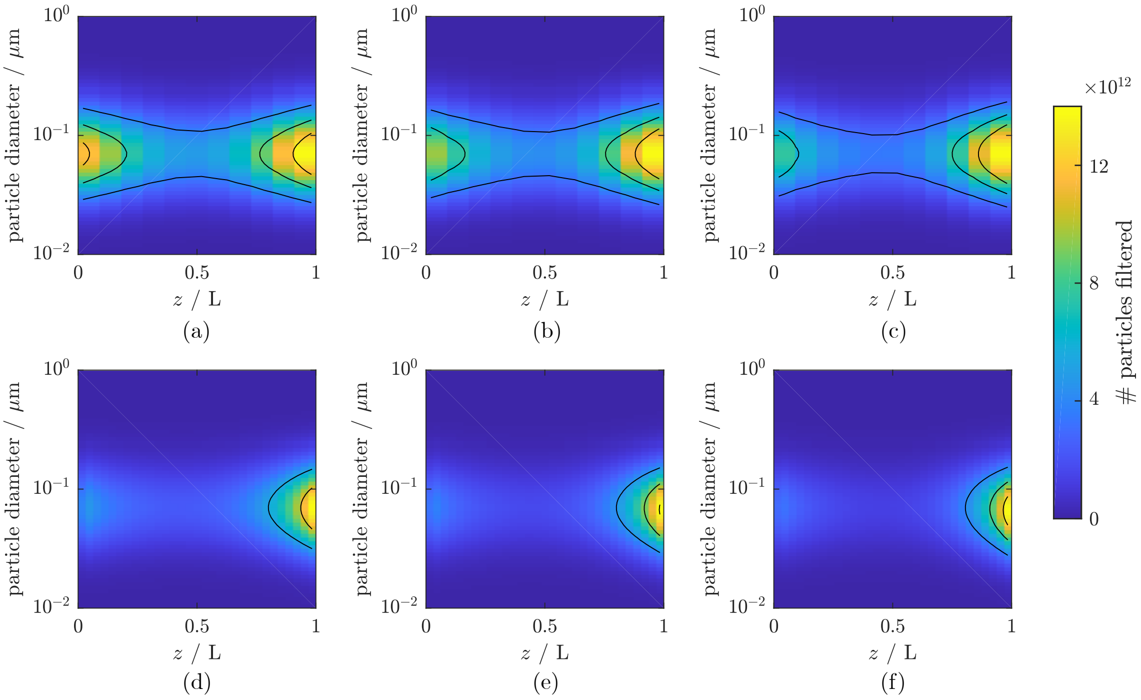

Fig. 6.18: Number of particles filtered as a function of PM diameter and axial position for $\mathrm{Re_c}$ = (a) 102, (b) 257, (c) 450, (d) 751, (e) 1016 and (f) 1251. Contours indicate values of 4, 8 and 12 $\times 10^{12}$.

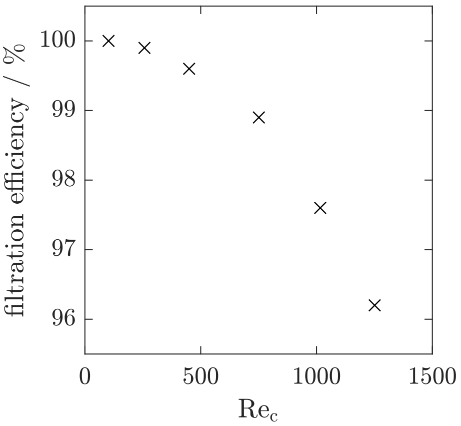

Fig. 6.19: Variation of total filtration efficiency with channel Reynolds number.

6.7 Discussion

The results presented in Section 6.6 are now discussed in three main sections. First, the results of the experimental and numerical methods are discussed by themselves. Second, the agreement between the numerical and the experimental results are explored in the context of the model formulations and values of parameters used. Finally, the effects on the filtration behaviour are briefly touched on.

The inlet and outlet channel axial velocities measured using MRI (Fig. 6.9) show non-linear decreases and increases respectively with axial position, consistent with the flow behaviour expected from previous work [1, 2, 14, 18, 34, 39]. This non-linearity creates the non-uniform through-wall velocity profiles also observed with MRI (Fig. 6.10). From the sensitivity study performed with the 1D model (Fig. 6.14), the origins of these features can be understood. The wall friction creates pressure losses proportional to the local gas velocity and causes gas to preferentially pass through the porous wall where the axial velocitiy is low in one of the channels, i.e. at the front or rear of the filter. The momentum convection term moves the 'cross-over' point towards the rear of the filter and creates the asymmetry seen in the velocity profiles at high flow rates. The permeability reflects the resistance to flow in the porous wall and affects the uniformity of the through-wall velocity along the filter.

The values of α calculated from the MRI data (Fig. 6.11) show how the cross-sectional flow profile changes along the filter length. The variation in measurements between channels are large at the front of the outlet channels and the rear of the inlet channels due to the low absolute velocity and hence high relative error in these regions. α is anticipated to take values of 1.377 for fully developed laminar flow (in a square duct with non-porous walls) and 1 for plug flow. The increase in α seen at the front of the inlet channel is consistent with the transition from a flat flow profile to developed laminar flow. This entry length appears to vary between around one-quarter to one-third (36 mm to 50 mm) the length of the filter. This agrees with common correlations for the length of entrance effects in a pipe [47, 48], which predict laminar entrance lengths in the range 14 mm to 50 mm for $\mathrm{Re_c} = 1000$. The sharp increase in α at the rear of the inlet channels is attributed to the large through-wall velocity in this region [28, 29]. The outlet channel values of α show less variation and appear near-constant around the model laminar value of 1.377. This is expected as the gas is stationary at the front of the outlet channels and the velocity slowly increases, so flow is always fully developed. As it is not yet feasible to make spatially resolved pressure measurements inside a filter without perturbing the gas flow, it is not possible to estimate values of F using the current MRI data. However, improvements to image resolution may allow F to be estimated from the gas shear rate at the wall in future.

The velocity predictions of the 3D CFD code agree well with the MRI measurements for $\mathrm{Re_c} = 102$ - 1251 (Figs. 6.9 and 6.10). At $\mathrm{Re_c} = 2972$, the predictions deviate significantly from the MRI results. This is attributed to the effects of turbulence in the channels. The values of α calculated from the CFD data also agree well with those from the MRI data (Fig. 6.11), further validating the CFD approach and confirming that the use of a uniform velocity boundary condition at the inlet was appropriate. The CFD values demonstrate more clearly the trends observed in the MRI values of α. The calculated values of F show a similar dependence on both flow development and local through-wall velocity (Fig. 6.12). These trends are expected to be somewhat contrary as a flat flow profile (smaller α) will have a larger shear rate at the wall than a fully developed profile (larger α).

The calculated values of α and F from the CFD data allowed comparison with the correlations of Bissett *et al.* [28]. From Fig. 6.13, the correlations predict the opposite behaviour of both α and F at the front of the inlet channels with increasing $\mathrm{Re_w}$. This is believed to be because the methods used by Bissett *et al.* and Kostoglou *et al.* [28, 29] assumed fully developed laminar flow, which is not observed in the first third of the filter length presently. The general behaviour of the correlations agrees with the observations from the MRI and 3D CFD results, although there appears to be some dependence on $\mathrm{Re_c}$ that is not captured by the correlations. There appears to be no evidence from the 3D CFD results that F will become negatively valued, as was predicted by Bissett *et al.* and Kostoglou *et al.*. One observation of note is that the extrapolated CFD values of α and F at $\mathrm{Re_w} = 0$ appear to be lower than those of the correlations. This is thought to be due to differences in boundary conditions at the wall interface: Bissett *et al.* and Kostoglou *et al.* used no-slip conditions ($v_z = 0$) at the wall surface, whereas the CFD used here allows for wall-slip. It is probable that future CFD work on a smaller scale and based on the filter microstructure, i.e. those by Koci *et al.* [17], could inform the appropriate boundary conditions for the wall surface.

At low flow rates ($\mathrm{Re_c} < 500$), the 1D model predictions agree well with the MRI results (Figs. 6.9 and 6.10), but the predictions deviate at higher flow rates. The main disagreement is the ‘cross-over’ point, which is primarily controlled by the momentum convection term. From Figs. 6.15 and 6.16, it appears that the new derivation of Watling *et al.* ($n = 1$) understates the momentum convection term. However, use of Bissett’s term

($n = 2$) still shows some deviation from the MRI results. This is attributed to the behaviour of α and F in the model. For the predictions shown in Figs. 6.9 and 6.10, the two factors are taken as constants (model A) whereas the 3D CFD results show that these are expected to vary along the filter length. This is in direct opposition to the original assumption that the through-wall velocity has negligible effect on the axial channel flows [21]. Despite the disagreement with the 3D CFD behaviour of α and F, inclusion of the correlations of Bissett *et al.* in the 1D model (model B) improves the agreement with the MRI results and gives near-coincident predictions with the 3D CFD. Hence, the 1D model allows the axial velocity profiles to be predicted to the same accuracy as the CFD code in a small fraction of the computation time (under 1 s compared to 8 h).

One problem Bissett *et al.* [28] and Kostoglou *et al.* [29] encountered was predictions of reverse flow in the inlet channels for $\mathrm{Re_w} > 2.8$, which they rejected as non-physical behaviour. However, the MRI and CFD results in this chapter show evidence of reverse axial flow at the end of the inlet channels (Fig. 6.20), suggesting that reverse flow features are physical under some conditions. This is consistent with the reverse flow seen in Fig. 4.14. Such effects are not seen for larger $\mathrm{Re_w}$ at the front of the inlet channels, possibly because either the effects of undeveloped flow inhibit these features or the presence of the plugs at the filter rear encourages them.

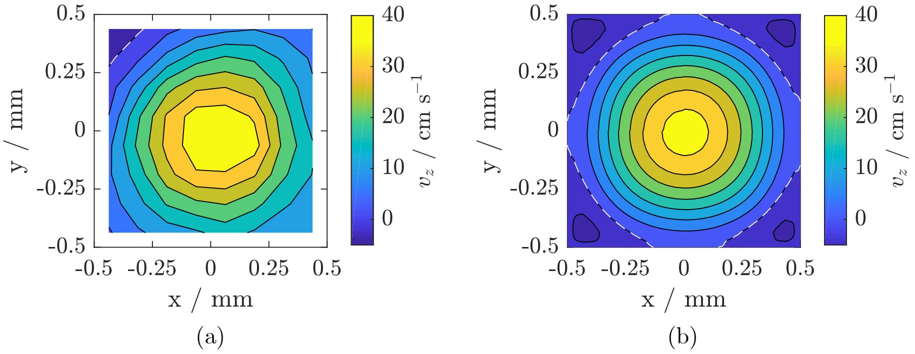

(a)
(b)

Fig. 6.20: Inlet channel axial velocity flow profiles showing reverse flow from (a) MRI and (b) CFD data for $\mathrm{Re_c} = 1251$ at $z/L = 0.914$., corresponding to a local $\mathrm{Re_w}$ of 6.0. The white dashed line indicates the contour of $v_z = 0$. Due to the resolution of the MRI method, the edges of the channels were not completely resolved.

One parameter that has not been discussed much in the literature is the wall permeability. The permeability is often a fitted value used to improve agreement between the measured and predicted pressure drop, rather than being independently calculated. Konstandopoulos *et al.* [33] proposed that permeabilities in the range $1 \times 10^{-13}\,\mathrm{m^2}$ to $1 \times 10^{-12}\,\mathrm{m^2}$ are representative of real-world DPFs, and has also shown the gas velocity profiles vary depending on the permeability [1]. Accurate measurement of the permeability, and the inertial permeability if the Forchheimer extension is used, require correct modelling of all pressure drop contributions. As discussed in Chapter 4, the entrance and exit effects are particularly difficult to model and may lead to inaccurate measurements of the permeability and hence poor prediction of the gas hydrodynamics. However, including gas velocity measurements in the fitting process, or other methods of estimation [17], may increase the accuracy of the wall permeability value and permit better empirical estimation of the entrance and exit effects. This will still require the correct modelling of the gas flow in order to not under or overestimate the permeability as the effects of α and F on the gas flow fields are not orthogonal to those of k (Fig. 6.14). One additional effect that may need to be accounted for in the application of these models to real-world filters in the dependence of the permeability on temperature. As temperature increases, the wall-slip of gas inside the porous walls increases and the permeability increases [16].

As discussed previously, the internal gas hydrodynamics also influence the filtration behaviour of the filter. In Section 6.6.4, an analytical model was used to observe the changes in filtration efficiency as the gas flow rate increases, resolved as functions of both axial position and PM diameter (Fig. 6.17). In terms of PM size, the greatest effect is seen for particles with diameter $\sim$1 µm; larger particles are deposited through interception, which is independent of the velocity, whilst smaller particles have large Stokes numbers and hence are affected little by velocity changes on this scale (Fig. 6.6). In terms of the axial position, the greatest velocity change is observed at the rear of the filter and so the greatest reduction in filtration efficiency is also observed. Using a representative particle number distribution allowed the number of filtered particles to be simulated across the filter length for different flow rates (Fig. 6.18). The modal particle diameter is well below 1 µm and so the filtration efficiency is largely unaffected at the present flow rates. Hence the flux of PM thorugh the wall, i.e. the gas through-wall velocity, is the greatest contributor to non-uniform filtration in these simulations. The total filtration efficiency still decreases with increasing flow rate due to the decrease in filtration efficiency as the local through-wall velocity increases. While this treatment is useful to qualitatively understand the effects of gas flow rate on filtration behaviour, it doesn't consider both any inertial effects, where particles deviate from the gas streamlines in the channels [2, 3], or unusual flow patterns not captured in the through-wall velocity, such as streamline separation at the front end of the filter [18].

6.8 Conclusions

Magnetic resonance velocity imaging has been used to measure both the axial and through-wall gas velocity along the length of a DPF sample at a range of gas flow rates ($\mathrm{Re_c}$ = 751 - 2972). Velocity encoded images were acquired along the filter length using compressed sensing at an isotropic spatial resolution of 140 µm px^{-1} with an acquisition time of 14 min, allowing measurement of the axial component of the gas velocity. These data then allowed the calculation of the transverse through-wall velocity. As the flow rate increased, the change in inlet and outlet channel velocities became more non-linear across the filter length, with the point at which they 'cross-over' moving toward the rear of the filter. This corresponded to a greater increase in the through-wall velocity at the rear of the filter and increased non-uniformity in the through-wall velocity profiles. These data were used as an input for an analytical filtration model, allowing the effect of increasing flow rate on the filtration of different diameter particles to be predicted. The spatial resolution of the MRI data allowed calculation of the momentum convection correction factor, α, which accounts for non-uniform flow profiles in the momentum equations of 1D numerical models. The value of α was observed to vary both between the inlet and outlet channels, and with both axial position and the local through-wall velocity.

3D CFD simulations of gas flow in a filter geometry were made in around 8 h per simulation. The calculated axial channel and through-wall velocity profiles agreed well with the MRI measurements for Re_c = 102 - 1251, allowing the CFD method to be used as a probe of the gas hydrodynamics in this range of flow rates. As the simulations returned both the gas velocity and pressure fields, it permitted both the momentum convection correction factor, α, and the wall friction factor, F, to be estimated. Both factors varied along the length of the filter, with different levels of variation in the inlet and outlet channels. The values of α agreed well with values calculated from the MRI data (Fig. 6.11). Most variation in both factors was seen in the inlet channel (Figs. 6.11 and 6.12) and was attributed to two causes. First, the effects of flow development at the front of the channel, where the initial flat flow profile develops into the expected parabolic flow profile; this gives a low value of α and a large value of F in this region due to the uniform flow profile and high wall shear rate. Second, the effects of high through-wall velocity at the rear of the filter is expected to cause an increase in α and a decrease in F. These calculations allowed comparison with the correlations of Bissett *et al.* [28]. While reasonable agreement was seen for the outlet channels, large deviations were observed for the values at the front of the inlet channels. This was attributed to the failure of the correlations to account for flow profile development at the filter front.

A contemporary 1D model was used to predict the axial channel and through-wall velocity profiles. The model required under 1 s to compute. Good agreement with both the MRI and 3D CFD results was seen at low flow rates, but agreement decreased as the flow rate increased. The disagreement was explored in the context of recent developments in the 1D modelling literature. First, the new derivation of the gas momentum convection term by Watling *et al.* [5] was found to worsen agreement between the 1D model and the MRI measurements. Second, inclusion of correlations to account for the variation of α and F with Re_w was found to improve agreement with the MRI measurements. This improvement is in spite of the discrepancies observed between the 3D CFD data and the correlations (Fig. 6.13), and hence it is thought that the effects of the through-wall velocity are more significant than flow development on the flow profile shape and wall friction inside filter channels.

An analytical filtration model was used to predict the filtration efficiency and number of particles filtered in a DPF as a function of filter axial position and particle diameter. The regions of highest through-wall gas velocity, i.e. the filter front and rear, showed reduced filtration efficiencies for particles with diameters ∼1 µm. However, for a representative particle number distribution, the highest deposition occurred in regions of the highest gas and hence PM flux through the filter wall. As the flow rate increased, this occurred mostly at the very rear of the filter.

6.9 References

[1] A. G. Konstandopoulos, J. H. Johnson. Wall-flow diesel particulate filters-their pressure drop and collection efficiency. *SAE Technical Paper Series* (1989) 890405. doi:10.4271/890405.

[2] S. Bensaid, D. Marchisio, D. Fino, G. Saracco, V. Specchia. Modelling of diesel particulate filtration in wall-flow traps. *Chemical Engineering Journal* (2009) 154 (1-3), 211–218.

[3] S. Bensaid, D. L. Marchisio, D. Fino. Numerical simulation of soot filtration and combustion within diesel particulate filters. *Chemical Engineering Science* (2010) 65 (1), 357–363. doi:10.1016/j.ces.2009.06.051.

[4] M. Masoudi. Hydrodynamics of Diesel Particulate Filters. *SAE Technical Paper Series* (2002) 2002-01-1016. doi:10.4271/2002-01-1016.

[5] T. Watling, M. Ravenscroft, J. Cleeton, I. Rees, D. Wilkins. Development of a Particulate Filter Model for the Prediction of Backpressure: Improved Momentum Balance and Entrance and Exit Effect Equations. *SAE International Journal of Engines* (2017) 10 (4), 1765–1794. doi:10.4271/2017-01-0974.

[6] I. Koptyug, S. Altobelli, E. Fukushima, A. Matveev, R. Sagdeev. Thermally polarized 1H NMR microimaging studies of liquid and gas flow in monolithic catalysts. *Journal of Magnetic Resonance* (2000) 147 (1), 36–42. doi:10.1006/jmre.2000.2186.

[7] A. Sederman, M. Mantle, L. Gladden. Quantitative 'real-time' imaging of multi-phase flow in ceramic monoliths. *Magnetic Resonance Imaging* (2003) 21 (3-4), 359–361. doi:10.1016/S0730-725X(03)00138-3.

[8] A. J. Sederman, J. J. Heras, M. D. Mantle, L. F. Gladden. MRI strategies for characterising two-phase flow in parallel channel ceramic monoliths. *Catalysis Today* (2007) 128 (1-2), 3–12. doi:10.1016/j.cattod.2007.04.012.

[9] B. Newling, C. C. Poirier, Y. Zhi, J. A. Rioux, A. J. Coristine, D. Roach, B. J. Balcom. Velocity imaging of highly turbulent gas flow. *Physical Review Letters* (2004) 93 (15), 154503. doi:10.1103/PhysRevLett.93.154503.

[10] D. J. Robbins, M. S. El-Bachir, L. F. Gladden, R. S. Cant, E. von Harbou. CFD modeling of single-phase flow in a packed bed with MRI validation. *AIChE Journal* (2012) 58 (12), 3904–3915. doi:10.1002/aic.13767.

[11] P. R. Gunjal, V. V. Ranade, R. V. Chaudhari. Computational study of a single-phase flow in packed beds of spheres. *AIChE Journal* (2005) 51 (2), 365–378. doi:10.1002/aic.10314.

[12] C. Boyce, J. Davidson, D. Holland, S. Scott, J. Dennis. The origin of pressure oscillations in slugging fluidized beds: Comparison of experimental results from magnetic resonance imaging with a discrete element model. *Chemical Engineering Science* (2014) 116, 611–622. doi:10.1016/J.CES.2014.05.041.

[13] I. Koptyug, S. Kabanikhin, K. Iskakov, V. Fenelonov, L. Khitrina, R. Sagdeev, V. Parmon. A quantitative NMR imaging study of mass transport in porous solids during drying. *Chemical Engineering Science* (2000) 55 (9), 1559–1571. doi:10.1016/S0009-2509(99)00404-2.

[14] N. P. Ramskill, A. P. York, A. J. Sederman, L. F. Gladden. Magnetic resonance velocity imaging of gas flow in a diesel particulate filter. *Chemical Engineering Science* (2017) 158, 490–499. doi:10.1016/j.ces.2016.10.017.

[15] B. R. Munson, P. M. Gerhart, A. L. Gerhart, J. I. Hochstein, D. F. Young, T. H. Okiishi. *Munson, Young, and Okiishi's Fundamentals of Fluid Mechanics.* 6th edition (2015).

[16] S. Aleksandrova, J. Saul, H. Medina, O. Garcia-Afonso, C. Lin, J. M. Herreros, M. Bevan, S. F. Benjamin. Gasoline Particulate Filter Wall Permeability Testing. *SAE International Journal of Engines* (2018) 11 (5), 571–584. doi:10.4271/03-11-05-0039.

[17] P. Kočí, M. Isoz, M. Plachá, A. Arvajová, M. Václavík, M. Svoboda, E. Price, V. Novák, D. Thompsett. 3D reconstruction and pore-scale modeling of coated catalytic filters for automotive exhaust gas aftertreatment. *Catalysis Today* (2019) 320, 165–174. doi:10.1016/J.CATTOD.2017.12.025.

[18] F. Sbrizzai, P. Faraldi, A. Soldati. Appraisal of three-dimensional numerical simulation for sub-micron particle deposition in a micro-porous ceramic filter. *Chemical Engineering Science* (2005) 60 (23), 6551–6563. doi:10.1016/j.ces.2005.05.038.

[19] G. Koltsakis, O. Haralampous, C. Depcik, J. C. Ragone. Catalyzed diesel particulate filter modeling. *Reviews in Chemical Engineering* (2013) 29 (1), 1–61. doi:10.1515/revce-2012-0008.

[20] S. Yang, C. Deng, Y. Gao, Y. He. Diesel particulate filter design simulation: A review. *Advances in Mechanical Engineering* (2016) 8 (3), 1–14. doi:10.1177/1687814016637328.

[21] E. J. Bissett. Mathematical model of the thermal regeneration of a wall-flow monolith diesel particulate filter. *Chemical Engineering Science* (1984) 39 (7-8), 1233–1244. doi:10.1016/0009-2509(84)85084-8.

[22] A. G. Konstandopoulos, M. Kostoglou, E. Skaperdas, E. Papaioannou, D. Zarvalis, E. Kladopoulou. Fundamental Studies of Diesel Particulate Filters: Transient Loading, Regeneration and Aging (2000) 2000-01-1016. doi:10.4271/2000-01-1016.

[23] B. J. Peters. Numerical simulation of a diesel particulate filter during loading and regeneration. In *American Society of Mechanical Engineers, Internal Combustion Engine Division (Publication) ICE*, volume 40. ASME (2003) pp. 619–630. doi: papers://B3F20CA2-9ACD-4BA1-A510-19A2EC38FE78/Paper/p542.

[24] A. G. Konstandopoulos, M. Kostoglou. Reciprocating flow regeneration of soot filters. *Combustion and Flame* (2000) 121 (3), 488–500. doi:10.1016/S0010-2180(99)00156-X.

[25] A. P. York, T. C. Watling, M. Ahmadinejad, D. Bergeal, P. R. Phillips, D. Swallow. Modeling the Emissions Control Performance of a Catalyzed Diesel Particulate Filter (CDPF) System for Light Duty Diesel Applications. *SAE International Journal of Fuels and Lubricants* (2009) 2 (1), 2009–01–1266. doi:10.4271/2009-01-1266.

[26] T. C. Watling, M. R. Ravenscroft, G. Avery. Development, validation and application of a model for an SCR catalyst coated diesel particulate filter. *Catalysis Today* (2012) 188 (1), 32–41. doi:10.1016/j.cattod.2012.02.007.

[27] L. Oxarango, P. Schmitz, M. Quintard. Laminar flow in channels with wall suction or injection: a new model to study multi-channel filtration systems. *Chemical Engineering Science* (2004) 59 (5), 1039–1051. doi:10.1016/J.CES.2003.10.027.

[28] E. J. Bissett, M. Kostoglou, A. G. Konstandopoulos. Frictional and heat transfer characteristics of flow in square porous tubes of wall-flow monoliths. *Chemical Engineering Science* (2012) 84, 255–265. doi:10.1016/J.CES.2012.08.012.

[29] M. Kostoglou, E. J. Bissett, A. G. Konstandopoulos. Improved Transfer Coefficients for Wall-Flow Monolithic Catalytic Reactors: Energy and Momentum Transport. *Industrial & Engineering Chemistry Research* (2012) 51 (40), 13062–13072. doi: 10.1021/ie3011098.

[30] W. Wang, E. J. Bissett. Frictional and Heat Transfer Characteristics of Flow in Triangle and Hexagon Channels of Wall-Flow Monoliths. *Emission Control Science and Technology* (2018) 4 (3), 198–218. doi:10.1007/s40825-018-0093-7.

[31] G. Koltsakis, O. Haralampous, N. Margaritis, Z. Samaras, C.-D. Vogt, E. Ohara, Y. Watanabe, T. Mizutani. 3-dimensional modeling of the regeneration in SiC particulate filters. *SAE Technical Paper Series* (2005) 2005-01-0953. doi:10.4271/2005-01-0953.

[32] C. Hinterberger, M. Olesen, R. Kaiser. 3D Simulation of Soot Loading and Regeneration of Diesel Particulate Filter Systems. *SAE Technical Paper Series* (2007) 2007-01-1143. doi:10.4271/2007-01-1143.

[33] A. G. Konstandopoulos, E. Skaperdas, M. Masoudi. Inertial Contributions to the Pressure Drop of Diesel Particulate Filters. *SAE Technical Paper Series* (2001) 2001-01-09. doi:10.4271/2001-01-0909.

[34] Z. G. Liu, R. K. Miller. Flow Distributions and Pressure Drops of Wall-Flow Diesel Particulate Filters. *SAE Technical Paper Series* (2002) 2002-01-1311. doi:10.4271/

2002-01-1311.

[35] H. Lee, K. O. Lee. Multi-layered mesh generation and user subroutine development based on an Eulerian–Eulerian approach for soot filtration visualization in a three-dimensional particulate filter model. *International Journal of Engine Research* (2014) 15 (8), 980–992. doi:10.1177/1468087414543707.

[36] V. Di Sarli, A. Di Benedetto. Modeling and simulation of soot combustion dynamics in a catalytic diesel particulate filter. *Chemical Engineering Science* (2015) 137, 69–78. doi:10.1016/J.CES.2015.06.011.

[37] V. Di Sarli, A. Di Benedetto. Combined effects of soot load and catalyst activity on the regeneration dynamics of catalytic diesel particulate filters. *AIChE Journal* (2018) 64 (5), 1714–1722. doi:10.1002/aic.16047.

[38] M. Schejbal, M. Marek, M. Kubíček, P. Kočí. Modelling of diesel filters for particulates removal. *Chemical Engineering Journal* (2009) 154 (1-3), 219–230. doi:10.1016/j.cej.2009.04.056.

[39] A. G. Konstandopoulos, E. Skaperdas, J. Warren, R. Allansson. Optimized Filter Design and Selection Criteria for Continuously Regenerating Diesel Particulate Traps. *SAE Technical Paper Series* (1999) 1999-01-04. doi:10.4271/1999-01-0468.

[40] N. P. Ramskill. *Magnetic Resonance Studies of Diesel Particulate Filters.* Doctoral thesis, University of Cambridge (2015).

[41] C. T. Lao, J. Akroyd, N. Eaves, M. Kraft. Modelling of secondary particulate emissions during the regeneration of Diesel Particulate Filters. *Energy Procedia* (2017) 142, 3560–3565. doi:10.1016/j.egypro.2017.12.245.

[42] M. Spiga, G. Morino. A symmetric solution for velocity profile in laminar flow through rectangular ducts. *International Communications in Heat and Mass Transfer* (1994) 21 (4), 469–475. doi:10.1016/0735-1933(94)90046-9.

[43] R. K. Shah, A. L. London. *Laminar flow forced convection in ducts: a source book for compact heat exchanger analytical data.* Academic Press (1978).

[44] D. E. Hall, C. J. Dickens. Measurement of the Number and Size Distribution of Particles Emitted from a Gasoline Direct Injection Vehicle. *SAE Technical Paper Series* (1999) 1999-01-3530.

[45] C. Real, O. Armas, R. Ballesteros, A. Gomez, a. Gómez. The effect of diesel engine operating conditions on exhaust particle size distributions. *Proceedings of the Institution of Mechanical Engineers, Part D: Journal of Automobile Engineering* (2008) 222 (8), 1513–1525. doi:10.1243/09544070JAUTO747.

[46] Dilo Gmbh. Dilo SF_6 apps (2011). [Online; accessed 11 October 2018].

[47] Y. A. Cengel, J. M. Cimbala. *Fluid mechanics: fundamentals and applications.* McGraw-Hill Higher Education (2006).

[48] T. L. Bergman, F. P. Incropera. *Fundamentals of heat and mass transfer.* 7th edition.

Wiley, Hoboken NJ (2011).

Chapter 7

Structure-transport changes in washcoated GPFs

7.1 Introduction

As noted in Chapter 1, the emissions profiles of diesel and gasoline engines differ due to the difference in engine operation and fuel composition. The result of this is that while the general principles of emission control technologies are transferable between diesel and gasoline vehicles, the latter will require different filter structures, operating conditions and washcoat application in order to achieve optimum function.

In addition to removing gaseous pollutants, catalytic washcoats are important for the filtration efficiency of GPFs. Due to the lower concentration of PM in gasoline exhausts compared to diesel exhausts, bare GPFs have a low initial filtration efficiency and require some level of soot loading before the efficiency increases to acceptable levels [1]. Problems may be encountered in keeping the soot loading at an optimum level due to passive regeneration in GPFs. This need for a base level of soot loading can be circumvented by using a washcoat on the filter. Washcoats reduce the pore space in the filter walls in a similar manner to captured PM and increase the filtration efficiency even at low soot loadings. However, suboptimal washcoat distribution can result in increased pressure drop and poor chemical conversion. Filters made from materials with high porosities ($< 60\%$) are sometimes used to negate the backpressure penalty of washcoat application [2]. As such, it is important to understand the relationship between the washcoating procedure, the washcoat distribution and the effect on gas transport within the filter.

This study aims to investigate the relationship between the structural and transport changes in GPFs with different washcoats applied. This is achieved by using a combination of traditional methods, MRI measurements and numerical modelling.

7.1.1 Washcoating materials and strategies

Catalysts are typically applied to monoliths on a support material, such as alumina (Al_2O_3), titania (TiO_2), vanadia (V_2O_5) and ceria (CeO_2). Supports typically perform multiple roles: to securely attach the catalyst to the substrate, to increase the surface area available for catalysis to occur on, and to ensure stability of the catalyst metal at elevated temperatures (i.e. to avoid unwanted sintering). Supports and catalysts are generally applied to monoliths by imbibing a liquid washcoat into the monolith. The washcoat is typically formulated as a slurry, with the solid support and catalyst in suspension, so that the solids can be deposited by removing the solvent. Evaporation is commonly used to achieve this, though sol-gel and precipitation-deposition methods also exist [3]. The nature of the liquid removal can greatly influence the deposition of the catalyst [4]. Processes such as microwave or freeze drying produce highly uniform deposition at a much higher temporal and energetic expense.

Historically, there have many different processes used to apply liquid washcoats to both flow-through and filter geometries. Such processes include: spraying washcoat into individual channels with multiple probes; soaking one end of the substrate in liquid, inverting and allowing the liquid to drain through; dipping the entire substrate into liquid and removing the excess through dripping or blowing air through the channels. However, many of these processes suffer from mechanical difficulties, loss of expensive catalyst material or lack of control over washcoat distribution [5]. The desired distribution is often a uniform coverage of washcoat along the entire length of the filter, either only in one or split between both of the channels. Illustrations of potential maldistributions of washcoat applied to both channels are shown in Fig. 7.1. However, these are not exhaustive and combinations of the maldistributions may occur. In addition to wastage of expensive materials, these can result in poor pressure drop, filtration and catalysis behaviour during operation. As such, it is imperative to both understand both this process and the effects of the washcoat distribution in order to optimise the performance of catalysed particulate filters.

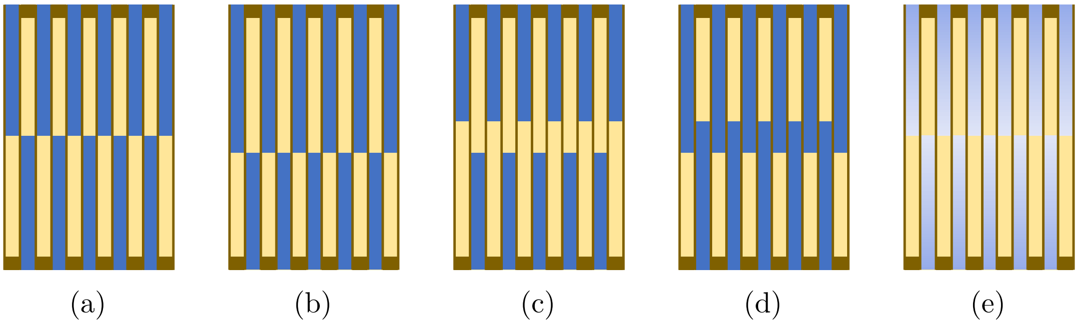
(a) (b) (c) (d) (e)

Fig. 7.1: Potential washcoat distributions in coated filters. (a) Symmetrical. (b) Asymmetrical. (c) 'Gap'. (d) 'Overlap'. (e) Non-uniform. Blue represents the washcoat slurry, yellow represents the filter substrate and brown illustrates the location of filter walls and plugs.

7.1.2 Permeability and porous media

One area of difficulty in the study of particulate filters and porous media more generally is relating the macroscopic permeability to the microscopic properties of porous media, e.g. the porosity and pore size distribution. As was discussed in Chapter 6, accurately estimating the permeability of filter substrates is difficult and relies on careful experimental performance and accurate modelling. Similar problems can arise when measuring the microscopic structure of porous materials, e.g. mercury intrusion porosimetry only measures the diameter of pore necks. However, even with accurate measurements, the exact relationship between the two lengthscales is unclear and may vary between systems. It is generally accepted that the permeability, k, scales with the square of some characteristic length, l_c,

$$k = f(\epsilon) l_\mathrm{c}^2. \tag{7.1}$$

The characteristic length is usually the mean pore diameter, d_pore or spherical collector diameter, D_p. The proportionality factor is a function of the porosity, ϵ, and is usually called the porosity function, $f(\epsilon)$. Several functions have been proposed, many of which are empirically derived. Three examples of such equations are listed in Table 7.1 and are representative of the most common functions used. However, the behaviour of these functions are often markedly different and it is not clear which ought to be chosen for a porous medium *a priori*.

Table 7.1: Common porosity equations.

Equation name	$f(\epsilon)$
Kozeny-Carman	$\epsilon^3/150(1-\epsilon)^2$
Kuwabara	$\frac{2}{9}\left(2-\epsilon-\frac{9}{5}(1-\epsilon)^{1/3}-\frac{1}{5}(1-\epsilon)^2\right)/(1-\epsilon)$
Hatch-Mavis-Wilsey	ϵ^6
Blake-Kozeny	$\epsilon^3/180(1-\epsilon)^2$

Models of particulate filters often use the porous wall permeability as a fitting parameter to achieve agreement between pressure drop measurements and predictions. However, this method only gives a global value of the permeability. In order to estimate the permeability at different spatial locations, which is necessary if filters with non-uniform washcoat distributions are to be accurately modelled, a different method is needed. Two possible approaches are now proposed. First, find which equation relating the permeability to the porosity and mean pore diameter is most appropriate and use it to calculate the permeability based on porosimetric data. Second, use spatially resolved measurements of the gas velocity in the model fit, with a spatially varying permeability as the fitting parameter. Both of these methods are explored in this chapter.

7.2 Scope of study

In this chapter, the feasibility of using MRI to probe GPF samples with real-world catalytic washcoats is assessed. Four GPF samples, one bare and three treated with different washcoating protocols, are characterised by visual inspection and mercury intrusion porosimetry (MIP) at three axial locations (front, middle and rear). MRI velocimetry, as implemented in Chapter 6, is then used to measure the effects of the washcoating procedure on the gas flow fields inside the filters. These effects are related to the structural changes due to the washcoating and novel modifications to a 1D model are made to allow prediction of the wall permeability using numerical methods. The permeability estimates and the mercury porosimetry results are compared to observe the relationship between the two. Finally, the pressure drop and filtration behaviour of the filters are simulated.

7.3 Literature review

Due to the commercial sensitivity of catalysed particulate filters and their manufacture, there is very little published on the efficacy of the different washcoating procedures; several patents have been filed but these do not allow for much comparison. As such, the exact methods used to produce catalytic filters in the literature are not known. However, many modern methods are based on the same general procedure illustrated in Fig. 7.2 [5, 6]. The substrate is held vertically above or below a dispensing chamber, and a hopper feeds a measured amount of washcoating liquid into the chamber, dosing one end of the substrate. The liquid is then forced into the bulk of the substrate through application of either positive or negative pressures. This is usually a pulse of air, a mechanical piston or a vacuum. The substrate is then removed, dried using hot air and then proceeds to the remaining steps e.g. calcination. Filter substrates can also be loaded from both ends: the washcoating liquid is introduced into the open channels of one end and forced through before the substrate is inverted and the same process is applied [7]. This offers some control over the spatial distribution of the catalyst, allowing for zoned filters [8, 9]. However, the exact amount of control these methods afford and their reproducibility is not fully known.

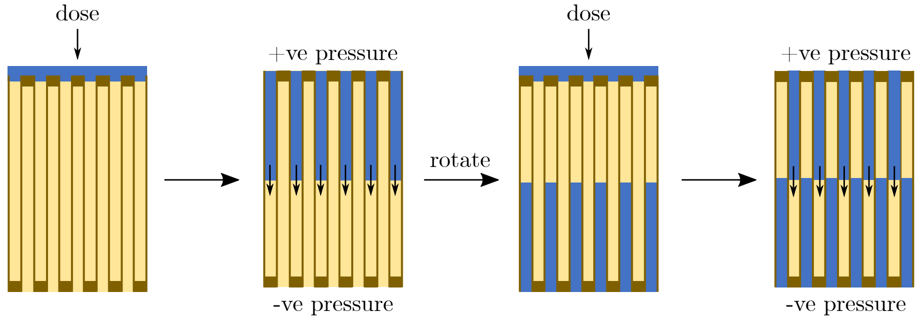

Fig. 7.2: General method for washcoating particulate filters. Blue represents the washcoat slurry, yellow represents the filter substrate and brown illustrates the location of filter walls and plugs.

The location of the catalyst washcoat both within and on the porous walls has been of interest for catalysed DPFs due to the importance of the wall in both pressure drop, catalysis and filtration behaviour. Novak *et al.* studied cordierite FTMs coated with various catalyst metals (Pt, Pd, Rh) and supports (alumina, ceria, barium oxides, magnesium oxides etc.) using X-ray μ-CT, finding that around 20% of the on-wall washcoat volume contained cracks or cavities [10]. Numerical simulations predicted that these cracks and cavities enhanced local gas diffusivity and improved catalyst performance. However, as the porous wall is a key part of filter operation and pressure drop behaviour, these results cannot be assumed to hold for catalysed filters. Vaclavik *et al.* studied three SiC DPF samples, one bare and two washcoated with a Cu-zeolite SCR catalyst (coverages of $1.2\,\mathrm{g\,in^{-3}}$ and

$1.9\,\mathrm{g\,in^{-3}}$) [11]. Three ranges of pore diameter were identified in the washcoated samples using MIP: macropores corresponding to the SiC substrate (∼18 µm), smaller macropores in the washcoat (50 nm - 3 µm) and meso/micropores attributed to the catalyst particles ($<$ 50 nm). Increasing the washcoat and catalyst loading caused the number of large macropores in the substrate to decrease while the number of the smaller pore types increased, with the overall porosity decreasing. This was consistent with the observation from SEM images showing the washcoat deposited inside the porous walls, which narrowed the original pore structure. Simulations performed using the 3D μ-CT data predicted that the washcoat decreased the effective diffusivity of imbibed gas, decreased the fraction of open pore connections and increased the tortuosity of the porous structure. Porosities measured using MIP, X-ray μ-CT and SEM were all in agreement, though the high-resolution SEM data suggested that the MIP underestimated the size of the SiC macropores as only the pore neck diameters are recovered. Pressure drop measurements showed that the addition of washcoat increased the backpressure across the filter, as expected. However, this increase did not appear to be linear with catalyst loading and is likely related to the microscopic changes in the porous structure. Stewart *et al.* found similar changes to the pore size distribution for a commercial SCR filter [12]. MIP measurements showed that the application of the washcoat reduced the sizes of pores in the SiC substrate and produced new pores with diameters ∼0.7 µm, creating a bimodal distribution for regions with only in-wall catalyst. One region containing a high loading of catalyst, both in- and on-wall, was found to have lost nearly all of the larger pores. Koci *et al.* built on the work of Vaclavik, using X-ray μ-CT to obtain porous structure data for simulations of through-wall gas flow [13]. Three cordierite GPF samples washcoated with γ-Al_2O_3 were studied, one each with washcoat in-wall, on-wall, and both in- and on-wall. MIP measurements of the porosity agreed well with the X-ray data, and showed similar pore size distribution changes compared with a bare GPF to those seen by Vaclavik *et al.* and Stewart *et al.* Simulations of gas flow revealed that gas flow through the wall can be highly heterogeneous. For only in-wall catalyst loading, many pathways through the porous structure are blocked and so significant channeling occurs. For only on-wall catalyst loading, cracks in the washcoat layer similarly act to channel flow through a small number of pathways. For both in-wall and on-wall, more homogeneous flow and better CO conversion is predicted but the coating scheme is considered impractical due to the severe increase in pressure drop.

The effects of washcoats on filter performance have been well documented. Maunula *et al.* compared a SiC DPF washcoated with a sol-gel to one dip-coated, finding that the former results in a lower pressure drop for the same amount of catalyst loading [14]; this was attributed to the smaller particle sizes in the sol-gel compared with the dip coat. Tsuneyoshi *et al.* explored the effects of increasing the γ-Al_2O_3 washcoat content of a SiC filter [15]. Both the filtration efficiency and pressure drop increased as more washcoat was added. The increase in filtration efficiency was most prevalent for PM greater than 30 nm in size, suggesting that the Brownian deposition mechanism is less affected by the structural

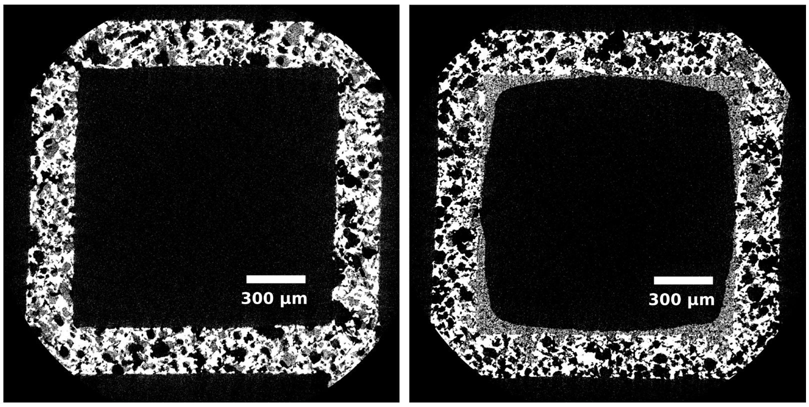

(a) (b)

Fig. 7.3: X-ray μ-CT images of filters with washcoat (a) in-wall and (b) on-wall and in-wall, taken from Koci *et al.* [13]. The filter substrate is shown in white and the washcoat in grey.

changes. The pressure drop increase was non-linear, likely due to non-linear changes in the wall permeability as the pore structure changes. Conversely, a linear increase in pressure drop was observed as soot loading increased, as expected from Darcy's law for a porous layer of linearly increasing thickness. Karamitros and Koltsakis, in their modelling of zoned SCR particulate filters, presented results showing a decrease in wall permeability as the catalyst loading increased [16]; this decrease was less pronounced for a soot loaded filter. However, it is not reported whether these results are empirical or simulated. Lambert *et al.* observed that while increasing washcoat content in a GPF improved the filtration efficiency of the filter, it also greatly increased the pressure drop to a degree that high washcoating levels may result in engine damage [1]. Kong and Yamamoto investigated the effects of washcoat applied in-wall and on-wall to a DPF with undisclosed properties [17]. Both types of application were found to increase the experimental pressure drop above that of the bare filter, though no significant difference was observed between them. However, the permeability of the on-wall catalyst layer was predicted to be lower than the in-wall catalyst. Using X-ray μ-CT and lattice-Boltzmann simulations of a $120\,\mu\text{m}\times120\,\mu\text{m}\times300\,\mu\text{m}$ section of filter wall, the authors studied the washcoat effects on gas flow and soot deposition. The on-wall washcoat was predicted to have little effect on the uniformity of flow in the wall compared to the bare DPF, whereas the in-wall washcoat narrowed the substrate pores at the incident face of the wall and increased the degree of channelling. However, the in-wall washcoat showed similar deposition behaviour to the bare DPF, with soot depositing in the filter wall before forming a cake on the wall surface. Soot deposited to a smaller depth in the in-wall washcoat substrate compared to the bare DPF. The on-wall washcoat showed different deposition behaviour, with the soot forming a cake on the washcoat layer. The on-wall washcoat was predicted to have a greater filtration efficiency than both the bare DPF and in-wall washcoat, and showed a smaller increase in pressure drop as the soot loading increased. However, these results may not be representative of true behaviour as it appears the porous structure of the washcoats was not resolved in the X-ray data and have instead been modelled as uniform porous materials. Liu *et al.* found that in the absence of soot and ash loading, GPFs with washcoats had lower initial filtration efficiency and higher backpressure than the bare filters [18]. This difference in filtration efficiency was observed to decrease for increasing gas flow rates. Once loaded with soot, the washcoated filters showed a faster increase in filtration efficiency than the bare filters. However, the backpressure of the loaded washcoated filters also increased more than for the loaded bare filters. It was also observed that accumulation of ash in the filter increased the filtration efficiency “significantly” with a smaller increase in pressure drop than for soot and washcoat loadings.

The spatial distribution of washcoat on the filter scale is also of great interest but is more difficult to measure. Early studies relied on visual inspection to identify regions of high and low catalyst loading, using the contrast between the bare substrate and the washcoat as a qualitative measure. Wahlberg *et al.* studied the application of a Cu/γ-Al_2O_3 to a cordierite FTM through both incipient wetness and deposition precipitation impregnation, finding that the former produced a more inhomogeneous coverage [19]. Vergunst *et al.* found that different drying methods produced different catalyst distributions for Ni/γ-Al_2O_3 on a cordierite FTM [4]. Static drying resulted in a layer of high catalyst loading at the exterior of the filter, whereas flowing air created a region of high loading at the incident face of the substrate (Fig. 7.4). Only microwave drying, freeze drying for a long time and application via deposition-precipitation gave uniform catalyst distributions. While the exact requirements of washcoating FTMs and DPFs are different, it has been shown via NMR studies that inhomogeneities during the drying process may impact catalyst distribution within DPFs as well as FTMs [20].

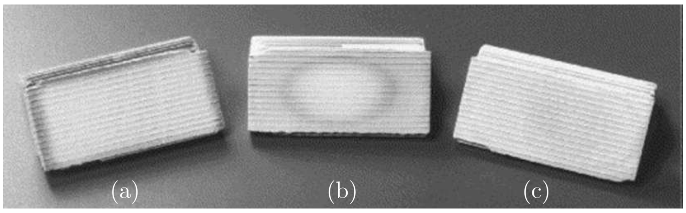

Fig. 7.4: Photograph showing $Ni(NO_3)_2$ catalyst distributions in FTMs after (a) 24 h static drying, (b) 1 h freeze drying followed by static drying and (c) 24 h freeze drying. The darker grey indicates regions of greater catalyst concentration. Taken from Vergunst *et al.* [4]

There are two major drawbacks with the prior visual methods: it is only sensitive to catalyst deposited on or close to the wall surface, and it offers no quantification of the loading. More recently, other methods have been used to better quantify the loading. Using T_1 contrasted MRI of water, Ismagilov *et al.* were able to identify regions of high catalyst content in Pt/γ-Al_2O_3 and Pd/γ-Al_2O_3 applied to FTMs [21]. However, such methods require additional calibration in order to be quantitative. Nishina *et al.* used terahertz wave CT to map the distribution of washcoat inside DPFs, using a half-coated FTM to validate the technique [22]. The study reported that while uniform catalyst loading was present in the centre of the filter, regions of high loading were found at the filter ends. However, it was not stated how the washcoat was applied to the filter. Toops *et al.* used a neutron tomography method to measure the catalyst distribution in a cordierite filter, observing that some washcoat was peeling away from the filter walls [23]. Stewart *et al.* used low resolution X-ray μ-CT to estimate the axial distribution of washcoat in a commerical SCR filter [12]. The results agreed with visual and high-resolution X-ray CT results, finding a region of very high catalyst loading in the centre of the filter (Fig. 7.5). This region featured both in-wall and on-wall washcoat, whereas the rest of the filter had catalyst only within the walls. While this is an interesting result, the commercial origin of the filter means the exact method of washcoat application is not known.

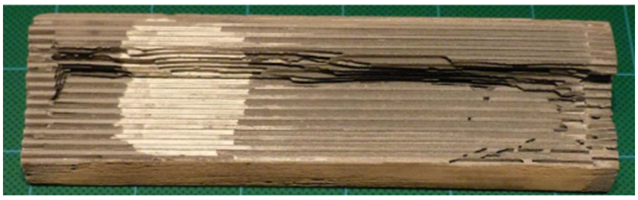

(a)

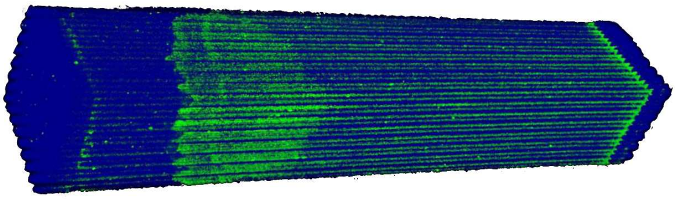

(b)

Fig. 7.5: (a) Photograph and (b) X-ray CT of a commerical SCR filter showing inhomogeneities in the axial washcoat distribution. The catalyst is shown in green and the filter substrate in blue. Taken from Stewart *et al.* [12].

Little work has focused on the effects of washcoat distribution on the internal hydrodynamics in catalysed filters. Aleksandrova *et al.* noted that the large spatial variation in washcoat distribution created difficulty in reliably measuring the permeability of catalysed GPFs [24]. Karamitos and Kostoglou presented the predicted through-wall velocity profiles for zoned SCR filters [16]. The filters were zoned with high loading in one half of the length and low loading in the other. Higher through-wall velocities were observed in the low loading regions due to their higher permeability, with a discontinuity between the two zones. The uniformity of flow was greater for the higher loading region. However, the uniformity of flow across the whole filter wall increased upon soot loading, reflecting the 'self-correction' effect observed by other workers [25].

7.4 Experimental

7.4.1 Materials

Four GPF samples were used in the present study. Washcoating was performed manually (i.e. not on a production line) on 2 inch diameter samples of a larger GPF by Emily Price at Johnson Matthey Technology Centre, Sonning Common, UK. The washcoat was made of γ-alumina, with a particle size distribution given in Fig. 7.6, suspended in a slurry. The GPF substrate was manufactured from cordierite with a total filter length of 114 mm, a plug length of 6 mm, channel side width of 1 mm and wall thickness of 0.3 mm. The first was used without any washcoat applied and is referred to as GPF A. The remaining samples were washcoated such that both the inlet and outlet channels were coated to half the distance between the channel opening and the opposite plug. GPF B had only the washcoat applied in-wall by dip coating, i.e. by being dipped into the washcoat slurry. GPF C was precision-coated, i.e. the method illustrated in Fig. 7.2, with catalytic washcoat to a coverage of $1.6\,\mathrm{g\,in^{-3}}$ Pd inside the porous walls. GPF D was dip-coated with catalytic washcoat to a coverage of $1.48\,\mathrm{g\,in^{-3}}$ Pd both on and inside the porous walls. All washcoated substrates were dried at 110 °C for 3 h and the catalytic substrates were also calcined at 500 °C for 5 h. The preparation and structure of GPF B and D are expected to be similar to samples CF1 and CF2 described by Koci *et al.* [13]; these are the filter substrates shown in Fig. 7.3.

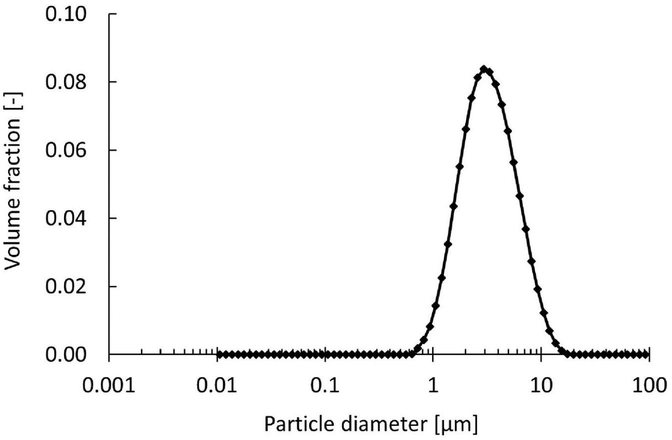

Fig. 7.6: Particle size distribution of Al_2O_3 in the applied washcoats derived from light scattering measurements. Taken from Koci *et al.* [13].

For the MRI experiments, 5×5 channel samples were cut from the larger filter cores. The samples were held in the magnet using the same method described in Section 6.4. Gas was supplied at a mass flow rate of $16\,\mathrm{g\,min^{-1}}$ and a pressure of 5.0 ± 0.1 bar(g) for all samples. Due to unavoidable flow bypass, the superficial velocities could not be kept exactly the same for each sample. However, they represent a similar flow regime in the range $\mathrm{Re_c} = 996 - 1127$.

7.4.2 Sample characterisation

The GPF samples were characterised in two ways: photographs of the sample front ends and axial cross-sections were taken as part of a visual inspection, and the pore size distributions and porosities of the filters and applied washcoats were measured using MIP. The MIP experiments were performed at Johnson Matthey Technology Centre, Sonning Common, UK by Maciah Smith using a Micrometrics AutoPore IV. Three samples of approximately $1\,\mathrm{cm}\times1\,\mathrm{cm}\times1\,\mathrm{cm}$ were cut from the front, middle and rear of each sample such that the pore size distribution was measured at three axial locations. The porosity and modal and mean pore diameters were calculated from these distributions. Only pores with a diameter less than $50\,\mu\mathrm{m}$ were included in the calculations to ensure that surface roughness did not affect the values.

7.4.3 Magnetic resonance

The magnetic resonance method used followed the protocol outlined in Section 6.4 with minor differences. Due to the shorter length of GPFs compared with DPFs, fewer images were acquired for each sample in this study. A narrower slice thickness of 5 mm was also used and the velocity gradient strength was $2.92\,\mathrm{G\,cm^{-1}}$.

7.5 Numerical methods

7.5.1 One-dimensional filter model

The one-dimensional model of gas flow in a filter described in Section 6.5 was used for the numerical simulations in this chapter. The momentum convection term of Bissett [26], i.e. $n = 2$, was used due to the better agreement with experimental velocity data (Chapter 6). Due to the wall Reynolds numbers present in the system, the correlations of Bissett *et al.* and Kostoglou *et al.* [27, 28] could not be used and the values of α and F were kept uniform across the filter length with values of 1.377 and 28.48 respectively. This is expected to slightly underestimate the through-wall velocity at the rear of the filter. The inlet velocity was chosen to match the average superficial velocity measured using the MRI method for each GPF sample. The wall thickness and channel diameters were assumed to be constant and uniform in the model.

The model was adapted to allow non-uniform wall permeabilities as a function of axial position. This modification allowed effective permeability profiles to be estimated for each GPF sample. This was achieved by first discretising the axial positions of the model to those of the velocity profiles using MRI. This ensured that the permeability profiles would be at the same spatial resolution as the MRI velocity profiles and not be subject to overfitting. The elements of the permeability profile, represented by the vector $\mathbf{k}$, were then used to minimise the objective function,

$$\mathbf{k} \in \operatorname{argmin}_{\mathbf{k}} \left\{ \frac{1}{2} \left\| \frac{\mathbf{y} - \mathcal{M}\mathbf{k}}{\sigma} \right\|_2^2 \right\}, \tag{7.2}$$

where y is the experimental velocity data, $\mathcal{M}$ is the 1D model operator that returns the predicted velocity data for a given permeability profile and σ is the error in the velocity measurement. This was performed using the minimisation function *fminsearch* in MATLAB with the constraint that all permeability profile elements must be positive. In order to estimate the error in the fit, 32 minimisations were run with random noise added to the initial guess. The standard deviation of the distribution of fitted values at each axial point was used as an estimate of the error in the fit at that point. The pressure drop across the filter was also calculated as a function of increasing flow rate.

7.5.2 Analytical filtration model

The filtration model and simulation method described in Chapter 6 is used to predict the filtration behaviour for the GPF samples studied presently. The through-wall velocities used were derived from the MRI results. The velocity data were linearly interpolated onto a Cartesian raster of 32 points. The simulations were adapted to allow for spatial variations in the porosity and mean pore size. The values obtained from the MIP results were used as representative values for the front, middle and rear thirds of the simulated filter length.

7.6 Results

The results of the current study are presented in four parts. First, the characterisation of the filter substrates using photographs and MIP is given. Second, the velocity profiles for each filter measured using MRI are shown. Third, the fitting of permeability profiles to the MRI velocity data using a 1D numerical model is shown. Finally, the pressure drop and filtration behaviour of the different substrates are simulated numerically.

7.6.1 Characterisation of filter and washcoats

The photographs taken for visual inspection of the filter samples are shown in Figs. 7.7 and 7.8. From the axial photographs (Fig. 7.7), GPFs A and C (a, c) show little to no visual variation along their lengths. GPF B (b) shows some modest variation along the inlet channels, with darker regions at the front and rear. The outlet channels show more pronounced variation, with a dark region at the front followed by a dark pattern in the filter centre. The rear half of the outlet channels appears uniform. All channels show a slight variation in appearance along the diameter of the channel, with the middle darker for the inlet channels and lighter for the outlet channels. GPF D (d) also shows spatial variation in appearance. In the centre of the filter, a small region around 2 mm to 4 mm in length is seen between darker regions. The inlet channels are lighter at the front and the outlet channels are lighter at the rear. A darker ring is also observed at the front of the filter. Inspection of the photographs of the filter ends reveals little difference between GPFs A, B and C (Fig. 7.8 (a-c)), with some white deposition seen on the plugs of GPFs B and C. However, washcoat deposits on the filter walls can be seen in the channels of GPF D (d). The extent to which the washcoat reduces the channel cross-sectional area varies between individual channels, though the maximum observed in the photograph is estimated at a 60% reduction.


(a) GPF A


(b) GPF B

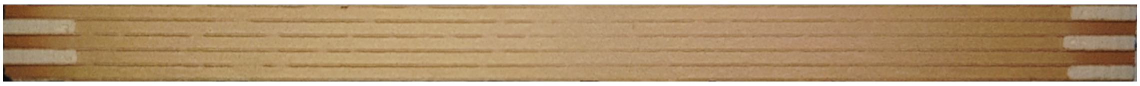
(c) GPF C


(d) GPF D

Fig. 7.7: Photographs of axial sections of GPF samples. The brightness and contrast have been increased for clarity. Two aspects of GPF D are shown.

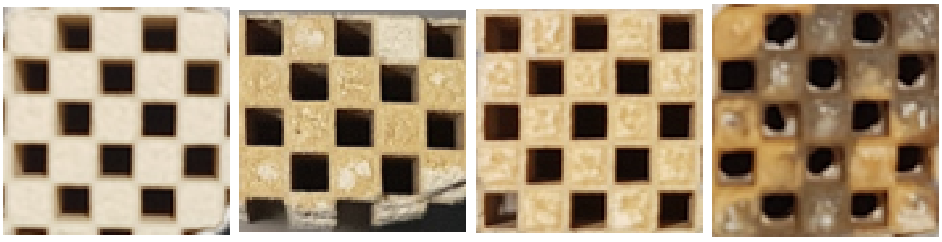
(a) GPF A (b) GPF B (c) GPF C (d) GPF D

Fig. 7.8: Photographs of the front ends of the GPF samples.

The pore size distributions obtained from the MIP data are shown in Fig. 7.9. The porosities and average pore sizes calculated from distributions are listed in Table 7.2. GPF A (a) shows very similar pore size distributions at the three positions, though the porosity is calculated to vary somewhat between them. This may be due to small errors in measuring the sample weight. For GPF B (b), the mean pore size is the same within error for the three sections, but the porosity at the middle is 6.5-8.2% lower than at the ends. The average pore diameters are generally lower than for GPF A. GPF C (c) shows similar porosities across the filter, with the front having a slightly lower porosity and the rear having a slightly higher respectively than the middle. Similar mean pore sizes were calculated for all three sections, all of which are greater than those of GPF A. GPF D (d) shows a much higher porosity in the middle of the filter compared with the front and rear, with the modal pore size also larger in the middle. However, the mean pore size is similar across all three sections and sometimes larger than for GPF A.

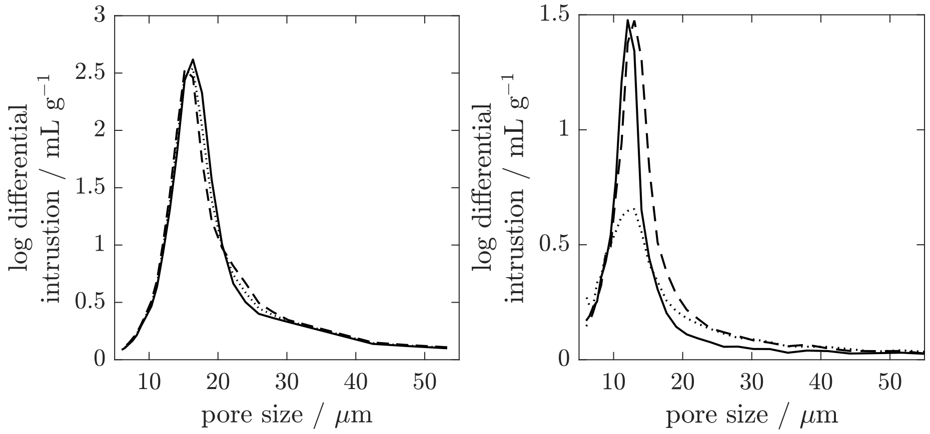

(a) GPF A

(b) GPF B

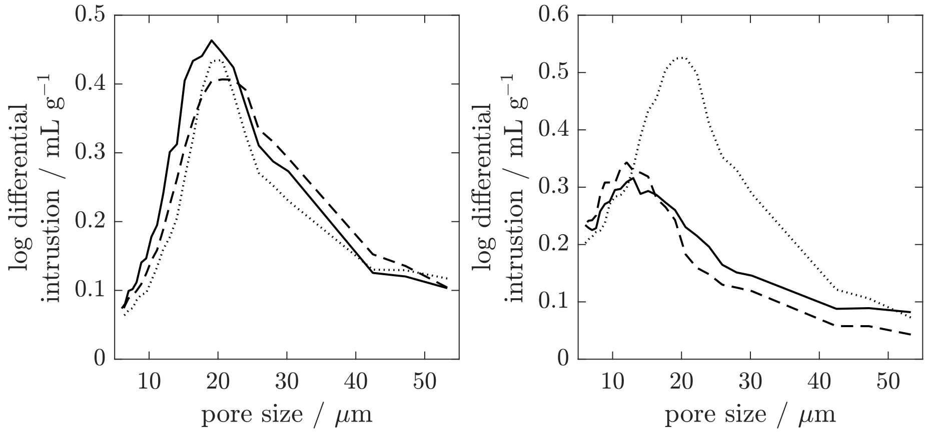

(c) GPF C

(d) GPF D

Fig. 7.9: MIP data for the (——) front, (·····) middle and (- - -) rear of the GPF samples. Pore size refers to the pore diameter.

7.6.2 Magnetic resonance imaging

Compatibility of catalysed GPF samples

As described in Chapter 4, a good magnetic susceptibility match is required between the SF_6 and the filter substrate in order to give quantitative velocity measurements. Whilst the plugged regions of the cordierite DPF (Fig. 4.7) showed significant magnetic field inhomogeneity, the 'bulk' region of the filter has a very uniform magnetic field and yields

Table 7.2: Porosity, ϵ, and modal and mean pore diameters, d_{pore}, of the GPF samples calculated from MIP data.

Sample	Porosity ϵ / %			Modal d_{pore} / µm			Mean d_{pore} / µm		
	Front	Middle	Rear	Front	Middle	Rear	Front	Middle	Rear
A	55.6	58.7	62.0	16 ± 1	16 ± 1	15 ± 1	21 ± 2	21 ± 2	21 ± 2
B	43.0	36.5	44.7	12 ± 1	13 ± 1	13 ± 1	16 ± 2	19 ± 2	17 ± 2
C	24.1	26.9	29.2	19 ± 1	21 ± 1	21 ± 1	26 ± 2	27 ± 2	27 ± 2
D	27.7	33.1	23.7	13 ± 1	21 ± 1	12 ± 1	24 ± 3	24 ± 2	21 ± 2

quantitative velocity data. However, the presence of palladium in the catalytic washcoat poses an additional problem as palladium metal is paramagnetic and will perturb the local magnetic field. In order to characterise the effect of the catalytic washcoat, velocity encoded images were acquired with no gas flow for each sample. The phase of signal in the channels is constant but offset from 0 rad. The images also showed some convection occurring in the central channel. This would not be present in the flowing system and so these images cannot be subtracted from the flowing MR data. Hence, the mean phase offset was calculated for each GPF sample and subtracted as a uniform correction factor. The values of the factors used are given in Table 7.3.

Table 7.3: Mean phase offsets measured for GPF samples under no flow conditions.

Sample	Phase offset / rad
A	+0.087
B	-0.055
C	-0.062
D	-0.074

As in Section 6.6.1, the volume flow rates calculated from the mass flow controller (shown by the horizontal lines) and the MRI data were compared to validate the velocity quantification (Fig. 7.10). The mean volume flow rate was calculated across all axial positions for each sample; the error bars shown are the standard deviation of these measurements. All four samples gave a mean volume flow rate within 7.5% of the value calculated from the mass flow controller.

Gas flow fields

MR velocity imaging was used to measure the axial channel and through-wall velocities in all four samples. The velocity profiles measured for each GPF sample are shown in Fig. 7.11. As in Fig. 6.9, the vertical error bars for the axial channel velocities represent the variation between individual channels in the sample. GPF A shows similar profiles to those measured for the SiC DPF sample in Chapter 6. The inlet and outlet channel velocities (a, i) decrease and increase non-linearly along the filter, with the through wall

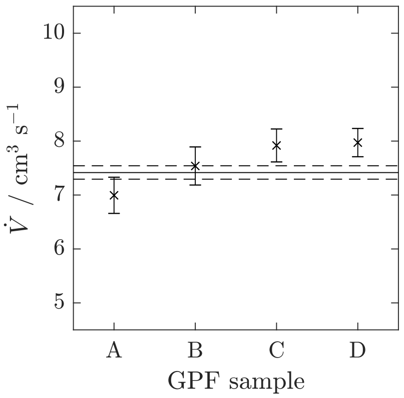

Fig. 7.10: Plot showing the expected volume flow rate from mass flow measurements (horizontal line) and the measured volume flow rates from MRI data for each GPF sample. The error in the expected volume flow rate is calculated from the error in the gas pressure and represented by the dashed lines. The error in the measured volume flow rates is the standard deviation of measurements along the axial length of each sample.

velocity (a, ii) showing a parabolic shape with greater velocity at the filter rear. The three washcoated GPF samples are reported in comparison to the bare GPF A results. GPF B shows broadly similar behaviour to GPF A but the channel velocities are 'flatter' at the front, middle and rear of the filter (b, i). This results in a lower through-wall velocity in these regions, as can be seen in (b, ii). GPF C has a more gradual and linear change in channel velocities in the front and middle of the filter, with a large change around $z/L = 0.7$ followed by another gradual change at the rear (c, i). These smaller changes similarly result in lower and more uniform thorugh-wall velocities in those regions (c, ii). GPF D shows substantially different behaviour to GPF A. In the channel velocities (d, i), the front and rear of the filter shows very small changes, whereas the gradient is very steep in the centre. This corresponds to high through-wall velocities in the very centre of the filter and low velocities at either end (d, ii).

One feature of note is the relatively large error bars for GPF D. As stated before, this reflects a large degree of variation between velocities in different channels as opposed to a larger error in the velocity measurements. Figure 7.12 shows the individual channel velocity profiles measured for GPF D, along with the through-wall velocity of gas leaving or entering each channel.

7.6.3 Numerical modelling of washcoated GPFs

Permeability profiles

In order to validate the numerical method of permeability profile fitting, channel velocity profiles were simulated using known ground-truth permeability profiles at a superficial velocity of $40\,\mathrm{cm\,s^{-1}}$. Random noise with a standard deviation of $1\,\mathrm{cm\,s^{-1}}$ was added to the simulated velocity data and the minimisation was run to produce fitted permeability profiles. These were compared with the original known profiles (Fig. 7.13). Three profiles

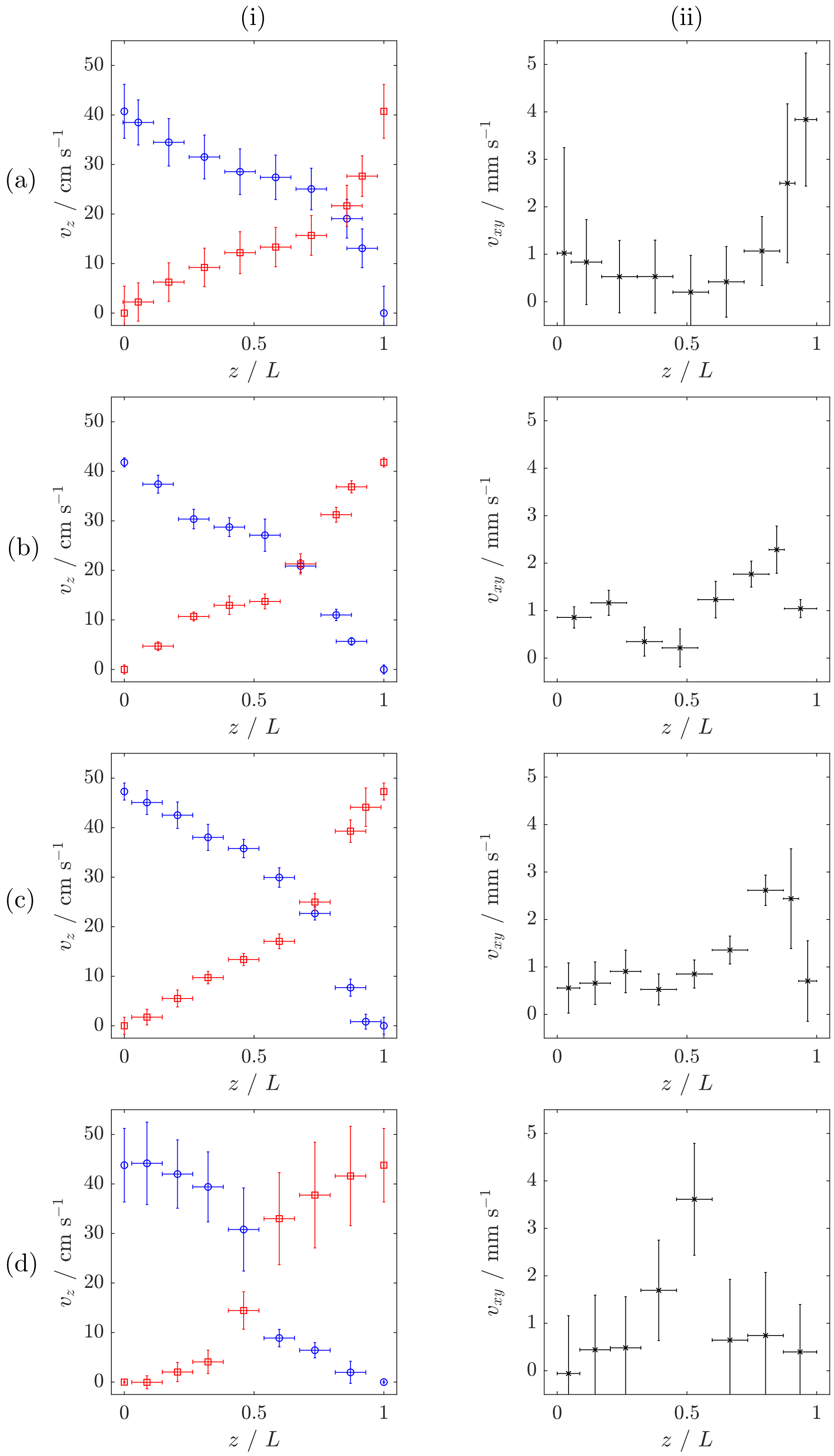

Fig. 7.11: MRI measurements of the (i) inlet and outlet channel velocities and (ii) through-wall velocities for (a) GPF A, (b) GPF B, (c) GPF C and (d) GPF D. The vertical error bars reflect the variation in gas velocity between channels and not the uncertainty in the velocity measurement (as in Chapter 6.)

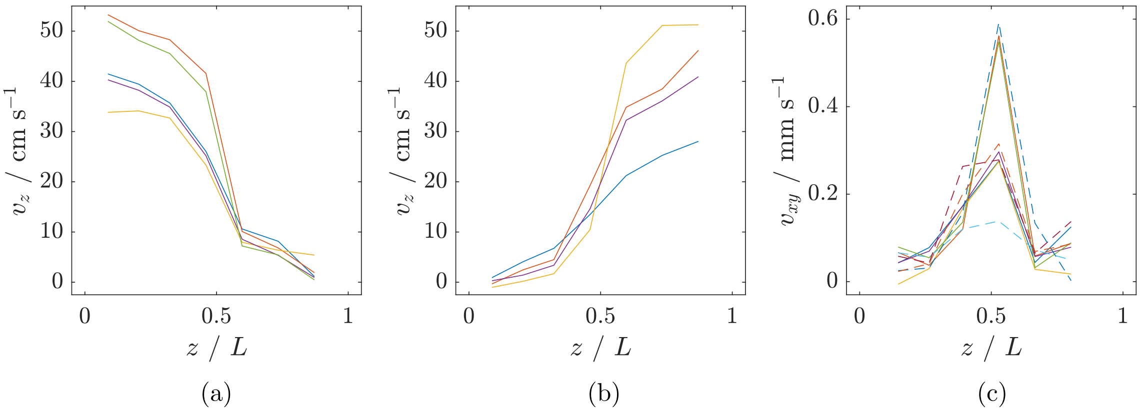

(a) (b) (c)

Fig. 7.12: Plots showing (a) inlet channel, (b) outlet channel and (c) through-wall velocities for individual channels in GPF D. In (c), solid lines indicate profiles calculated from inlet channel velocities and dotted lines indicate those calculated from outlet channel velocities.

were used to represent expected washcoat distributions: a uniform profile (a), a ‘gap’ profile (b) and an ‘overlap’ profile (c). Good agreement is seen between the fitted and ground-truth profiles within the uncertainty of the fit. As the greatest variation in the velocity profiles is observed between permeabilities of $1 \times 10^{-14}\,\mathrm{m}^2$ to $1 \times 10^{-12}\,\mathrm{m}^2$ for $v_{\mathrm{sf}} \approx 40\,\mathrm{cm\,s^{-1}}$, the fitting will be most sensitive to permeability values in this range.

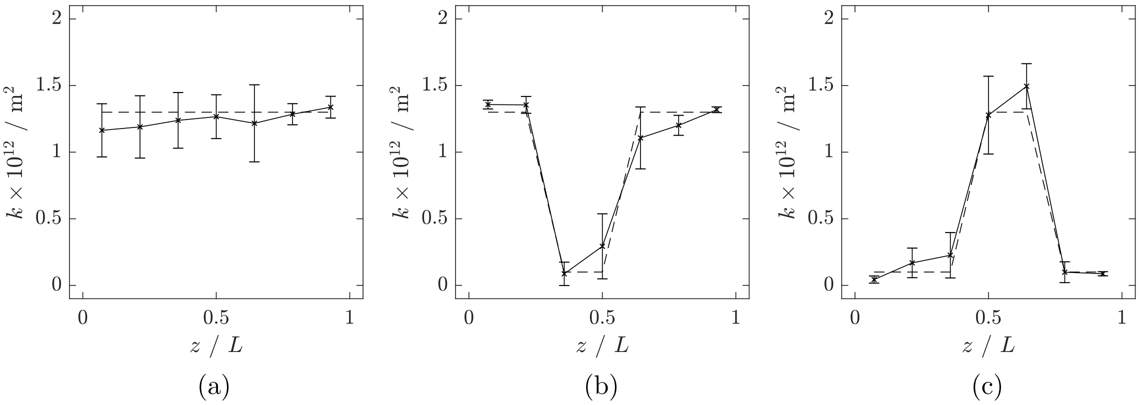

(a) (b) (c)

Fig. 7.13: Comparisons of ground-truth (- - -) and fitted permeability profiles (——) for (a) a uniform distribution, (b) a ‘gap’ distribution and (c) an ‘overlap’ distribution.

The numerical method was applied to the MRI axial velocity profiles for all GPF samples shown in Fig. 7.11. The fitted permeability profiles are shown in Fig. 7.14 (i) and the fitted velocity profiles are shown in Fig. 7.14 (ii) by the solid lines. For comparison, the velocity profiles predicted using uniform permeability profiles at the mean value of the fitted profiles are shown by the dotted lines. For GPF B (b), two regions of low permeability are observed, one in the middle of the filter and one at the rear. The middle region corresponds to the ‘flat’ section of the axial velocity profile and low through-wall velocities compared with the bare filter; the rear of the filter similarly shows low through-wall velocity (Fig. 7.11 (b)). GPF C (c) shows a more uniform profile, though slightly lower permeabilities are observed at the front and rear of the sample. These again correspond to regions with lower through-wall velocity (Fig. 7.11 (c)). GPF D (d) shows two large regions of very low permeability at the front and rear, with a sharp peak in the centre. This follows the through-wall velocity profile seen in Fig. 7.11 (d), where most of the gas passes through the middle of the filter. For all three GPF samples, the predicted velocity profile for a mean-value uniform permeability is different to that for the fitted non-uniform permeability (ii), with the greatest deviation seen for GPF D (d).

The permeability profiles for each filter were averaged in the front, middle and rear thirds of the filter length. These averaged values were divided by the square of the mean pore diameter measured using MIP (Table 7.2) and plotted against the porosity in Fig. 7.15. The porosity functions, $f(\epsilon)$, listed in Table 7.1 are also plotted for comparison. The general trend shown is that k/d_{pore}^2 increases with increasing porosity and all four porosity functions give the correct order of magnitude predictions, however none of the functions give good predictions for all samples. In particular, the values for GPF A appear to deviate strongly from the behaviour of all functions.

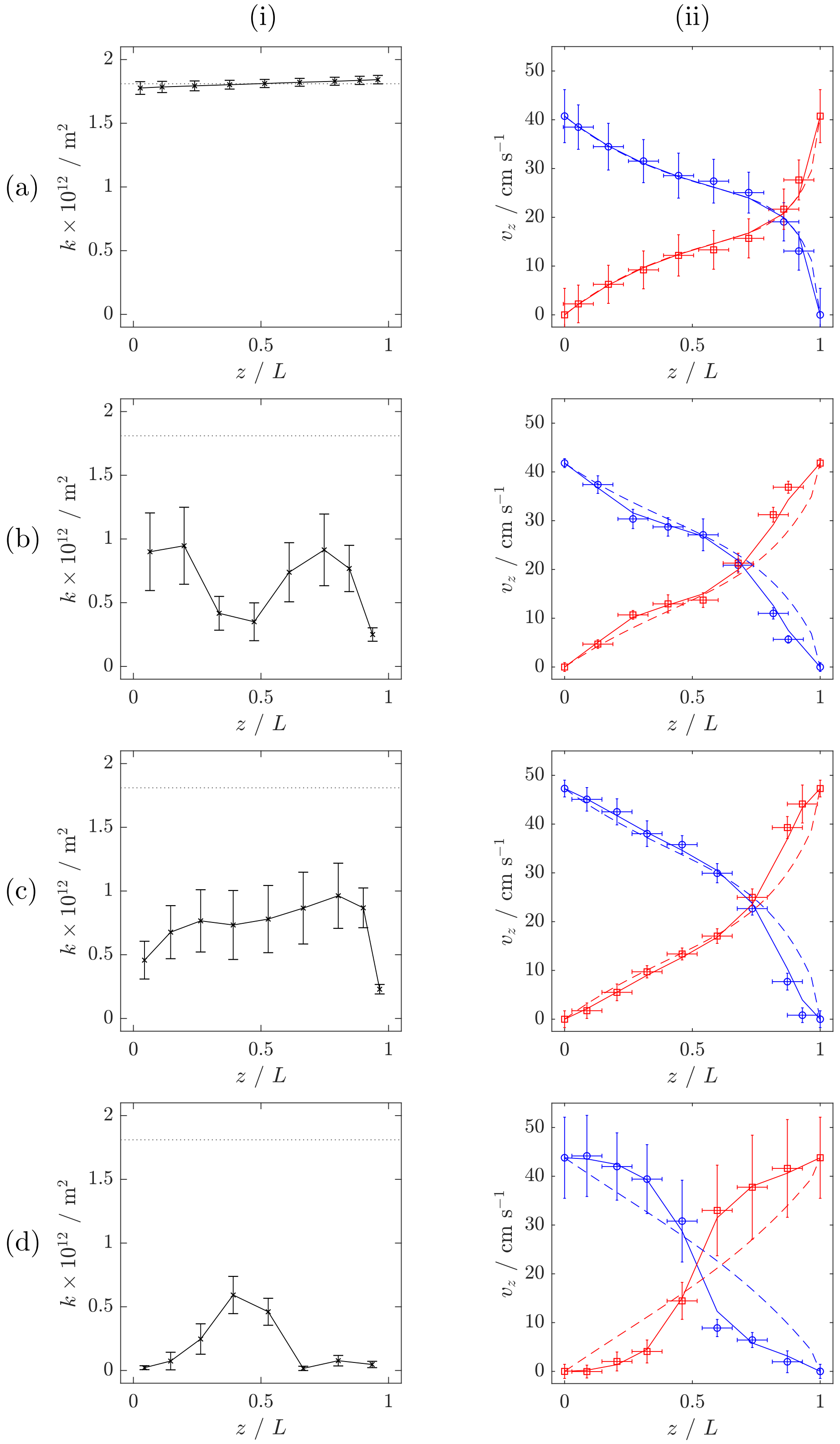

Fig. 7.14: (i) Permeability profiles from fitting the 1D model predictions to the MRI velocity measurements. The mean permeability of GPF A is shown by the horizontal dotted line. (ii) Axial velocity model predictions using the fitted permeability profiles (solid lines) and the mean fitted permeability (dotted) shown with the MRI measurements. Data are shown for GPFs A - D (a-d).

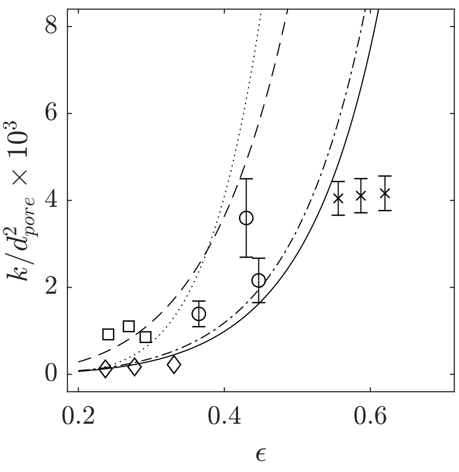

Fig. 7.15: Plot showing the relationship between the porosity, permeability and mean pore diameter of GPFs (×) A, (○) B, (□) C and (◇) D. The (——) Kozeny-Carmen, (- - -) Kuwabara, (·····) Hatch-Mavis-Wilsey and (-·-·) Blake-Kozeny porosity function are also plotted for comparison. Vertical error bars are calculated from the error in the permeability profile fit and are not shown where the error is smaller than the plot marker.

Filter operation

The pressure drop behaviour of each sample with increasing flow rate was simulated using the 1D model (Fig. 7.16). The bare GPF behaviour is also included for comparison (shown by the black dotted line). Using the fitted permeability profiles shown in Fig. 7.14 (a), the catalysed samples show a greater predicted pressure drop increase than the bare sample (solid lines). GPF D (on-wall and in-wall catalyst) shows the greatest increase, with GPFs B and C showing intermediate but similar behaviour. When using permeability profiles that are uniform with the mean value of the fitted profiles, all coated samples show a lower predicted pressure drop increase (dotted lines). The relative undeprediction in the pressure drop gradients due to using the mean permeability were 9%, 13% and 12% for GPFs B, C and D respectively.

The predicted number of filtered particles as a function of particle diameter and axial position is shown in Fig. 7.17 for each sample. GPF A (a) shows similar behaviour to the bare DPF substrate used in Chapter 6 as expected. GPF B and C (b,c) are somewhat similar to GPF A with most PM predicted to deposit at the rear of the filter, however there are regions of low deposition where the through-wall velocity (and hence PM flux) is lower. GPF D (d) has the most striking behaviour, with most filtration occurring in the centre of the filter. The overall filtration efficiency of GPFs A-D was calculated as 88.9%, 97.5%, 98.7% and 85.5% respectively.

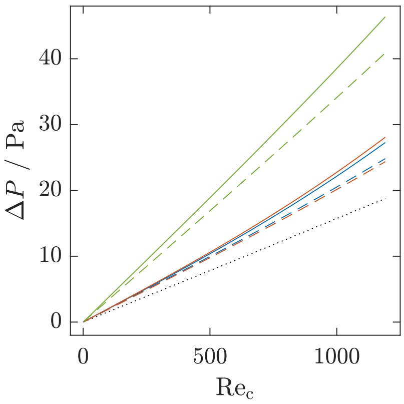

Fig. 7.16: Simulations of the pressure drop behaviour of GPFs B (blue), C (red) and D (green) with increasing $\mathrm{Re_c}$. Solid lines show simulations run with the non-uniform permeability profiles and dashed lines show simulations run with uniform profiles with the mean permeability. The black dotted line shows the behaviour of GPF A.

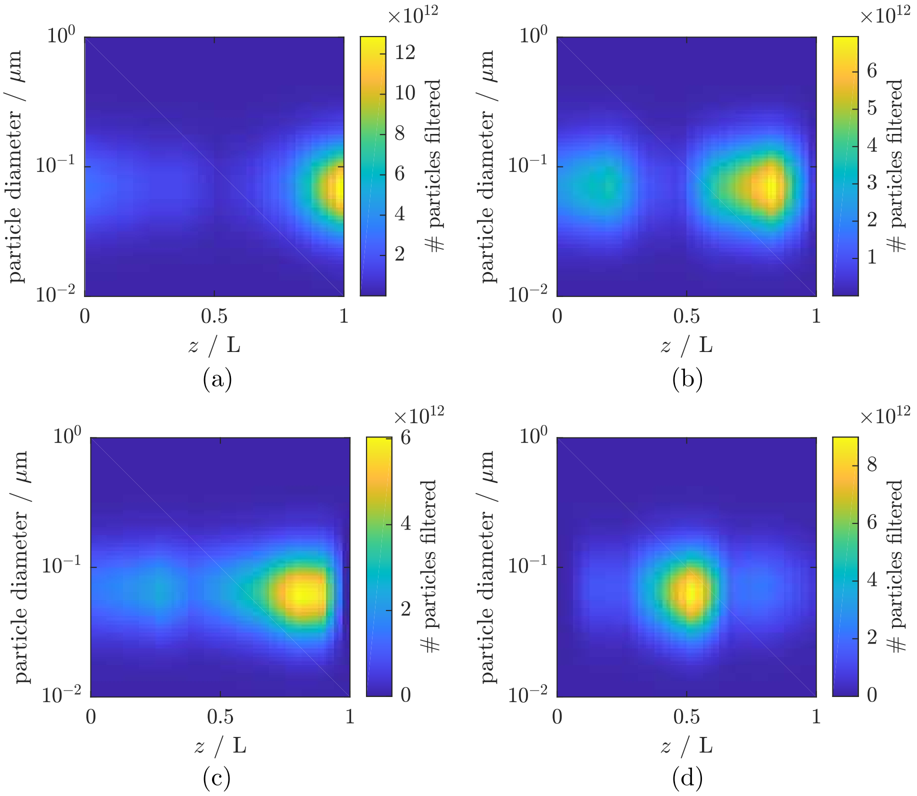

Fig. 7.17: Calculated number of particles filtered as a function of PM diameter and axial position for GPF (a) A, (b) B, (c) C and (d) D.

7.7 Discussion

The photographs of the GPF samples used in this study (Figs. 7.7 and 7.8) suggest that non-uniform washcoat distributions will be a concern for dip-coated samples (GPFs B and D) as obvious heterogeneities in the substrate appearance are observed. One interesting observation was the washcoat layer inside the channels of GPF D (Fig. 7.8 (d)). The thickness of the layer appeared to vary both between and within channels, and was thought to be the cause of the large variation in channel velocities observed for GPF D (Fig. 7.12). The visual observations are consistent with the quantitative MIP measurements, which show much greater variation in the porosity and pore size distributions as a function of spatial location for the two dip-coated samples. This may be expected as the dip-coating method requires several applications of the washcoat slurry which may be more difficult to apply consistently. The washcoat rheology may also affect the microscopic distribution of the washcoat, i.e. it may change if pores are partially or wholly filled by washcoat. Details of the washcoat rheology were not available however. The presence of washcoat particles in the filter pores is expected to reduced some pore diameters to below 1 µm [13] and the washcoat particles themselves are porous, meaning the porosity values calculated here are likely underestimates of the true porosity.

The MRI measurements of gas velocity reveal the effects that the washcoat application has on the gas transport within a filter Fig. 7.11. The general expectation is that regions with high washcoat loadings will have a greater resistance to gas flow and so will experience a lower local through-wall velocity. From this, a qualitative understanding of the washcoat distribution can be inferred. This can be seen for GPF B (b), which has a lower through-wall velocity at the filter centre, and for GPF D (d), which has a high through-wall velocity at the centre. However, GPF C (c) also shows noticable deviations from the bare filter (a), with lower through-wall velocities at the very front and rear of the filter. This is despite GPF C showing no visible heterogeneities and only small spatial variations in the pore structure. As such, it may not be possible to fully anticipate any gas flow perturbations from a visual inspection or routine MIP measurements. This may have important implications for quality control during the manufacturing process.

In Chapter 6, it was established that a 1D numerical model can accurately predict the gas velocities inside filter geometries. Figure 7.13 demonstrated that this model can also be used to estimate the variation in wall permeability along a filter length by fitting the model predictions to velocity data, providing a non-destructive way of probing the wall structure by measuring perturbations to the gas transport. By applying this method to the MRI velocity data acquired for the four GPF samples, estimates of the wall permeability and hence the washcoat distribution were obtained for the samples (Fig. 7.14 (i)). These estimates agreed well with the expectations from the destructive MIP measurements, e.g. GPF B showing an ‘overlap’ distribution and GPF D a ‘gap’ distribution. All the washcoated samples estimated a lower permeability at all positions compared to the bare sample (GPF A), as expected and again consistent with the MIP data. The permeability profiles also revealed non-uniformities on a smaller scale than the MIP measurements. GPF C, whilst largely uniform in the middle, shows lower permeabilities at the front and rear. This is thought to be due to migration of the washcoat during the drying process and is similar to the observations of Nishina *et al.* [22]. Koci *et al.* also observed high variation in the local permeability of similarly washcoated samples [13]. This variation occurred over scales of about the channel diameter and local measurements were between 50% and 250% of the mean permeability. The mean permeabilities Koci *et al.* found for CF1 and CF2 (corresponding to GPFs C and D) were $1.2 \times 10^{-12}\,\mathrm{m}^2$ and $0.6 \times 10^{-12}\,\mathrm{m}^2$ respectively. These reported values are similar to the higher permeability predicted in the current study (approximately $1 \times 10^{-12}\,\mathrm{m}^2$ and $0.6 \times 10^{-12}\,\mathrm{m}^2$ respectively) and so may reflect the regions of least washcoat application.

It is expected from the literature that the application of washcoat will affect the pressure drop and filtration behaviours of a filter, though the effects of non-uniform washcoat distributions are not known. Simulations performed using the mean value of the estimated permeability profiles predicted deviations in both the velocity profiles (Fig. 7.14 (ii)) and pressure drop responses (Fig. 7.16) compared with using a uniform permeability set to the mean value of the estimated profiles. For experimentally measured pressure drops, this means that the permeability will be underestimated if a uniform permeability across the filter is assumed. Similarly for PM filtration, the washcoat distribution affects the location and efficiency of PM deposition (Fig. 7.17). Due to the size distributions expected for gasoline PM, the changes in pore structure from washcoat application (Table 7.2) are expected to be minor contributors to the changes in filtration efficiency, with the majority resulting from the changes to the through-wall velocity and hence PM flux. In particular, it appears that washcoat loadings that create small regions of large through-wall velocities, as in GPF D, may cause a reduction in the overall filtration efficiency. This is in contrast to the expected behaviour of washcoat application whereby the filtration efficiency increases.

7.8 Conclusions

Four GPF samples were prepared with different washcoating procedures: one without washcoat (A), one with non-catalytic washcoat applied in-wall by dip coating (B), one with catalytic washcoat applied in-wall by precision coating (C), and one with catalytic washcoat applied both in-wall and on-wall by dip coating (D). A visual inspection revealed both dip coated samples (GPFs B and D) had non-uniformities in their appearance. GPF D also had visible washcoat layers at the front and rear; the thickness and distribution of these layers varied between different channels. Mercury intrusion porosimetry performed at three spatial locations (front, middle and rear) of each sample similarly revealed spatial non-uniformities in the porosity of the dip coated samples; GPF B showed a lower porosity in the middle and GPF D showed a higher porosity. The precision coated filter showed some variation in porosity but much less than observed in the dip coated samples. From these results, dip coating appears to be a less reliable method for applying a uniform washcoat to filters.

Magnetic resonance velocity imaging was used to measure the axial and through-wall velocity profiles in all four samples, including those with paramagnetic Pd in the washcoat, for gas flows of $\mathrm{Re}_\mathrm{c} \approx 1000$. The observed velocity profiles varied greatly between the different filter samples. Greatest deviation from the bare substrate flow profiles was observed for GPF D, which also showed the greatest variation in gas velocity between different channels. The perturbations in the through-wall velocity profiles qualitatively agreed with the mercury porosimetry measurements.

A 1D numerical model of gas flow in a filter was used to non-destructively predict the wall permeability in each sample. This was performed by fitting the velocity predictions of the model to the MRI measurements and allowing spatial variation of the wall permeability. The results agreed with the porosimetry measurements and revealed variations in wall structure on a smaller scale. Hence the MRI method gives information on both transport and structure from the same measurement. GPF C showed a uniform permeability profile for most of the filter but lower permeabilities at the very front and rear. It was predicted with the model that using a uniform, mean permeability, as is measured from pressure drop measurements, gives incorrect velocity profile predictions and underpredicts the pressure drop response with increasing flow rate.

From these results, the washcoating process appears to greatly impact the structure of and gas transport inside filters. In particular, non-uniform washcoat distributions are seen for both in-wall and on-wall washcoat loading, and for dip and precision coating methods. The degree of non-uniformity appears to be lower for precision coating. Non-uniform washcoat distribution cause perturbations in the gas transport that adversely affects the pressure drop response and may worsen filtration or catalyst behaviour. It is unclear as to the relative contribution of washcoat formulation or application process to these issues and further work will be required.

7.9 References

[1] C. Lambert, T. Chanko, D. Dobson, X. Liu, J. Pakko. Gasoline Particle Filter Development. *Emission Control Science and Technology* (2017) 3 (1), 105–111. doi: 10.1007/s40825-016-0055-x.

[2] Y. Ito, T. Shimoda, T. Aoki, K. Yuuki, H. Sakamoto, K. Kato, D. Thier, P. Kattouah, E. Ohara, C. Vogt. Next Generation of Ceramic Wall Flow Gasoline Particulate Filter with Integrated Three Way Catalyst. *SAE Technical Paper Series* (2015) 2015-01-1073. doi:10.4271/2015-01-1073.

[3] T. A. Nijhuis, A. E. W. Beers, T. Vergunst, I. Hoek, F. Kapteijn, J. Moulijn. Preparation of monolithic catalysts. *Catalysis Reviews* (2001) 43 (4), 345–380. doi: 10.1081/CR-120001807.

[4] T. Vergunst, F. Kapteijn, J. A. Moulijn. Monolithic catalysts - Non-uniform active phase distribution by impregnation. *Applied Catalysis A: General* (2001) 213 (2), 179–187. doi:10.1016/S0926-860X(00)00896-6.

[5] D. Aderhold, A. Haynes, M. Spencer, D. Winterborn. Monolith coating apparatus and method therefor (2006) U.S. Patent 7,147,892.

[6] D. Roberts, A. Bortz, A. Troland, R. Rose, R. Fortner. Method of coating a substrate with a catalyst component (2014) U.S. Patent 2014/0356530 A1.

[7] G. Chandler, K. Flanagan, P. Phillips, P. Schofield, M. Spencer, H. Strutt. Coating a monolith substrate with catalyst component (2014) U.S. Patent 8,703,236.

[8] M. J. Hazlett, W. S. Epling. Heterogeneous catalyst design: Zoned and layered catalysts in diesel vehicle aftertreatment monolith reactors. *The Canadian Journal of Chemical Engineering* (2019) 97 (1), 188–206. doi:10.1002/cjce.23293.

[9] H. Nakayama, Y. Banno, H. Mochizuki, H. Hara, A. Takayama, M. Nagata, Y. Sasaki, S. Yoneyama. Development of GPF Using Micro-CT Measurement and Numerical Analytical Technique. *Topics in Catalysis* (2019) pp. 1–7. doi:10.1007/s11244-019-01136-7.

[10] V. Novák, P. Kočí, T. Gregor, J.-S. Choi, F. Štěpánek, M. Marek. Effect of cavities and cracks on diffusivity in coated catalyst layer. *Catalysis Today* (2013) 216, 142–149. doi:10.1016/J.CATTOD.2013.07.002.

[11] M. Václavík, M. Plachá, P. Kočí, M. Svoboda, T. Hotchkiss, V. Novák, D. Thompsett. Structure characterisation of catalytic particulate filters for automotive exhaust gas aftertreatment. *Materials Characterization* (2017) 134, 311–318. doi:10.1016/j.matchar.2017.11.011.

[12] M. L. Stewart, C. J. Kamp, F. Gao, Y. Wang, M. H. Engelhard. Coating Distribution in a Commercial SCR Filter. *Emission Control Science and Technology* (2018) 4 (4), 260–270. doi:10.1007/s40825-018-0097-3.

[13] P. Kočí, M. Isoz, M. Plachá, A. Arvajová, M. Václavík, M. Svoboda, E. Price, V. Novák, D. Thompsett. 3D reconstruction and pore-scale modeling of coated catalytic filters for automotive exhaust gas aftertreatment. *Catalysis Today* (2019) 320, 165–174. doi:10.1016/J.CATTOD.2017.12.025.

[14] P. M. T. Maunula, M. Louhelainen, P. Juvonen, and T. Kinnunen. Catalyzed Particulate Filters ofr Mobile Diesel Applications (2007). doi:http://dx.doi.org/10.4271/2007-01-0041.

[15] K. Tsuneyoshi, O. Takagi, K. Yamamoto. Effects of Washcoat on Initial PM Filtration Efficiency and Pressure Drop in SiC DPF. *SAE Technical Paper Series* (2011) 2011-01-0817. doi:10.4271/2011-01-0817.

[16] D. Karamitros, G. Koltsakis. Model-based optimization of catalyst zoning on SCR-coated particulate filters. *Chemical Engineering Science* (2017) 173, 514–524. doi:10.1016/J.CES.2017.08.016.

[17] H. Kong, K. Yamamoto. Simulation on soot deposition in in-wall and on-wall catalyzed diesel particulate filters. *Catalysis Today* (2018) 332, 89–93. doi:10.1016/J.CATTOD.2018.07.022.

[18] X. Liu, T. Chanko, C. Lambert, M. Maricq, F. Motor. Gasoline Particulate Filter Efficiency and Backpressure at Very Low Mileage. *SAE Technical Paper* (2018) 2018-01-1259. doi:10.4271/2018-01-1259.

[19] A. Wahlberg, L. J. Pettersson, K. Bruce, M. Andersson, K. Jansson. Preparation, evaluation and characterization of copper catalysts for ethanol fuelled diesel engines. *Applied Catalysis B: Environmental* (1999) 23 (4), 271–281. doi:10.1016/S0926-3373(99)00083-1.

[20] N. P. Ramskill. *Magnetic Resonance Studies of Diesel Particulate Filters*. Doctoral thesis, University of Cambridge (2015).

[21] Z. R. Ismagilov, S. A. Yashnik, A. A. Matveev, I. V. Koptyug, J. A. Moulijn. Characteristics of drying and active component distribution in alumina monoliths using ^{1}H-NMR imaging. *Catalysis Today* (2005) 105 (3-4), 484–491. doi:10.1016/j.cattod.2005.06.054.

[22] S. Nishina, K. Takeuchi, M. Shinohara, M. Imamura, M. Shibata, Y. Hashimoto, F. Watanabe. Novel Nondestructive Imaging Analysis for Catalyst Washcoat Loading and DPF Soot Distribution Using Terahertz Wave Computed Tomography. *SAE International Journal of Fuels and Lubricants* (2011) 5 (1), 2011–01–2064. doi:10.4271/2011-01-2064.

[23] T. J. Toops, H. Z. Bilheux, S. Voisin, J. Gregor, L. Walker, A. Strzelec, C. E. Finney, J. A. Pihl. Neutron tomography of particulate filters: a non-destructive investigation tool for applied and industrial research. *Nuclear Instruments and Methods in Physics Research Section A: Accelerators, Spectrometers, Detectors and Associated Equipment* (2013) 729, 581–588. doi:10.1016/J.NIMA.2013.08.033.

[24] S. Aleksandrova, J. Saul, H. Medina, O. Garcia-Afonso, C. Lin, J. M. Herreros, M. Bevan, S. F. Benjamin. Gasoline Particulate Filter Wall Permeability Testing. *SAE International Journal of Engines* (2018) 03-11-05-0039. doi:10.4271/03-11-05-0039.

[25] S. Bensaid, D. L. Marchisio, D. Fino. Numerical simulation of soot filtration and combustion within diesel particulate filters. *Chemical Engineering Science* (2010) 65 (1), 357–363. doi:10.1016/j.ces.2009.06.051.

[26] E. J. Bissett. Mathematical model of the thermal regeneration of a wall-flow monolith diesel particulate filter. *Chemical Engineering Science* (1984) 39 (7-8), 1233–1244. doi:10.1016/0009-2509(84)85084-8.

[27] E. J. Bissett, M. Kostoglou, A. G. Konstandopoulos. Frictional and heat transfer characteristics of flow in square porous tubes of wall-flow monoliths. *Chemical Engineering Science* (2012) 84, 255–265. doi:10.1016/J.CES.2012.08.012.

[28] M. Kostoglou, E. J. Bissett, A. G. Konstandopoulos. Improved Transfer Coefficients for Wall-Flow Monolithic Catalytic Reactors: Energy and Momentum Transport. *Industrial & Engineering Chemistry Research* (2012) 51 (40), 13062–13072. doi:10.1021/ie3011098.

Chapter 8

Structure-transport evolution in operating commercial GPFs

8.1 Introduction

During the operation of an automobile, PM-laden exhaust gas passes through the particulate filter and the soot is deposited inside. However, the micro- and macroscopic distribution of this soot deposition impacts the subsequent filtration behaviour, pressure drop, regeneration behaviour and ultimately the useful lifetime of the filter. Hence, a complete understanding of the filtration process is needed in order to optimise the function of particulate filters. An overview of the principle effects of soot loading is given here.

During the first stages of filtration, soot particles deposit in the pores of the filter wall and narrow the pore structure, decreasing the wall permeability and increasing Darcy losses. After a certain amount of soot loading, the PM begins to deposit on the surface of the walls and forms a seperate layer known as the soot cake. Continued filtration results in growth of the soot cake and further increases in the pressure drop across the filter wall. This is illustrated in Fig. 8.1. At very high loadings, soot can accumulate greatly at the rear of the inlet channels, blocking them and reducing the effective length of the filter.

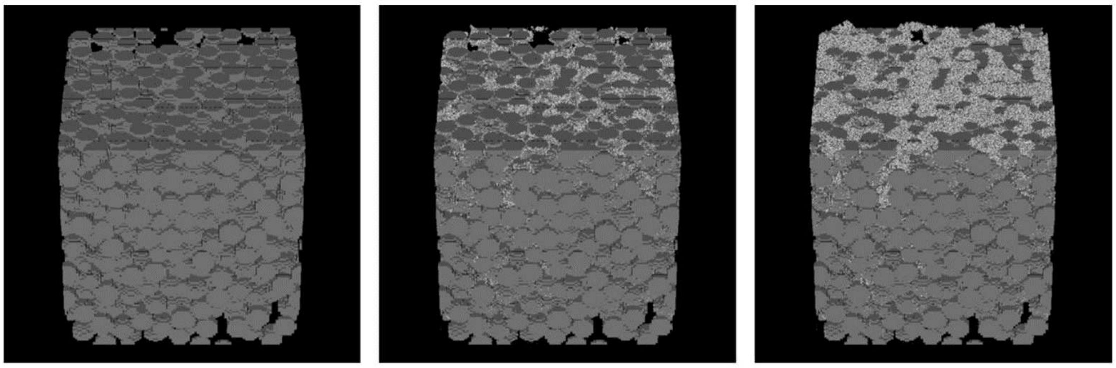

(a) (b) (c)

Fig. 8.1: Simulations showing the microscopic distribution of 0.2 µm diameter particles (light grey) depositing in a model porous wall (dark grey) after (a) 0, (b) 2×10^6 and (c) 5×10^6 particles deposited. Taken from [1].

In addition to the filtration of soot-based PM, particulate filters also capture ash particles. Ash is typically formed from inorganic compounds present in the engine oil and are not readily oxidised to gaseous species. Because of this, ash cannot be removed through thermal regeneration processes and will remain in the filter. This can be beneficial as it can improve the filtration efficiency of gasoline particulate filters under low soot loadings, but this occurs at the detriment of increased pressure drop across the filter and possible deactivation of the catalyst. This deactivation can occur due to poisoning, typically from phosphorus, sulfur, zinc and calcium-containing species, or from blocking of pores in the filter. As the ash content of exhaust gas is low compared to the PM content, ash build-ups are not expected to be a problem for low-mileage vehicles.

The filtration of soot and ash particles is expected to be highly affected by the gas transport inside filters. As most particulates are under 1 µm in diameter, they will largely follow the gas streamlines in the filter and so high PM flux will occur in regions of high through-wall velocity. However, as the deposited particulates change the filter structure, this will perturb the gas flow fields and hence the filtration behaviour of the entire filter. Similarly, the regeneration process is also expected to be dependent on the gas hydrodynamics as this will control both the heat and mass transfer of oxidative species.

While modelling and macroscopic measurements of these effects have been performed by many authors, there is a lack of experimental work focusing on the relationship between the filter structure, the gas transport and the perturbations of these by the loaded soot. This chapter aims to explore this relationship using MRI and 1D modelling.

8.2 Scope of study

In this chapter, the effects of soot loading on the structure of the filter porous wall and gas transport inside the filter are probed using the MRI methods of previous chapters. Two commercial catalysed GPFs were used, one with an in-wall catalyst and one with an on-wall catalyst. Samples from each filter were loaded with PM from a real-world gasoline engine. Three different loading protocols were used. The gas flow fields inside the filter samples were measured using MRI velocimetry. This data was then used to estimate the permeability profiles for each filter sample. Together, the evolution of the gas flow fields and porous wall permeability with soot loading are explored and related.

8.3 Literature review

Due to complicated nature of filter structures, many studies have focused on global measurements, e.g. filtration efficiency and pressure drop. Konstandopoulos and Johnson developed one of the first models of flow and filtration in a DPF system [2]. The underlying flow descriptions, based on Bissett's original 1D model [3] were validated against pressure drop measurements. The filtration model was formulated using analytical expressions for Brownian and interception collections on a single spherical collector, and was validated using collection efficiency measurements for particles over 0.1 µm in diameter. This model was later extended to allow for transient loading and regeneration [4], showing good agreement with pressure drop measurements for a range of soot loadings and filter properties. The model predicted the filtration efficiency to increase with loading time as more soot accumulates in the filter, especially for particles with diameters in the range 0.1 µm to 1 µm. All filters studied showed the expected pressure drop behaviour with increasing soot load, i.e. an initial induction period followed by a linear increase. Work by Sappok and Wong investigated the effects of lubricant-derived ash on the pressure drop of DPFs [5]. The increase in pressure drop with increasing ash load followed the same trends expected from soot loading, though ash showed a lower increase in pressure drop than soot for the same mass loading. At high ash loadings, plugs were observed to form at the rear of the inlet channels, though these had a lower density than the ash found in the cake layers. The presence of ash also affected the sensitivity of the pressure drop to soot loading; higher ash loadings caused a greater relative increasing in pressure drop with soot loading. Custer *et al.* performed a similar study with GPFs, loading samples with up to $30.5\,\mathrm{g\,l^{-1}}$ of ash and observing similar behaviour in the pressure drop response [6]. Lambert *et al.* also studied the effects of ash on filter performance, this time extending to the filtration behaviour [7]. Low ash loads of 1 g to 2 g increased the filtration efficiency from around 60% to 80% for a relatively modest increase in pressure drop (20-30%) compared with a bare GPF. Liu *et al.* extended this work to study the effects of washcoat in addition to ash loading [8]. Filters with applied washcoat showed lower filtration efficiencies than their bare counterpart under no soot or ash loading. This was attributed to the narrowing of pore diameters by the washcoat causing an increase in gas Peclet number and a reduction in Brownian deposition of small particulates. The addition of ash to the washcoated filters improved their filtration efficiency. All filters studied showed the expected pressure drop behaviour with increasing soot load. However, while the ash-laden filters had a greater pressure drop at low soot loading, they showed a lower pressure drop at higher soot loadings.

There has been interest in the microscopic mechanisms and effects of soot deposition, i.e. the interaction of the PM with the porous structure of the filter and the resulting changes to it. Due to the difficult and often destructive nature of measuring microstructure, many authors have used simulations to study the process. Hayashi *et al.* simulated the flow of gas and deposition of soot inside the filter wall using Lattice Boltzmann and Brownian dynamics methods with the wall being modelled as a packing of spheres [1]. The authors found that the filtration efficiency decreased as the the collector sphere diameter increased, ostensibly due to the higher interstitial gas velocity as the porosity decreases. Jiang *et al.* performed similar simulations exploring the effect of ash loading on filtration efficiency [9]. For no ash loading, the filtration efficiency was predicted to be unity for very small and large particles but lower for those with diameters in the range 100 µm to 300 µm. As the ash loading was increased, the filtration efficiency in this range was predicted to increase, as was the pressure drop. Gong *et al.* applied a heterogeneous multiscale filtration model to a GPF geometry, allowing both transient and spatially resolved simulations of filtration across the porous wall [10]. As filtration proceeded, the model predicted the mean collector diameter to increase, most particulates to deposit in the first 20% of the wall thickness and the filtration efficiency to increase. While pressure drop predictions agreed well with measurements, the simulations underpredicted the overall filtration efficiency. Custer *et al.* observed that above a critical loading of between $4\,\mathrm{g\,l^{-1}}$ and $8\,\mathrm{g\,l^{-1}}$, ash plugs began to form at the rear of the inlet channels [6]. This was attributed to the switch of deposition mechanism from deep bed filtration in the pores to cake layer filtration on the surface which is then blown down the channels. The authors hypothesised that the ash loading in the pores prevents deep bed filtration of subsequent soot, forcing a cake layer to form and improving the pressure drop response of the filter. Kamp *et al.* took an experimental approach, measuring the pressure drop across and microstructure of ash-laden cordierite wafers [11]. It was found that the packing density had a large effect on the permeability of the wafer, with the calculated permeabilities varying over nearly four orders of magnitude. X-ray μ-CT images showed ash deposits located primarily on the outside of the filter wall and not inside the porous structure. Kong and Yamamoto performed simulations of gas and soot flow through two catalysed DPFs [12]. The two samples possessed on-wall and in-wall catalysts respectively, and the microstructure was measured using X-ray CT. The authors modelled the washcoat as a uniform porous medium described by Darcy's law. The simulations predicted similar pressure drop behaviour for both samples. The in-wall catalyst narrowed the porous structure and increased flow channelling, whereas the on-wall catalyst had little effect on the wall pores and so the flow behaviour was relatively unchanged compared to the bare substrate. This is in contrast to the findings of Koci *et al.* who found that the microstructure of the on-wall catalyst is important in determining the gas transport to the pores of the filter wall [13]. This discrepancy is likely due to the differences in modelling of the washcoat layer. Kong and Yamamoto predicted that, for the in-wall catalyst, soot initially deposits in the first $100\,\mu\mathrm{m}$ of the filter wall before the pores become too constricted and the soot forms a cake layer on the surface. It is this two-step behaviour that gives rise to the induction-linear behaviour of the pressure drop as soot is filtered. For the on-wall catalyst, the soot formed a cake layer immediately on the catalyst layer. However, this is expected to be incorrect for anything other than a perfectly uniform and crack-free catalyst coating.

Knowledge of the soot loading distribution within a filter is important to ensure successful operation and regeneration of the filter system. However, the structure of particulate filters makes measuring the soot distribution difficult. Some studies have successfully applied a small number of imaging modalities to this problem. Ismail *et al.* demonstrated neutron tomography as a method of measuring the spatial location of soot deposition in DPFs [14]. Neutrons, unlike X-rays, are scattered by hydrogen atoms and so are sensitive to the hydrocarbon constituents of PM. The study found agreement between the neutron tomography data and 'direct measurements' to within 16%, though it is not specified what these 'direct measurements' are. Time on neutron beams can be scarce and the only subsequent use of the technique was by Toops *et al.*, who used the method to probe washcoat and soot locations in cordierite filters [15]. Toops found largely uniform axial soot deposition for loadings of $3\,\mathrm{g\,l^{-1}}$, $5\,\mathrm{g\,l^{-1}}$ and $7\,\mathrm{g\,l^{-1}}$ in terms of soot cake thickness. Nishina *et al.*, using a Terhertz wave tomography technique, found a similar uniform profile for a catalysed DPF loaded with $1\,\mathrm{g\,l^{-1}}$ of PM, though more PM was observed at the filter rear for a loading of $3\,\mathrm{g\,l^{-1}}$ [16]. Foley *et al.* used a similar Terahertz technique to measure the axial deposition profiles in a catalysed filter [17]. After soot loading, the axial distribution was found to be near-uniform with a slight decrease at the front, increase at the rear and a small dip in the centre. The distribution was similar following passive regeneration but was more uniform following an active regeneration.

In lieu of a standardised, cheap and robust methodology for measuring the PM distribution in filters, investigators have used numerical models to simulate the filtration process and derive distributions from this. Sbrizzai *et al.* performed 3D CFD simulations of gas and PM flow in a particulate filter system, with particulate diameters of $0.2\,\mathrm{\mu m}$ and $2\,\mathrm{\mu m}$ [18]. Due to the *vena contracta* predicted at the filter entrance, little deposition occurred in the first fifth of the filter length. The profile for the rest of the filter largely followed the shape of the through-wall velocity profile, with a slighlty increased deposition at the filter rear (Fig. 8.2 (a)). The authors noted that filtration occurred more at the edges of the filter wall (i.e. at the channel corners) than in the wall centre. Bensaid *et al.* performed similar simulations for 0.1, 0.2, 0.5 and $2\,\mathrm{\mu m}$ diameter particulates [19]. The $2\,\mathrm{\mu m}$ particles showed a similar deposition profile as predicted by Sbrizzai *et al.*, however all smaller diameters were predicted to follow the through-wall velocity shape and showed no deviation due to *vena contracta* (Fig. 8.2 (b)). Over longer timescales, the deposition profile was predicted to become more uniform as the soot layer grows and reduces the local permeability of the filter wall; the soot cake thickness predictions were found to agree with SEM measurements of a sooted filter [20]. More recently, Kong *et al.* have used a lattice Boltzmann cellular automation model, building on the previous work probing microscopic deposition, to simulate gas flow and soot deposition across the entire length of a filter. The authors studied three superficial flow rates, $1\,\mathrm{m\,s^{-1}}$, $3\,\mathrm{m\,s^{-1}}$ and $6\,\mathrm{m\,s^{-1}}$ ($\mathrm{Re_c} \approx 30$, 90 and 180 respectively), and three PM diameters, $0.01\,\mathrm{\mu m}$, $0.1\,\mathrm{\mu m}$ and $1\,\mathrm{\mu m}$ [21]. The permeability of the porous wall was not specified but the porosity was 38.16%. At $1\,\mathrm{m\,s^{-1}}$, the PM deposition profile for all sizes was largely uniform along the length of the filter, which may reflect the through-wall velocity profile given the porosity used. If so, this would be in agreement with the previous work of Sbrizzai and Bensaid. At $6\,\mathrm{m\,s^{-1}}$, deposition of all PM sizes was predicted to be greater at the rear of the filter, with little deposition at the front. Most particles were predicted to deposit in the first 20% of the porous wall.

There has been very little work performed on the impact of soot loading on the gas transport inside the filter. The only experimental work on this is by York *et al.*, who measured the gas flow fields inside a PF that had been loaded with soot from a Lister-Petter engine [22]. The nature of the engine meant that only the effects of high soot loading were observed. The soot loading had three main effects on the gas flow fields. First, the change

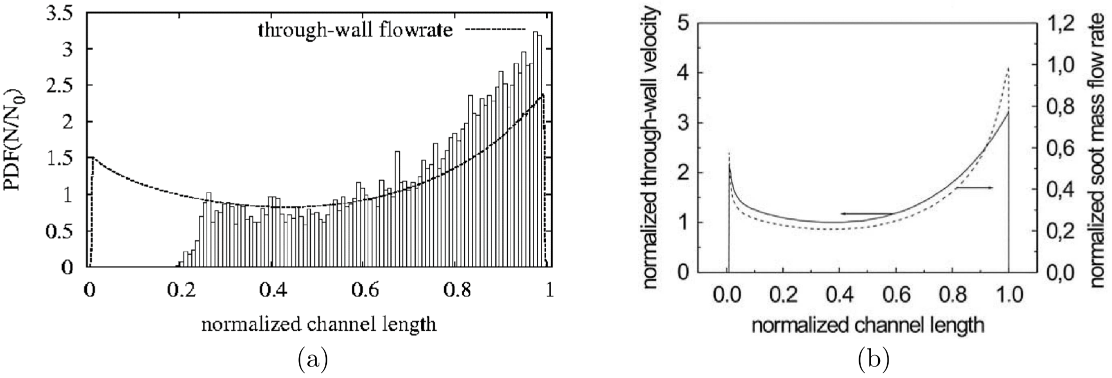

(a) (b)

Fig. 8.2: (a) Predicted through-wall velocity (solid line) and mass flow rate of 0.1 µm diameter particles (histogram) from Sbrizzai *et al.* [18]. (b) Predicted through-wall velocity (solid line) and mass flow rate of 0.2 µm diameter particles (dotted line) from Bensaid *et al.* [19].

in axial velocity with axial position became much more linear, corresponding to a more uniform through-wall velocity as expected from a reduction in wall permeability. Second, the cross-sectional flow profile in the channels became narrower as a soot cake formed. Third, the through-wall velocity decreased greatly at the very rear of the filter as soot plugs formed. The latter two phenomena are illustrated in Fig. 8.3. This demonstrates the extreme effects of soot loading and why regeneration is required. However, it does not elucidate the transient soot loading behaviour or the effects of moderate soot loadings.

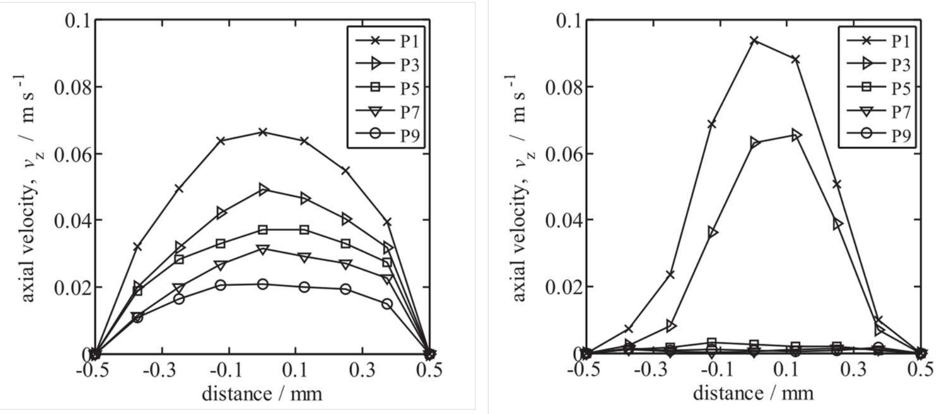

(a) (b)

Fig. 8.3: Velocity profiles inside inlet channels for (a) a soot-free DPF and (b) a heavily sooted DPF. P1 to P9 refer to increasing axial positions along the filter length. Taken from York *et al.* [22].

8.4 Experimental

8.4.1 Materials

Two commercial filters supplied by Johnson Matthey were used in this study. The filters differed in their washcoat properties; one had washcoat applied in-wall only (GPF A) and one had washcoat applied on-wall only (GPF B). The washcoat on both filters contained a platinum group metal catalyst. Both filters were made of a cordierite substrate with a total length of 155 mm, a plug length of 5 mm, square channel side length of 1 mm and a wall thickness of 0.3 mm.

8.4.2 Soot loading

Soot loading was performed using a 2 l, 4 cylinder GDI turbocharged engine. Such engines are typical of modern-day gasoline powered passenger automobiles. The engine was run at 2100 rpm, producing a torque of 60 N m. Three 25 mm diameter cores were bored from the centre of each filter, each acting as a sample for the soot loading. The filter sample to be loaded was held downstream inside the exhuast manifold. The manifold was surrounded by a furnace, allowing the temperature of the filter to be held at different temperatures. A temperature of 300 °C was chosen as representative of real-world gasoline exhausts; the temperature was measured using a thermocouple inserted into the manifold upstream of the filter. This temperature is expected to facilitate some degree of passive regeneration within the filter. Two pressure transducers were placed either side of the filter sample, allowing measurement of the pressure drop during the loading process. Measurements were made at 180 ms intervals at both transducers. The pressure readings were subtracted and averaged over 2 min intervals to give the transient pressure drop. Three sooting protocols were used. The first was no soot loading (protocol I). The second was normal running of the engine for 50 min (protocol II). The third was normal running of the engine for 50 min, followed by 10 min of accelerated soot loading (protocol III). This was achieved by delaying the fuel injection by a crank-shaft angle of 50 degrees. All soot loading was performed by Ammar Wahbi, George Brinklow and Kyriakos Kallis at the Department of Mechanical Engineering, University of Birmingham. Photographs along the length of each substrate were taken to observe any changes to the filter appearance.

8.4.3 Magnetic resonance imaging

The magnetic resonance experiments were performed following the protocol of Chapters 6 and 7. Eleven images were acquired along the length of the filter, each with a slice width of 6 mm. A gas pressure of 5.0±0.1 bar(g) and mass flow rate of 16 g min^{-1} was used for each sample. Due to the differences in flow bypass and overall filter permeability, this did not result in similar channel Reynolds numbers for all filter samples. Axial velocity profiles were acquired for both GPF samples after all three soot loading protocols. The mean volume flow for each sample agreed with the value calculated from the mass flow rate to within 8.5%. The through-wall velocities were calculated for each based on the gas mass balance. Velocity profiles inside the inlet channels were extracted from the MR velocity images through the mid-point of the channels parallel to the filter wall. The fitting of model predicted velocity profiles to the MRI data was performed as described in Chapter 7.

8.5 Results

The results of the study are presented here in three parts. First, the effects of the soot loading on the pressure drop and the appearance of the filter samples are shown. Second, the changes to the gas transport are shown in the velocity data extracted from the MRI results. Finally, the predicted changes to the filter wall permeability using 1D modelling are given.

8.5.1 Soot loading

The pressure drop measurements across each filter made during soot loading are shown in Fig. 8.4. For GPF A (a), the pressure drop response for protocol II is largely uniform at ∼6.5 kPa across the loading time. Protocol III shows a small increase in the first 10 min of loading followed by a uniform pressure drop until 50 min. This uniform region is ∼2 kPa greater than measured for the protocol II sample. After 50 min, a large increase in pressure drop to 14 kPa is seen. For GPF B (b), the measured response for both protocol II and III are relatively constant for the initial 50 min of loading. The pressure drop for protocol II is about 2 kPa lower than for protocol III. After 50 min, the pressure drop for protocol III increases by about 2 kPa.

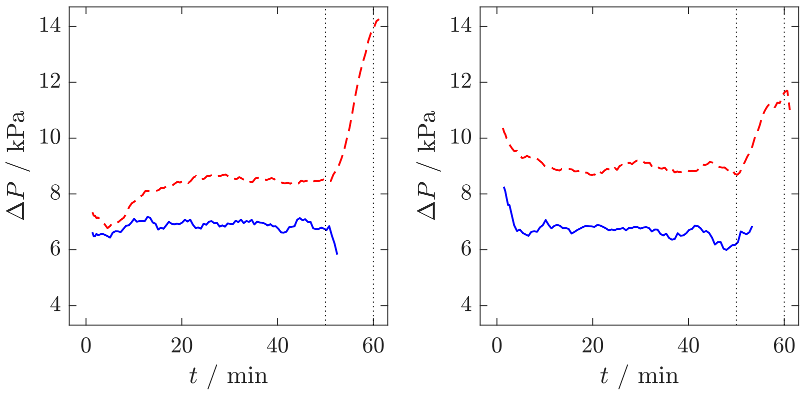

(a) (b)

Fig. 8.4: Pressure drop measurements for the samples (a) GPF A and (b) GPF B subject to loading protocols (——) II and (- - -) III. The vertical dotted lines indicate loading times of 50 min and 60 min.

Photographs of both filter samples after each soot loading protocol are shown in Fig. 8.5. For GPF A (a-c), a clear tide mark is visible in the centre of the filter in the absence of soot (a). Dark regions are also visible in the inlet channels in the front half of the filter and in the outlet channels in the rear half. The regions are most pronounced at the filter ends and taper towards the middle of each channel as they progress to the filter centre. After protocol II (b), GPF A is visibly similar to the soot-free sample but appears darker in the central region and in the inlet channels towards the filter rear. After protocol III (c), the inlet channels are much darker over most of the filter length due to soot deposition, with the central tide-mark region showing less change. For GPF B (d-f), no tide-marks or other obvious drying-relating features are seen with no soot present, though the inlet-channel is visibly darker in the front three-quarters of the filter (d). The outlet channels are lighter and more uniform in appearance for most of the filter length but are visibly darker at the very rear of the filter. After protocol II (e), the inlet channel appears darker, though this may be due to different levels of washcoat present in the sample. After protocol III (f), the inlet channels are much darker at the rear of the filter due to visible soot deposition. The outlet channels look slightly darker at the channel corners in this region but it is not clear if this is due to soot or washcoat.

(a) GPF A, Protocol I

(b) GPF A, Protocol II

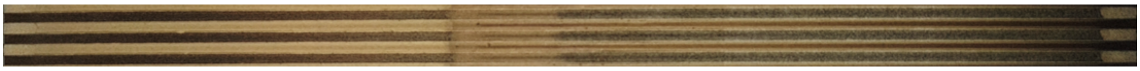

(c) GPF A, Protocol III

(d) GPF B, Protocol I

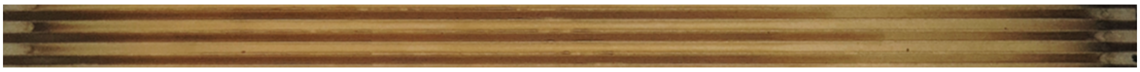

(e) GPF B, Protocol II

(f) GPF B, Protocol III

Fig. 8.5: Axial photographs of GPF (a-c) A and (d-f) B after each soot loading protocol. The brightness and contrast have been increased for clarity. The white marks in (f) are strands of PTFE tape that remained after the sample was unwrapped following the MRI experiments.

8.5.2 Magnetic resonance imaging

The velocity profiles measured for GPF A are shown in Fig. 8.6 for (a) axial and (b) through-wall velocities. Under no soot loading (i), the axial velocity profile resembles those for filters with uniform wall permeability (Chapter 6). The through-wall velocity profile is mostly U-shaped but with a low velocity at the rear and a more uniform velocity at the front. After protocol I of soot loading (ii), the axial profile has only changed slightly, with the change in velocity more linear and the cross-over point occurring further forward in the filter. This registers as a more uniform through-wall velocity, although there is still a parabola-like section in the filter centre. After an additional 10 min of accelerated loading (protocol II), the axial velocity profile shows a linear decrease and increase in the inlet and outlet channel velocity respectively. This corresponds to a highly uniform through-wall velocity profile. One observation is that despite a constant mass flow rate of gas used for all experiments, the most sooted filter (iii) has a lower superficial velocity.

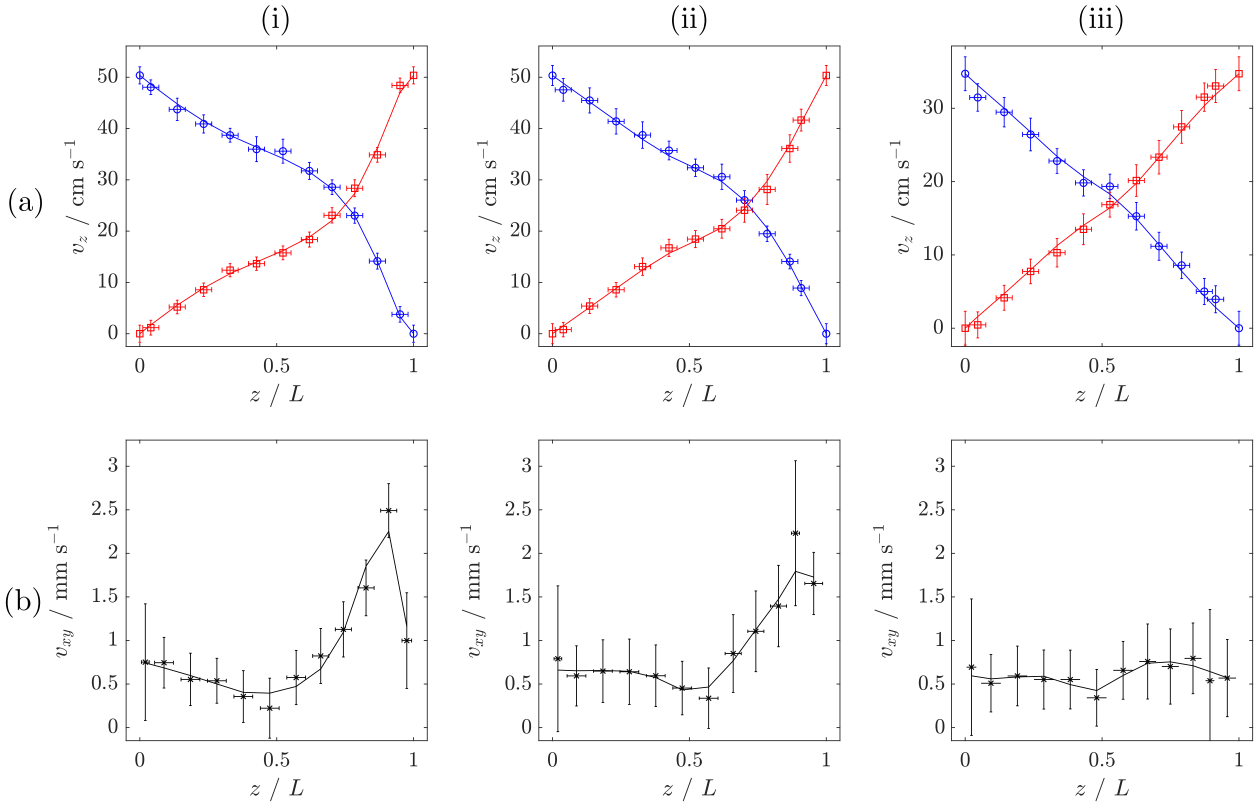

Fig. 8.6: MRI measurements (markers) of the (i) inlet (○) and outlet (□) channel velocities and (ii) through-wall velocities (×) for GPF A with soot loading (a) protocol I, (b) protocol II and (c) protocol III. Lines show the predicted profiles from the 1D model with the fitted permeability profiles.

The velocity profiles for GPF B are shown in Fig. 8.7 for (a) axial and (b) through-wall velocities. Under no soot loading (i), most gas is observed to pass through the filter wall in the rear third of the filter length. The axial velocity profile is largely flat at the front and middle of the filter length with a rapid change around $x/L = 0.8$, causing a large through-wall velocity in this region. After 50 min of soot loading (ii), the general shape of the velocity profiles are similar, though there appears to be a lower thorugh-wall velocity at the very end of the filter. After an additional 10 min of accelerated soot loading (iii), the profiles still look similar. The superficial velocity varies between each level of soot loading.

Axial velocity profiles were extracted from the central inlet channel of each MRI dataset. to show the evolution of the flow profile at different axial positions with increasing soot load. The velocity profiles are shown for both GPF samples in Fig. 8.8 at axial positions of $z/L = 0.14$, 0.33, 0.52, 0.70 and 0.87, referred to as P1, P2, P3, P4 and P5. GPF A (Fig. 8.8 (a)) shows flatter profiles toward the front of the filter that become more parabolic in shape towards the filter rear for all soot loading. The profiles at P1 to P4 are closely bunched for

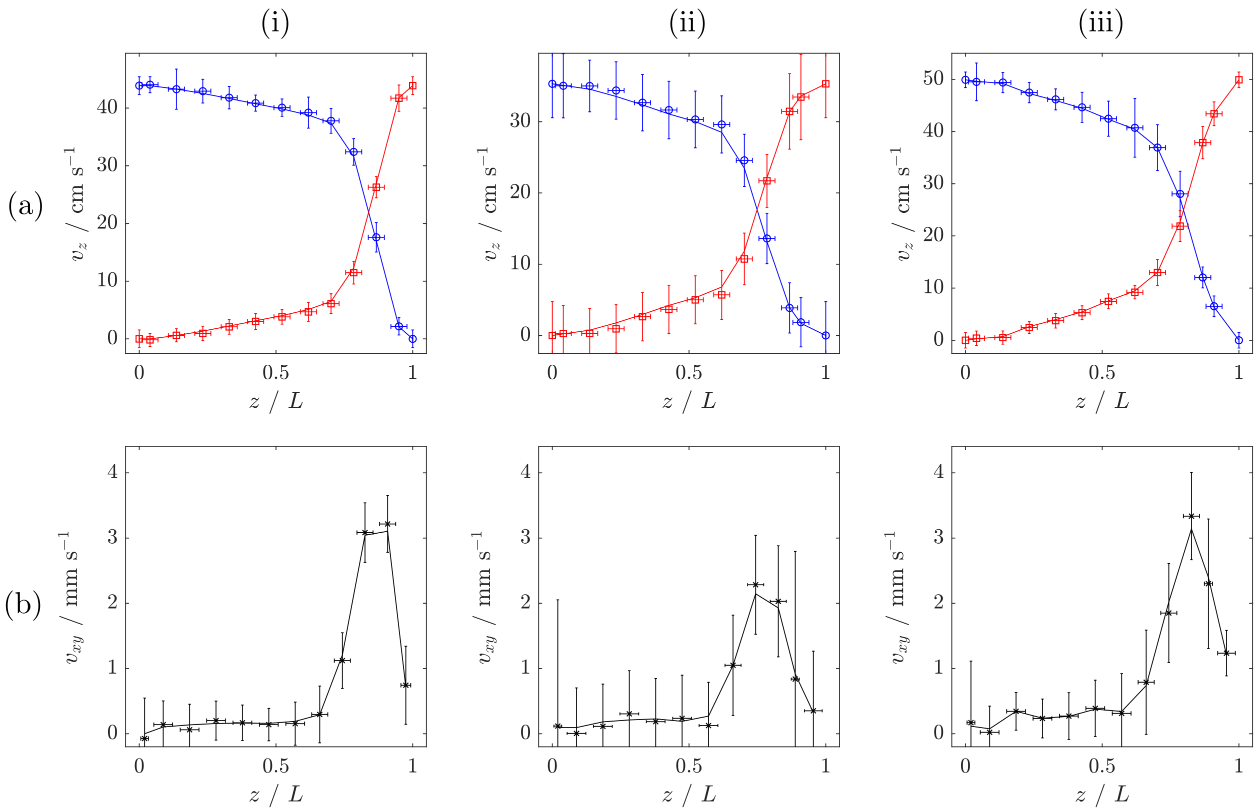

Fig. 8.7: MRI measurements (markers) of the (i) inlet (○) and outlet (□) channel velocities and (ii) through-wall velocities (×) for GPF B with soot loading (a) protocol I, (b) protocol II and (c) protocol III. Lines show the predicted profiles form the 1D model with the fitted permeability profiles.

the soot-free sample (i) but become more spaced out as the soot loading increases. Some profiles show step-like features towards the channel edge e.g. P5 in (i), P3 in (ii) and P1 and P3 in (iii). At the highest soot loading (iii), the shape of the flow profiles at P4 and P5 are narrower than the expected paraboloid. For GPF B (Fig. 8.8 (b)), the flow profiles at P1 to P4 are closely bunched for all three soot loadings. The shape of the profiles become less flat at greater axial positions. As the soot loading increases, the velocity profiles at P5 become narrower.

8.5.3 Numerical modelling

The axial velocity profile predictions from the 1D model were fitted to the MRI measurements for both GPF samples at all soot loadings. The predicted velocity profiles are shown in Figs. 8.6 and 8.7 by the solid lines. The corresponding fitted permeability profiles are shown in Fig. 8.9.

GPF A (Fig. 8.9 (a)) shows a non-uniform permeability profile under no soot loading (i) with a greater permeability in the rear half of the filter ($\sim 1.1 \times 10^{-12}\,\mathrm{m}^2$) compared to the front half ($\sim 0.6 \times 10^{-12}\,\mathrm{m}^2$). After 50 min of soot loading, the permeability across the whole filter is lower and more uniform with a mean of $\sim 0.4 \times 10^{-12}\,\mathrm{m}^2$. Regions of lower

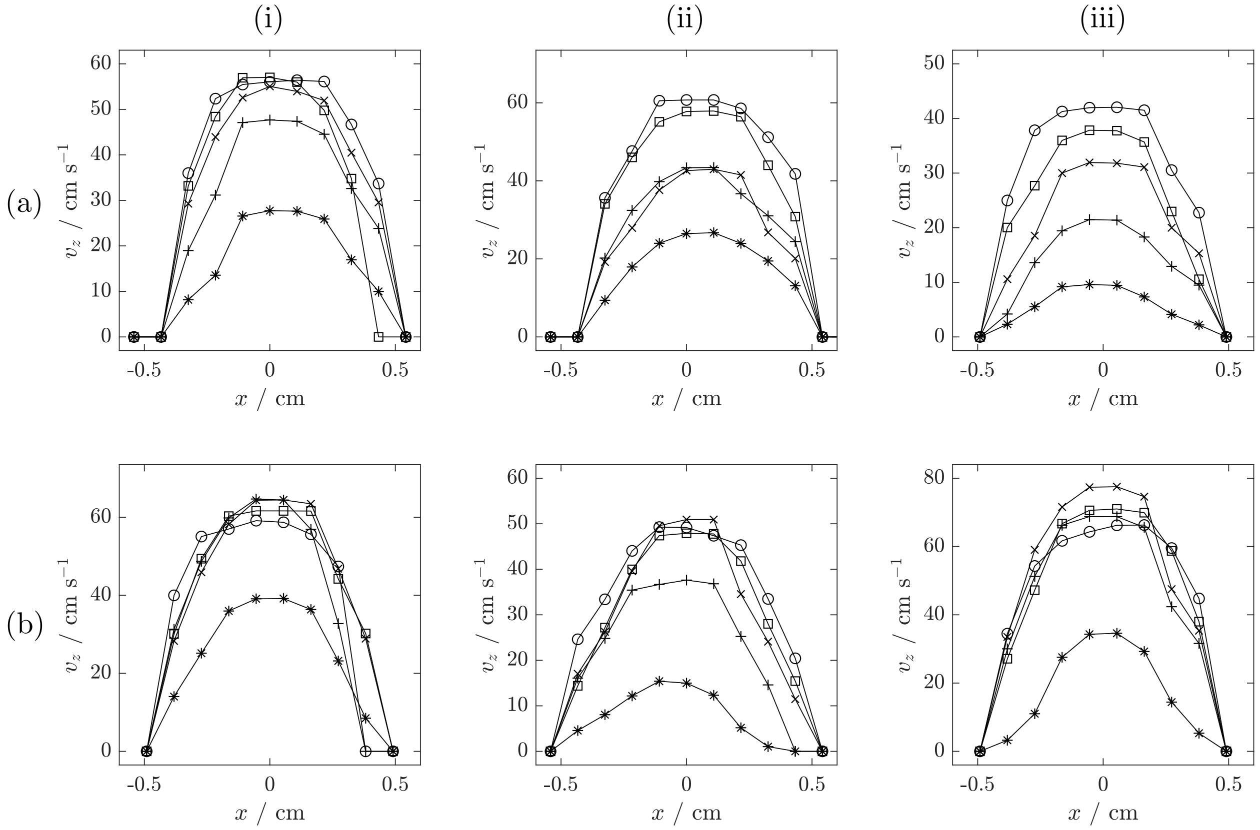

Fig. 8.8: Axial velocity flow profiles for (a) GPF A and (b) GPF B after loading protocols (i) I, (ii) II and (iii) III. Profiles are shown at axial positions of $z/L =$ (□) 0.14, (○) 0.33, (×) 0.52, (+) 0.70 and (✳) 0.87. Lines are shown as a guide for the eye.

permeability are present at the front, middle and rear of the filter. The greatest reduction in the profile has occurred at the filter rear. After an additional 10 min of accelerated soot loading, the permeability is similarly lower and more uniform, with a mean value of $\sim 0.2 \times 10^{-12}\,\mathrm{m}^2$.

GPF B (Fig. 8.9 (b)), under no soot loading, has a non-uniform permeability profile. The permeability in the first three-quarters of the filter length (under $0.2 \times 10^{-13}\,\mathrm{m}^2$) is much lower than in the final quarter, which is around $0.4 \times 10^{-12}\,\mathrm{m}^2$. After 50 min of soot loading (ii), the region of high permeability observed at the rear has decreased to around $0.2 \times 10^{-12}\,\mathrm{m}^2$ but is still markedly greater than the front of the filter. After an additional 10 min of accelerated soot loading, the rear section of the filter has again reduced in permeability to under $0.1 \times 10^{-12}\,\mathrm{m}^2$. The permeability in the front three-quarters of the filter length does not change significantly with soot loading.

The mean permeability for both samples at each soot loading is given in Table 8.1. The error shown is the standard deviation of the mean of each fitted permeability profile. The permeability of both GPFs decreases with increased soot loading and the mean permeability of GPF A is greater than that of GPF B for all protocols.

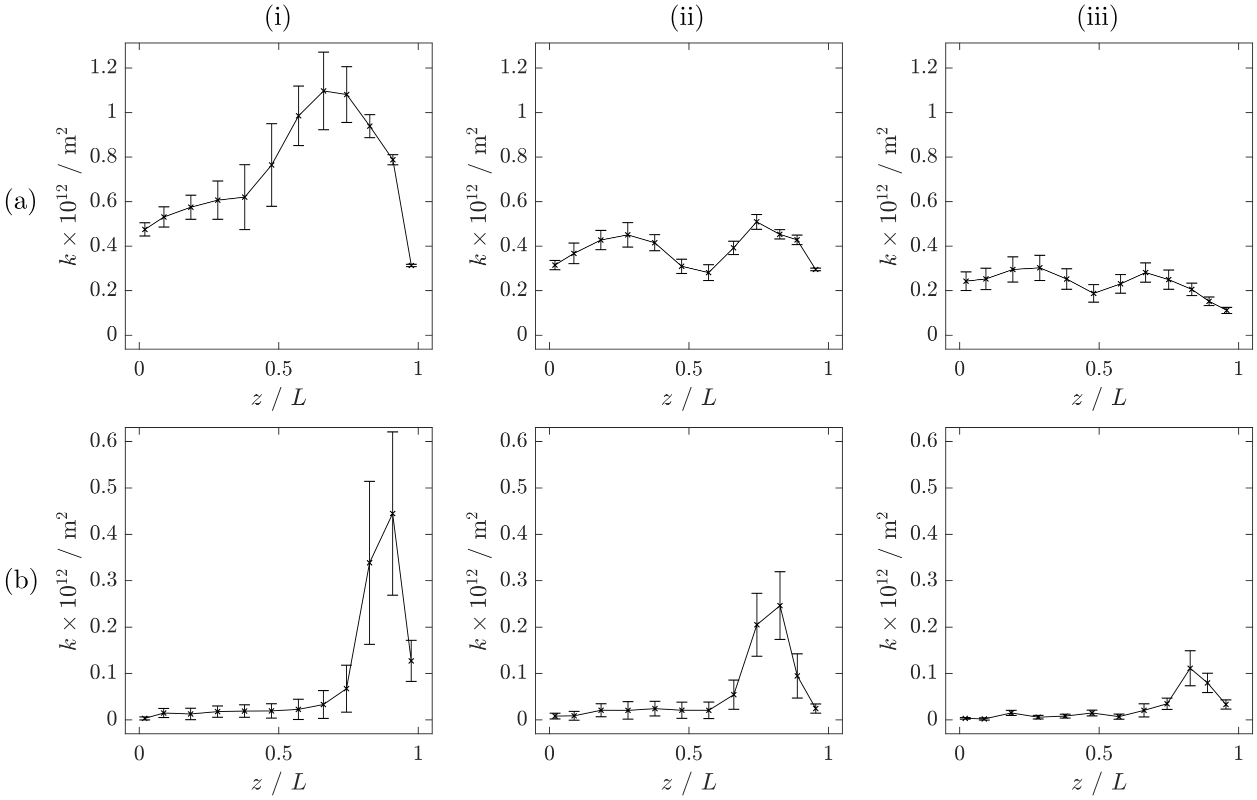

Fig. 8.9: Fitted permeability profiles for (a) GPF A and (b) GPF (b) for sooting protocols (i) I, (ii) II and (iii) III. Lines are shown as a guide for the eye.

Table 8.1: Mean fitted permeabilities for GPFs A and B under the different soot loading protocols. All values are given as $10^{-12}\,\mathrm{m}^2$.

Protocol	GPF A	GPF B
I	0.73 ± 0.07	0.09 ± 0.04
II	0.39 ± 0.07	0.06 ± 0.02
III	0.23 ± 0.04	0.03 ± 0.01

8.6 Discussion

Despite the samples used for soot loading being cut from the same commercial filter and the same engine conditions being used, the pressure drop measurements shown in Fig. 8.4 show different responses for protocols II and III. While this may be due to inconsistencies in the engine operation, it is thought that heterogeneities in the washcoat distribution are responsible; the differences in tide-mark location in GPF A suggest that the radial distribution of washcoat is not uniform in filters (Fig. 8.5 (a-c)). A greater amount of washcoat in one sample would decrease the overall permeability and increase the pressure drop necessary to achieve the desired engine torque. This may contribute the differences in superficial gas velocity seen in GPF B (Fig. 8.7); increased washcoat loading can cause a lower overall permeability and increase flow bypass.

The MRI velocimetry results for both GPF samples under protocol I show that non-uniform washcoat distributions are also present in commercially prepared catalysed GPFs. This is consistent with the observations of Stewart *et al.* [23] and agrees with the visible tide-mark in the centre of the filter (Fig. 8.5 (a)). GPF A shows two distinct regions in the fitted permeability profiles and GPF B shows a region of high permeability at the filter rear (Fig. 8.9 (i)). This is thought to be a result of the washcoating procedure that likely follows the method shown in Fig. 7.2. As discussed in Chapter 7, it may not be obvious from routine quality control measurements that an undesirable washcoat distribution has been produced. This may result in suboptimal filter behaviour, including excessive pressure drop, non-uniform soot loading and poor catalytic conversion. GPF B is predicted to load most soot at the very rear of the filter where the least catalyst loading is expected. This may cause poor regeneration behaviour, an unexpected pressure drop response and lower conversion of other gaseous pollutants. Further investigation into this will certainly be needed.

As a particulate filter operates, it is expected that regions of high through-wall velocity will have a greater loading of soot due to the correspondingly high mass flow of PM. This is observed in both GPF samples; the axial locations that show the greatest reduction in permeability (Fig. 8.9) correspond to the regions of highest through-wall velocity (Fig. 8.6 (b), Fig. 8.7 (b)) and most visible soot deposition (Fig. 8.5). For GPF A, this is primarily the filter rear but also the filter front to a lesser extent. For GPF B, this is the rear fifth of the filter. As the soot decreases the permeability in these regions, the relative through-wall velocity also decreases, increasing the uniformity of both profiles. This demonstrates the 'self-correction' effect predicted by other workers [20, 24]. Two limitations of this method are that it cannot quantify the soot loading and it cannot differentiate between different diameters of soot particle. However, other techniques such as gravimetric analysis or microscopy may allow these to be related to the MRI results. This may allow subsequent comparisons between MRI measurements and models of soot deposition in filters.

As soot loading occurs, the soot may deposit either inside the porous wall or on the wall surface as a cake layer. Visual inspection of the 5×5 channel samples of the filters showed a slight change in the substrate colour after protocol II (Fig. 8.5 (b,e)) and possible soot cakes after protocol III (Fig. 8.5 (c,f)). However, the microscopic location and amount of soot in the filters is not presently known. The axial velocity profiles inside the inlet channels (Fig. 8.8) show changes at the filter rear for both GPF A and B with increasing soot load. The profiles become 'narrower' with lower velocity towards the wall. This is similar to the profiles observed by York *et al.* [22] for high soot loadings in a DPF and may be consistent with the development of a soot cake layer in these regions. These regions also correspond to the largest reductions in wall permeability for both filters (Fig. 8.9), consistent with the visual inspection. The velocity profiles also show differences between regions of less soot loading, such as the step-like features described previously. It is not currently known if these are due to physical effects, e.g. washcoat distribution, or experimental artefacts.

8.7 Conclusions

Samples from two commercial catalysed GPFs with different washcoat locations (in-wall and on-wall) were loaded with different amounts of soot from a real-world gasoline engine. Pressure drop measurements were made for each sample. Different pressure drop responses were observed for the sample filter under the same engine conditions for the same loading time. This was attributed to non-uniform washcoat distributions inside the commercial filters.

Magnetic resonance velocity imaging was used to measure the gas velocity inside the filter samples. For the filter with an in-wall washcoat, the axial velocity profiles become more linear and the through-wall velocity profile more uniform with increasing soot loading. The filter with an on-wall washcoat showed a highly non-uniform through wall velocity with no soot loading, with most gas passing through the last fifth of the filter length. The velocity profiles changed only slightly with increasing soot loading. Both filters showed a narrowing of the cross-sectional flow profile toward the filter rear as the soot loading increased.

Numerical modelling was used to estimate the spatially resolved wall permeability for each filter and soot loading. Both filters showed non-uniform permeability profiles with no soot loading. As the loading increased, the permeability of both filters decreased and the profiles became more uniform. The greatest reductions in permeability were observed in the regions of highest through-wall velocity i.e. the regions where the highest mass flux of PM is expected. This is consistent with the findings of previous workers and with visual inspection of the filter samples after soot loading.

8.8 References

[1] H. Hayashi, S. Kubo. Computer simulation study on filtration of soot particles in diesel particulate filter. *Computers & Mathematics with Applications* (2008) 55 (7), 1450–1460. doi:10.1016/J.CAMWA.2007.08.012.

[2] A. G. Konstandopoulos, J. H. Johnson. Wall-Flow Diesel Particulate Filters-Their Pressure Drop and Collection Efficiency. *SAE Technical Paper Series* (1989) 890405, 810113. doi:10.4271/890405.

[3] E. J. Bissett. Mathematical model of the thermal regeneration of a wall-flow monolith diesel particulate filter. *Chemical Engineering Science* (1984) 39 (7-8), 1233–1244. doi:10.1016/0009-2509(84)85084-8.

[4] A. G. Konstandopoulos, M. Kostoglou, E. Skaperdas, E. Papaioannou, D. Zarvalis, E. Kladopoulou. Fundamental Studies of Diesel Particulate Filters: Transient Loading, Regeneration and Aging. *SAE Technical Paper Series* (2000) 2000-01-1016. doi:10.4271/2000-01-1016.

[5] A. Sappok, V. W. Wong. Lubricant-Derived Ash Properties and Their Effects on Diesel Particulate Filter Pressure-Drop Performance. *Journal of Engineering for Gas Turbines and Power* (2011) 133 (3), 032805. doi:10.1115/1.4001944.

[6] N. Custer, C. J. Kamp, A. Sappok, J. Pakko, C. Lambert, C. Boerensen, V. Wong. Lubricant-Derived Ash Impact on Gasoline Particulate Filter Performance. *SAE International Journal of Engines* (2016) 9 (3), 2016–01–0942. doi:10.4271/2016-01-0942.

[7] C. K. Lambert, T. Chanko, M. Jagner, J. Hangas, X. Liu, J. Pakko, C. J. Kamp. Analysis of Ash in Low Mileage, Rapid Aged, and High Mileage Gasoline Exhaust Particle Filters. *SAE International Journal of Engines* (2017) 10 (4), 2017–01–0930. doi:10.4271/2017-01-0930.

[8] X. Liu, T. Chanko, C. Lambert, M. Maricq. Gasoline Particulate Filter Efficiency and Backpressure at Very Low Mileage. *SAE Technical Paper Series* (2018) 2018-01-1259. doi:10.4271/2018-01-1259.

[9] J. Jiang, J. Gong, W. Liu, T. Chen, C. Zhong. Analysis on filtration characteristic of wall-flow filter for ash deposition in cake. *Journal of Aerosol Science* (2016) 95, 73–83. doi:10.1016/J.JAEROSCI.2016.01.009.

[10] J. Gong, S. Viswanathan, D. A. Rothamer, D. E. Foster, C. J. Rutland. Dynamic Heterogeneous Multiscale Filtration Model: Probing Micro- and Macroscopic Filtration Characteristics of Gasoline Particulate Filters. *Environmental Science & Technology* (2017) 51 (19), 11196–11204. doi:10.1021/acs.est.7b02535.

[11] C. J. Kamp, S. Zhang, S. Bagi, V. Wong, G. Monahan, A. Sappok, Y. Wang. Ash Permeability Determination in the Diesel Particulate Filter from Ultra-High Resolution 3D X-Ray Imaging and Image-Based Direct Numerical Simulations. *SAE International Journal of Fuels and Lubricants* (2017) 10 (2), 2017–01–0927. doi:10.4271/2017-01-0927.

[12] H. Kong, K. Yamamoto. Simulation on soot deposition in in-wall and on-wall catalyzed diesel particulate filters. *Catalysis Today* (2018) 332, 89–93. doi:10.1016/J.CATTOD.2018.07.022.

[13] P. Kočí, M. Isoz, M. Plachá, A. Arvajová, M. Václavík, M. Svoboda, E. Price, V. Novák, D. Thompsett. 3D reconstruction and pore-scale modeling of coated catalytic filters for automotive exhaust gas aftertreatment. *Catalysis Today* (2019) 320, 165–174. doi:10.1016/J.CATTOD.2017.12.025.

[14] B. Ismail, D. Ewing, J.-S. Chang, J. S. Cotton. Development of a non-destructive neutron radiography technique to measure the three-dimensional soot deposition profiles in diesel engine exhaust systems. *Journal of Aerosol Science* (2004) 35 (10), 1275–1288. doi:10.1016/J.JAEROSCI.2004.04.007.

[15] T. J. Toops, H. Z. Bilheux, S. Voisin, J. Gregor, L. Walker, A. Strzelec, C. E. Finney, J. A. Pihl. Neutron tomography of particulate filters: a non-destructive investigation

tool for applied and industrial research. *Nuclear Instruments and Methods in Physics Research Section A: Accelerators, Spectrometers, Detectors and Associated Equipment* (2013) 729, 581–588. doi:10.1016/J.NIMA.2013.08.033.

[16] S. Nishina, K. Takeuchi, M. Shinohara, M. Imamura, M. Shibata, Y. Hashimoto, F. Watanabe. Novel Nondestructive Imaging Analysis for Catalyst Washcoat Loading and DPF Soot Distribution Using Terahertz Wave Computed Tomography. *SAE International Journal of Fuels and Lubricants* (2011) 5 (1), 2011–01–2064. doi: 10.4271/2011-01-2064.

[17] R. Foley, J. Johnson, J. Naber, L. Rogoski. Experimental Measurements of Particulate Matter Distribution in a Catalyzed Particulate Filter. *Emission Control Science and Technology* (2015) 1 (1), 32–48. doi:10.1007/s40825-014-0005-4.

[18] F. Sbrizzai, P. Faraldi, A. Soldati. Appraisal of three-dimensional numerical simulation for sub-micron particle deposition in a micro-porous ceramic filter. *Chemical Engineering Science* (2005) 60 (23), 6551–6563. doi:10.1016/j.ces.2005.05.038.

[19] S. Bensaid, D. Marchisio, D. Fino, G. Saracco, V. Specchia. Modelling of diesel particulate filtration in wall-flow traps. *Chemical Engineering Journal* (2009) 154 (1-3), 211–218.

[20] S. Bensaid, D. L. Marchisio, D. Fino. Numerical simulation of soot filtration and combustion within diesel particulate filters. *Chemical Engineering Science* (2010) 65 (1), 357–363. doi:10.1016/j.ces.2009.06.051.

[21] X. Kong, Z. Li, D. Cai, B. Shen, Y. Zhang. Numerical simulation of the particle filtration process inside porous walls using lattice Boltzmann method. *Chemical Engineering Science* (2019) 202, 282–299. doi:10.1016/J.CES.2019.03.040.

[22] A. P. E. York, T. C. Watling, N. P. Ramskill, L. F. Gladden, A. J. Sederman, A. Tsolakis, J. M. Herreros, I. Lefort. Visualization of the Gas Flow Field within a Diesel Particulate Filter Using Magnetic Resonance Imaging. *SAE Technical Paper Series* (2015) 2015-01-2009. doi:10.4271/2015-01-2009.

[23] M. L. Stewart, C. J. Kamp, F. Gao, Y. Wang, M. H. Engelhard. Coating Distribution in a Commercial SCR Filter. *Emission Control Science and Technology* (2018) 4 (4), 260–270. doi:10.1007/s40825-018-0097-3.

[24] D. Karamitros, G. Koltsakis. Model-based optimization of catalyst zoning on SCR-coated particulate filters. *Chemical Engineering Science* (2017) 173, 514–524. doi: 10.1016/J.CES.2017.08.016.

Chapter 9

Feasibility study of propagator measurements in filters

9.1 Introduction

MRI velocimetry provides an invaluable method of measuring the gas flow fields inside particulate filters, which can then be used to validate models (Chapter 6) and observe the effects of washcoat (Chapter 7) and soot loading (Chapter 8). However, the nature of the measurement, i.e. the relatively long measurement times (140 min to 280 min per filter sample per flow rate), means that it has poor time resolution and is only suitable for measuring steady state gas flow. This is in contrast to the operation of particulate filters on running vehicles, which is highly transient. In order to permit transient MR measurements of gas in particulate filters, an alternative methodology is required.

The time-consuming component of the method used in Chapter 6 is the acquisition of sufficient **k**-space points to produce an image with sufficient resolution to resolve between the inlet and outlet channels. Acquisition times in other systems, such as the flow of complex fluids through pipes [1] or in couette cells [2], have been reduced by decreasing the dimensionality of the data acquired. In the former case, the need for spatial resolution has been completely removed and the rheological parameters of the system can be estimated directly from **q**-space measurements through the use of cumulant and Bayesian analysis [1, 3]. This is essentially using the fluid velocity distribution, or propagator, to characterise the system.

NMR propagators have been used to study a variety of different dynamics systems, including bubble columns [4], granular beds [5], and flow through packed beds [6, 7] and rock cores [8, 9]. It is hypothesised that by making measurements of the NMR propagator along the length of a filter, the gas hydrodynamics inside the filter may be probed on a shorter timescale. To a first approximation, the filter geometry is two square pipes with increasing and decreasing fluid velocities. It is well known that for laminar flow in a cylindrical pipe, the radial flow profile is described by a quadratic function and the propagator is described by a top-hat function. This allows analytical models to be fit to both the propagator and **q**-space response, from which parameters such as the mean velocity can be extracted. However, flow in a square pipe does not have such a simple solution for the flow profile. Several series solutions have been found [10, 11] but no simple analytical solution appears to exist. This is further complicated by the porous walls: these place finite velocity boundary conditions on the problem and distort the flow profile from the non-porous case (Fig. 9.1) [12, 13]. Similarly, the flow profile at the front of the filter is flat and undeveloped. These factors may make methods such as Bayesian analysis more difficult.

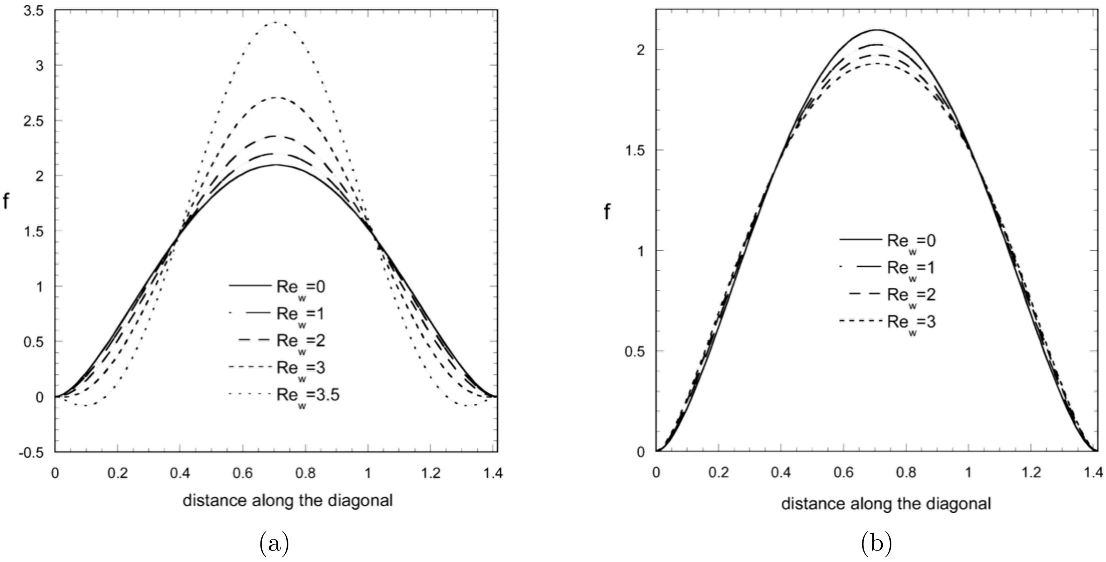

Fig. 9.1: Predicted perturbations to the cross-sectional flow profile in the (a) inlet and (b) outlet channels caused by through-wall velocity of increasing Re_w. Taken from Kostoglou *et al.* [13]

One measurement of flow inside a filter geometry was made by Dr Nicholas Ramskill, shown in Fig. 9.2. The axial and transverse velocity propagators of water flowing along a pair of DPF channels was measured with spatial resolution perpendicular to the channels. The axial velocity (a) is readily resolvable and shows the paraboloid flow profile expected. The transverse velocity (b) is less clear but the positive and negative components corresponding to the through-wall velocity are still distinguishable. This demonstrates that such NMR propagator measurements are feasible using water. However, the experimental details are not known and success may not be possible with gaseous species.

9.2 Scope of study

This chapter aims to test the feasibility of using NMR propagator measurements to study the gas flow in particulate filters at a higher temporal resolution. In particular, the feasibility of applying data fitting to measured propagators in order to extract useful parameters is explored. The velocity profiles of laminar flow in a cylindrical and a square pipe are calculated and their velocity distributions are estimated. 1D z-v_z and z-v_x propagators, i.e. spatially-resolved measurements of the v_z and v_x distribution along the z direction, are simulated from previous CFD results to assess the utility and feasibility of making such measurements. Comparisons between the propagator simulations and the methods used prior in this thesis are made. The effects of diffusion blurring are also considered.

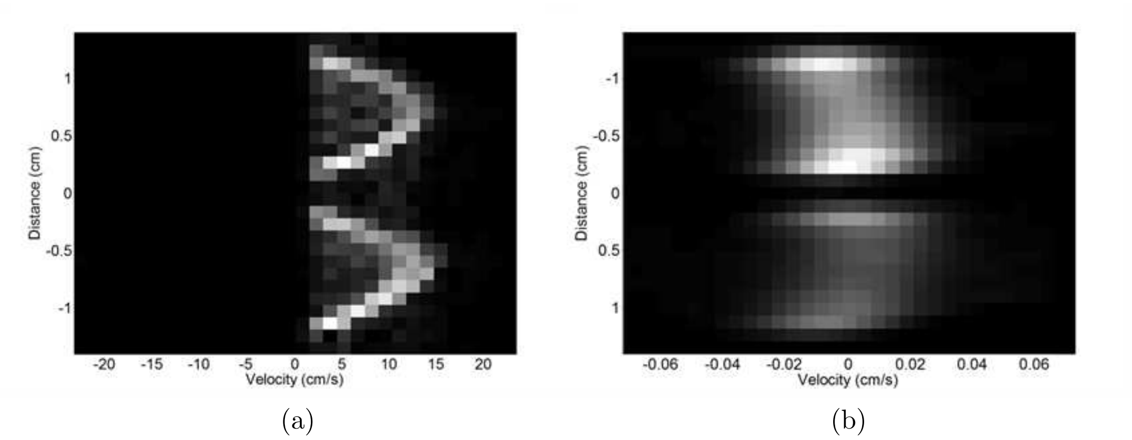

Fig. 9.2: Spatially resolved propagators of water showing (a) axial and (b) transverse through-wall flow in a DPF channel pair (Dr Nicholas Ramskill, unpublished).

9.3 Numerical methods

9.3.1 Flow profiles

The velocity distribution for steady-state, incompressible flow inside a geometry can be calculated by solving the Navier-Stokes equation with the appropriate boundary conditions. In these cases, the boundary conditions are no-slip (i.e. $v_z = 0$) at the edge of the pipe.

For a cylindrical pipe or duct, an analytical solution can be obtained due to the axisymmetric geometry. The well-known solution, described as a function of the radial position from the pipe centre, r, is:

$$v_z(r) = 2\,\langle v_z \rangle \left(1 - r^2/R^2\right), \tag{9.1}$$

where $\langle v_z \rangle$ is the mean axial velocity and R is the pipe radius.

For a square pipe, the solution is more complicated as the symmetry does not simplify the Navier-Stokes equation. Though a simple analytical solution has not been found, several series solutions have. The solution of Bruus [11] is:

$$v_z(x, y) \propto \sum_{n,\mathrm{odd}}^{\infty} \frac{1}{n^3} \left[1 - \frac{\cosh(n\pi x/a)}{\cosh(n\pi/2)}\right] \sin\left(n\pi \frac{y}{a}\right), \tag{9.2}$$

where a is the side length of the square pipe.

The flow profiles for both geometries were calculated numerically in MATLAB® on a 2048 × 2048 raster. For the square pipe, the first 50 terms in the series solution were computed; addition of further terms resulted in a relative difference in mean velocity of less than 10^{-9}. Each flow profile was binned to give the velocity distribution or propagator.

9.3.2 Propagator simulation

The CFD data used in this chapter is taken from Chapter 6 and the method is given there. The data corresponded to $\mathrm{Re_c} = 751$. The data was segmented to separate the inlet and outlet channels; the data corresponding to gas inside the filter wall was not used as the signal relaxes at a great enough rate that it does not contribute to the observed NMR signal. The components of the velocity vector, (v_x, v_y, v_z), were independently binned to give the 'pure advection' propagator. 128 bins were used to simulate a reasonable velocity raster size for an MRI propagator measurement. For v_z, lower and upper velocity bin limits of $-5.6\,\mathrm{cm\,s^{-1}}$ and $67.6\,\mathrm{cm\,s^{-1}}$ respectively were used. For v_x and v_y, limits of $-3\,\mathrm{mm\,s^{-1}}$ and $3\,\mathrm{mm\,s^{-1}}$ were used. This was performed at 128 spatial points along the axial (z) direction, giving a spatial resolution of 1.14 mm per point.

To simulate the effects of diffusion, the simulated propagator was Fourier transformed along the velocity axis, giving a 1D profile of **q**-space data. The **q**-space data was then multiplied with a Gaussian envelope,

$$E(\mathbf{q}) = \exp\left[-4\pi^2 \mathbf{q}^2 \Delta D_0\right], \tag{9.3}$$

where Δ is the observation time and D_0 is the self-diffusion coefficient of the fluid to be simulated. The **q**-space data was then inverse Fourier transformed along the **q** axis to give the diffusion-blurred propagator. Three fluids were simulated in this study: liquid water with $D_0 = 2 \times 10^{-9}\,\mathrm{m^2\,s^{-1}}$ and $\Delta = 100\,\mathrm{ms}$, gaseous $\mathrm{SF_6}$ with $D_0 = 3 \times 10^{-7}\,\mathrm{m^2\,s^{-1}}$ and $\Delta = 1.74\,\mathrm{ms}$, and gaseous propane with $D_0 = 1.1 \times 10^{-6}\,\mathrm{m^2\,s^{-1}}$ and $\Delta = 100\,\mathrm{ms}$.

9.4 Results

9.4.1 Flow profiles and propagators in pipes

The dimensionless flow profile for laminar flow in a square pipe, calculated using the method of Bruus [11], is shown in Fig. 9.3 (a). The flow profile for a cylindrical pipe is shown in (b) for comparison. Both profiles are qualitatively similar with the greatest velocity in the centre and zero velocity at the pipe edges.

The velocity distributions, i.e. the propagators, are shown for both square and cylindrical pipes in Fig. 9.4. The propagator for the cylindrical pipe is a top-hat function as expected from the literature i.e. an equal number of spins at each velocity between $v_z = 0$ and $v_z = 2\langle v_z \rangle$. The square pipe has a greater proportion of spins with slower axial velocities, with a non-linear decrease in the propagator value as the velocity increases. The maximum velocity is greater than for the cylindrical pipe.

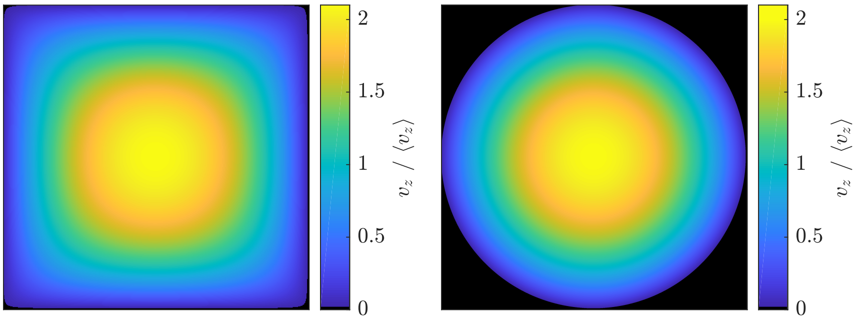

(a) (b)

Fig. 9.3: Cross-sectional flow profiles for laminar flow in (a) a square pipe and (b) a cylindrical pipe. Black signifies regions with no fluid.

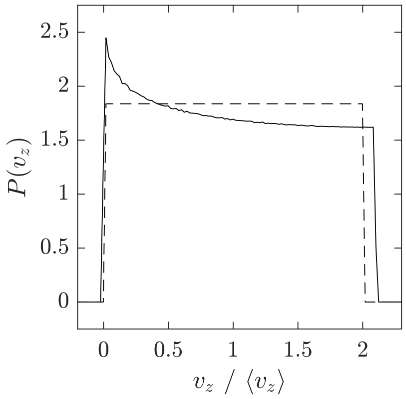

Fig. 9.4: Velocity distributions or propagators for laminar flow in a square pipe (——) and a cylindrical pipe (- - -).

9.4.2 Filter propagator simulations

Axial velocities

The velocity distribution from the CFD simulation results, i.e. the ‘pure advection’ propagator, is shown in Fig. 9.5. The mean velocities in the inlet and outlet channels are shown by the solid and dashed white lines respectively. The contributions of the inlet and outlet channels can be see qualitatively by the two ‘leading edges’ that decrease and increase in peak velocity respectively as z increases. These edges are always greater in velocity than the corresponding mean velocities. For the inlet channel, the leading edge increases in velocity and has a greater propagator value for the first fifth of the filter length. The ‘cross-over’ of the edges occurs at a greater value of z than the mean velocities. At the rear of the filter, negative velocities are seen in the inlet channel contribution.

Slices from the simulated axial velocity propagator at axial positions of $z/L = 0.25$, 0.5 and 0.75 are shown in Fig. 9.6. The data are resolved between the inlet (dashed) and outlet (dotted) channels. The propagator at each axial point takes the form of two near-top hat functions, each corresponding to the inlet and outlet channel contributions. The exact shape of the propagator appears to change with the axial position in the filter. In (a),

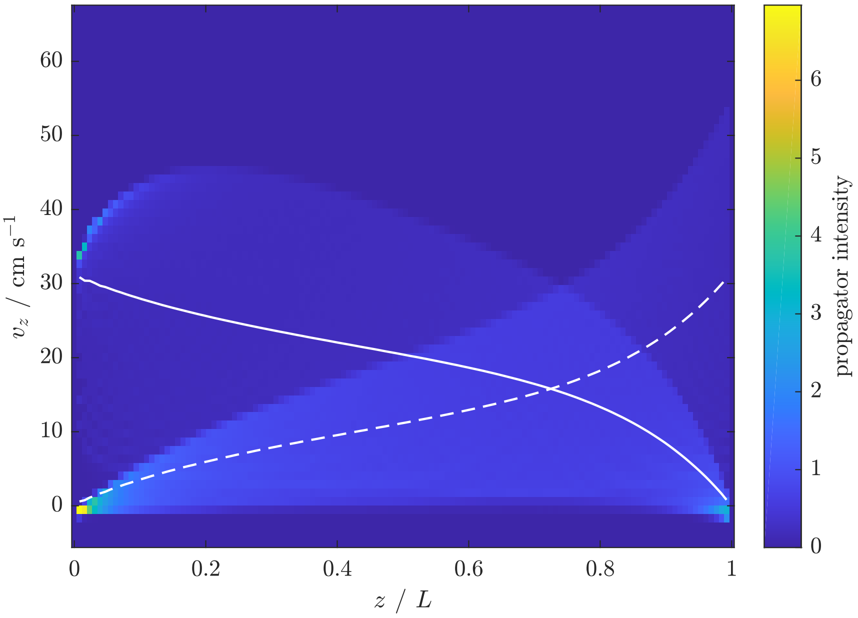

Fig. 9.5: Simulated z-v_z propagator for gas flow in a filter at $\mathrm{Re_c}= 751$. The data has no diffusion blurring. The solid and dashed white lines show the mean inlet and outlet channel velocities respectively.

both the inlet and outlet channels have slight 'u'-shapes in their propagator profiles, which then change to profile more similar to the propagator in Fig. 9.4. In (c), the inlet channel maintains a similar propagator shape while the outlet channel is closer to a top-hat. When the difference in mean velocity between the channels is large, the two contributions can be easily distinguished by eye (a, b). However, when the mean velocities are similar, the overall propagator appears the same as one of the individual channels (c).

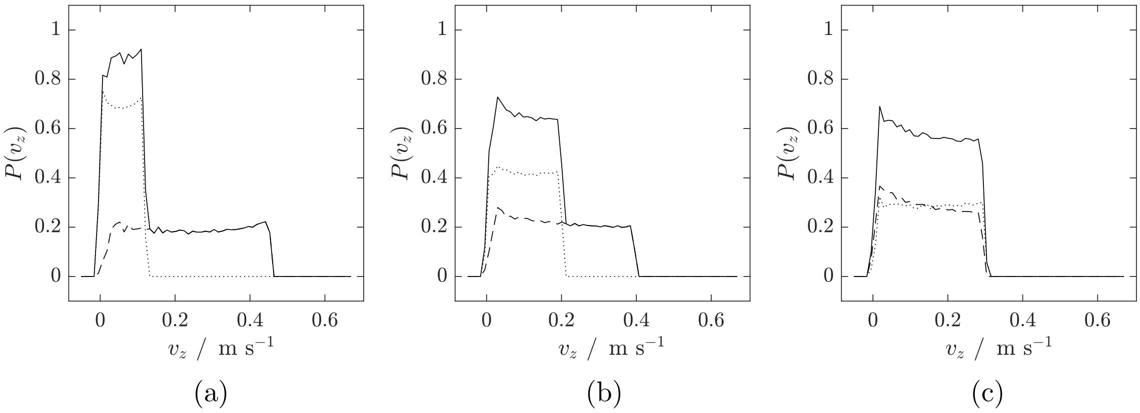

(a) (b) (c)

Fig. 9.6: v_z propagators taken from Fig. 9.5 at $z/L =$ (a) 0.25, (b) 0.5 and (c) 0.75. The dashed and dotted lines indicate the contributions from the inlet and outlet channels respectively.

Figure 9.7 shows the effects of diffusion blurring on the axial velocity propagator for (a) water, (b) SF_6 and (c) propane. Water shows slight blurring but is almost identical in appearance to the pure advection propagator. SF_6 shows significant diffusion blurring and a lower maximum intensity but the general features of the propagator are still distinguishable. Propane shows more blurring than water but much less than SF_6.

Transverse velocities

The distribution of the x-component of the CFD simulated velocity vector is shown in Fig. 9.8. The distribution is symmetric about $v_x = 0$. The shape expected for the through-wall velocity profile, i.e. a skewed paraboloid, can be seen by the regions of high intensity for both positive and negative velocities. The propagator value is non-zero for zero and low velocities due to the low transverse velocities present at the middle of each channel where the axial velocity is greatest. An additional feature is seen in the inlet channel in the first fifth of the filter length where a component of the velocity rapidly decays to zero.

Diffusion blurring was applied to the pure advection propagator and a slice through $x/L = 0.5$ was taken to illustrate the effects (Fig. 9.9). The unblurred propagator shows two sharp peaks either side of $v_x = 0$. The propagator for water is blurred but two maxima can still be observed. For SF_6 and propane, the blurring is so severe that no propagator can be observed.

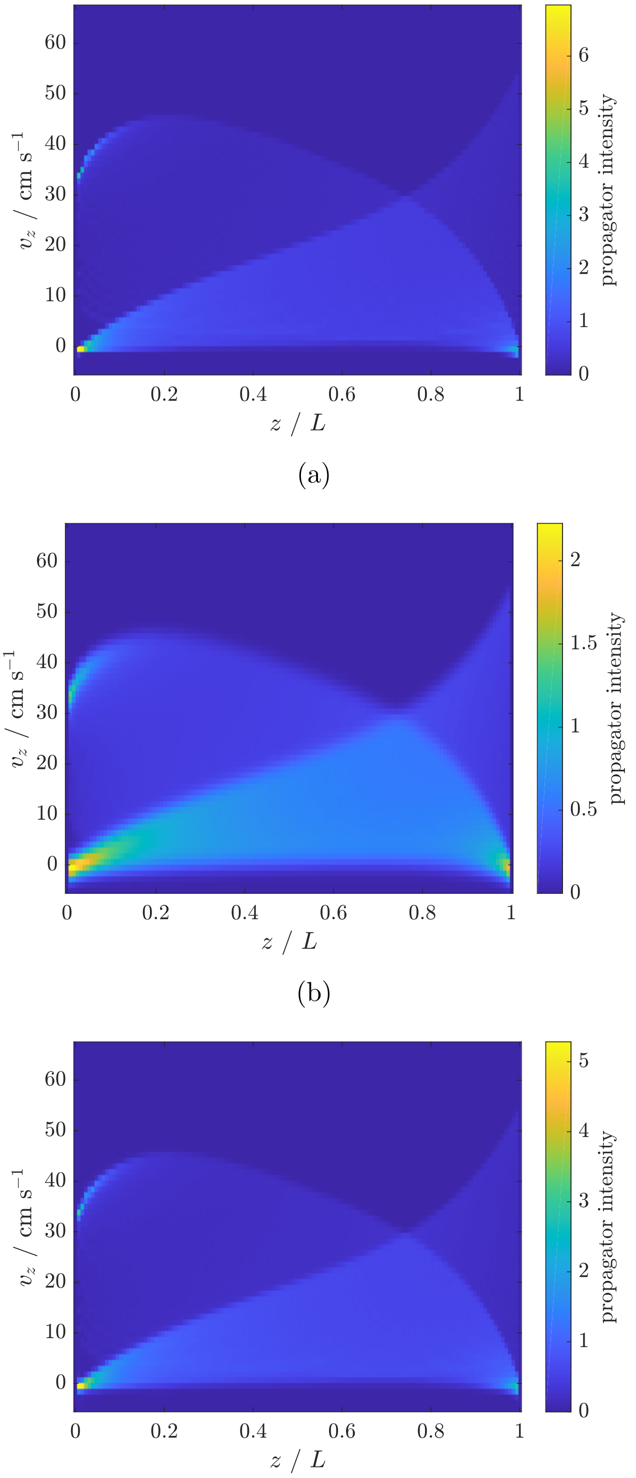

(a)

(b)

(c)

Fig. 9.7: z-v_z propagator from Fig. 9.5 with diffusion blurring applied to simulate (a) liquid water, (b) SF_6 and (c) propane.

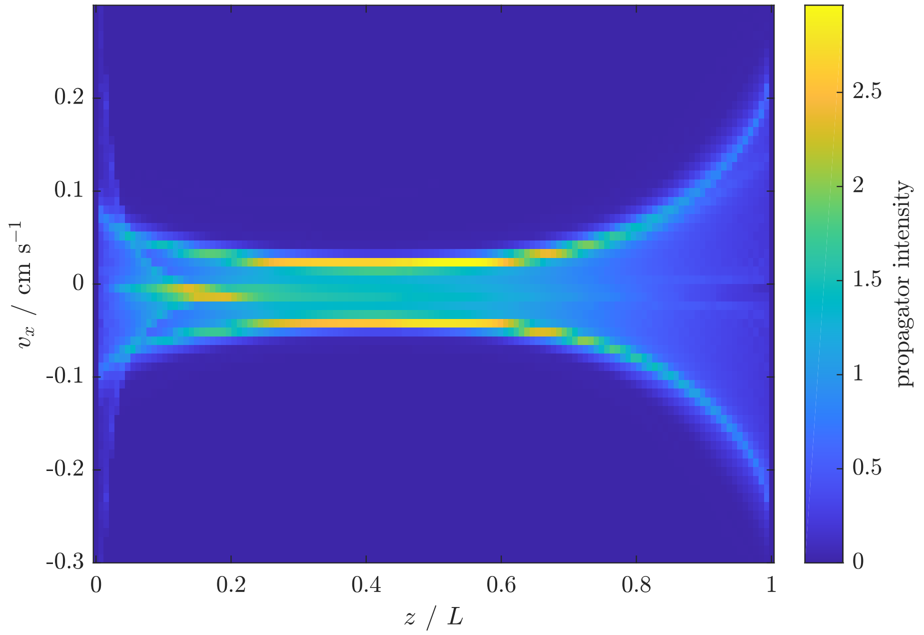

Fig. 9.8: Simulated z-v_x propagator for gas flow in a filter at Re$_\mathrm{c}$= 751. The data has no diffusion blurring.

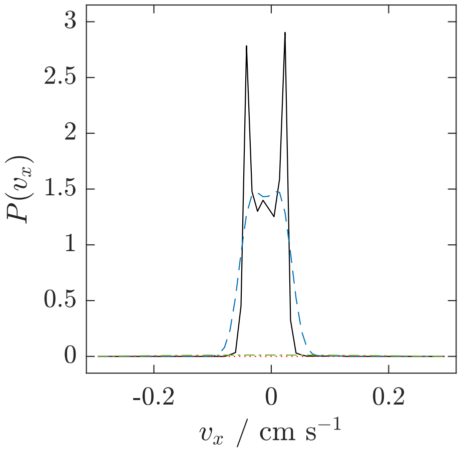

Fig. 9.9: v_x propagators taken from Fig. 9.5 at $z/L = 0.5$ for (—) no diffusion, (- - -) liquid water, (⋯⋯) SF$_6$ and (-·-·) propane.

9.5 Discussion

While the flow profile for developed laminar flow in a square pipe is qualitatively similar to that in a cylindrical pipe (Fig. 9.3), it is not described by a similarly simple mathematical expression. The increased perimeter of the square pipe means there is more lower velocity fluid than in the cylindrical pipe, which is clearly visible in the expected propagators (Fig. 9.4). This lack of a simple analytical description means that, even with the assumption of negligible transverse flow, the propagator cannot be described analytically and so simple model fitting is not feasible for NMR measurements of the propagator. However, state-of-the-art methods such as machine learning may provide a way of extracting useful parameters from such measurements.

The simulated z-v_z propagator still reveals interesting phenomena in spite of the difficulty in extracting parameters from it (Fig. 9.5). The increasing propagator 'edge' of the inlet channel is due to the development of the flow profile as gas enters the filter. This effect will increase the complexity in numerical analysis of propagator measurements as large changes in the flow profile shape are expected as a function of both axial position and Reynolds number. The features in the simulated propagator largely mimic those seen in the mean channel velocities. Reverse flows at the end of the inlet channels are also seen, consistent with the observations in Chapters 4 and 6.

The simulated z-v_x propagator shows the transverse velocities expected in the filter channels (Fig. 9.8), however it does not necessarily reflect the through-wall velocity expected either inside the porous wall or as a volume flow average across the wall. There are two major components observable in the simulated propagator. The first extends across the entire filter and is qualitatively similar to the through-wall velocity expected from measurements and simulations (Chapter 6). The second occurs in the inlet channel in the first fifth of the filter and is attributed to the development of the flow profile in this region. As the flow is developing from a flat profile to that shown in Fig. 9.3 (a), mass and momentum must be transferred towards the centre of the channel to compensate the increase in velocity along the centre line. This may inhibit the flow of gas through the porous wall and hence reduce the mass flow of PM through the wall in the first section of the filter, which Bensaid *et al.* [14] attributed to a *vena contracta*. However, the MRI results from Chapter 4 suggest that the effects of flow contraction are localised to the plugged region and the CFD data that the present simulations are based on have no contraction, which suggests that the reduction in PM mass flow through the wall is due to the development of the laminar flow profile. Further experimental and simulation work may be required to identify and understand any impedance to filtration in the front part of the filter.

As discussed in Chapter 3, the large diffusion coefficients of gases impose stricter limits on the displacements and velocities that can be measured using NMR. Simulating diffusion blurring in the simulated propagators helps understand these limits. For the measurements of v_z, the diffusion blurring is visible but does not obscure the major features of the propagators (Fig. 9.7). This is due to the relatively high ratio of advective motion to diffusive motion, even for SF_6. The effect of the blurring on the expected SNR can be seen by comparing the maximum intensities of the propagators - SF_6 shows a smaller maximum instensity and hence NMR signal, and so will have a lower SNR than water or propane. For the transverse velocities, the effects of diffusion blurring are much more severe due to the lower absolute velocity (Fig. 9.9). The two peaks for water are just visible, whereas the propagators for both gases are too significantly broadened to show any response. As such, it is not expected that the through-wall velocity can be directly measured using gas-phase NMR or MRI.

The results in this chapter do not consider many of the additional experimental and physical challenges posed by gas-phase MRI. Any experiments performed will also need to consider the effects of relaxation, in-flow and out-flow, magnetic susceptibility matches and SNR. The choice of pulse sequence will also be important. Frequency encoded methods will allow shorter acquisition times at the cost of robustness and SNR. The filter geometry will also need considering as many filters are longer than the active region of the NMR r.f. coil. This would require the filter to be physically moved within the magnet in order to acquire data for the full length unless a shorter sample could be used.

9.6 Conclusions

Results from the previous CFD study (Chapter 6) of gas flow inside a DPF geometry have been used to simulate NMR propagators of the same phenomena at $\mathrm{Re_c} = 751$. Axial and transverse velocity distributions were computed at 128 axial points along the filter length by binning the v_z and v_x results inside the inlet and outlet channels. The results inside the porous walls were not considered to reflect the lack of signal observed there in previous MRI experiments. The effects of diffusion were applied to the velocity distributions to produce simulated z-v_z and z-v_x propagators for water, SF_6 and propane.

The z-v_z propagator agreed qualitatively with the results from Chapter 6. The velocity distribution in each channel resembled a top-hat function with perturbations at the higher and lower velocities, consistent with expectations from previous work. The distributions cannot be described by analytical expressions. Flow development in the inlet channel could be seen in the first fifth of the filter, and negative velocities, i.e. reverse flows, were observed at the end of the inlet channel. Diffusion blurring for the gases visibly blurred the propagators but the main features were still observable. Hence, z-v_z propagators may be used in principle to study flow in particulate filters. However, there may be difficulty in accurately quantifying the gas velocity in both channels.

The z-v_x propagator showed the transverse velocities present within the filter channels and agreed qualitatively with previous results i.e. highest through-wall velocity at the filter rear and lowest in the centre. A flow feature, starting with a high velocity at the front of the filter and decreasing quickly into the filter, was observed in the first fifth of the filter length in the inlet channel. This was attributed to the development of the flow profile and is thought to inhibit the through-wall velocity in this region as it is directed to the centre of the inlet channel. The effects of diffusion blurring were observed for a slice at the centre of the filter, where the through-wall velocity is lowest. The blurring for liquid water was significant but the non-zero through-wall velocity could still be distinguished. However, the blurring for both gases was so severe that no propagator could be observed. Hence, direct measurements of the through-wall velocity using gas-phase MRI are probably not presently feasible, which is consistent with the advection-to-diffusion ratio calculated in Chapter 3. The approach taken in this study also does not include any relaxation or magnetic susceptibility effects, which are predicted to further reduce the achievable measurement resolutions due to increased signal attenuation.

9.7 References

[1] T. W. Blythe, A. J. Sederman, J. Mitchell, E. H. Stitt, A. P. E. York, L. F. Gladden. Characterising the rheology of non-Newtonian fluids using PFG-NMR and cumulant analysis. *Journal of Magnetic Resonance* (2015) 255, 122–31. doi:10.1016/j.jmr.2015.03.015.

[2] C. J. Davies, A. J. Sederman, C. J. Pipe, G. H. McKinley, L. F. Gladden, M. L. Johns. Rapid measurement of transient velocity evolution using GERVAIS. *Journal of Magnetic Resonance* (2010) 202 (1), 93–101. doi:10.1016/J.JMR.2009.10.004.

[3] T. W. Blythe, A. J. Sederman, E. H. Stitt, A. P. York, L. F. Gladden. PFG NMR and Bayesian analysis to characterise non-Newtonian fluids. *Journal of Magnetic Resonance* (2017) 274, 103–114. doi:10.1016/j.jmr.2016.11.003.

[4] A. B. Tayler, D. J. Holland, A. J. Sederman, L. F. Gladden. Applications of ultra-fast MRI to high voidage bubbly flow: Measurement of bubble size distributions, interfacial area and hydrodynamics. *Chemical Engineering Science* (2012) 71, 468–483. doi:10.1016/j.ces.2011.11.014.

[5] J. Huntley, T. Martin, M. Mantle, M. Shattuck, A. Sederman, R. Wildman, L. Gladden, N. Halliwell. NMR measurements and hydrodynamic simulations of phase-resolved velocity distributions within a three-dimensional vibrofluidized granular bed. *Proceedings of the Royal Society A: Mathematical, Physical and Engineering Sciences* (2007) 463, 2519–2542. doi:10.1098/rspa.2007.1885.

[6] S. L. Codd, S. A. Altobelli. A PGSE study of propane gas flow through model porous bead packs. *Journal of Magnetic Resonance* (2003) 163 (1), 16–22. doi:10.1016/S1090-7807(03)00111-3.

[7] M. Mantle, A. Sederman, L. Gladden. Single- and two-phase flow in fixed-bed reactors: MRI flow visualisation and lattice-Boltzmann simulations. *Chemical Engineering Science* (2001) 56 (2), 523–529. doi:10.1016/S0009-2509(00)00256-6.

[8] A. Colbourne, A. Sederman, M. Mantle, L. Gladden. Accelerating flow propagator measurements for the investigation of reactive transport in porous media. *Journal of Magnetic Resonance* (2016) 272, 68–72. doi:10.1016/J.JMR.2016.08.018.

[9] D. W. de Kort, A. Reci, N. P. Ramskill, M. Appel, H. de Jong, M. D. Mantle, A. J. Sederman, L. F. Gladden. Acquisition of spatially-resolved displacement propagators using compressed sensing APGSTE-RARE MRI. *Journal of Magnetic Resonance* (2018) 295, 45–56. doi:10.1016/J.JMR.2018.07.012.

[10] M. Spiga, G. Morino. A symmetric solution for velocity profile in laminar flow through rectangular ducts. *International Communications in Heat and Mass Transfer* (1994) 21 (4), 469–475. doi:10.1016/0735-1933(94)90046-9.

[11] H. Bruus. *Theoretical Microfluidics.* Oxford University Press (2007). doi:10.5860/choice.45-5602.

[12] E. J. Bissett, M. Kostoglou, A. G. Konstandopoulos. Frictional and heat transfer characteristics of flow in square porous tubes of wall-flow monoliths. *Chemical Engineering Science* (2012) 84, 255–265. doi:10.1016/J.CES.2012.08.012.

[13] M. Kostoglou, E. J. Bissett, A. G. Konstandopoulos. Improved Transfer Coefficients for Wall-Flow Monolithic Catalytic Reactors: Energy and Momentum Transport. *Industrial & Engineering Chemistry Research* (2012) 51 (40), 13062–13072. doi:10.1021/ie3011098.

[14] S. Bensaid, D. Marchisio, D. Fino, G. Saracco, V. Specchia. Modelling of diesel particulate filtration in wall-flow traps. *Chemical Engineering Journal* (2009) 154 (1-3), 211–218.

Chapter 10

Conclusions and future work

In this thesis, magnetic resonance imaging methods have been used to study gas flow in particulate filter systems. In this chapter, the conclusions drawn in each chapter are summarised and possible future avenues of investigation are explored.

10.1 Conclusions

The work in this thesis can larely be separated into two halves: work focusing on the underlying and fundamental hydrodynamics in particulate filters systems and methods of modelling those, and the preparation and operation of real-world particulate filters. These are summarised separately here.

10.1.1 Underlying hydrodynamics and modelling of filter systems

In Chapter 4, the behaviour of gas entering and exiting a diesel particulate filter was probed using 2D and 3D MRI measurements of gas velocity and turbulent diffusivity. These regions are predicted to have a large impact on the pressure drop behaviour of filter systems and possibly the filtration behaviour, but have not been investigated experimentally before. The MRI results generally agreed with expected phenomena from previous numerical studies in the literature. Gas flow entering the filter was observed to contract smoothly into the inlet channels, with an initially flat flow profile from the large diameter pipe upstream of the filter. Turbulent effects were observed in the plugged region of the entrance, attributed to a small degree of flow separation from the walls, and at the boundary of the plugged and non-plugged region, thought to be due to the sudden transverse velocity the develops. At the filter exit, high velocity jets were observed to form as gas leaves the outlet channels. Negative velocities were observed between some of the jets, corresponding to recirculating flows. Such phenomena was also observed at the end of the inlet channels. Turbulent effects were seen at the interface of the jets and recirculations downstream of the filter, but also in the plugged region of the outlet channels. Consideration of the all turbulent phenomena observed at both regions showed a dependence on the square of the channel Reynolds number, with a ratio of 23:77 between the entrance and exit proportionality constants.

In Chapter 5, preliminary CFD studies were performed to understand the influence of geometry, turbulence and slice averaging on the simulation results and any comparisons with MRI results. Both geometries with porous and non-porous walls (i.e. only the contraction and expansion at the entrance and exit are simulated) showed the broad flow phenomena expected from the MRI results in Chapter 4. This may allow the entrance and exit effects to be decoupled from any internal hydrodynamic effects in future simulations. It is important to select an appropriate turbulence model for the simulations: using a laminar model overpredicted the length of the exit jets, whereas a k-ϵ model predicted the jets to dissipate almost instantaneously. Slice averaging effects were also found to be significant, reducing the apparent maximum velocity in the channels and making the matching of CFD and experimental velocities more challenging.

The hydrodynamics inside particulate filters was investigated in Chapter 6. MRI was used to acquire velocity images along the length of a DPF at several flow rates, allowing the spatial resolution of the inlet and outlet channel velocities to be measured with increasing flow rate. From this data, the through-wall velocity could be calculated along the filter length. As the flow rate increased, more gas was observed to flow through the very rear of the filter and the through-wall velocity became much less uniform. This was predicted to have negative effects on the overall filtration efficiency. Negative velocities were also observed at the rear of the inlet channels. The data also allowed comparison with the predictions from 3D CFD and 1D numerical models. The 3D CFD predictions matched well for channel Reynolds numbers below 1500; it is thought that turbulent effects above this threshold are responsible for disagreement. Because of the agreement in gas velocity, the CFD data could be used to probe the flow profile shape and wall friction behaviour. Both were observed to vary along the length of the filter. Literature correlations for this variation agreed qualitatively for the rear half of the filter but not the front half. This was attributed to the development of flow from a flat to a laminar profile in the first fifth of the filter, which was not considered in the literature correlations. The predictions of the 1D model agreed well at low flow rates but deviated as the channel Reynolds number increased. This was due to two factors: understatement of the momentum convection term in the model, and the assumption of constant flow profile shape and wall friction. Inclusion of a different momentum convection term and the aforementioned correlations improved the 1D model predictions to the point of coincidence with the 3D CFD predictions.

Chapter 9 explores the potential use of NMR propagators in studying gas flow in particulate filters. The CFD predictions validated in Chapter 6 are processed to give simulated propagators for both axial and transverse velocity in the filter channels. While the general flow phenomena expected and observed in previous MRI experiments are also observable, the difficulty in separating the inlet and outlet channel contributions and in mathematically describing the propagator shape precludes quantification. The simulation of diffusion blurring strongly suggests that while the axial velocity components will be measurable, the transverse components will be practically impossible to measure for gas-phase species.

10.1.2 Preparation and operation of real-world filters

In order to meet legal limits on the emission of gaseous pollutants, particulate filters are typically coated with a catalytic washcoat to combine their function with that of a catalytic converter. Application of a washcoat changes the structure of the filter and its porous wall, and hence will change the gas hydrodynamics. Chapter 7 explored the effects of washcoat application on the structure of and transport inside GPFs. Three washcoated filters and one untreated filter were used. Both visual inspection and mercury intrusion porosimetry revealed non-uniform washcoat distributions along the length of the treated filters, with more heterogeneity observed in the dip-coated samples compared with the precision-coated sample. Magnetic resonance velocity imaging was then used to measure the axial and through-wall gas velocity along the filter length. The gas hydrodynamics varied greatly between all GPFs studied. Regions with higher expected washcoat loadings were observed to have relatively smaller through-wall velocities as compared to the washcoat-free GPF. A 1D numerical model, validated in Chapter 6, allowed the spatially-varying wall permeability to be estimated from the velocity measurements; these estimates agreed well with the previous porosimetry results. The predicted pressure drop behaviour using these estimated permeability profiles deviated from the behaviour expected from a uniform permeability. It is also anticipated that non-uniform distributions of washcoat will impact the filtration, regeneration and catalytic behaviour of the filters.

As exhaust gas flows through particulate filters, PM is accumulated in the pores of the filter wall and on the surface of the walls, changing the microstructure of the filter. This in turn affects the gas transport in the filter and hence the filtration behaviour. Chapter 8 investigated the changes in gas transport and wall permeability with increasing soot load using the methods of Chapter 6 and Chapter 7. Two filter samples with different washcoat applications (in-wall and on-wall) were loaded with soot from a commerical passenger GDI engine to three levels. The soot-free filters showed non-uniform washcoat application; due to the commercial nature of the filters, it was not known if this was intentional or not. Both filters showed non-uniform wall permeabilities even without any soot loading; this was attributed to heterogeneous distributions of washcoat inside the filters. As soot was loaded in the filters, the average wall permeability decreased with the regions of initially higher permeability (i.e. those with higher through-wall velocities) decreasing more. This is consistent with previous observations that regions of high through-wall velocity filter more soot due to the higher mass flux of PM. The velocity profile at the rear of the filters was also observed to narrow with increasing soot load, which may indicate the presence of a soot cake in this region.

10.2 Future work

As discussed in Chapter 4, the behaviour of gas entering and exiting a particulate filter can be a significant contributor to the pressure loss and possibly affect filtration behaviour. Future work may focus on improving the CFD codes used to simulate this behaviour and increase agreement with the now-feasible measurements. In particular, any wall-effects or influences from non-ideal flow patterns may be studied to assess their effects, if any: MRI has previously been used to study jet-jet interactions and wall effects in fluidised beds [1]. These results may provide useful information for other models that include entrance and exit effects or account for radial variations in parameters across the filter substrate.

It is known from simulations and experiments that the gas flow upstream of the filter is non-uniform [2–6]. This is largely due to the shape of the inlet diffuser, usually a conical shape, which is needed due to the difference in diameter between the exhaust manifold and the filter can. Various geometries have been predicted and observed to generate large eddies in the diffuser, increasing the pressure loss across the system. In addition, the non-uniform flow can cause radial heterogeneities in filtration and regeneration behaviour [7]. Magnetic resonance velocity imaging is well suited to measure gas flow fields and may be a useful tool in optimising diffuser geometries and validating simulation results.

Chapter 6 explored the numerical modelling of gas flow inside and showed agreement between MRI measurements and 3D CFD simulations of the gas velocity and flow profiles. This gives confidence in using the CFD method to predict gas behaviour in other situations. It may be useful in informing lower dimensional models, such as the 1D model also used, to more accurately describe flow development, flow profile and wall friction effects. However, validation of the 3D CFD method was only achieved for low Reynolds number flows; higher Reynolds numbers ($\mathrm{Re}_\mathrm{c} > 1500$) showed deviation from the MRI measurements that was attributed to the absence of a turbulence model to describe the onset of turbulence in the system. Development of the CFD method, specifically the selection of an appropriate turbulence model to describe the transitional effects expected, may extend the valid range of the method.

Chapter 7 explored the effects of washcoating on a small number of GPF samples and proved effective in measuring both gas flow and wall permeability perturbations. Given the small sample size, it may prove fruitful to apply the method to a wider range of washcoated samples to better understand the effects of different washcoat rheologies, application methods and drying protocols on the final washcoat distribution. Comparison with other characterisation methods, such as X-ray μ-CT or electron microscopy, may help validate or improve the MRI method. In particular, the permeability estimates would ideally be compared with values obtained from pressure drop measurements [8] or pore-scale simulations [9] for validation. Similarly, improvements to the 1D model used in the permeability fitting may increase the accuracy and confidence in the permeability estimates.

Chapter 8 similarly explored the effects of soot loading on two commercial GPF samples at three levels of soot loading. More information may be gained by combining the MRI results with other *operando* measurements, such as the concentration of gaseous species or the PM mass or number. This may allow for comparisons with and development of numerical models. Likewise, quantifying the soot loading through gravimetric means may permit comparison with other work and a further understanding of the interaction between the soot loading and the changes in gas transport. Future work may also look to add more temporal data points by using more degrees in soot loading, or to make *in situ* transient measurements whereby fast measurements are made whilst soot is being loaded. The latter will likely require careful experimental design to ensure that the soot loading is representative and may require a bespoke filter geometry to fit in the active region of the spectrometer and r.f. coil. Such measurements would be highly useful in validating various models of filtration behaviour.

10.3 References

[1] M. Pore, D. J. Holland, T. C. Chandrasekera, C. R. Müller, A. J. Sederman, J. S. Dennis, L. F. Gladden, J. F. Davidson. Magnetic resonance studies of a gas–solids fluidised bed: Jet–jet and jet–wall interactions. *Particuology* (2010) 8 (6), 617–622. doi:10.1016/J.PARTIC.2010.07.015.

[2] C. Turner, D. Thornhill, G. McCullough, S. Patel. Comparison of Experimental PIV Data and CFD Simulations for Flow in a Diesel Particulate Filter Inlet Diffuser. *SAE International Journal of Engines* (2011) 4 (1), 1556–1570. doi:10.4271/2011-01-1241.

[3] M. Mu, X. Li, J. Aslam, Y. Qiu, H. Yang, G. Kou, Y. Wang. A Study of Shape Optimization Method on Connection Cones for Diesel Particulate Filter (DPF). In *Volume 12: Transportation Systems.* ASME (2016) doi:10.1115/IMECE2016-66080.

[4] G. S. Kulkarni, S. N. Singh, V. Seshadri, R. Mohan. Optimum diffuser geometry for the automotive catalytic converter. *Indian Journal of Engineering and Materials Sciences* (2003) 10 (1), 5–13.

[5] M. Mu, J. Sjöblom, H. Ström, X. Li, M. Mu, J. Sjöblom, H. Ström, X. Li. Analysis of the Flow Field from Connection Cones to Monolith Reactors. *Energies* (2019) 12 (3), 455. doi:10.3390/en12030455.

[6] S. Benjamin, C. Roberts. Three-dimensional modelling of NOx and particulate traps using CFD: A porous medium approach. *Applied Mathematical Modelling* (2007) 31 (11), 2446–2460. doi:10.1016/J.APM.2006.10.015.

[7] F. Sbrizzai, R. Verzicco, M. F. Pidria, A. Soldati. Mechanisms for selective radial dispersion of microparticles in the transitional region of a confined turbulent round jet. *International Journal of Multiphase Flow* (2004) 30 (11), 1389–1417. doi:10.1016/J.IJMULTIPHASEFLOW.2004.07.004.

[8] S. Aleksandrova, J. Saul, H. Medina, O. Garcia-Afonso, C. Lin, J. M. Herreros, M. Bevan, S. F. Benjamin. Gasoline Particulate Filter Wall Permeability Testing. *SAE International Journal of Engines* (2018) 11 (5), 03–11–05–0039. doi:10.4271/03-11-05-0039.

[9] P. Kočí, M. Isoz, M. Plachá, A. Arvajová, M. Václavík, M. Svoboda, E. Price, V. Novák, D. Thompsett. 3D reconstruction and pore-scale modeling of coated catalytic filters for automotive exhaust gas aftertreatment. *Catalysis Today* (2019) 320, 165–174. doi:10.1016/J.CATTOD.2017.12.025.

Appendix A

Sulfur hexafluoride recycling rig

For all gas flow experiments, a recycling rig was used to minimise the release of sulfur hexafluoride to atmosphere. This is due to the high Global Warming Potential (GWP) of SF_6 (around 22,800 times greater than CO_2 over 100 years.) A schematic of the rig is given in Fig. A.1 and the components labelled are listed in Table A.1. A DILO Piccolo compressor (M-101) was used to supply high pressure SF_6 to the high pressure reservoir (T-102). The high pressure gas then flowed through the flow loop. The flow loop consisted of upstream and downstream pressure gauges (PI-103, PI-104, GE Druck 104) and a Bronkhurst mass flow controller (FC-101, model F-113AC-M50-AAD-55-E) in addition to the flow cell used for each study. The flow cell was located between L-101 and L-112 and held inside the spectrometer. Gas flow and pressure through the flow loop was controlled using a bypass needle valve (V-112). The gas was then collected in a low pressure reservoir (T-102) for subsequent recycling through the compressor.

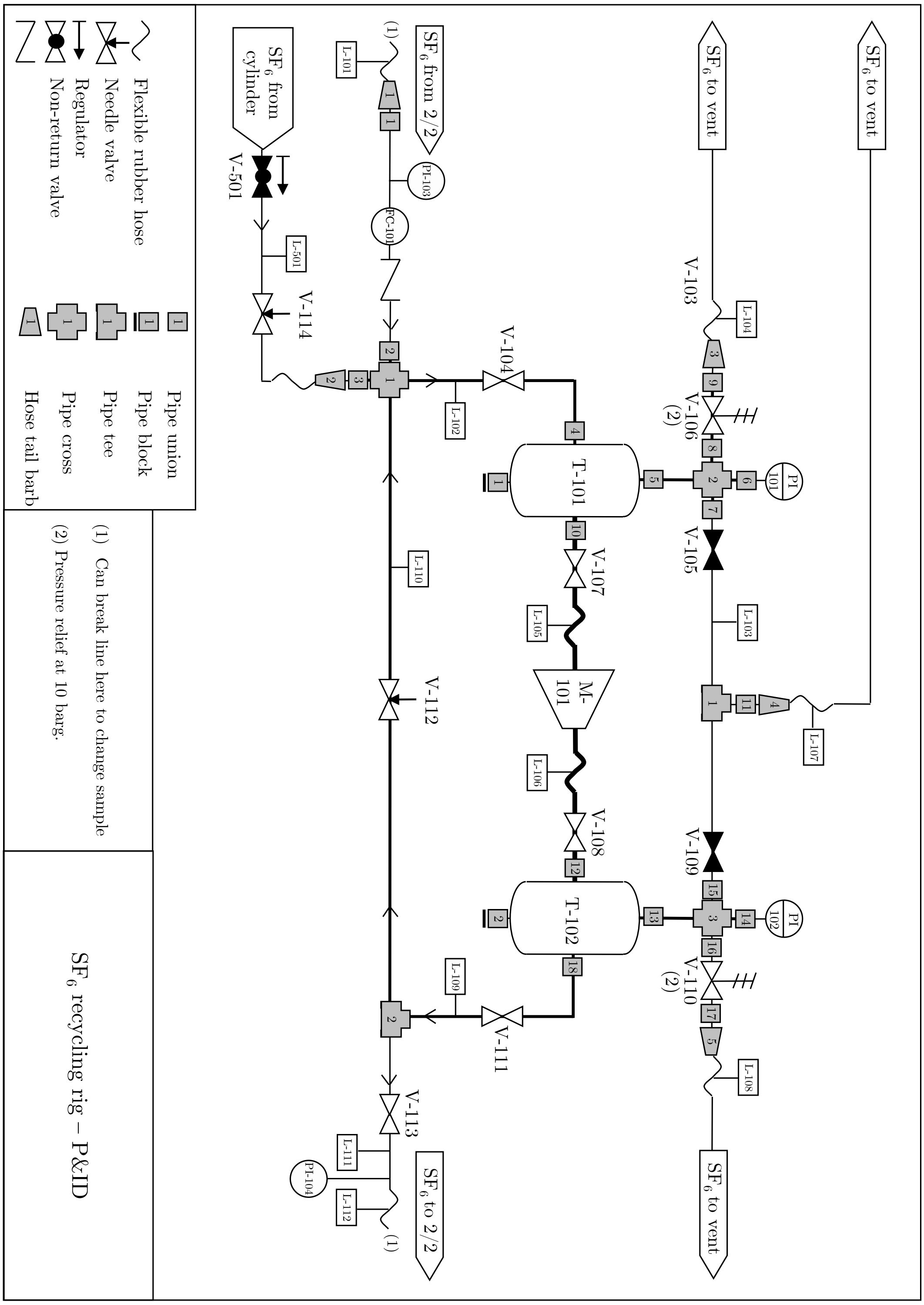

Fig. A.1: P&ID of the recycling SF$_6$ rig used in gas phase MR experiments.

Table A.1: List of rig components labelled in Fig. A.1.

Label	Description
T-101	Pre-compressor receiver, 6 litres
T-102	Post-compressor receiver, 6 litres
M-101	Compressor (DILO Piccolo model B022R01)
M-201	Gas mass flow controller
M-401	Pre-compressor particle filter
M-402	Dry filter
M-403	Post-compressor particle filter
PI-101	Pre-compressor receiver pressure indicator
PI-102	Post-compressor receiver pressure indicator
PI-103	Downstream system pressure indicator
PI-104	Upstream system pressure indicator
FC-101	Mass flow controller
V-103	Recirculation rig inlet non-return valve
V-104	Pre-compressor receiver inlet shut-off valve (normally open)
V-105	Pre-compressor receiver exhaust valve (normally closed)
V-106	Pre-compressor receiver pressure relief valve (10 barg)
V-107	Pre-compressor shut-off valve (normally open)
V-108	Post-compressor shut-off valve (normally open)
V-109	Post-compressor receiver exhaust valve (normally closed)
V-110	Post-compressor receiver pressure relief valve (10 barg)
V-111	Post-compressor receiver shut-off valve (normally open)
V-112	Gas recycle line needle valve
V-113	Recirculation rig outlet shut-off valve (normally open)
V-114	Needle valve between cylinder and recirculation unit (closed during operation)
V-401	Pre-compressor pressure reducer (down to 5 barg)
V-402	Post-compressor check (non-return) valve
V-501	Gas cylinder regulator (normally closed)

Appendix B

Filtration efficiency model

The analytical model used to estimate the filtration efficiency in Chapters 6 and 7 is that of Konstandopoulos *et al.* and is described below. In the original work, it is proposed that the filter wall can be described as a signle spherical collector of diameter D_c that exhibits an overall filtration efficiency of η_T. As discussed in Chapter 1, there are three principle mechanisms through which PM can be filtered: intertial impact, interception and Brownian diffusion. Inertial impact is dominant for larger particles with high inertia and characterised by large Stokes numbers, and is not expected to be significant for the PM sizes encountered in diesel exhaust. Hence, only the contributions of the interception and Brownian diffusion mechanisms are considered in this model. The total efficiency is determined by the contributions of both the Brownian efficiency η_B and the interception efficiency η_I.

Brownian filtration efficiency

The contribution of the Brownian efficiency for a single sphere collector is given by

$$\eta_{\mathrm{B}} = 3.5 K_\epsilon \mathrm{Pe}^{-2/3}. \tag{B.1}$$

K_ϵ is the Kuwubara correction term, which accounts for the effect that neighbouring collectors have on the single sphere collector, which is assumed to be isolated. The correction term is given by

$$K_\epsilon = \left(\frac{\epsilon}{2 - \epsilon - \frac{9}{5}(1-\epsilon)^{1/3} - \frac{1}{5}(1-\epsilon)^2} \right)^{1/3}, \tag{B.2}$$

where ϵ is the porosity of the wall. The Peclet number, Pe, is given by

$$\mathrm{Pe} = \frac{v'_{xy} D_{\mathrm{c}}}{D_{\mathrm{s}}}, \tag{B.3}$$

where v'_{xy} is the interstitial velocity of gas through the filter wall, given by $v'_{xy} = v_{xy}/\epsilon$. v_{xy} is the average through-wall velocity from the MRI measurements. D_{s} is the particle diffusivity, calculated from the Stokes-Einstein equation,

$$D_{\mathrm{s}} = \frac{k_{\mathrm{B}} T C_{\mathrm{C}}}{3\pi\mu D_{\mathrm{p}}}, \tag{B.4}$$

where k_{B} is the Boltzmann constant, T is the temperature, μ is the dynamic viscosity of the gas, D_{p} is the PM diameter and C_{C} is the Stokes-Cunningham slip correction factor.

This factor corrects for the drag force on the solid particles as the no-slip assumption cannot be made when the mean-free path, λ, of the PM approaches the particle diameter, which is expected for the sizes typical of diesel PM. The factor is given by

$$C_\mathrm{C} = 1 + \mathrm{Kn}\left\{\alpha + \beta \exp\left[\frac{\gamma D_\mathrm{p}}{\lambda}\right]\right\}, \tag{B.5}$$

where Kn is the Knundsen number, $\alpha = 1.257$, $\beta = 0.4$ and $\gamma = 1.1$. Finally, the size of the single sphere collector is given by

$$D_\mathrm{c} = 1.5\frac{1-\epsilon}{\epsilon}d_\mathrm{pore}, \tag{B.6}$$

where d_pore is the mean pore size of the filter wall.

Interception efficiency

The efficiency of the single sphere collector by the interception mechanism is

$$\eta_\mathrm{I} = 1.5N^2\frac{K_\epsilon^3}{(1+N)^s}, \tag{B.7}$$

where N is the ratio of the PM and single sphere collector diameters, $D_\mathrm{p}/D_\mathrm{c}$, and s is given by

$$s = \frac{3-2\epsilon}{3\epsilon}. \tag{B.8}$$

Total filtration efficiency

Assuming that the contributions of the two mechanisms are independent, the total filtration efficiency η_T is simply the sum of the contributions, $\eta_\mathrm{B} + \eta_\mathrm{I}$. To obtain the total filtration efficiency across the entire filter wall E, the single sphere collector efficiency must be integrated over the thickness of the wall, w_w. Calculating this gives the final result,

$$E = 1 - \exp\left[-1.5\frac{1-\epsilon}{\epsilon}\frac{w_\mathrm{w}}{D_\mathrm{c}}\eta_\mathrm{T}\right]. \tag{B.9}$$